UNDERSTANDING THE EQUATORIAL OCEAN: THEORETICAL AND OBSERVATIONAL STUDIES

Anna Rabitti

Anna Rabitti

NIOZ Royal Netherlands Institute for Sea Research
Department of Physical Oceanography

Present address:
Royal Netherlands Institute for Sea Research
Department of Physical Oceanography
PO box 59, 1790AB Den Burg, Netherlands
Anna.Rabitti@nioz.nl

Cover picture: Detail of an omen collection on clay tablet from Uruk/Warka (Iraq), 312-141 BC.
ⓒ Royal Museums of Art and History – Brussels.
Used upon permission of Prof. dr. Eric Gubel, Senior Keeper Antiquity Dpt.

This illustrated text covers the omens which can be deduced from the observation of the moon and the planets. According to a system which has hitherto not been deciphered, a month and a planet are assigned to each of the twelve peaks of the chart. The resemblance to the periodic internal wave ray trajectories in a fluid sphere as the one in figure 4.9b on page 112 is surprising and fascinating.

UNDERSTANDING THE EQUATORIAL OCEAN: THEORETICAL AND OBSERVATIONAL STUDIES

BEGRIP VAN DE EQUATORIALE OCEAAN: THEORETISCHE EN WAARNEMINGSSTUDIES

(met een samenvatting in het Nederlands)

Proefschrift

ter verkrijging van de graad van doctor aan de Universiteit Utrecht op gezag van de rector magnificus, prof.dr. G.J. van der Zwaan, ingevolge het besluit van het college voor promoties in het openbaar te verdedigen op dinsdag 26 januari 2016 des middags te 12.45 uur

door

ANNA RABITTI

geboren op 1 januari 1985
te Venetië, Italië

to Teo,
welcome on board!

"None believes in models,
except those who develop them.
Everybody believes in observations,
except those who collect them."

CONTENTS

SUMMARY

From a fluid dynamics point of view, our ocean can be at first described as a rotating, stratified fluid. While at mid- and high-latitudes rotation and stratification are relatively well understood and represented in the equations of motion, this is not true for a vast portion of the ocean: the equatorial regions ($\pm 2.5°$). Because of these shortcomings, many aspects of the equatorial dynamics remain to date unexplained, and with them a clear picture of the role of equatorial dynamics in the global ocean circulation.

Moreover, observations have long shown that, dynamically, the oceans differ in the narrow belt near the equator compared to off-equatorial regions. Some of the features characterising the equatorial belt have been identified; for example, the Equatorial Deep Jets (EDJs), and the anomalous internal wave field and mixing properties, but they still lack a complete and coherent understanding. The transition between equatorial and off-equatorial regions also lacks a proper localisation and interpretation.

In this thesis work, we have investigated how the notion of an "equatorial boundary layer" can be used, theoretically and observationally, and how it can be of help in overcoming the existing limits of our understanding.

First, the concept of "equatorial boundary layer" can be interpreted as a wave-guide for surface and interfacial equatorial waves. In chapter 2 we thus review the analytical wave solutions for the equations of motion in the equatorial case. In particular, we explore the consequences of restoring the non-traditional terms back in the classical set of equations. These terms are related to the horizontal component of the Coriolis force, and are usually neglected in mid-latitude dynamics. However, their inclusion is well motivated at low-latitudes. For surface and interfacial waves, a non-traditional system of equations implies a coupling between vertical and meridional coordinates, and leads to non-separable equations of motion and to new analytical wave solutions (both of Kelvin type and with non-vanishing meridional velocity). Remarkably, the traditional dynamics cannot be described as a particular limiting case of a more general and robust non-traditional theory, but instead supports waves that simply cannot exist when the full Coriolis force is considered.

If, on the other hand, one is interested in the deep equatorial dynamics, exploring the role of low-latitude, three-dimensional internal waves analytically is impossible. At the end of chapter 2 we show why this is the case, and thus motivate the approach adopted in chapters 3 and 4. There, a three-dimensional, internal wave ray tracing algorithm is developed and applied to the spherical

shell domain and to the full fluid sphere as paradigmatic examples of the study of internal wave dynamics in geometries of geophysical (and astrophysical) relevance. The ray tracing approach exploits the fact that internal wave energy propagates along rays with a fixed inclination with respect to the restoring force, given by the wave frequency. In symmetry breaking domains such as the spherical shell (chapter 3), interactions between rays and domain boundaries give rise to trapping of particular rays (frequencies) first to meridional planes, and second to internal wave attractors. These limiting ray trajectories might be also interpreted as "internal boundary layers" and their occurrence in the equatorial region is suggestive of a possible role they might play in the real ocean in collecting energy from off-equatorial regions towards the equator, and in triggering mixing and high shear hot spots far from the ocean boundaries.

The study of the idealised full sphere case (chapter 4) enables us to interpret results from three-dimensional ray tracing, since the sphere is one of the very few domains where analytical solutions for internal waves are known. A comparison between results obtained with the new algorithm and the old wave solutions reveals the value of ray tracing. No one-to-one correspondence is found between the two approaches. However, ray tracing is shown to be a robust tool when one is interested in the general regularity (or non-regularity) of a system. In fact, we can now extend to a three-dimensional framework the correspondence, generally valid in two-dimensional domains, periodic orbits = regular solutions, attractors = singular solutions, chaotic orbits = null solutions. The three-dimensional ray tracing also unveils a new class of solutions, both in the spherical shell and in the sphere, that for their intrinsically three-dimensional nature were not described with the classical, separable analytical solutions. Because of these new issues, within this thesis, chapter 4 is perhaps the one opening the largest number of questions: on what we know on internal wave dynamics in fully bounded domains, and which would be the best way to describe and follow their propagation.

In chapter 5 we leave the idealised domains and rays and we turn to ocean observations, using a set of *in situ* data collected in the western equatorial Atlantic Ocean. The data set consists of a CTD/LADCP transect at 38°W, between 0° and 2°N, and of current time series from December 2007 to July 2009 at about 37°W, between 0° and 2.5°N, with different vertical resolution, between 500 and 4500 m. A direct evaluation of non-traditional terms in the geostrophic context shows that they are just too weak to either be measured in a quasi-synoptic transect, or to actively play a role in the dynamics. However, even the classical, equatorial geostrophy fails near the equator in explaining observations. Because of the strong baroclinic pressure gradient, no balance is in fact observed in the quasi-synoptic transect without at least a 30 km spatial smoothing, suggesting the importance of the time dependent terms. Furthermore, we have been able to isolate various equatorial features, brought to light by different and indepen-

dent measurements (hydrography and currents). The spatial superposition of features that at first sight appear unrelated - small vertical structure in the current field, anomalous mixing properties and latitudinally varying near-inertial wave polarization properties - suggests indeed the existence of an "equatorial boundary layer", whose location is related to the distribution of planetary angular momentum in the region, and that is dynamically distinct from the off-equatorial regions. The transition is observed to take place at about 1.5°N. The presence of observational hints of equatorial, low-frequency internal wave trapping can be interpreted as the link between findings in chapter 5 and those in chapter 3. However, meridional and vertical resolution of the data are unfortunately insufficient to make definitive statements on this issue.

By means of a variety of approaches, the present study points out the challenges in understanding equatorial ocean dynamics. It is fascinating to think of how standard theory fails in accurately describing such a big portion of our ocean. Here, we suggest that the notion of "equatorial boundary layer" can be of help when apparently unrelated features come together, indeed making the low-latitude belt a distinct place from the more familiar mid-latitude regions, a place where usual approximations fall short, classical dynamical balances break down, and where terms in the equations of motion, which are negligible in other parts of the domain, become important.

SAMENVATTING

Vanuit vloeistofdynamisch perspectief kan onze oceaan gezien worden als een roterende, gelaagde vloeistof. Hoewel op gematigde en hoge breedtes, rotatie en gelaagdheid relatief goed begrepen en beschreven worden in onze bewegingsvergelijkingen, is dit voor een belangrijk deel van de oceaan niet het geval: de gordel rond de evenaar (±2.5°). Vanwege deze tekortkomingen blijven veel aspecten van de equatoriale dynamica onverklaard. Daarmee ontbreekt een helder beeld van de rol van de equatoriale dynamica in de gobale oceaancirculatie.

Sterker, waarnemingen laten al sinds lang zien dat de oceaan in een nauwe gordel rond de evenaar dynamisch verschilt met gebieden daarbuiten. Sommige verschijnselen die de equatoriale gordel karakteriseren zijn bekend; bijvoorbeeld de Equatoriale Diepe Stromen, en het afwijkende interne golfveld met diens mengingseigenschappen, maar zij missen nog compleet en samenhangend begrip. De overgang tussen de equatoriale zone en de gebieden daarbuiten is ook onvoldoende gelocaliseerd en geïnterpreteerd.

In dit proefschrift is onderzocht hoe het begrip "equatoriale grenslaag" gebruikt kan worden, theoretisch alswel observationeel, en hoe dit ons beperkte inzicht daarin kan verbreden.

Ten eerste kan het begrip "equatoriale grenslaag" geïnterpreteerd worden als golfgids voor equatoriale oppervlakte- en grensvlakgolven. In hoofdstuk 2 geven we daarom een overzicht van analytische equatoriale golfoplossingen van de bewegingsvergelijkingen. Speciaal onderzoeken we de gevolgen van het meenemen van niet-traditionele termen. Deze termen zijn gerelateerd aan de horizontale component van de Corioliskracht, die op gematigde breedtes gewoonlijk verwaarloosd worden. Echter, er zijn goede redenen om ze rond de evenaar wel mee te nemen. Voor oppervlakte- en grensvlakgolven, impliceren de niet-traditionele vergelijkingen een koppeling van verticale en meridionale coördinaten, en leiden tot niet-separeerbare bewegingsvergelijkingen en nieuwe analytische golfoplossingen (beiden Kelvingolven met niet-verdwijnende meridionale snelheid). Opmerkelijker wijs kan de traditionele dynamica niet verkregen worden als een speciaal geval van de meer algemene, en meer robuuste niet-traditionele theorie, maar lijkt deze golven te dragen die simpelweg niet kunnen bestaan wanneer de volledige Corioliskracht wordt meegenomen.

Wanneer men echter geïnteresseerd is in diepe equatoriale dynamica blijkt aan de andere kant beschouwing van de rol van nabij-equatoriale, driedimensionale golven analytisch onmogelijk. Aan het eind van hoofdstuk 2 laten we zien

waarom dat het geval is en motiveren daarmee de aanpak die in hoofdstukken 3 en 4 gevolgd wordt.

Daar wordt een driedimensionaal algoritme ontwikkeld om interne golfpaden te volgen. Dit wordt toegepast in een bolschil en in de volledig met vloeistof gevulde bol als sprekende voorbeelden van de studie naar interne golfdynamica in domeinen met geofysische (en astrofysische) relevantie. Deze stralenmethode gebruikt het feit dat interne golfenergie propageert langs paden die een vaste hoek maken met de richting van de terugdrijvende kracht, een hoek bepaald door de golffrequentie. In symmetrie-brekende domeinen, zoals de bolschil (hoofdstuk 3), leiden interacties van golfstralen met domeinranden tot invanging van speciale golfstralen (frequenties), invanging ten eerste op meridionale vlakken, en ten tweede op interne golfaantrekkers. Deze limietbanen kunnen zelf ook als "interne grenslagen" geïnterpreteerd worden. Hun aanwezigheid in het equatoriale gebied suggereert de mogelijke rol die ze in de echte oceaan zouden kunnen spelen als vergaarbakken van golfenergie afkomstig vanaf gematigde breedtes, en als plekken waar, ver van oceaanranden, menging en sterke schering geïnduceerd kunnen worden.

De studie naar golfgedrag in een bolvormig domein (hoofdstuk 4) stelt ons in staat om de resultaten van de drie-dimensionale stralenmethode te interpreteren omdat de bol een van de weinige domeinvormen is waarvoor interne golfoplossingen bekend zijn. Een vergelijking van de resultaten verkregen met het nieuwe algoritme en de oude golfoplossingen laat de echte waarde van de stralenmethode zien. Er is geen een-op-een correspondentie tussen beide methodes. Echter, de stralenmethode blijkt een robuust gereedschap wanneer men geïnteresseerd is in de algehele regelmatigheid (of onregelmatigheid) van het systeem. In feite kunnen we hiermee nu ook in drie dimensies de samenhang vaststellen die in het algemeen in twee-dimensionale domeinen bestaat tussen periodieke = regelmatige oplossingen, aantrekkers = singuliere oplossingen, en chaotische banen= geen oplossingen. De constructie van driedimensionale golfpaden laat ook het bestaan van een nieuwe klasse van oplossingen zien, zowel in de bolschil als in de bol, welke, vanwege hun intrinsiek driedimensionale aard, niet beschreven worden door de klassieke verzameling van scheidbare analytische oplossingen.

Vanwege deze aspecten oppert hoofdstuk 4 uit dit proefschrift wellicht de meeste vragen: over wat we van interne golven in volledig gevulde vloeistofbasins precies weten en over wat de beste manier is om ze te beschrijven en te volgen.

In hoofdstuk 5 verlaten we de geïdealiseerde vloeistofdomeinen en golfstralen en wenden we ons tot oceaanobservaties, gebruikmakend van *in situ* waarnemingen in de Westelijk-equatoriale Atlantische Oceaan. De waarnemingen zijn verkregen langs een CTD/LADCP-raai op 38°W, tussen 0° en 2°N, en, in de vorm van tijdreeksen, met behulp van stroommeters/ADCPs verankerd van

December 2007 tot Juli 2009 op ca 37°W, tussen 0° en 2.5°N, met wisselend oplossend vermogen tussen 500 en 4500 m diepte. Een directe evaluatie van niet-traditionele termen in geostrofe context laat zien dat ze te zwak zijn, zowel om quasi-synoptisch direct gemeten te kunnen worden, alswel om dynamisch een actieve rol te kunnen spelen. Echter, ook klassieke equatoriale geostrofie kan de waarnemingen niet verklaren. Vanwege de sterke barokliene drukgradïent bestaat er in feite helemaal geen quasi-synoptische balans over deze raai, tenminste niet zonder een 30 km ruimtelijke middeling toe te passen, hetgeen het belang van tijdsafhankelijke termen onderstreept.

Daarnaast hebben we enkele equatoriale verschijnselen weten te isoleren, zichtbaar gemaakt door verschillende soorten onafhankelijke metingen (hydrografie, stromingen). De ruimtelijke superpositie van verschijnselen die op het eerste oog niet gerelateerd zijn - kleine verticale structuren in het stromingsveld, abnormale menging, en breedtegraad-afhankelijke polarisatie van nabij-inertiaal golven -, suggereren de aanwezigheid van een "equatoriale grenslaag" wiens locatie gerelateerd is aan de ruimtelijke verdeling van impulsmoment en die dynamisch verschilt van andere gebieden. De overgang tussen beiden lijkt rond 1.5°N plaats te vinden. De aanwezigheid van op waarnemingen gebaseerde suggesties van equatoriale, laagfrequente interne golf-invanging kan geïnterpreteerd worden als de verbinding tussen de bevindingen in hoofdstuk 5 en die in hoofdstuk 3. Echter, de meridionale en verticale resolutie van de waarnemingen is helaas onvoldoende om op dit gebied solide conclusies te trekken.

Gebruikmakend aan een veelheid van methodes wijst deze studie op de uitdagingen die er liggen bij het begrijpen van equatoriale dynamica. Het is fascinerend te zien hoe standaard theorie tekortschiet in het beschrijven van grote delen van de oceaan. Hier stellen we voor dat introductie van het concept "equatoriale grenslaag" behulpzaam kan zijn wanneer verschillende verschijnselen bij elkaar worden gebracht, wat er, inderdaad, toe leidt dat de gordel met lage breedtegraden ander gedrag vertoont dan de meer bekende gematigde breedtes. Dit is daarmee een plek waar gewone benaderingen tekort schieten, de klassieke krachtenbalans niet meer opgaat, en waar termen in de bewegingsvergelijkingen die elders verwaarloosbaar zijn belangrijk worden.

1

INTRODUCTION

1.1 THE EQUATORIAL OCEAN

There are many ways to describe our ocean. From a fluid dynamics point of view, it can be at first described using only two of its many characteristics: rotation and density stratification. Earth's rotation has shaped our planet and its surface, and keeps on influencing ocean and atmosphere's motion day after day. Ocean's density stratification is due to a combination of several geophysical processes, such as insolation, wind, fresh water input, turbulent processes, etc., unevenly distributed at different locations and depths. If one is interested in understanding and modelling currents and waves in the ocean, these two aspects cannot be neglected. However, while at mid- and high-latitudes rotation and stratification are relatively well understood and represented in the equations of motion, there is a vast portion of the ocean where the role of rotation is exceptional and difficult to capture, and where stratification and related properties are still unclear. This is the equatorial ocean.

We loosely define the equatorial ocean as the latitudinal region between 2.5°South and 2.5°North. This latitudinal extension is however very small compared to its extent in longitude, larger than 120° in the Pacific Ocean and larger than 40° in the Atlantic Ocean. The volume of equatorial ocean water is thus not negligible, and its zonal extent allows for large wind energy input. Moreover, this ocean belt is characterised by the highest average insolation per year. It follows that the equatorial regions play a fundamental role in the global ocean circulation, controlling the exchanges between the two hemispheres as well as an important part of the heat exchange between ocean and atmosphere.

Understanding equatorial dynamics constitutes thus a crucial step towards a better representation of the whole Earth's climate system, particularly of interest in recent years, as we are facing unprecedented rapid changes in the delicate equilibrium of our planet [IPCC, 2014]. However, despite its importance, many aspects of the equatorial ocean dynamics remain to date unexplained. This limited understanding is due both to observational and theoretical shortcomings.

In fact, observations in all three oceans have long shown that dynamically the oceans differ in the narrow belt near the equator compared to off-equatorial regions. Some of the features characterising the equatorial belt have been already theoretically or observationally identified, for example, the Equatorial Deep Jets (EDJs) [Cromwell, 1953; Cromwell *et al.*, 1954; Firing, 1987; Ponte and Luyten, 1989; Weisberg and Horigan, 1981; Reppin *et al.*, 1999; Gouriou *et al.*, 2001; Send *et al.*, 2002; Dengler and Quadfasel, 2002; Bunge *et al.*, 2008], the anomalous internal wave field and mixing properties [Colin de Verdière and Schopp, 1994; Gregg *et al.*, 2003; van Haren, 2005; Gerkema *et al.*, 2008], but they still lack a complete and coherent understanding.

The main consequence of this lack of understanding of low latitude dynamics, and, in particular, of deep equatorial mean current and wave field, is that both ocean atlases and climate models, often give a very simplified picture of many physical processes in this band, and particularly, that those of small-scale are badly represented, if at all. It follows that the value of observations and models is limited, and often a blank stripe replaces the inadequate field or model outcome in this latitudinal belt (see for example figure 1.1, or similar outcomes as in, for example, Alford [2003]; Alford and Zhao [2007b]; Juliano and Alves [2007]; Dong *et al.* [2014]). Consequently, reliability in the equatorial regions is substantially lower than in mid-latitude regions, and commonly accepted to be so. Moreover, the transition between equatorial and off-equatorial regions also lacks a proper framework of interpretation, in relation, for example, to the dynamics of cross-equatorial transport. In fact, it is neither obvious how these changes in dynamics imply the observed sharp transitions (which are much sharper than existing models predict [Gregg *et al.*, 2003]), nor how the choking effect of this band of zonal currents (the EDJs) affects the meridional transport of heat, especially in the Atlantic Ocean, of crucial relevance to Western European climate, and how global climate change might disturb and alter all these processes. As we have seen in figure 1.1, global models are of little use at these low-latitudes.

In the following section an overview is given of the diverse challenges one is facing when dealing with equatorial dynamics and its peculiar combination of rotation and stratification.

1.2 CHALLENGES IN UNDERSTANDING EQUATORIAL DYNAMICS

We have said that all three oceans show profound differences in the narrow belt near the equator when compared to off-equatorial regions. But which aspects of the dynamics, both theoretical and observational, are characterising these regions?
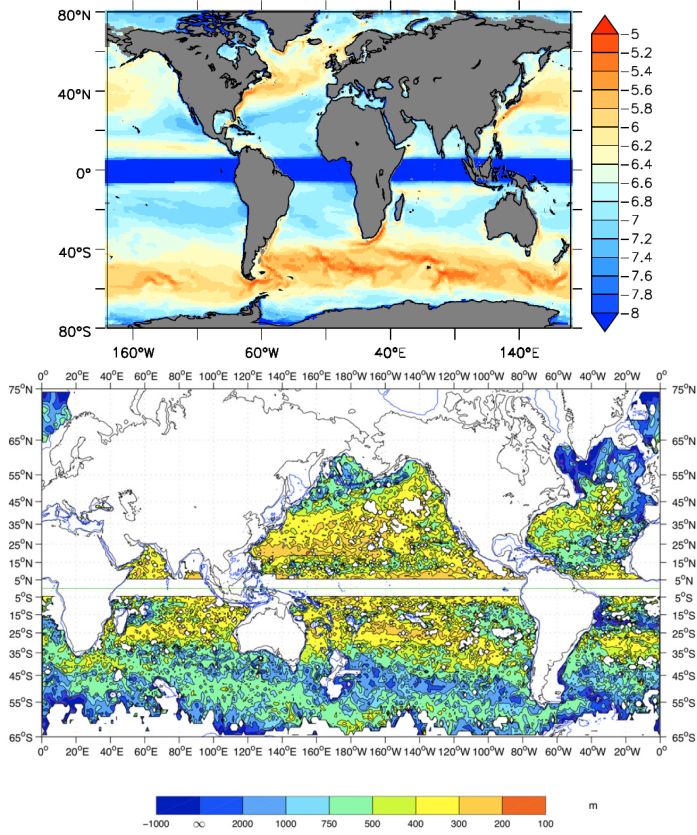
Figure 1.1: Top panel: Surface energy input F by near inertial waves from model [Jochum *et al.*, 2013]. Units are $\log_{10}(F/(m^3s^{-3}))$. The flux in the band near the equator is left out because of technical problems in the estimation. Figure from Olbers and Eden [2013]. Bottom Panel: Eddy Kinetic Energy (EKE) baroclinicity measured by $1000/\ln(EKE_{surf}/EKE_{1000m})$ (m). Negative values correspond to EKE_{1000m} greater than EKE_{surf} where EKE_{surf} comes from altimetry. The used model is not valid within $\pm 3°$ of the equator, as it mainly relies on classical geostrophic calculations. Figure from Ollitrault and Colin de Verdière [2014].

1.2.1 *Traditional and non-traditional equatorial dynamics*

The most upfront equatorial feature is certainly its geographic location on the planet. Along the equator, at latitude $\phi = 0°$, the Coriolis parameter $f = 2\Omega \sin \phi$ vanishes, where $\Omega = 7.292 \times 10^{-5} s^{-1}$ represents the Earth angular velocity (see figure 1.2). In the equations of motion, f is not only the Coriolis parameter associated with the strongest (horizontal) components of the velocities, but it is also, in the classical approximation of the equations - so classical to be called *traditional* [Laplace, 1878] - the one and only component of the Coriolis force appearing in the equations. It is clear that this last approximation becomes problematic in the equatorial region, as it does in all kinds of motion with a manifestly vertical character (such as deep convection) or for low-frequency motions with short horizontal scales (such as for internal inertia-gravity waves, see Gerkema *et al.* [2008] for a comprehensive review on the topic). However, retaining non-traditional terms in the governing equations, namely the terms related to the neglected horizontal component of the Coriolis force, bears some remarkable consequences: not only do basic equalities like hydrostatic equilibrium and geostrophic balance need to be reformulated, but, most importantly, separability of the equations of motion into horizontal and vertical components is no longer possible, profoundly changing the symmetry properties of the mathematical system in analysis and its solvability [Gerkema *et al.*, 2008]. As we will see in chapter 2, traditional, analytical models of equatorial dynamics [Matsuno, 1966], in fact, are all over-symmetrised, and have all taken advantage of the use of the method of separation of variables. Results obtained making use of the traditional approximation have highly influenced our general interpretation and understanding of ocean current and wave dynamics [Greenspan, 1968; LeBlond and Mysak, 1978; Gill, 1982; Cushman-Roisin and Beckers, 2011], with major consequences on processes that include mesoscale flows, and, in particular, equatorial dynamics and internal waves. On the other hand, assessing the role of the non-traditional terms in the real ocean is still debated [Gill, 1971; Joyce *et al.*, 1988; van Haren and Millot, 2005; Gerkema *et al.*, 2008], to which we will contribute with observational results from the equatorial western Atlantic Ocean in chapter 5.

1.2.2 *Classical equatorial waves*

The use of the traditional approximation in the equations of motion, constitutes the first step towards building the classical set of wave solutions for very low-latitudes [Matsuno, 1966]. Solutions are initially obtained for a single-layer, homogeneous, incompressible fluid with a free surface, and are called *equatorial* Poincaré (inertia-gravity), Kelvin, Rossby and Yanai waves for their similari-
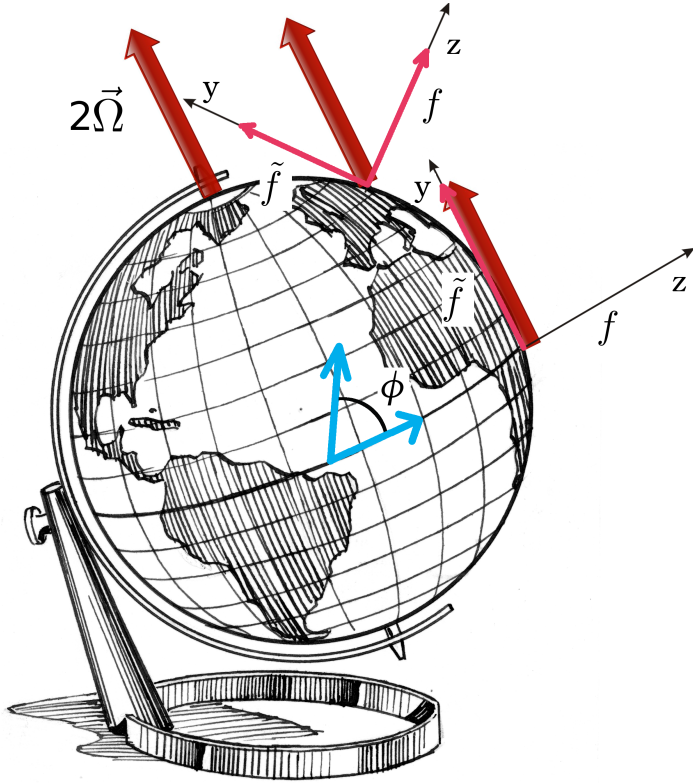
Figure 1.2: A vectorial representation of the Coriolis parameter $2\vec{\Omega}$, in red at the North Pole, is aligned to the Earth's rotation axis. The same vector is also shown when translated to different locations on the Earth's surface. Its local decomposition is presented at mid-latitudes ($2\vec{\Omega} = \hat{e}_y\,2\Omega\cos\phi + \hat{e}_z\,2\Omega\sin\phi \equiv \hat{e}_y\tilde{f} + \hat{e}_z f$) and at the equator ($\phi = 0$), where $2\vec{\Omega} = \hat{e}_y\,2\Omega\cos\phi = \hat{e}\tilde{f}$, and $f = 2\Omega\sin\phi = 0$.

ties with their *mid-latitude* counterparts. These waves all share a characteristic: they are trapped near the equator, meaning that they have appreciable amplitude only in the vicinity of the equator. The equator is thus acting as a wave guide. These waves, travelling at the surface or along the sharp equatorial thermocline, are used to interpret observations (with small or large differences with their theoretical predictions) in the equatorial ocean [Johnson and McPhaden, 1993; Zheng, 1995; Chelton and Schlax, 1996] and equatorial atmosphere [Wallace and Kousky, 1968; Wang and Rui, 1990; Canziani *et al.*, 1994, 1995]. While it is thus tempting to consider the issue of equatorial waves as solved, we have to understand that solutions so far considered are based on an approximation that actually breaks down at the low-latitudes. Consequences of this breaking are in fact unknown, but improving our understanding on this issue might help in the future in filling the blank bands in figure 1.1, and not only for surface features.

1.2.3 *Equatorial Deep Jets*

The quest for a more robust description of equatorial waves is not only motivated by mathematical integrity arguments and coherency. In fact, equatorial planetary waves as the ones derived in Matsuno [1966], including their baroclinic counterparts, or combinations, have so far failed to capture the observed strength, time and spatial scales of the complex equatorial current system [Eriksen, 1981, 1982a; O'Neill and Luyten, 1984; Hua *et al.*, 1997; Muench and Kunze, 1994, 1999, 2000; Hua *et al.*, 2008; Fruman *et al.*, 2009; Ascani *et al.*, 2010]. This has been brought to light by deep velocity profiles made in the three oceans [Cromwell, 1953; Cromwell *et al.*, 1954; Firing, 1987; Ponte and Luyten, 1989; Weisberg and Horigan, 1981; Reppin *et al.*, 1999; Gouriou *et al.*, 2001; Send *et al.*, 2002; Dengler and Quadfasel, 2002; Youngs and Johnson, 2015], revealing equatorial current patterns surprisingly similar not only in the three ocean basins, but also similar to what is observed in the equatorial regions of the Earth atmosphere as well as in the atmosphere of rotating planets or stars [Galperin, 2004]. A series of stacked, alternating zonal currents, called Equatorial Deep Jets (EDJs) dominates the equatorial current field within approximately $\pm 1.5°$ (see figure 1.3 for a classic example from the Pacific Ocean), between the thermocline (about 100 m) and 2500 m [Firing, 1987; Gouriou *et al.*, 1999; Dengler and Quadfasel, 2002; Bourlès *et al.*, 2003], or bottom [Brandt *et al.*, 2011]. Typical velocities are of about 0.2 m/s). These zonal currents are conventionally referred to as jets, although, usually, an interannual to annual variability is associated to their magnitude and direction [Bunge *et al.*, 2008]. Remarkably, their meridional velocity component is observed to vary faster, and over a much shorter vertical scales in all three Oceans [O'Neill, 1984;
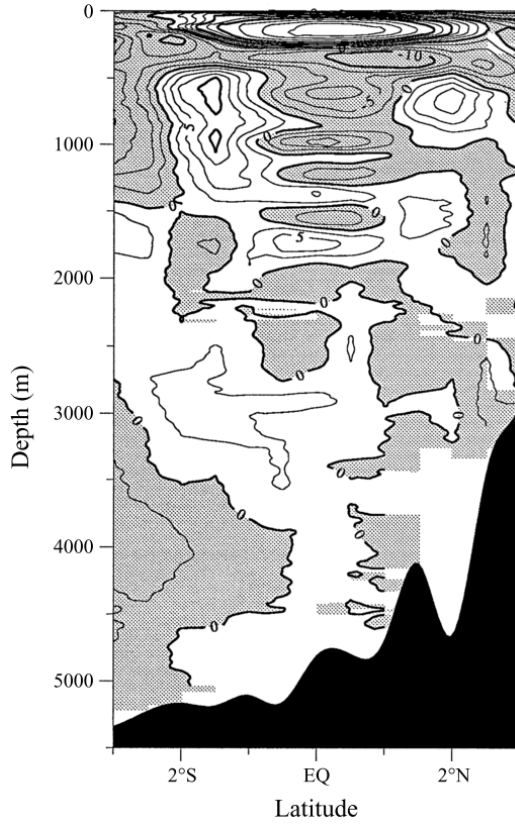
Figure 1.3: Time-mean zonal velocity (cm/s) in the Central Pacific (at 159°W) resulting from an 18 month average (February 1982 - June 1983) from the PEQUOD data set. Westward flow is shaded. Figure is from Firing [1987].
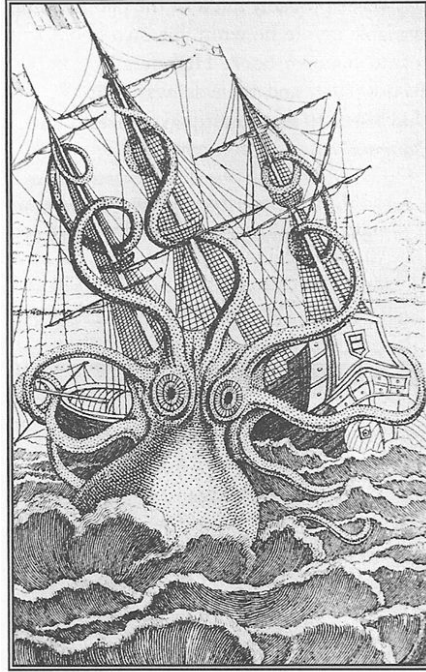
Figure 1.4: Example of inhabitant of the deep ocean interacting with surface activities. This was before sea-going oceanographers started to investigate internal waves. The drawing, by Pierre Denys de Montfort, is dated 1802.

Reppin *et al.*, 1999; Dengler and Quadfasel, 2002; Bunge *et al.*, 2007; Dengler and Quadfasel, 2002]. Despite the recent observational progress and the subsequent access to larger and larger data sets of *in situ* measurements, to date, the mechanisms for the formation, maintenance and dissipation of the EDJs, and for the intertwining of the two horizontal components of the velocity, still remain unclear.

1.2.4 *Low-latitude internal waves*

The EDJs puzzle indicates that not only surface and thermocline dynamics still pose theoretical and observational challenges, but also the deeper current and wave fields demand a coherent interpretation. For example, the same equatorial trapping of low-frequency waves pointed out by Matsuno [1966] for surface

waves was also found by Bretherton [1964] for *internal* waves in a meridional plane. Internal waves are waves that travel within any kind of stratified fluid and, different from the surface waves, present their maximum amplitude in the interior of the fluid and not at its boundary. Stratification might not only be built by density, but also by angular momentum, giving rise to internal gravity waves or inertial (gyroscopic) waves, respectively. A combination of the two restoring forces, gravity and Coriolis force, is also possible and results in the combined internal inertia-gravity waves. Although a common feature to all geo- and astrophysical stratified fluids (ocean, atmosphere, planet's liquid cores and stellar atmospheres), direct observations of internal waves in the ocean are relatively recent and sparsely resolved. The deep ocean, in fact, was considered a quiescent abyss populated by mysterious pelagic, gigantic creatures (see figure 1.4), and was not scientifically approached until the beginning of the last century.

Perhaps one of the first observations of internal waves is due to Helland-Hansen and Nansen [1909]. They found that temperature profiles may change substantially within the course of hours at the same location, and they ascribed this to the presence of "puzzling waves". To date, despite the huge progress made observing internal waves with *in situ* techniques [Eriksen, 1998; Thorpe, 1999; van Haren *et al.*, 2002; Kunze *et al.*, 2002; Lien *et al.*, 2002; van Haren and Millot, 2004; Carter *et al.*, 2005; van Haren and Gostiaux, 2010; van Haren *et al.*, 2012; Alford *et al.*, 2012, 2015], or satellite [Brandt *et al.*, 2002; da Silva *et al.*, 2012], and despite the advances in understanding with theoretical [Lvov and Tabak, 2001; Lvov *et al.*, 2004; Gerkema and Exarchou, 2008; St. Laurent, 2002], numerical [Ogilvie and Lin, 2004; Alford and Zhao, 2007a; Nikurashin and Ferrari, 2013; Buijsman *et al.*, 2014] and experimental [Swart *et al.*, 2010; Manders and Maas, 2003; Hollerbach *et al.*, 2004; Hazewinkel *et al.*, 2011b; Mercier *et al.*, 2013] means, these waves still conserve a "puzzling" fame, perhaps for their sometimes counter-intuitive properties, or for their challenging mathematical description.

Interest in the possible role these "puzzling waves" could play in the equatorial dynamics is not new. The equatorial internal wave field has been in fact already pointed at as one of the possible mechanisms playing a role in the maintenance of the EDJs [Hua *et al.*, 1997; Muench and Kunze, 1999, 2000] via wave-wave and wave-current interactions. An observed downward propagation of the jets in the Atlantic ocean [Bunge *et al.*, 2008; Brandt *et al.*, 2011], with consequent upward energy propagation, suggests an internal generation mechanism, in contrast to surface (wind) forcing. It is worth noting that the low-latitude region is the location where the internal wave frequency band is the widest (classically ranging from the local f, vanishing at $\phi = 0°$, to the local buoyancy frequency N, usually of the order of $10^{-3}s^{-1}$), and thus the most energetic. Moreover, it is where, for geometrical reasons (see chapter 3), their behaviour might become even more "puzzling". Why? This requires here

a brief introduction to some basic concepts on internal wave dynamics, while the reader is referred to chapters 3 and 4 for further details.

In fact, analytical solutions for internal waves in enclosed domains are known only for exceptionally symmetric geometries (such as the full sphere, see Bryan [1889] and chapter 4 of this thesis). Alternatively, an approximated approach, the so called *ray theory* [Whitham, 1974; Broutman *et al.*, 2004] has been developed to study propagation of internal waves in arbitrarily shaped enclosed geometries, such as, for example, our ocean and atmosphere. Ray theory is based on the simple observation that in uniformly stratified, or uniformly rotating fluids, internal waves propagate along beams whose direction is univocally set by the ratio of the perturbing frequency and a frequency representing the environmental conditions (rotation and/or density stratification). It follows that internal waves propagate in an oblique fashion with respect to the acting restoring force(s). Admittedly, this might have contributed to their "puzzling" fame.

Conservation of their propagation angle upon interaction with the domain's walls can lead to the approach of a so called *internal wave attractor* [Maas and Lam, 1995]. These interesting features are easily understood in terms of ray theory: ray trajectories in arbitrarily shaped containers are generally not closed but, by repeated reflections from the boundaries, converge to a limit cycle (the attractor), in which all the wave energy is concentrated [Maas, 2005], see for example figure 1.5 for the representation of a two-dimensional *equatorial* internal wave attractor on a meridional plane. The existence of attractors reveals the pathological nature of internal waves in enclosed domains, a system described by a hyperbolic problem. Results known for already seventy-five years [Høiland, 1962; Stern, 1963; Bretherton, 1964; Stewartson and Rickard, 1969; Stewartson, 1971, 1972; Israeli, 1972; Maas and Lam, 1995; Rieutord and Valdettaro, 1997; Dintrans *et al.*, 1999; Rieutord *et al.*, 2000; Maas, 2001; Ogilvie, 2005; Maas and Harlander, 2007] showed that in this case, internal wave eigenspectra appear to be infinitely degenerate and dense and as such differ strongly from the isolated and non-degenerate spectra of the more classical elliptic problems. The discreteness of the spectrum and smoothness of the eigenmodes is also lost when the symmetry in boundary orientation is broken, as it is in any geophysical configuration, and in the low-latitude belt in particular. In an ideal, inviscid, linear description, one thus generically obtains continuous spectra and attractors, whose spatial structure is both frequency- and domain-dependent, bearing no little consequences on the local dynamics. In fact, in this setting, along attracting trajectories, singularities in the velocity field might arise, with a corresponding infinite magnification of kinetic energy density. Wave attractor singularities are dynamically important since they represent possible local hot spots of energy density, mixing and wave-wave interactions [Harlander and Maas, 2006; Scolan *et al.*, 2013], with consequences for the mean flow [Maas, 2001]. Re-
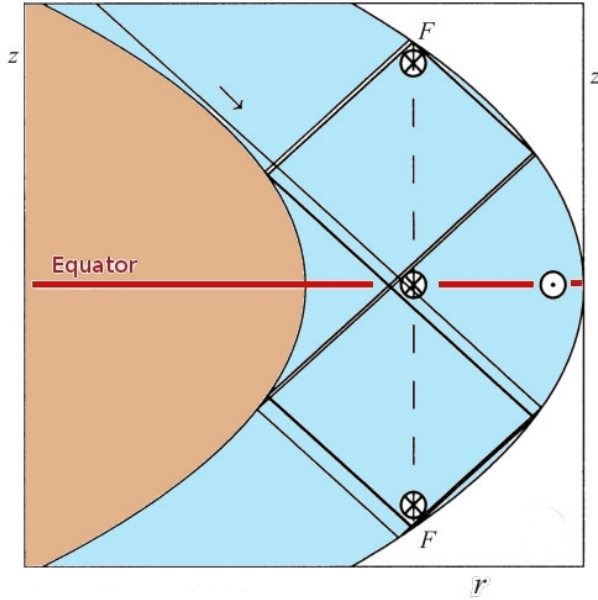
Figure 1.5: Sketch of characteristics (solid lines) in a vertical cross-section of a rotating spherical shell (inner core in brown) filled with homogeneous fluid (blue). Rotation axis z is along the ordinate; cylindrical distance r along the abscissa. The figure demonstrates equatorial trapping [Bretherton, 1964] and focusing of characteristics (and waves), leading to mixing of angular momentum. This accelerated water will subsequently spread axially (dashed line) from focusing locations F, leading to a band of eastward (cyclonic) flow, like the oceanic, near-surface north and south equatorial counter-currents, and like the subsurface equatorial undercurrent. At the surface of the equatorial plane, angular momentum mixing decelerates fluid, predicting an (anticyclonic) westward flow, like the oceanic surface equatorial current. Notice that for visual clarity this figure has been compressed in the axial direction by a factor 4. Figure modified from Maas [2001].

markably, in geophysical settings, these attractors are found to be particularly active in the low latitude belt [Maas, 2001; Maas and Harlander, 2007]. Their existence seems inescapable theoretically, and they are in fact easily observed in laboratory (see figure 2.10 for an example of attractor observed in the fluid dynamics laboratory of the Physical Oceanography Department at the Royal NIOZ) and numerical models, but their existence and role in the ocean still needs to be proven and investigated. This is due to a combination of factors, such as the lack of spatial resolution of *in situ* measurements as well as the lack of instruments that are able to resolve the intrinsically three-dimensional internal wave field. Moreover, the simultaneous occurrence of other phenomena might also limit their presence, as well as our capability to observe them, for example, the internal scattering due to non-uniformity of the stratification, or viscous damping processes, or the large (horizontal) scale of the ocean.

Interestingly, a traditional approach to the equations of motion is able to completely mask the existence of internal wave attractors, excluding them from having any role at all in determining local or mesoscale dynamics.

1.2.5 *A short note on El Niño and La Niña*

We cannot avoid mentioning here, in an overview of equatorial phenomena and challenges, that part of the interest in large-scale currents and wave-current interactions in the equatorial band did not arise only because of its wave guide behaviour, or for its peculiar internal wave field, but also, or perhaps mainly, because, by the 1980's, scientists came to realise that equatorial, interfacial waves constitute one of the key factors in explaining ENSO (the El Niño-Southern Oscillation phenomenon). In short, ENSO is a naturally occurring phenomenon that involves fluctuating ocean temperatures in the equatorial Pacific. The pattern generally fluctuates between two states: warmer than normal central and eastern equatorial Pacific sea surface temperatures (El Niño, warm phase) and cooler than normal central and eastern equatorial Pacific sea surface temperatures (La Niña, cold phase). When temperatures in the ENSO region of the Pacific are near average it is known as ENSO neutral, meaning that the oscillation is neither in a warm nor cool phase. Temperature anomalies in the Pacific Ocean are then associated with temperature, precipitation and wind anomalies on land. ENSO thus cause disastrous flooding in countries like Peru and Ecuador as well as heavy droughts in large areas of South America, Indonesia, and Australia, but its impact can be felt over much wider areas, considering its large influence on the climatic and environmental conditions in distant parts of the world [Ludescher *et al.*, 2013]. Interestingly, the interplay between equatorial currents in the ocean and atmosphere is one of the major generating mechanisms for El Niño, and La Niña phenomena [Dijkstra and Burgers, 2002;

Izumo, 2005; Fedorov and Brown, 2009; Constantin, 2012b]. This means that a better representation and understanding of equatorial waves would lead to an improved and better-timed forecasting system, with consequent large benefits for the population in the regions directly affected by ENSO. The complex pattern of the coupled ocean-atmosphere leading to ENSO is far beyond the scope of this work, and it will not be considered in this thesis, which will focus more on the deep equatorial dynamics and internal wave-current system. The interested reader is referred to dedicated monographs such as the one by Philander [1990] or Dijkstra and Burgers [2002] and references therein.

As chapter 2 aims to show, it is interesting to notice, however, how low-latitude geophysical dynamics, despite its great societal impact, did not always receive in literature the deserved level of attention and accuracy in its interpretation.

1.2.6 *The "equatorial boundary layer"*

While discussing the challenges one is facing once interested in equatorial dynamics, this thesis also intends to reinforce the concept of "equatorial boundary layer" in the context of the oceanographic community. This interpretation of the near-equatorial region is in fact not new, especially not for theoretical or laboratory studies of geophysical flows, where strong model simplifications are required to find and interpret solutions. Nevertheless, we believe that this approach is also useful to highlight fundamental properties of the equatorial region in the real ocean.

In general, we can define a "boundary layer" as a small region where a solution to a partial differential equation undergoes a large change. The existence of a boundary layer implies thus a local breakdown of the classical dynamical balances (e.g. geostrophy, Sverdrup relation) and implies that terms in the equations of motion, which are negligible in other parts of the domain (namely, at the mid-latitudes) become important near this boundary [Pedlosky, 1982]. In these special regions, wave energy density usually blows up and waves can break. Consequences can then be enormous in terms of wave momentum flux and diapycnal mixing. The equatorial features listed so far, both theoretical and observational, are all contrasting with mid-latitude behaviour, and thus suggestive of an interpretation of the low-latitude regions in terms of an "equatorial boundary layer". Interestingly, a univocal definition for this "boundary layer" does not exist, and we can actually account for four different interpretations, as well for four different spatial locations, respectively.

1. A first interpretation of the "equatorial boundary layer", also in historical terms, views, as we have previously seen, the equatorial belt as a wave guide: the combination of a pronounced thermocline and the changing

sign of the Coriolis parameter make the equatorial region a guide for various types of waves, such as equatorial Kelvin and Rossby waves, or Yanai waves [Stern, 1963; Matsuno, 1966; Edwards and Pedlosky, 1998; D'Orgeville *et al.*, 2007]. This definition of "equatorial boundary layer" corresponds to a region spanning ±2.5° of latitude around the equator itself.

2. "Equatorial *internal* boundary layers" [Harlander and Maas, 2006, 2007], emerging for solutions of hyperbolic boundary value problems in fully confined domains, are also theoretically predicted to occur at the equator, as a result of the interaction of internal wave characteristic paths with the local geometry [Bretherton, 1964; Stewartson and Rickard, 1969; Stewartson, 1971, 1972; Dintrans *et al.*, 1999]. Spatially, these *internal* boundary layers lie along the possibly occurring internal wave attractor's closed paths, the limit cycles of the ray web (see figure 1.5) [Maas and Lam, 1995; Maas, 2001].

3. A third interpretation of "equatorial boundary layer" emerges as a region encapsulated by the ocean surface and the cylindrical surface tangent to the ocean floor and parallel to the Earth's rotation axis (figure 1.6). The latter surface, given an average ocean depth of 4 km, would surface at ±2.0° of latitude. From this simple argument, it follows that the area confined within ±2° is characterised by a different dynamics, when compared to that at higher latitudes. Outside this equatorial band, the height of the water column parallel to the rotation axis increases with distance from the axis, while the opposite is true in the equatorial region, where the height of the water column parallel to the rotation axis decreases with distance from this axis, vanishing at the equatorial surface. This, in principle, bears repercussions for the direction of propagation of topographic Rossby waves in the equatorial region, where they should surprisingly propagate eastward.

4. Finally, the transition zone from the equator to the mid-latitudes, both due to interpretation 1 or 3, (the red vertical line in figure 1.6), might also itself be considered a boundary layer, as a matching surface between two, differently behaving domains. An example of this approach can be found in Gill [1971].

1.3 THE CONTENT OF THIS THESIS

The structure of this thesis summarises the parabola of the underlying work. The analysis of equatorial features in our oceans has been in fact initially moti-
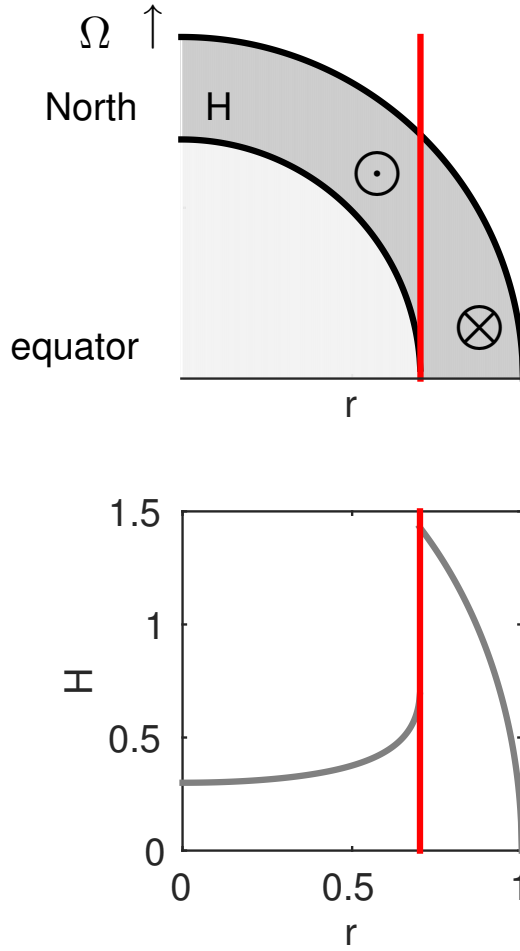
Figure 1.6: Top panel: meridional view of the thickness of an idealised ocean (shaded in grey) in the northern hemisphere. Rotation axis is along the ordinate; cylindrical distance r along the abscissa. H is the height of the ocean layer parallel to the rotation axis. The direction of topographic Rossby waves is indicated in the panel, westward in the off-equatorial region, eastward (!) in the equatorial region. Bottom panel: The value of H is plotted as it radially varies. The polar value for H is arbitrarily set to 0.3. In both panels the red line corresponds to the cylindrical surface tangent to the ocean floor and parallel to the Earth's rotation axis.

vated by simple observations of low latitude phenomena, common among the three ocean basins, the Earth atmosphere, and other planet's atmospheres or stars, being very distinct from the general mid-latitude behaviour. The topic has then been tackled from very different perspectives. We will have to go through all chapters, and through all the variety of approaches adopted, to eventually come back to ocean measurements, and be able to point out in which sense, from the observational point of view, the low-latitude region can indeed be considered a "boundary layer", where rotation and stratification combine differently than in other locations on our planet.

In a nutshell, the questions that will be addressed in this study are the following:

- Is the classical set of equatorial waves, commonly used in literature [Matsuno, 1966], a valid tool for describing equatorial dynamics? If not, what are its limitations and how can it be improved?

- In literature, theoretical studies on internal wave rays have been restricted to two-dimensional domains. In the context of geophysical studies, this corresponded to meridional (zonally symmetric) settings. Only recently, numerical and laboratory experiments have started investigating a three-dimensional approach to ray tracing [Manders and Maas, 2004; Maas, 2005; Hazewinkel, 2010; Hazewinkel *et al.*, 2011b]. Is the idea of equatorial internal wave attractors still valid when we allow waves to propagate zonally too, a step towards a more realistic representation of the real phenomenon?

- Which are actually the power and the limitations of the three-dimensional ray tracing approach in studying internal wave dynamics in enclosed domains?

- Turning to observations, in what sense can the equatorial region be considered a boundary layer? And how do the observed equatorial features, distinct from those at mid-latitudes, relate with the previous theoretical findings and with literature?

The chapters of this thesis will now be briefly introduced. They have been written such that they are self-contained, for the convenience of both the reader and the author.

1.3.1   *Chapter 2: an analytical approach*

We started the study with an analytical approach to equatorial wave dynamics. In chapter 2 the relevant equations of motion for geophysical fluids are

presented, with special emphasis on the scale analysis, approximations and assumptions leading to the traditional and the non-traditional equatorial β-plane. First, the traditional system of equations is solved for surface and interfacial waves. This constitutes textbook material, and serves as an introduction and sets a context for further steps. Non-traditional terms are then added to the system, for vanishing and non-vanishing meridional velocities. General free wave solutions present themselves in terms of Hermite polynomials with imaginary argument, which however are hardly reconcilable with the classical set of equatorial planetary waves used in literature [Matsuno, 1966]. The main reason for this is that, when non-traditional Coriolis terms are included in the equations of motion, the vertical and meridional components of the equations of motion are no longer separable. Consequently, it is not possible to apply asymptotic boundary conditions in the meridional direction (equatorial trapping) while demanding a rigid bottom and/or a material surface on top. Obviously, this result applies even more dramatically when one is interested in the equatorial internal wave field, and the fluid is confined within two rigid boundaries. In chapter 2, a formal introduction to internal waves is also given, and in particular to the problem of internal waves in confined domains of geophysical relevance, such as the spherical shell geometry. An equation describing internal wave motion in a confined domain has been derived using fully anisotropic length scales but two equal velocity scales. This generalisation of the Stern's equation [Stern, 1963] (or of the stratified Stern's equation [Maas and Harlander, 2007]) requires no zonal axisymmetry, and thus the validity of results in Maas and Harlander [2007] on the occurrence of equatorial wave attractors has been extended to more realistic settings, with length and velocity scales matching the observed situation at the equator and accounting for zonal inhomogeneities (meridional continents?). Summarising, it seems that the three-dimensional character introduced in the system, either by considering non traditional terms in the case of surface waves, or by considering internal waves in enclosed domains, is destroying the picture of equatorial wave dynamics as presented in all textbooks. The power of classical solutions, in fact, is *weakened* by the addition of simple realistic ingredient(s), whose inclusion, however, appears to be natural and well motivated when interested in low-latitude wave dynamics. Solutions for the full internal wave problem, an ill-posed hyperbolic boundary value problem [Rieutord *et al.*, 2000], are not available, and by the end of this chapter we should understand why. Approaches and methodologies used in the following chapters of this thesis reflect the difficulties and the issues evidenced in this chapter, as they address non-traditional equatorial wave dynamics using different tools and perspectives.

1.3.2 *Chapter 3 and 4: a ray-tracing approach*

We understood that a complete analytical description and understanding of internal waves in arbitrarily shaped enclosed domains, such as the ocean, is still missing. However, other (numerical) tools are available for the investigation of this problem. In chapter 3 the linear, inertial wave field is studied by means of three-dimensional ray tracing in spherical shell domains, as a paradigmatic, challenging and simplified case study for the broader class of inertia-gravity waves in geophysical and astrophysical contexts. Rays are here classically interpreted as representative of energy paths. But, in contrast with previous studies, they are now launched with a non-zero initial zonal component, allowing for a more realistic, localised forcing, and the development of azimuthal inhomogeneities. In the shell geometry, meridional planes are found acting as internal waves attractors for ray trajectories. However, this collapse from three to two-dimensions constitutes only the first step of the focusing mechanism. In fact, once a ray trajectory has been trapped onto one particular meridional plane, then the already known, two-dimensional focusing mechanisms come into play, leading to the development of two-dimensional, "classical" internal wave attractors [Maas and Harlander, 2007].

Moreover, using three-dimensional ray tracing, the existence of trajectories that are not subject to meridional trapping is also observed. Their dynamics was not captured by the previous, purely meridional studies and unveils a new class of possible solutions for inertial waves in the spherical shell. Internal wave attractors, and their role of providing the momentum needed at the low latitudes to trigger and maintain the observed, strong and coherent zonal flows are now proven to work also when three-dimensional effects, and zonal inhomogeneities are considered.

When we have in mind the equatorial ocean, with all its complexity in terms of currents, waves and hydrography, it is clear that the case studied in chapter 3 is too idealised for the results to be directly applied to realistic settings. However, moving towards a more realistic representation of equatorial internal wave attractors, namely a three-dimensional setting, also poses some new and fundamental questions on how to interpret and use the obtained results. In fact, the role of the characteristics of an hyperbolic boundary value problem in a three-dimensional environment is by no means clear or trivial. Nor it is clear if the classical interpretation, generally valid in two-dimensional domains (periodic orbits = regular solutions, attractors = singular solutions, chaotic orbits = null solutions), can be applied. Surprisingly or not, to investigate this issue, an even more idealised case has to be taken into account to be able to directly compare known, three-dimensional analytical solutions to the characteristic paths.

In chapter 4, the behaviour of inertial waves is thus investigated by means of the same three-dimensional ray tracing algorithm, but now applied to a rotating spherical container, filled with homogeneous fluid. We still considered only the linear, inviscid case. In this domain, the classical, two-dimensional association between regular modes and periodic trajectories can be directly tested in a fully three-dimensional setting, since analytical solutions for inertial waves in the sphere are known for over a century [Bryan, 1889].

Eventually, three-dimensional, *repelling* periodic trajectories are found and classified on the basis of the frequency and spatial structure, although the associated frequencies are hardly reconcilable to the ones found in Bryan [1889]. Chaotic orbits are not found, as expected in the full sphere, while invariant, non domain-filling, orbits constitute the majority of the trajectories in the domain. Results from chapter 4 are not straightforward, and we can say that they intriguingly present indeed more new questions then answers. Overall, it appears that three-dimensional ray dynamics constitutes a valid approach to infer general information on the spectrum and regularity properties of a system, but the relation between frequency values, trajectory structures and associated wave field is still not clear.

1.3.3 *Chapter 5: bridging theory and observations*

We started from some general observations as motivation, we passed through an analytical approach and to different idealisations of the problem of internal waves in fully enclosed geophysical domains, and we eventually come back to observations in chapter 5. Here we present a new data set from the equatorial deep western Atlantic Ocean, that we want to analyse with new eyes, after all that we have learned in the previous chapters. The data set consists of a CTD/LADCP transect at 38°W, between 0° and 2°N, and of three Acoustic Doppler Current Profilers and 23 moored current meters at 5 different locations, between 0° and 2.5°N, along approximately 37.5°W. Time series span about 1.5 years, from December 2007 to July 2009, and have an average temporal resolution of 15 minutes. From the hydographic and current measurements we isolate several and diverse equatorial features, that all together suggest the existence of an "equatorial boundary layer", spatially well-defined and mainly related to the distribution of planetary angular momentum in the region. As we have seen before, the idea of an "equatorial boundary layer" is not new from a theoretical point of view, but it is here investigated for the first time by means of *in situ* measurements. Perhaps the reader can already foresee that bridging theory and observations is not always an easy task, especially when one is facing the limited spatial and temporal resolution of the measurements (although these are very high compared with the average observational dataset), and especially in a

region of the ocean where observations are not only in general scarce and scattered, but also the theoretical understanding shows gaps of similar significance. That is why the value of the "equatorial boundary layer" as a framework of interpretation is twofold. Not only does it point out the observational gaps that we need to fill, but it also stimulates some further, and necessary, theoretical developments.

1.3.4   *Chapter 6: conclusions and outlook*

A summary and a discussion of the results of the entire work is presented in chapter 6, evaluating the initial research questions, stated at the beginning of this section. Reconciling the findings from such a diversified approach to the equatorial regions constitutes clearly a challenge *per se*. However it is necessary if one is interested in combining different perspectives to further stimulate the progress of the topic. It comes with no surprise that the major difficulties are encountered when theory developed for highly idealised models are tested on real world observations, but this by no means should be considered a "failure". On the contrary, we hope that all the old and new questions brought to light by this thesis can help in the design and in the motivation of renewed, more focused, observational efforts in the equatorial region, as well as in driving theoretical, and experimental advances in the context of internal wave dynamics in enclosed domains, in geophysical contexts, and beyond.

2

EQUATORIAL WAVE DYNAMICS

To describe wave motion in our Earth's ocean, we choose a reference frame with the origin set on the Earth's surface and rotating with the Earth (see figure 1.2). We take the x-axis to be the longitudinal direction (horizontally, positive eastward, not shown in figure 1.2), the y-axis to be the latitudinal direction (horizontally, positive northward) and the z-axis to be the vertical direction (positive radially outwards). We take the Earth to be a perfect sphere of radius $a = 6371 \times 10^3$ m, which has a constant rotational speed of $\Omega = 7.292 \times 10^{-5}$ s^{-1}. In this framework, the Coriolis parameter associated to the latter can be expressed in vector form as $[0, \tilde{f}, f] = [0, 2\Omega \cos\phi, 2\Omega \sin\phi]$, with ϕ being the local latitude. The governing equations for linear, inviscid Boussinesq ocean waves are then given by (see, for example LeBlond and Mysak [1978] or Gill [1982])

$$u_t - fv + \tilde{f}w = -p_x \tag{2.1a}$$
$$v_t + fu = -p_y \tag{2.1b}$$
$$w_t - \tilde{f}u = -p_z + b \tag{2.1c}$$
$$b_t + N^2 w = 0 \tag{2.1d}$$

together with the equation of incompressibility

$$u_x + v_y + w_z = 0 \tag{2.2}$$

where subscripts represent partial derivatives. Here p is the modified pressure, meaning the pressure without the hydrostatic contribution and divided by the constant reference density ρ_*. The total density field is then composed of this reference density ρ_* plus the static, vertically varying part, $\rho_0(z)$, plus the spatio-temporally varying part $\rho(\vec{x}, t)$, which are successively smaller in magnitude. Buoyancy b in equations (2.1c) and (2.1d) is defined as

$$b = -g\rho/\rho_* \tag{2.3}$$

while buoyancy frequency N obtained from

$$N^2 = -\frac{g}{\rho_*}\frac{d\rho_0}{dz} \tag{2.4}$$

where $g = 9.8 \ m/s^2$ is the standard gravitational acceleration at the Earth's surface. Modelling equatorial waves as linear, assuming thus small amplitude waves, could in principle clash with the strong zonal currents observed at the equator. At this stage, however, it is not clear whether these strong zonal currents exist in addition to the waves or because of the waves, via wave-wave

and current-wave interaction mechanisms. For this reason, we first aim only for a robust analytical description of equatorial wave dynamics, avoiding any hypothesis on the existence and nature of the background state, that would need a careful justification. Given that equatorial dynamics is for relatively long time known (cit) and the numerous works dedicated to this subject (cit), and given the presence of an "Equatorial dynamics" chapter in every oceanographic textbook (cit), one is led to consider this oceanographic topic as already solved, at least in its linear and inviscid formulation. We shall see in this chapter that, perhaps surprisingly, this is not the case, and we are still far from mastering a comprehensive and robust analytical description of low-latitude current and wave systems.

This allows us to start our study with a simplified picture. It is clear, in fact, that the system (2.1)-(2.2) is more approachable compared to the non linear and viscous counterparts, and one has always to remember its limitation: linear waves might locally amplify, and other (non-linear, viscous) mechanisms could come into play, profoundly modifying the dynamics of the supported waves. However, we leave all these complexities for a later stage. Furthermore, all waves considered will be free solutions to the equation of motions. The unforced wave solutions presented here eventually allow to treat forced systems in the low frequency limit using, for example, the method of Green's functions (see for example Dijkstra [2008]). Based on it, adjustment processes on time-dependent changes in the forcing (like the surface wind stress) could also be modelled.

All equatorial waves derived in this chapter will then be solutions of the system (2.1)-(2.2), together with the appropriate boundary conditions.

2.1.1 *The equatorial β-plane*

Because one is usually interested in oceanic motions of limited horizontal extent, and because of the mathematical problems involved in dealing with spherical polar projection of the Coriolis parameter, it is desirable to introduce a Cartesian linear expansion of the trigonometric functions appearing in equations (2.1), centred at ϕ_0, the origin of our system of reference. When the equatorial case is considered ($\phi_0 = 0$), this yields to the classical equatorial β-plane approximation for the Coriolis parameter [Gill, 1982; Gallagher and Saint-Raymond, 2007; Fedorov and Brown, 2009]

$$f = 2\Omega \sin \phi_0 + (2\Omega \cos \phi_0 / a) y = \beta y \tag{2.5a}$$
$$\tilde{f} = 2\Omega \cos \phi_0 = 2\Omega \tag{2.5b}$$

with $\beta = 2\Omega/a = 2.3 \times 10^{-11} \, m^{-1}s^{-1}$. The meridional coordinate y measures the meridional distance from the equator (positive northward). Near the equator, the new set of equations thus reads:

$$u_t - \beta y v + 2\Omega w = -p_x \tag{2.6a}$$
$$v_t + \beta y u = -p_y \tag{2.6b}$$
$$w_t - 2\Omega u = -p_z + b \tag{2.6c}$$
$$b_t + N^2 w = 0 \tag{2.6d}$$

and the incompressibility condition is unchanged:

$$u_x + v_y + w_z = 0. \tag{2.7}$$

In order to determine the meridional extent of the region where the β-plane approximation is valid, it is useful to use the concept of *Rossby deformation radius* R. This measures the length at which rotational effects (represented by the Coriolis parameter) become as important as gravity waves (represented by their phase velocity). At mid-latitudes R reads

$$R = \frac{\sqrt{g'h}}{f} = \frac{c}{f} \tag{2.8}$$

and indeed governs the horizontal extent of generic geophysical dynamical structures. Following the standard notation, c is the typical velocity of a travelling, long interfacial gravity wave, g' is the reduced gravity (gravity multiplying the ratio of maximum vertical density change and the reference density) and h is the water layer thickness, meaning the equivalent depth in a two-layer fluid [LeBlond and Mysak, 1978], which simplifies to the shallow layer depths for disparate layer depths. As f varies with y, so does R. If this distance from a given meridional position y includes the equator, the formal blow-up of R implies that equatorial dynamics must supersede mid-latitude dynamics. Thus, a criterion to determine the width R_{eq} of the equatorial region can be chosen such that $R_{eq} = R$ at $y = R_{eq}$, yielding the definition of the *equatorial Rossby deformation radius*:

$$R_{eq} = \sqrt{\frac{c}{\beta}}. \tag{2.9}$$

For a value of $c = \sqrt{g'h} \sim 1.4 \, m/s$, obtained taking $h = 200 \, m$, typical of a travelling thermocline wave in the tropical Pacific Ocean [Philander, 1990], we estimate $R_{eq} \sim= 250 \, km$, or an equatorial latitudinal width of $\pm 2.25°$. This will constitute the geographical domain of all waves studied in this chapter. We recall that here only an oceanic case is considered: because the stratification of the atmosphere is much stronger than that of the ocean, the equatorial radius of deformation in the atmosphere will then be several times larger.

2.1.2 Traditional or non-traditional equatorial waves?

Facing the complexity of the geophysical equations (2.1)-(2.2) and in the noble effort of simplification, it has become "traditional" [Eckart, 1960] to neglect the component of the Coriolis force parallel to the local horizontal, on the basis of arguments that date back to Laplace [1878], and that can be summarised as follows. Looking at the system of equations (2.1), we notice that the force associated with the f (traditional) terms is due to, and induces, only horizontal movements. For the $\tilde{f}$ (non-traditional) terms, on the other hand, the opposite is true, and the vertical direction is always involved. The associated force, in fact, is either due to a vertical velocity or induces a vertical acceleration. The justification for this traditional approximation follows the simple observation that the depth of the oceans (and atmosphere) is thin compared to the radius of the Earth. For Coriolis (rotational) effects to be important, times scales need to be of the order of $2\pi/\Omega^{-1}$ or larger, but low-frequency motions usually have large spatial scales, that are therefore necessarily nearly horizontal. Vertical excursions are of secondary importance. This, in practice, renders the velocity and pressure fields nearly hydrostatic, and renders the non-traditional Coriolis terms insignificant compared to the traditional ones. Similarly, strong vertical stratification in density, which again suppresses vertical motions, also restricts the possible role of the $\tilde{f}$-terms.

If in equations (2.6) we assume monochromatic waves of frequency ω and employ the classical scaling

$$[x,y,z,\omega,u,v,w,p,b] = (L,L,H,N(H/L),U,U,U(H/L),NHU,NU),$$

the momentum and buoyancy equations then reduce to

$$i\omega u - yv + \frac{2\Omega}{N}w = -p_x \tag{2.10a}$$

$$i\omega v + yu = -p_y \tag{2.10b}$$

$$i\left(\frac{H}{L}\right)^2\omega w - \frac{2\Omega}{N}u = -p_z - b \tag{2.10c}$$

$$i\omega b + w = 0. \tag{2.10d}$$

In practice, the traditional approximation consists in neglecting terms in (2.10a) and (2.10c) preceded by $2\Omega/N$, considering this quantity to be small.

The argument proposed works fine for almost all geophysical applications. However, it certainly poses some problems when the equatorial case is addressed. As stated in classical text books, when dealing with equations (2.6), since $f = 2\Omega\sin\phi = 0$ at the equator ($y = 0$), to be consistent we should *not* neglect the Coriolis terms associated with the horizontal component of the Earth rotation [LeBlond and Mysak, 1978]. Moreover, the traditional ap-

proximation can become problematic near the equator not only for geometrical reasons ($\tilde{f} \gg f$), but also in the presence of motions with a manifestly vertical character. The assumption that $2\Omega/N \ll 1$ is indeed questionable in some deeper parts of the ocean, or wherever the stratification is weak (as in the presence of deep convection), or when low-frequency motions with short horizontal scales occur (see for example van Haren and Millot [2004]). The traditional approximation is, in fact, as the name suggests, an approximation, and as all approximations bears some limitations in the representation and understanding of the phenomena that are described taking advantage of it. For an extensive review on "Geophysical and astrophysical fluid dynamics beyond the traditional approximation" we refer the interested reader to the work by Gerkema *et al.* [2008].

It can come as a surprise, then, that many studies on equatorial wave dynamics, current-wave interaction, and abyssal cross-equatorial flow have not taken into account the effects of the non-traditional components of the Coriolis force. In particular, studies involving the propagation of equatorial Kelvin and Rossby waves [Matsuno, 1966], all common geophysical fluid dynamics textbooks (e.g. LeBlond and Mysak [1978]) and all reviews on more or less applied related topics [Dijkstra and Burgers, 2002; Fedorov and Brown, 2009; Cushman-Roisin and Beckers, 2011] neglect this horizontal component. However, we will soon understand why, as we will proceed through this chapter, anticipating, that when the traditional approximation is not adopted, solutions for (2.1)-(2.2) become elusive.

2.2 TRADITIONAL SURFACE AND INTERFACIAL WAVES

This section constitutes a review of the classical equatorial surface and interfacial wave solutions obtained from equations (2.1) and (2.2) in the traditional framework. This is done to have an overview on the conceptual models and solutions used to date in the interpretation of more or less complex equatorial phenomena. The reader who is familiar with classical equatorial wave dynamics may skip this section, and go directly to section 2.3 for the non-traditional counterpart.

2.2.1 *The shallow water model*

We follow here the classical approach as in Matsuno [1966], one of the seminal papers on the topic, even when conceived in an atmospheric context. A so-called divergent, barotropic model is adopted, meaning that a thin layer of incompressible and homogeneous ($N = 0$) fluid with free surface is considered, whose motion is characterised by a small aspect ratio $\delta = H/L \ll 1$. Neglecting
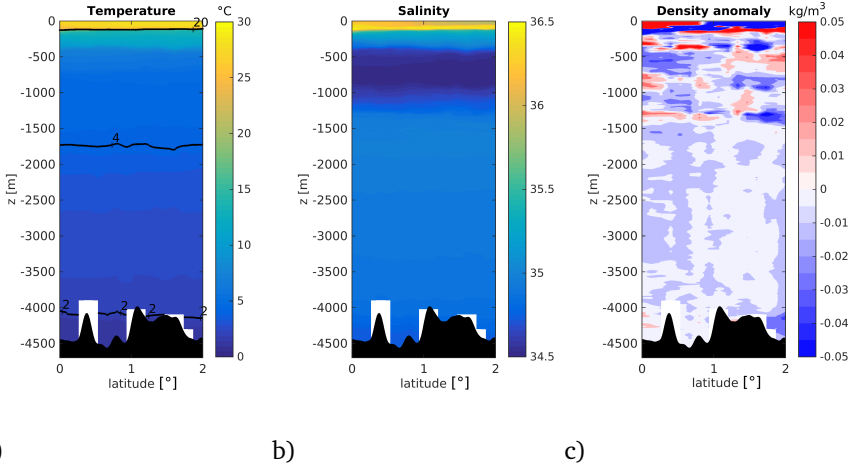
Figure 2.1: a) Temperature, b) salinity and c) density anomalies with respect to a meridional mean from an equatorial CTD transect. Data have been taken in the western Atlantic Ocean, at 38°W, at 16 stations between 0 to 2°N, 8' apart, from surface to bottom; vertical resolution is 1 m. For details, see chapter 5.

the corresponding term in equation (2.10c), we obtain the so-called equatorial *shallow water* equations, describing the motion of a free surface $\eta(x, y, t)$ under hydrostatic balance. At the surface, the following kinematic and dynamic linearised boundary conditions apply:

$$p|_{z=0} = g\eta \tag{2.11a}$$
$$w|_{z=0} = \eta_t. \tag{2.11b}$$

The *shallow water*, traditional equatorial β-plane equations of motion and continuity then read

$$u_t - \beta y v = -g\eta_x \tag{2.12a}$$
$$v_t + \beta y u = -g\eta_y \tag{2.12b}$$
$$H(u_x + v_y) + \eta_t = 0. \tag{2.12c}$$

2.2.2 *The reduced gravity model*

If the one-layer representation of the equatorial ocean of the *shallow water* model in equations (2.12) may appear too simplistic, the *reduced gravity* model

27
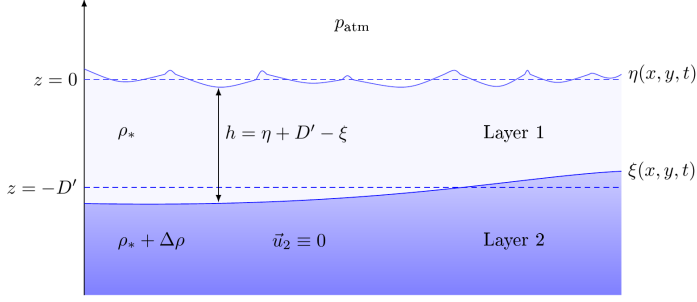
Figure 2.2: Sketch of the *reduced gravity* model. ξ is the deviation of the thermocline/interface from its mean value $-D'$. Layer 2 is regarded as motionless and infinitely deep, in analogy with figure 2.1.

(or $1\frac{1}{2}$ layer model, Fedorov and Brown [2009]) constitutes the simplest representation of the observed thermal (and density) structure of the equatorial ocean, as seen for example in figure 2.1: a shallow layer of relatively warm water overlies a much deeper layer of cold water, the two layers being separated by a sharp thermocline. Layer models allow in fact similar treatment of ocean phenomena occurring at the surface and in the interior along this interface. This is useful not only from an analytical perspective, in order to describe interfacial wave propagation along the equatorial thermocline, but also in numerical modelling, where the number of layers can be easily increased. Consider then two layers of water with different densities, separated by a material surface, as depicted in figure 2.2.

The neutral position of this interface is at $-D'$, and its dynamical position is described by the field $\xi(x, y, t)$. Hence, the thickness h of the upper layer (layer 1 in figure 2.2), of density ρ_*, is $h(x, y, t) = \eta(x, y, t) + D' - \xi(x, y, t)$, where a typical value for D' is 100 m, and for ξ 10 m. A higher density $\rho_* + \Delta\rho$ is assumed in the lower layer (layer 2 in figure 2.2), which furthermore is supposed to be motionless ($\vec{u}_2 = 0$) and infinitely deep. Then the hydrostatic equation

$$\partial_z p_2 = -(\rho_* + \Delta\rho)g \tag{2.13}$$

applies for pressure p_2 in the lower layer. At the interface, two new boundary conditions hold, namely

$$p_1|_{z=-D'+\xi} = p_2|_{z=-D'+\xi} \tag{2.14a}$$

$$\frac{D(z + D' - \xi)}{Dt}\Big|_{z=-D'+\xi} = 0 \tag{2.14b}$$
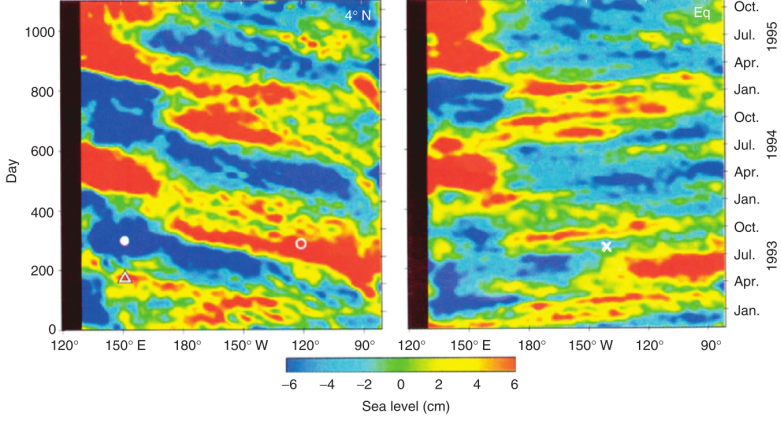
Figure 2.3: Time-longitude sections of filtered sea level in the Pacific Ocean along 4°N and the equator. A section along 4°S is almost identical to the 4°N section. In the time evolution, it is possible to identify the eastward and westward propagating sea level signals, respectively a Kelvin and a Rossby wave signature; from Chelton and Schlax [1996].

Note that in the first of the two boundary conditions the actual pressure appears ($p = p_0 + \tilde{p}$), as the hydrostatic background pressure is different for each layer. A relation between the sea surface elevation and the thermocline elevation can thus be established. Evaluating the dynamic boundary condition, it is found that

$$p_2 = -g(\rho_* + \Delta\rho)(z + D' - \xi) + \rho_* gh + p_{atm}. \tag{2.15}$$

However, since $\vec{u}_2 = 0$, it is clear that the horizontal gradient $\nabla_H \equiv (\partial_x, \partial_y)$ of p_2 vanishes. Computing then ∇_H of (2.15) then yields

$$\nabla_H \xi = -\frac{\rho_*}{\Delta\rho} \nabla_H \eta. \tag{2.16}$$

This insight is very important, as it states that small changes in sea surface are related to big and oppositely directed changes in the thermocline elevation. In practice, the sea surface elevation that is obtained for example from satellite data allows then an interpretation in terms of thermocline elevation changes (example in figure 2.3). The final form for the reduced gravity model can thus be written as

$$u_t - \beta y v = -g' h_x \tag{2.17a}$$

$$v_t + \beta y u = -g' h_y \tag{2.17b}$$

$$D'(u_x + v_y) + h_t = 0. \tag{2.17c}$$

29

in complete analogy with the shallow water set in equations (2.12), except that here 1) g is replaced by $g' = \frac{\Delta\rho}{\rho_*} g$, called *reduced gravity*, 2) the depth of the Layer 1 (h) appears instead of the surface elevation η and 3) the neutral position of the interface D' appears instead of the total layer depth H.

It follows that analytical solutions of systems (2.12) and (2.17), that will be presented in the following sections, are structurally identical and valid for both models. This means that the addition of a realistic two-layer structure does not alter the nature of the supported waves, while providing typical velocities values much closer to observations.

2.2.3 *Equatorial Kelvin waves*

Coastal Kelvin waves arise from a balance between Coriolis force and an exponential sea surface gradient, supported by a vertical sidewall. They are named after Lord Kelvin (W. Thomson), who proposed them for the first time in Thomson [1879]. In an equatorial Kelvin wave however the Coriolis force and sea surface gradient both vanish at the equator. A stationary balance between the pressure gradient and Coriolis force can be established in the meridional direction in the vicinity of the equator because objects travelling eastwards (which, as we shall see, is the case for equatorial Kelvin waves) are deflected towards the right (left) in the northern (southern) hemisphere. In analogy with the coastal Kelvin waves, equatorial Kelvin waves are in fact characterised by a vanishing meridional velocity,

$$v \equiv 0. \tag{2.18}$$

In the shallow water model, the governing set of equations is then:

$$u_t = -g\eta_x \tag{2.19a}$$
$$\beta y u = -g\eta_y \tag{2.19b}$$
$$Hu_x + \eta_t = 0. \tag{2.19c}$$

Combining (2.19a) and (2.19c) two wave equations are found:

$$u_{tt} - c^2 u_{xx} = 0 \tag{2.20a}$$
$$\eta_{tt} - c^2 \eta_{xx} = 0 \tag{2.20b}$$
$$\tag{2.20c}$$

with

$$c^2 = gH \tag{2.21}$$

where c denotes the phase velocity. Eliminating η using (2.19a) and (2.19b), and inserting in the resulting equation an ansatz

$$u \propto e^{i(kx - \omega t)} \mathscr{F}(y) \tag{2.22}$$

yields an equation governing the meridional dependency of the wave. This equation can be easily integrated,

$$\partial_y (\ln \mathcal{F}) = -\frac{k\beta}{\omega} y = -\frac{\beta}{c} y \tag{2.23}$$

such that

$$\mathcal{F} = e^{-\frac{\beta}{2c} y^2}. \tag{2.24}$$

It follows that the zonal phase velocity (c) of the wave must be positive in order to avoid unbounded solutions that are exponentially increasing for large values of $|y|$. From the phase velocity c in equation (2.21), we can calculate the group velocity and we obtain:

$$c_{gr} = \frac{\partial \omega}{\partial k} = c \tag{2.25}$$

The positive sign of the group velocity indicates that these waves can only travel eastwards, as anticipated at the beginning of this section. From an observational point of view, they correspond to the disturbances shown in the right-hand side of figure 2.3. The whole set of physical fields explicitly reads:

$$u_k = U \cos(k(x - \sqrt{Hg}\, t) + \phi) e^{-\frac{\beta}{\sqrt{Hg}} y^2} \tag{2.26a}$$

$$w_k = -Uk(z + H) \sin(k(x - \sqrt{Hg}\, t) + \phi) e^{-\frac{\beta}{\sqrt{Hg}} y^2} \tag{2.26b}$$

$$\eta_k = -\frac{H}{g} u_k \tag{2.26c}$$

where ϕ denotes a phase, related to an arbitrary choice of initial time. Note that there is a phase shift of $\pi/2$ between u and w. The vertical velocity w is obtained from the continuity equation, since it satisfies the linearised surface boundary conditions in equation (2.11b).

With $H = \mathcal{O}(10^3)\ m$, a typical velocity for an equatorial Kelvin wave travelling at the surface is $c = \mathcal{O}(10^2)\ m/s$. The scale on which it decays in the meridional direction, the equatorial Rossby deformation radius, is $R_{eq} = \sqrt{c/\beta} = \mathcal{O}(10^3)\ km$! This sounds quite large for an equatorial phenomenon and may violate the assumptions made in order to use the equatorial β-plane approximation. We can consider, however, an analogous wave but this time travelling at the thermocline, instead of at the surface. Taking advantage of the *reduced gravity* model (section 2.2.2), typical values become realistic. All results obtained in this section remain valid but the numerical values change as now $c = \sqrt{D'g'}$. Typical relative density differences in the ocean are of $\mathcal{O}(10^{-3})$: taking then a realistic upper layer depth of $D' = \mathcal{O}(10^2)\ m$, a typical velocity for an equatorial Kelvin wave travelling at the thermocline results $c = \mathcal{O}(1)\ m/s$, consistent

with phase velocity values observed, for example, in the Pacific Ocean [Chelton and Schlax, 1996; Soares *et al.*, 1999; Wakata, 2007]. This setting also yields a realistic Rossby deformation radius $R_{eq} = \mathcal{O}(10^2)\ km$.

2.2.4 *Equatorial waves with non zero meridional velocity*

We consider now the full *reduced gravity* set of equations (2.17) with $v \neq 0$. To tackle the system, a single equation for v can be derived as follows [Lighthill, 1969]: firstly, an equation describing the time evolution of the vertical component of the vorticity $\nabla \times \vec{u}$ is derived by crossdifferentiating equation 2.17a and equation 2.17b, stating

$$\partial_t(v_x - u_y - \frac{\beta}{D'}yh) + \beta v = 0 \tag{2.27}$$

The variables u and h can then be eliminated by computing

$$(2.17b)_{tt} - g \cdot (2.17c)_{ty} - \beta y \cdot (2.17a)_t - D'g' \cdot (2.27)_x.$$

The demanded relation then reads

$$\partial_t(v_{tt} - c^2(v_{xx} + v_{yy}) + (\beta y)^2 v) - c^2 \beta v_x = 0. \tag{2.28}$$

Here, $c = \sqrt{D'g'}$ is understood. Looking for plane-wave solutions of the form $v = V(y)e^{i(kx-\omega t)}$, a differential equation that determines the meridional structure is found,

$$V_{yy} + ((\frac{\omega}{c})^2 - k^2 - \frac{k\beta}{\omega} - (\frac{\beta}{c})^2 y^2)V = 0 \tag{2.29}$$

Introducing the dimensionless quantities

$$\hat{y} = \sqrt{\frac{\beta}{c}}y = \frac{1}{R_{eq}}y \qquad \hat{\omega} = \frac{\omega}{\sqrt{\beta c}} \qquad \hat{k} = R_{eq}k \tag{2.30}$$

and choosing an ansatz $V = e^{-\hat{y}^2/2}\mathcal{H}(\hat{y})$, equation (2.29) eventually transform into Hermite's eigenvalue problem

$$\mathcal{H}''_n - 2\hat{y}\mathcal{H}'_n + 2n\mathcal{H}_n = 0 \quad \text{with} \quad 2n+1 = \hat{\omega}^2 - \hat{k}^2 - \frac{\hat{k}}{\hat{\omega}}. \tag{2.31}$$

For integer eigenvalues $n \in \mathbb{N}_0 = \{0, 1, 2, \ldots\}$ the Hermite polynomials $\mathcal{H}_n = (-1)^n e^{\hat{y}^2}(d/d\hat{y})^n e^{-\hat{y}^2}$ constitute appropriate solutions which remain bounded as $\hat{y} \to \pm\infty$. The meridional structure is then covered by parabolic cylinder functions, $V_n = e^{-\hat{y}^2/2}\mathcal{H}_n$. The other fields can then be obtained by eliminating
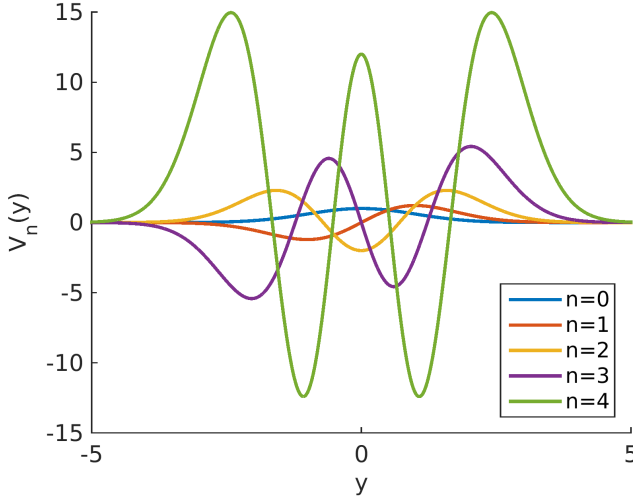
Figure 2.4: The first five meridional structure functions $V_n = e^{-\hat{y}^2/2} \mathscr{H}_n(\hat{y})$. For odd n, the functions are odd and all their extrema lie off the equator. As expected, the functions are even for even n, with local maxima occurring at the equator.

one variable from equations (2.17a-2.17c), respectively. Using the recurrence relation $\mathscr{H}_n' = 2n\mathscr{H}_{n-1}$, the whole solution reads

$$v_{n,k} = (-1)^n e^{i(kx-\omega t)} e^{\hat{y}^2/2} \frac{d^n}{d\hat{y}^n} e^{-\hat{y}^2} = e^{i(kx-\omega t)} V_n(y) \qquad (2.32a)$$

$$u_{n,k} = i\frac{2n\hat{k}V_{n-1} - \hat{\omega}\hat{y}V_n}{\hat{k}^2 - \hat{\omega}^2} e^{i(kx-\omega t)} \qquad (2.32b)$$

$$h_{n,k} = i\frac{D'}{c} \frac{2n\hat{\omega}V_{n-1} - \hat{k}\hat{y}V_n}{\hat{k}^2 - \hat{\omega}^2} e^{i(kx-\omega t)}. \qquad (2.32c)$$

Note that here $\hat{\omega} = \hat{\omega}(n, \hat{k})$ is understood, and corresponds to the three roots of the equation at the right hand side of (2.31). The first meridional structure functions are depicted in figure 2.4. As one can see from this picture, the waves are confined to a region of a few R_{eq} from the Equator.
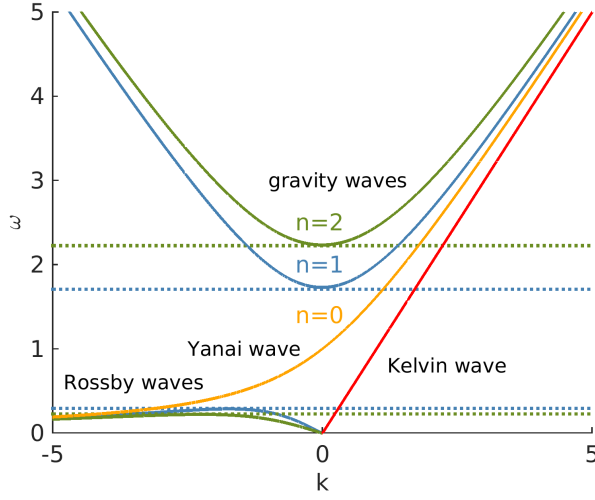
Figure 2.5: Dispersion relation diagram of shallow water equatorial waves from equation (2.33), with frequencies as functions of wave number. Only waves for positive frequencies are shown, but a specular picture is obtained for negative frequencies. The dotted lines indicate the limiting frequencies for each n in equation (2.34). The Kelvin wave (red line) has been artificially added, while its westward propagating counterpart, has to be discarded (see text)

.

2.2.5 *Summary of the obtained solutions*

In order to review all different types of obtained waves in this model, the dispersion relation is obtained from the definition (2.31) of the eigenvalue n, which is most easily regarded as a quadratic equation for $\hat{k}(\hat{\omega})$:

$$\hat{k}^2 + \frac{\hat{k}}{\hat{\omega}} + (2n + 1 - \hat{\omega}^2) = 0, \hat{k}_{1,2} = -\frac{1}{2\hat{\omega}} \pm \frac{1}{2}\sqrt{(\frac{1}{\hat{\omega}} - 2\hat{\omega})^2 - 8n} \quad (2.33)$$

Three different types of waves appear to be contained in this dispersion relation. An overview is shown in the classical diagram in figure 2.5 [Matsuno, 1966; LeBlond and Mysak, 1978]. For a given $n > 0$ two real roots are provided if the determinant is positive, which is the case if

$$\hat{\omega} < \sqrt{\frac{1}{2} + n - \sqrt{n(n+1)}} \quad \text{or} \quad \hat{\omega} > \sqrt{\frac{1}{2} + n + \sqrt{n(n+1)}}. \quad (2.34)$$

Here $\hat{\omega} > 0$ is understood.

34

For *low frequencies*, obeying the left inequality, the term $\hat{\omega}^2$ in the left-hand side of equation (2.33) can be neglected. The approximate result is

$$\hat{\omega} \approx \frac{-\hat{k}}{\hat{k}^2 + (2n+1)}. \tag{2.35}$$

This is the typical dispersion relation for the so called equatorial *Rossby* or *planetary* waves (bottom left in figure 2.5). This class of waves is always travelling westwards, as the zonal phase velocity $\hat{\omega}/\hat{k}$ is negative. However, the group velocity can still become positive for high wave numbers (short waves).

For *high frequencies*, the right-hand side inequality of (2.34) holds. Dropping the term with $1/\hat{\omega}$ in the left-hand side of equation 2.33 then gives

$$\hat{\omega} \approx \pm\sqrt{\hat{k}^2 + (2n+1)}, \tag{2.36}$$

which approximates the dispersion relation for the so-called *Poincaré* or *gravity* waves (upper part in figure 2.5), that travel in either direction. Lastly, if $n = 0$, equation 2.33 can be written as $(\hat{\omega} + \hat{k})(\hat{\omega}^2 - \hat{\omega}\hat{k} - 1)$. From the second bracket, a third type of equatorial wave has the dispersion relation

$$\hat{k} = \hat{\omega} - \frac{1}{\hat{\omega}}. \tag{2.37}$$

This wave is called *Yanai wave* or *mixed Rossby-gravity wave* (blue line in figure 2.5), as it behaves like a Rossby wave for low frequencies and like a gravity-inertial wave for high frequencies. It is the only wave without a frequency gap. The other root, in case $n = 0$, is $\hat{\omega} = -c\hat{k}$, which implies that the meridional velocity is $v = C \cdot e^{-y^2/2}e^{ik(x+ct)}$. The remaining fields then must not be computed with equations (2.32b) and (2.32c) as the denominator becomes zero. Going back to the original system (2.17a)-(2.17c) and assuming that

$$u = \tilde{u}(y)e^{ik(x+ct)} \qquad \text{and} \qquad h = \tilde{h}(y)e^{ik(x+ct)}, \tag{2.38}$$

the meridional structure is determined by the differential equations

$$y\tilde{u} - \tilde{u}' = i\left(\frac{1}{\hat{k}}(1-\hat{y}^2) - \hat{k}\right)e^{-y^2/2} \tag{2.39a}$$

$$y\tilde{h} - \tilde{h}' = i\frac{c}{g}\left(\hat{k} - \frac{\hat{y}^2}{\hat{k}}\right)e^{-y^2/2}. \tag{2.39b}$$

The solutions to these equations turn out to be proportional to $e^{y^2/2}$ (except for the very special case $\hat{k} = \sqrt{1/2}$): they do not match the boundary conditions and are thus discarded. However, there is another wave belonging to the full spectrum, namely the equatorial Kelvin wave already discussed in section 2.2.3.

In fact, an equation for v was deduced to obtain the dispersion relation in (2.33). It follows that the case $v = 0$ got lost, even if it obviously also belongs to the spectrum of the full system equations (2.17a)-(2.17c). In order to have the complete picture in figure 2.5, the Kelvin wave dispersion relation (red line) has been added. Altogether, these wave solutions form a complete set of eigenfunctions for the unforced system (see for example LeBlond and Mysak [1978]).

LIMITATIONS OF THE TRADITIONAL APPROACH   On a first glimpse, the classical shallow water theory of equatorial waves as presented in this section gives a complete and satisfying picture of large-scale processes taking place in the upper part of the water column. It becomes particularly interesting as it provides a complete set of functions (in terms of Hermite polynomials) that allow to describe various disturbances and forcings. However, several questionable points come along with this theory, that are calling for improvements.

As first, shallow water values for typical velocities and spatial scales are, as we have seen, absolutely unrealistic. It follows that the choice for the reduced gravity model rather than for the shallow water model is often made, motivated by the better matching of observed velocity, which seems to be a somewhat arbitrary argument.

On the other hand, the use of the reduced gravity model implies, as we have seen in section 2.2.2, several approximations: on the scale of motions, on the relative strength between the Coriolis parameter and the local stratification and, most importantly, in the assumption of an infinitely sharp thermocline and a completely motionless lower layer. All these elements are far from representing a realistic oceanic situation. Another interesting point lies in the interpretation of the shallow water equations: regarding them as depth integrated relations over the whole water layer H, all interior dynamics within that layer is neglected, with consequences that are difficult to predict.

It follows, for example, that not all of the more general solutions that will be derived in the following sections will find their counterparts in these traditional equatorial wave solutions in any suitable limit, nor after depth integration. This profoundly undermines the validity of the shallow water equations, at least in this particular, equatorial context. At last, observational verification of these long wave theories is, in practice, extremely challenging: data are noisy on the long time scales considered here, and they involve so many processes on shorter time scales such as tides and weather (wind and buoyancy) forcing, that it is difficult to properly isolate different signals. It follows that the necessary preprocessing and filtering of measurements, together with a *traditional* (in all meanings) and consolidated framework of interpretation, might strongly influence the outcome of this kind of data analysis.

Several combinations of these equatorial waves have been used in literature in a long lasting effort of explaining observed equatorial phenomena, such as the observed vertical (and horizontal) variations of strong zonal equatorial currents (from the Equatorial Under Current (EUC), see for example Philander [1973, 1980], to the Equatorial Deep Jets (EDJs), see for example Firing [1987]; Gouriou *et al.* [1999]; Dengler and Quadfasel [2002]; Send *et al.* [2002]), with little to no success in capturing the correct time and spatial scales.

Despite the nice and neat picture presented in figure 2.5, presented in many oceanographic textbooks, the understanding of equatorial wave dynamics is nowadays far from being complete, and the analytical description of equatorial waves far from being robust.

2.3 NON TRADITIONAL SURFACE AND INTERFACIAL EQUATORIAL WAVES

We attempt here to generalise the analytical representation of surface and interfacial equatorial waves. To do so, we start including the non-traditional terms in the general equations of motions. Motivations for solving the traditional or the non-traditional set of equations have been given in section 2.1.2. These are well summarised in LeBlond and Mysak [1978], who also anticipate the results of this current section.

> *Since $f = 2\Omega \sin \phi = 0$ at the equator ($y = 0$), we should not neglect the Coriolis terms associated with the horizontal component of the Earth rotation to be consistent with a β-plane approach. The problem of wave propagation is, however, not separable in terms of vertical and horizontal dependencies when $\tilde{f}$ is retained, and it is then very difficult to proceed with the analysis.*

The fact that these concerns were expressed already 30 years ago should not be read as a failure, but as a proof of the challenging character of the issue, and of its urgency. We shall see in the following that they were, indeed, right. Despite the difficulties, we are obviously not the first ones embarking on a non-traditional generalisation of equatorial waves dynamics. Conscious that a vast literature [Kasahara, 2003; Fruman, 2009; Stewart, 2011; Roundy and Janiga, 2012; Chan and Shepherd, 2013; Constantin, 2012b,a; Constantin and Germain, 2013] on the subject exists, we report here about few of the most significant analytical works on the subject, relevant for our study.

Kasahara [2003] studied the case of a non-hydrostatic, compressible, stratified and rotating fluid on a non-traditional f-plane, bounded by rigid horizontal surfaces. However, he poses periodic boundary conditions in both the zonal and meridional directions, and the model is thus not suitable for equatorial applications. Supported also by some numerical computations, he concludes that the impact of the horizontal component of the Coriolis term on gravity waves

are relatively minor. Nevertheless, if accurate calculations of the divergent flow components are desired, then it is unreasonable to neglect the role of $\tilde{f}$-terms. Likewise, it is not justifiable to neglect the role of $\tilde{f}$-terms in a stratified model if our interest is in the wave motions whose frequencies are close to the Coriolis frequency.

Fruman [2009], on the other hand, focused on equatorial waves and aims explicitly to a generalisation of Matsuno's classical description. He considers meridionally confined, zonally propagating waves on a non-traditional equatorial β-plane. In contrast to Kasahara [2003], his model is hydrostatic. Kelvin, Rossby, inertia-gravity, and mixed Rossby-gravity modes are generalised from the traditional case, however, some limitations are present. In fact the hydrostatic nature of the system in analysis allows for a separable form of the solutions, leading to dispersion relations similar to the ones in Matsuno [1966]. In fact, if the dispersion relation of Fruman [2009] is plotted for a constant vertical wave number it looks exactly like the classical dispersion relation depicted in figure 2.5. Hence, one is tempted to think that Fruman [2009]'s work is just the generalisation of Matsuno's theory. However, all solutions in Fruman [2009] break down if N is taken to be zero, and there is no way to retrieve Matsuno's model, that does not account for buoyancy, using a certain limit. Separable solutions are also used by Raymond [2001] for the case of non-traditional equatorial Kelvin waves in the atmospheric context, since no boundary conditions are used at all.

Eventually, Roundy and Janiga [2012] extended the solutions from Fruman [2009] to a non hydrostatic context. They *a priori* used solutions in a separable form (the atmospheric case is analysed, and no upper boundary condition considered) retrieving all classical equatorial wave classes [Matsuno, 1966], modified from the non-traditional terms. However, they do not provide the explicit expression of the solutions. Roundy and Janiga [2012] also claim that the shallow-water model of Matsuno [1966] can be easily obtained in the limit of $\tilde{f} \to 0$, however, it is not particularly evident how this result can be achieved, considering that $N \neq 0$.

In the following, linear, non hydrostatic equatorial waves are studied on a non-traditional β-plane. For Kelvin waves (section 2.3.1), a stratified fluid is considered, while for waves with non zero meridional velocity (section 2.3.2) an homogeneous fluid is considered.

In contrast to previous studies, we do not use an ansatz of a full separable solution $\propto e^{i\alpha x} e^{i\beta y} e^{i\gamma z}$ is not taken from the beginning, bringing to light some critical issues from which all equatorial waves suffer.

We remark that the analysis presented in this chapter is, at the moment of the writing of this thesis, just a theoretical exercise, and, as it is the case in many other works on the topic, the aim of the study is not "to discuss the possibility

of this kind of wave motion to exist in the atmosphere and oceans" [Kasahara, 2003].

2.3.1 *Non traditional equatorial Kelvin waves*

As we have seen in the previous sections, equatorial Kelvin waves apparently constitute a key ingredient in the observed equatorial surface (or thermocline) dynamics: they can be triggered by remote effects through propagating baroclinic waves in the ocean [Boulanger and Fu, 1996], as well as by local wind forcing. Westerly (easterly) winds blowing over the equator can also cause downwelling-(upwelling-)favourable equatorially trapped Kelvin waves that radiate into the eastern ocean, deepening (shoaling) the thermocline [Rao *et al.*, 2010]. For these reasons, equatorial Kelvin waves are also thought to play a role in the ENSO phenomenon [Giese and Harrison, 1990; Yang and Giese, 2013].

Classic Kelvin wave motion is unidirectional, being everywhere parallel to the equator, and Kelvin waves propagate eastward without dispersion (section 2.2.3, equation (2.21)): in each plane of constant latitude the motion is thus exactly the same as in a corresponding non rotating fluid. Moreover, Kelvin waves constitute the simplest equatorial wave that can be analytically modelled, and thus it comes as no surprise that our attempt to extend equatorial wave dynamics in a non-traditional setting will start from this class of waves.

The system presented in equations (2.6) and (2.2) is here used with $v \equiv 0$:

$$u_t + 2\Omega w = -p_x \tag{2.40a}$$
$$\beta y u = -p_y \tag{2.40b}$$
$$w_t - 2\Omega u = -p_z + b \tag{2.40c}$$
$$b_t + N^2 w = 0 \tag{2.40d}$$
$$u_x + w_z = 0. \tag{2.40e}$$

The buoyancy frequency N is here taken to be a positive constant for the sake of simplicity, corresponding to a linear stratification. This will allow us to use, in a later step, the method of characteristics. Moreover, non-hydrostatic motion is considered, in line with the non-traditional approach. Assuming that the time dependence of b is given, as usual, by $e^{-i\omega t}$, one can use equation (2.40d) to eliminate b from equation (2.40c). From the continuity equation (2.40e), a stream function $\psi(x, y, z)$ can then be introduced, such that

$$u = -\psi_z e^{-i\omega t} \qquad \text{and} \qquad w = \psi_x e^{-i\omega t}. \tag{2.41}$$

where the time dependence is also separated for further convenience. The pressure can be eliminated from eq. (2.40a)- (2.40c) by pairwise combination of

derivatives of these equations (this corresponds to taking the curl). Using the substitutions:

$$\alpha^2 = \frac{N^2}{\omega^2} - 1 \qquad \text{and} \qquad \tilde{\omega} = \omega - \frac{N^2}{\omega} = -\alpha^2 \omega \tag{2.42}$$

the new system then reads:

$$\psi_{zz} - \alpha^2 \psi_{xx} = 0 \tag{2.43a}$$

$$-2\Omega \partial_x (\frac{y}{a} \psi_z + \psi_y) = i\omega \psi_{zy} \tag{2.43b}$$

$$2\Omega \partial_z (\frac{y}{a} \psi_z + \psi_y) = i\tilde{\omega} \psi_{xy}. \tag{2.43c}$$

At this stage, one remark can be made: this system would still be valid if N (and hence α) were functions of the vertical coordinate z. As the way of solving it would then change drastically, this case is not inspected here. The aim is now to find solutions to the system (2.43) for different limiting cases of the ratios between the parameters as well as for different boundary conditions.

New coordinates can then be introduced that are motivated by the characteristic curves of the equations in analysis [Courant and Hilbert, 1953], reading

$$\chi_+ = x + \alpha z \qquad \chi_- = x - \alpha z \qquad \xi = \frac{y^2}{2a}. \tag{2.44}$$

The solution of the equation (2.43a) can be written as a superposition of two functions depending either on χ_+ or χ_-,

$$\psi = G^+(\chi_+, \xi) + G^-(\chi_-, \xi). \tag{2.45}$$

Inserting this in the two remaining equations (2.43b) and (2.43c), they can be decoupled easily and thus yield one equation for each component of ψ,

$$\partial_{\chi_+} [(\frac{i\omega}{2\Omega} + \frac{1}{\alpha})\partial_\xi + \partial_{\chi_+}] G^+(\chi_+, \xi) = 0 \tag{2.46a}$$

$$\partial_{\chi_-} [(\frac{i\omega}{2\Omega} - \frac{1}{\alpha})\partial_\xi + \partial_{\chi_-}] G^-(\chi_-, \xi) = 0. \tag{2.46b}$$

Using the substitution $\gamma^\pm = \frac{i\omega}{2\Omega} \pm \frac{1}{\alpha}$ and integrating once, both equations take the same form,

$$(\gamma^\pm \partial_\xi + \partial_{\chi_\pm}) G^\pm(\chi_\pm, \xi) = C^\pm(\xi). \tag{2.47}$$

Here, the $C^\pm$ are arbitrary functions of ξ only. Dropping the index for a moment, the solution of the latter equation turns out to be

$$G(\chi, \xi) = G_H(\xi - \gamma\chi) + \frac{1}{\gamma} \int_{\xi_0}^{\xi} C(\tilde{\xi}) d\tilde{\xi}. \tag{2.48}$$

This corresponds to the solution of the inhomogeneous equation (2.47). The solution G_H of the corresponding homogeneous equation depends only on $(\xi - \gamma\chi)$. Note however that the constants $C^\pm$ do not have any particular physical meaning. As they depend on y only and consequently drop out by computing the velocities from ψ (see relations (2.41)), we set them to zero. Hence, the stream function reads

$$\psi = G^+(\xi - \gamma^+\chi_+) + G^-(\xi - \gamma^-\chi_-), \tag{2.49}$$

or, in the old coordinates

$$\psi = G^+(\frac{y^2}{2a} - i(\frac{\omega}{2\Omega} - \frac{i}{\alpha})(x + \alpha z)) + G^-(\frac{y^2}{2a} - i(\frac{\omega}{2\Omega} + \frac{i}{\alpha})(x - \alpha z)). \tag{2.50}$$

SOLUTIONS WITH A FIXED BOUNDARY   Most settings in oceanographic context involve at least one fixed boundary (bottom or/and surface), where the normal velocity must vanish. In the following, it is inspected whether solutions to equations (2.43) can satisfy this type of boundary condition. A fixed boundary is considered, which at this point can be chosen, without loss of generality, at the bottom, at $z = 0$. The condition

$$\psi_x|_{z=0} = w|_{z=0} = 0 \tag{2.51}$$

reads, in terms of the new coordinates

$$\partial_{\chi_+} G^+|_{\chi_+=\chi} + \partial_{\chi_-} G^-|_{\chi_-=\chi} = 0, \tag{2.52}$$

where $\chi_+ = \chi_- = \chi$ at $z = 0$. Using the explicit form of the solution (2.48), the condition

$$-\gamma^+(G_H^+)'(\xi - \gamma^+\chi) = \gamma^-(G_H^-)'(\xi - \gamma^-\chi) \qquad \forall \chi, \xi \tag{2.53}$$

results. This can not be satisfied by any function. In fact, the two functions G_H^+ and G_H^- have different arguments, being $\gamma^+ \neq \gamma^-$ by definition, and thus can satisfy equation (2.53) only in case they both vanish. This demonstrates that boundary conditions at a fixed boundary cannot be satisfied by the set (2.43).

EXPONENTIALLY DECAYING SOLUTIONS   We have shown that non-traditional equatorial Kelvin waves can not exist in the presence of a fixed boundary. However, solutions for non-traditional Kelvin waves at the surface (or, analogously, at one interface), and decaying exponentially with depth are possible, and already described in literature, for example in section 3.3. of Raymond [2001] (note that there the atmospheric case is in analysis, and thus waves are decreasing exponentially with *height*). These waves do not feel the influence of the bottom and are trapped near the surface. The boundary condition $\psi|_{z=-H} = 0$ is thus replaced by the asymptotic condition,

$$\lim_{z \to -\infty} \psi = 0. \tag{2.54}$$

By inserting an ansatz of the kind $p = e^{-i\omega t}(P^+ G^+ + P^- G^-)$ with a priori unknown constants $P^\pm$ in the original system (2.40a)-(2.40c), the pressure can be expressed in terms of the stream function according to

$$p = -2\Omega \alpha e^{-i\omega t}(\gamma^+ G^+ - \gamma^- G^-). \tag{2.55}$$

With the convenient choice

$$G_k^+(X) = A_k^+ e^{-Xk/(\frac{\omega}{2\Omega}+1)},$$

only

$$G_k^- = A_k^- e^{-\frac{y^2}{2}\frac{k\beta}{\omega+2\Omega}} e^{k(ix+z)}$$

vanishes for $z \to -\infty$ and hence one has to choose $G_k^+ \equiv 0$. The classic, surface dynamic boundary condition $p_t = gw$ at $z = 0$ then yields the dispersion relation

$$k = \frac{\omega^2}{g}(\frac{2\Omega}{\omega} - \sqrt{1-(\frac{N}{\omega})^2}). \tag{2.56}$$

The wave number k will become complex in the classical case of $N > \omega$ which leads to a rather complicated mixed oscillating and decaying behaviour both in x and z.

Additionally, another problem is present: as the wave number in the zonal direction only differs by a factor i from the wave number in the vertical direction, the asymptotic condition (2.54) can only be satisfied for deep water waves, that is, for modes with

$$k \gg \frac{1}{H}. \tag{2.57}$$

As typically $H \approx 4$ km, this leads to relatively short waves in the zonal direction that do not match with observations.

TRADITIONAL KELVIN WAVES IN A STRATIFIED FLUID   It is possible to relax the long wave approximation and to include stratification in our description, neglecting, however, the non-traditional terms ($\gamma^+ \approx \gamma^-$), in order to meet the boundary conditions. In case of $\omega^2 < N^2$, α is real and γ splits in a real and an imaginary part, neither of which can be easily neglected. Thus, $\omega^2 > N^2$ is instead taken in the following, leading to the real parameter

$$\tilde{\alpha} = \frac{\alpha}{i} = \sqrt{1 - \frac{N}{\omega}}. \tag{2.58}$$

The condition on the frequency then changes and reads

$$\omega^2 \gg 4\Omega^2 + N^2. \tag{2.59}$$

Again using $G(X) = \sum_k G_k = \sum_k A_k e^{-k\frac{2\Omega}{\omega}X}$, the contribution for a single k is

$$\psi_k = e^{-\frac{y^2}{2}\frac{k\beta}{\omega}} e^{ikx} (A_k^+ e^{-\tilde{\alpha}kz} + A_k^- e^{+\tilde{\alpha}kz}). \tag{2.60}$$

Following the same reasoning as in the previous section and demanding a vanishing ψ at the lower boundary, the solution is first recast as

$$\psi_k = A_k e^{-\frac{y^2}{2}\frac{k\beta}{\omega}} e^{ikx} \sinh(\tilde{\alpha}k(z+H)). \tag{2.61}$$

At the upper boundary, the linearised boundary conditions can be then applied again. We then obtain

$$\omega^2 = -\frac{gk}{\tilde{\alpha}} \frac{(G^+ + G^-)}{(G^+ - G^-)}\Big|_{z=0} = \frac{gk}{\tilde{\alpha}} \tanh(\tilde{\alpha}kH). \tag{2.62}$$

Not surprisingly, this dispersion relation looks very similar to the one describing surface gravity waves in a non-rotating fluid. It is, however, considerably more complicated since the factor $\tilde{\alpha}$ appears, that accounts for stratification effects but also depends on ω.

2.3.2 *Non traditional equatorial waves with non zero meridional velocity*

In this section, equatorially (meridionally) bounded solutions with a non-vanishing meridional velocity are studied on a non-traditional equatorial β-plane. This constitutes an attempt to generalise to a non-traditional setting the work of Matsuno [1966].

GOVERNING EQUATIONS   A non hydrostatic, homogeneous case is here considered. The solutions will turn out to be of a form similar to the solutions obtained in section 2.2.4. The methodology used is however different, as one now has to start from the non-traditional set of equations, written for further convenience in vectorial form as

$$\vec{u}_t + 2\vec{\Omega} \times \vec{u} = -\nabla p \qquad \text{where} \qquad \vec{\Omega} = \Omega(\hat{e}_y + \frac{y}{a}\hat{e}_z). \tag{2.63}$$

Taking the curl yields the vorticity balances

$$(\nabla \times \vec{u})_t + \beta v \hat{e}_z - 2\Omega L \vec{u} = 0, \tag{2.64}$$

where, as usual, $\beta = 2\Omega/a$ and

$$L = \partial_y + \frac{y}{a}\partial_z. \tag{2.65}$$

Now, it is assumed, again, that for all quantities the time dependency can be expressed with the factor $e^{-i\omega t}$, such that the substitution $\partial_t \to -i\omega$ can be

made. Taking the curl gives then, after using the continuity condition, $\nabla \cdot \vec{u} = 0$,

$$i\omega \Delta \vec{u} + \beta \begin{pmatrix} v_y - w_y \\ -v_x \\ u_z \end{pmatrix} - \frac{2\Omega}{i\omega} L \begin{pmatrix} 0 \\ 0 \\ \beta v \end{pmatrix} + \frac{4\Omega^2}{i\omega} L^2 \begin{pmatrix} u \\ v \\ w \end{pmatrix} = 0. \qquad (2.66)$$

Here, the square of L has to be computed using Leibniz's rule,

$$L^2 = \partial_y^2 + 2\frac{y}{a}\partial_z\partial_y + (\frac{y}{a})^2\partial_z^2 + \frac{1}{a}\partial_z.$$

To solve this set of equations we notice that the second line constitutes an equation for v alone, the meridional component of the velocity. First all quantities are assumed to be proportional to e^{ikx}, substituting $\partial_x \to ik$, such that a single Fourier component is considered at the time. This is possible without loss of generality as there are no mixed derivatives or couplings that involve the zonal direction. Furthermore, a normalised frequency $\omega' = \frac{\omega}{2\Omega}$ will be used from now onward, and the prime immediately dropped. The second line then eventually reads

$$[-(\omega^2 k^2 + \frac{\omega k}{a}) + (\omega^2 - 1)\partial_y^2 + (\omega^2 - \frac{y^2}{a^2})\partial_z^2 - 2\frac{y}{a}\partial_y\partial_z - \frac{1}{a}\partial_z]v = 0. \quad (2.67)$$

The behaviour of the latter equation is then analysed by means of its characteristic curves. This approach provides a convenient set of coordinates. Equation (2.67) in fact has oscillatory solutions only if it is of hyperbolic type. We shall see later that this happens when $\omega < 1$. Anticipating this result, scales can then be conveniently introduced that facilitate the analysis by setting the factor in front of ∂_y^2 equal to one:

$$(k,l) = \frac{1}{a}(k',l') \quad y = a\sqrt{1-\omega^2}y' \quad (x,z) = a(x',z') \quad t = \frac{1}{2\Omega}t' \quad (2.68)$$

and, analogously, immediately dropping the primes. With this scaling, 2.67 becomes

$$[-\mu^2 - \partial_y^2 + (\omega^2 - (1-\omega^2)y^2)\partial_z^2 - 2y\partial_y\partial_z - \partial_z]v = 0, \qquad (2.69)$$

where

$$\mu^2 = \omega k(1 + \omega k). \qquad (2.70)$$

We will see in section 2.4.4 that equation (2.69) can be compared to equation (2.105), and is an extended version of the so called Stern's equation, first derived by Stern [1963]. Comparing it to Stern's equation, in fact, two additional

terms appear: μ^2, due to the zonal wave propagation which is ruled out by assumption in Stern's original equation, and the factor $\omega^2 y^2$ of the vertical partial derivative, because the model here considered is non-hydrostatic. One should thus be able to compare the solutions obtained in this section to results from the Stern equation by looking at the case $\omega^2 \ll 1$ and $k = 0$ (and consequently $\mu = 0$). We now classify the the PDE (2.69), following the usual notation

$$A d_{yy} + 2B d_{yz} + C d_{zz} + \text{lower order terms} = 0 \qquad (2.71)$$

and we look at the discriminant δ. For equation (2.69)

$$A = -1, \qquad B = -y, \qquad C = \omega^2 - (1 - \omega^2) y^2. \qquad (2.72)$$

and $\delta = AC - B^2 = -\omega^2(1 + y^2) < 0$. The equation is thus hyperbolic for all values of y, if, as it was anticipated, $\omega < 1$. The relation determining the two characteristics is then

$$\frac{dz}{dy} = \frac{B \pm \sqrt{-\delta}}{A} = y \pm \omega \sqrt{y^2 + 1}. \qquad (2.73)$$

This means that new coordinates resulting from

$$z - \int \frac{B \pm \sqrt{-\delta}}{A} dy = \chi_\pm$$

will render the PDE of the form

$$\partial_{\chi_+} \partial_{\chi_-} v + \cdots = 0$$

where only a mixed derivative appears. The mixed derivative can be removed by introducing

$$\hat{\xi} = \chi_+ + \chi_- = 2z - 2 \int \frac{B}{A} dy = 2z - y^2 \qquad (2.74a)$$

$$\hat{\eta} = \chi_+ - \chi_- = -2 \int \frac{\sqrt{-\delta}}{A} dy = \omega y \sqrt{y^2 + 1} + \omega \ln(2(\sqrt{y^2 + 1} + y)). \qquad (2.74b)$$

The $\hat{\eta}$ coordinate is clearly not very practical, but as it is only a function of y, it is worth trying a simplified approach. Hence, we introduce more convenient coordinates:

$$\xi = z - y^2/2 \qquad (2.75a)$$

$$\eta = y. \qquad (2.75b)$$

Equation (2.69) then takes a simpler form, namely

$$[\mu^2 + \partial_\eta^2 - \omega^2(1 + \eta^2)\partial_\xi^2] v = 0. \qquad (2.76)$$

GENERAL FREE SOLUTIONS   Adopting all manipulations made so far to the system in (2.66) and using the continuity equation in the first line to replace w_z, the governing equations then read

$$(-\omega^2 k^2 + \omega^2(1+\eta^2)\partial_\xi^2 - \partial_\eta^2) \begin{pmatrix} u \\ v \\ w \end{pmatrix} +$$

$$-i\omega \begin{pmatrix} (\frac{2}{\sqrt{1-\omega^2}})(v_\eta - \eta v_\xi) + iku \\ -ikv \\ u_\xi \end{pmatrix} +$$

$$+ \begin{pmatrix} 0 \\ 0 \\ (\frac{1}{\sqrt{1-\omega^2}})(v_\eta - \omega^2 \eta v_\xi) \end{pmatrix} = 0.$$

(2.77)

We note that the u-equation appears in this form as a forced version of the v-equation. This latter one can be solved by transforming it to Hermite's differential equation in two steps. First, a separation of variable $v = e^{l\xi}V(\eta)$ is performed, yielding

$$[\mu^2 + \partial_\eta^2 - \omega^2(1+\eta^2)l^2]V(\eta) = 0.$$

(2.78)

By taking $V = e^{-\omega l\eta^2/2}\mathscr{H}(\sqrt{\omega l}\eta)$, one finally arrives at Hermite's equation (with $n \in \mathbb{N}_0 = \{0,1,2,\dots\}$):

$$\mathscr{H}_n'' - 2\sqrt{\omega l}\eta\mathscr{H}_n' + 2n\mathscr{H} = 0,$$

(2.79)

where

$$2n + 1 = \frac{\omega}{l}(k^2 - l^2 + \frac{k}{\omega}).$$

(2.80)

The solutions are then Hermite polynomials $\mathscr{H}_n$, that were already discussed in section 2.2.4. Again, only solutions satisfying the quantization condition of $n \in \mathbb{N}_0$ can be accepted, as all other solutions diverge for $y \to \pm\infty$. This yields the dispersion relation in equation (2.80).

Note that this transformation works out only for an exponential separation ansatz $v \propto e^{l\xi}$, as an oscillatory ansatz $v \propto e^{il\xi}$ would render some coefficients in the dispersion relation imaginary, such that no $n \in \mathbb{N}_0$ could be found. The resulting analogue for equation (2.78) in case of an oscillatory ansatz could be solved in terms of Whittaker functions. In this latter case, however, it is by no
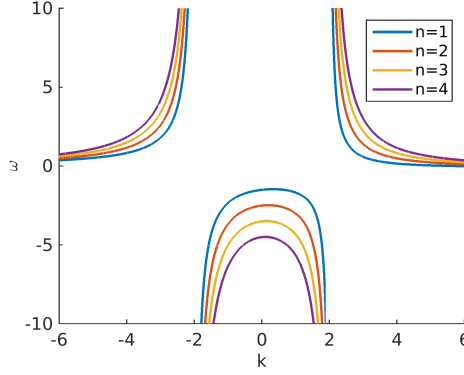
Figure 2.6: The dispersion relation in equation 2.80, with frequencies as functions of wave number. Here the case of $l = 2$ and different values of n, according to the legend.

means clear how to solve the remaining PDEs for u and w. Moreover, problems with discontinuities of the Whittaker functions at $y = 0$ (the equator) would appear.

Writing the dispersion relation in equation (2.80) in terms of dimensional quantities yield

$$\omega_n = -\beta \frac{k - (2n+1)l}{k^2 - l^2}. \tag{2.81}$$

Here $k \neq l$ is intended, since the case $k = l$ necessarily corresponds to $n = 0$ (equation (2.80)) and thus $\mathcal{H}_0 = 1$. This result differs from the dispersion relation in equation (2.31) given by Matsuno [1966]; notably, it is linear in ω. Moreover, equation (2.81) resembles the dispersion relation of Rossby waves induced by the β-effect, see for example LeBlond and Mysak [1978], here a quadratic subtraction replaces the quadratic summation in the denominator. In order to get (2.81), the assumption of an exponential rather than an oscillatory behaviour in the vertical is essential. As the vertical wave number also applies to the meridional coordinate, an imaginary number would destroy the proper asymptotic limit. Figure 2.6 shows the dispersion relation for fixed l and different values of n.

Altogether, a single component of the meridional velocity that is characterised by the wave numbers (k, l, n) can be written (still in scaled quantities according to (2.68))

$$v_{k,l,n} = \sqrt{1 - \omega_n^2}\, e^{i(kx - \omega_n t) + l(z - (1+\omega_n)\frac{y^2}{2})} \mathcal{H}_n(y\sqrt{\omega_n l}). \tag{2.82}$$

Here, a frequency-dependent amplitude factor was put in for further convenience. From this result, the other velocity components can be determined and it follows that they must be proportional to the same exponential function. To explicitly write an expression for u and w we can use the recurrence relations for Hermite polynomials

$$X\mathscr{H}_n(X) = \frac{1}{2}\mathscr{H}_{n+1}(X) + n\mathscr{H}_{n-1}(X) \text{ and } \mathscr{H}'_n(X) = 2n\mathscr{H}_{n-1}(X). \quad (2.83)$$

These recurrence relations allow to convert the y-dependencies as well as the derivatives with respect to y into algebraic relations. Hence, the components of u and w corresponding to a certain $v_{k,l,n}$ are linear combinations of $\mathscr{H}_{n+1}$ and $\mathscr{H}_{n-1}$, like in section 2.2.4. To compute the coefficients of these linear combinations, we first compute u from the first line of equation (2.77), that does not depend on w, and then proceed with the third line of equation (2.77). The result is

$$u_{k,l,n} = -i\sqrt{\frac{l}{\omega_n}}e^{i(kx-\omega_n t)+l(z-(1+\omega_n)\frac{y^2}{2})}\left(\frac{\omega_n-1}{l-k}n\mathscr{H}_{n-1} + \frac{1}{2}\frac{\omega_n+1}{l+k}\mathscr{H}_{n+1}\right)$$

$$(2.84a)$$

$$w_{k,l,n} = \sqrt{\frac{l}{\omega_n}}e^{i(kx-\omega_n t)+l(z-(1+\omega_n)\frac{y^2}{2})}\left(-\frac{\omega_n-1}{l-k}n\mathscr{H}_{n-1} + \frac{1}{2}\frac{\omega_n+1}{l+k}\mathscr{H}_{n+1}\right),$$

$$(2.84b)$$

where the argument of the Hermite polynomials is $y\sqrt{\omega_n l}$. These solutions also satisfy the continuity equation. The contribution to the pressure field follows from the first momentum equation in equation (2.63), yielding

$$p = \frac{\tilde{p}}{\rho_* 2\Omega a} = i\frac{1-\omega^2}{l-k}\frac{1}{\sqrt{\omega l}}e^{i(kx-\omega_n t)+l(z-(1+\omega_n)\frac{y^2}{2})}\left(n\mathscr{H}_{n-1} - \frac{1}{2}\mathscr{H}_{n+1}\right).$$

$$(2.85)$$

The meridional dependence in the exponential reads in dimensional coordinates (see scaling in (2.68))

$$l'(1+\omega')\frac{y'^2}{2} = l\frac{2\Omega}{2\Omega-\omega}\frac{y^2}{2}, \quad (2.86)$$

where $\omega < 2\Omega$ by assumption, since we are studying here the regime for which we have oscillatory type of solutions (equation (2.67) is hyperbolic).

2.3.3 Concluding remarks

The current attempt to a non-traditional generalisation of geophysical, equatorial waves adds to the many existing ones (i.e. Kasahara [2003]; Raymond

[2001]; Fruman [2009]; Roundy and Janiga [2012]). The difference with these previous studies lies, all in all, in the fact that here an oceanic case is considered, while the atmospheric case is considered in the large majority of previous studies on this topic. Oceanic, non-traditional, equatorial waves have been also previously considered (i.e. Hua *et al.* [1997], or Stewart [2011]) but with completely different perspectives (mainly inclusion of non-traditional terms in existing numerical codes). Fundamental issues such as the ones addressed in this section are barely present in literature, and, to our knowledge, no lucid study on non-traditional equatorial waves exists, probably because of the lack of conclusive findings, as we have seen in the previous sections. In fact, when ocean waves and appropriate boundary conditions are considered, the ansatz of solutions being proportional to e^{ilz} is not taken a priori (as in *all* the abovementioned works), and non separability of the y and z dependencies brings all the complexities we tried to face. Using a separability ansatz in (2.77), although in ξ, η coordinates, is in fact the only way a dispersion relation can be found.

It is remarkable that all velocity components u, v, w retrieved in section 2.3.2 share the same non-trivial z-dependency. This is in contrast with the classical solutions of Matsuno [1966], where only the vertical velocity is (linearly) dependent on z. This reflects to the fact that it is not possible to go from the solutions presented in this section to Matsuno's solutions by taking a certain limit, like it was possible with the equatorial Kelvin waves in section 2.3.1. One reason certainly lies in the interpretation and use of the shallow water equations in Matsuno [1966], where all interior effects are neglected. In fact, if one assumes that the horizontal velocity components u and v do not depend on z, whole classes of solutions are immediately excluded.

We can finally consider here the limiting case of low frequencies $\omega/2\Omega \ll 1$ and zonal symmetry $k = 0$ (common assumptions when internal waves are considered, as in Stern [1963]; Bretherton [1964]; Maas and Harlander [2007]). Then, the dispersion relation equation (2.81) is reduced to

$$\omega_n = -\beta \frac{2n+1}{l} \qquad (2.87)$$

This allows to eliminate the wave number l, but in turn implies that the scale factor $\sqrt{\omega_n l}$ inside the Hermite polynomials becomes imaginary. These functions look quite different from Hermite polynomials with real argument, especially as they have only two extremal points at any order. In figure 2.7, they are depicted for different values of n.

By comparing solutions for the zonally symmetric case depicted in figure 2.7 to the Hermite polynomials in figure 2.4, it appears that all even complex Hermite polynomials have a structure roughly akin to the mode $n = 2$ (in figure
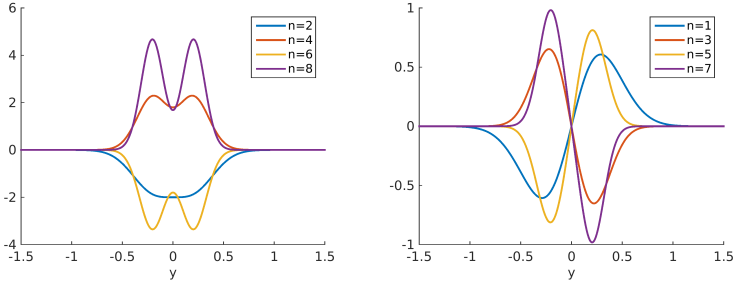
Figure 2.7: Amplitude values for functions of the type $e^{\frac{2n+1}{2\omega}\hat{y}^2}\mathscr{H}_n(i\sqrt{2n+1}\cdot\hat{y})$ for $\hat{\omega} = -0.25$. The purely real functions, for even n, are shown on the left hand side, the purely imaginary functions, for odd n, on the right hand side. Note that the different modes have all the same number of extrema or nodes, in contrast with figure 2.4. Moreover the amplitude differences between modes are large (3 orders of magnitude between, for example $n = 2$ and $n = 8$): for displaying, amplitudes (positive) are then arbitrarily chosen to fit the figure.

2.4). Noticeably, of all various waves found in the classical (Matsuno's) theory, it is this mode $n = 2$ which is often used to explain observational results as mentioned at the end of section 2.2.4 [Wakata, 2007]. In the light of the solutions found in this section in a non-traditional context, observational results might invite for a new interpretation.

We have learned in this section that when both equatorial trapping and vertical boundary conditions are considered, problems arise as a consequence of the coupling between y and z-directions of the system. Among other issues, it is seemingly impossible to impose an asymptotic boundary condition in one of these directions, say y, while demanding fixed boundaries in the other direction, say z, or vice versa. One way out of this dilemma might be the introduction of fixed boundaries in y-direction. In the context of internal inertia-gravity waves, this approach finds its justification in the existence of *turning surfaces*, acting as impenetrable walls for waves, and will be discussed in section 2.4.1.

2.4 INTERNAL WAVES

So far, all waves discussed in this chapter have been *surface* or *interfacial waves*, as they had their maximum amplitude at the sea surface, or at a deeper density interface, such as the thermocline. This type of waves are the most familiar to us, as surface waves are the ones we are used to observe while lying at the beach, or sailing on a ship. Interfacial waves are more difficult to observe with the naked eye, however they can bear a distinctive signature up to the surface as well.

50

However, in the quest for a robust representation of equatorial wave dynamics, another class of waves must also be taken into consideration: *internal waves*, especially if one is interested in deep equatorial phenomena. Internal waves are waves that travel within any kind of stratified fluid (ocean included) and, in contrast to the surface waves, present their maximum amplitude in the interior of the fluid and not at its boundary. Stratification might be built in density, but also in angular momentum, giving rise to internal gravity waves or inertial (gyroscopic) waves, respectively. A combination of the two restoring forces, gravity and rotation, is also possible and results in the combined internal inertia-gravity waves.

These waves could in principle also play an important role in the equatorial dynamics, possibly interacting with the mean current field via wave-wave and wave-current processes. In the rest of this thesis, internal waves in the equatorial ocean will be studied by means of ray-tracing and observationally, since no explicit analytical representation of equatorial internal waves it known at present. The follow-up of this section has in fact to be read as the rationale for this lack of analytical results, and the formal justification for using alternative, non analytic approaches to study internal waves at the equator (or elsewhere).

A short overview on general internal wave theory is given in section 2.4.1. The interested reader can refer to any book of geophysical fluid dynamics (for example LeBlond and Mysak [1978] or Gill [1982]) or to Gerkema and Zimmerman [2008] for a more extensive introduction to the topic. We will then highlight the difficulties arising when internal waves are studied in confined basins, such as in our Earth's ocean (section 2.4.2), in order to focus eventually to a low latitude setting (section 2.4.4).

2.4.1 *Internal inertia-gravity waves: general theory*

In a rotating, stratified fluid like the ocean, buoyancy as well as Coriolis force can act as restoring forces to a water parcel and can support internal waves of the inertia-gravity type. The set of equations of motion and continuity considered here to describe such oscillations is again (2.1) and (2.2), that we rewrite here assuming, as usual, the time dependency of all quantities is $e^{-i\omega t}$ and N is constant:

$$-i\omega u - f v + \tilde{f} w = -p_x \tag{2.88a}$$

$$-i\omega v + f u = -p_y \tag{2.88b}$$

$$-i\omega w (1 - \frac{N^2}{\omega^2}) - \tilde{f} u = -p_z \tag{2.88c}$$

$$u_x + v_y + w_z = 0. \tag{2.88d}$$

In this set the buoyancy term in the right hand side of equation (2.1c) has been eliminated using equation (2.1d). We are retaining here the non-traditional terms, and we are thus on the so-called $f, \tilde{f}$-plane. We can now write the velocity components in terms of the pressure,

$$u = \frac{(i\omega p_x - f p_y)(\omega^2 - N^2) + \tilde{f}\omega^2 p_z}{(f^2 - \omega^2)(\omega^2 - N^2) + \tilde{f}\omega^2} \qquad (2.89a)$$

$$v = -\frac{i}{\omega}(fu + p_y) \qquad (2.89b)$$

$$w = \frac{i}{\omega(1 - \frac{N^2}{\omega^2})}(\tilde{f}u - p_z) \qquad (2.89c)$$

and, using equation (2.88d), an equation for pressure only can be derived, the so-called Poincaré equation (christened by Cartan [1922]), which reads, in its three-dimensional form:

$$(\omega^2 - N^2)p_{xx} + (\omega^2 - N^2 - \tilde{f}^2)p_{yy} - 2f\tilde{f}p_{yz} + (\omega^2 - f^2)p_{zz} = 0. \quad (2.90)$$

It follows that plane wave solutions of the kind $p \propto e^{i\vec{k}\vec{x}}$, where the wave number vector is $\vec{k} = (k, l, m)$ are subject to the dispersion relation

$$\omega^2 = N^2 \frac{k^2 + l^2}{k^2 + l^2 + m^2} + 4\Omega^2 \frac{(l\cos\phi + m\sin\phi)^2}{k^2 + l^2 + m^2}. \qquad (2.91)$$

This relation is usually and conveniently rewritten in terms of θ, the angle between $\vec{k}$ and the horizontal plane (defined as the plane perpendicular to the local gravity vector), and α is the angle between $\vec{k}$ and the local Coriolis parameter $\vec{\Omega} = (0, \Omega\cos\phi, \Omega\sin\phi)$, and reads

$$\omega^2 = N^2 \cos^2\theta + 4\Omega^2 \cos^2\alpha. \qquad (2.92)$$

This dispersion relation reveals an interesting feature of internal waves: in distinction to what is valid for the surface wave case, frequency in this case only fixes these relevant angles (α and θ), and not the absolute value of $\vec{k}$. Internal waves retain their angle with respect to the and are then *monoclinic* and not, as surface waves, *monochromatic*. We shall see in chapters 3 and 4 that this aspect of internal waves lies at the core of the ray tracing technique used for the study of internal waves.

It is clear from the dispersion relation in equation (2.92) that the internal wave frequency range is bounded by the condition

$$\omega^2 < N^2 + 4\Omega^2. \qquad (2.93)$$

Furthermore, the group velocity for internal waves reads

$$\vec{c}_{gr} = \frac{1}{\omega \vec{k}^2} [\vec{k}^2 \begin{pmatrix} N^2 k \\ (N^2 + 4\Omega^2 \cos^2 \phi) l \\ 4\Omega^2 \sin^2 \phi m \end{pmatrix} +$$

$$-(N^2(k^2 + l^2) + 4\Omega^2(l^2 \cos^2 \phi + m^2 \sin^2 \phi)) \begin{pmatrix} k \\ l \\ m \end{pmatrix}].$$

(2.94)

For internal waves the group velocity is always perpendicular to $\vec{k}$, and hence wave energy always propagate perpendicular to phase velocity.

To analyse the Poincaré PDE in (2.90) we will first consider the case of axisymmetric (zonally symmetric) motion, which means $\partial_x \equiv 0$. Only derivatives in y and z then remain, and the factors in front of these terms are

$$A = \omega^2 - N^2 - \tilde{f}^2 \qquad B = -f\tilde{f} \qquad C = \omega^2 - f^2. \tag{2.95}$$

Oscillating solutions then exist when

$$AC - B^2 = \omega^2(\omega^2 - N^2 - 4\Omega^2) + 4\Omega^2 N^2 \sin^2 \phi < 0. \tag{2.96}$$

This is the condition for eq. (2.90) to be of the hyperbolic type, and it also illustrates the symmetric role of N and 2Ω. We can now solve the last equation for a certain latitude ϕ, in case of a given ω, in order to define the corresponding "critical latitudes" [Hughes, 1964; LeBlond and Mysak, 1978; Gerkema *et al.*, 2008]:

$$\phi_\omega^c = \pm \arcsin[\frac{\omega^2}{4\Omega^2} + \frac{\omega^2}{N^2}(1 - \frac{\omega^2}{4\Omega^2})]^{1/2}. \tag{2.97}$$

For a given frequency, propagating waves can exist only in a latitudinal belt defined by the two critical latitudes, see figure 2.8.

Waves travelling polewards that are forced at low latitudes can thus only reach their critical latitude ϕ_ω^c. There they encounter the corresponding "turning surface", an imaginary barrier connecting the sea surface to the ocean floor, beyond which only exponentially decaying solutions exist and the medium becomes non-permeable (for that specific ω). This fact could motivate the use of fixed boundaries in the y-direction under certain circumstances, as speculated at the end of section 2.3.2. It is worth noting that the definition of the critical latitudes strongly depends on the presence of non-traditional terms: by looking at the traditional version ($\tilde{f} \equiv 0$) of the hyperbolicity condition in equation (2.96)

$$(\omega_{TA}^2 - f^2)(\omega_{TA}^2 - N^2) < 0 \Rightarrow \min(|f|, N) < \omega_{TA} < \max(|f|, N), \tag{2.98}$$
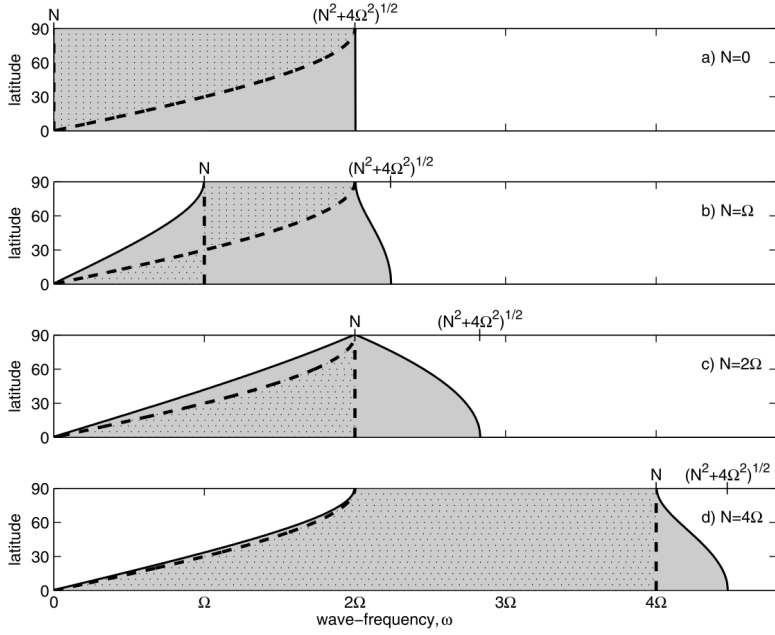
Figure 2.8: Internal wave frequency range as a function of latitude (only the positive latitudes are shown, the plot is symmetric in the southern hemisphere). Stratification increases from (a) $N = 0$, (b) $N = \Omega$,(c) $N = 2\Omega$,to (d) $N = 4\Omega$. Typically, $N > 2\Omega$ is in fact found in the ocean. The boundaries of the range (in grey) are indicated by solid curves: they represent the critical latitude ϕ_ω^c for each ω, and are described by equation (2.97). For comparison, the range as obtained under the TA is also shown (dashed lines and dotted regions). (b) and (d) nicely show the symmetric role played by N and 2Ω in the non-traditional framework. Figure from Gerkema *et al.* [2008]

it appears that only one of the bounds on frequency is latitude-dependent under the traditional approximation. This corresponds to the definition of the "traditional" critical latitude

$$\phi_\omega^{c,TA} = \pm \arcsin\left(\frac{\omega}{2\Omega}\right), \tag{2.99}$$

whereas the buoyancy frequency N constitutes the second bound in the traditional case. Thus, the curves in figure 2.8 are then cut by the dashed line associated with N.

Equation (2.99) also corresponds to the non-traditional critical latitudes in case of a homogeneous, rotating fluid confined to a spherical container or a spherical shell. In this case, no turning surface occurs, but $\phi_\omega^{c,TA}$ corresponds to the latitude where the internal wave energy rays of frequency ω have the same inclination as the tangent to the local topography. As we shall see in section 2.4.2, and, in more detail, in chapters 3 and 4, this criticality might give rise to local singularities, possibly affecting the whole wave field.

We like to recall here that the approach to turning latitudes adopted here is based on an $f, \tilde{f}$-plane, following, for example LeBlond and Mysak [1978] or Gerkema *et al.* [2008]. While catching some basic features of turning surfaces like their existence and the fact that they depend also on the non-traditional terms, it does however neither account for curvature terms of the domain nor for a non-constant buoyancy frequency N. It was put forward for example by Friedlander [1982] and Winters *et al.* [2011], respectively, that both effects independently can cause the turning surfaces to become dependent on the radial coordinate (in other words, on depth).

2.4.2 *Internal waves in a confined domain: the ocean case*

In the preceding section, we have derived the three-dimensional Poincaré equation (2.90), describing the pressure field of internal waves propagating in an infinite domain. In two-dimensions, an internal wave streamfunction can be derived satisfying an equivalent equation. Moreover, both the rotation axis and the gravity vector orientation were kept fixed. However, on Earth, the relative orientation between gravity vector and rotation axis clearly depends upon position, and moreover, waves travel in a confined ocean, ideally contained between the sea-surface and the sea-floor as in a thin, spherical shell of water wrapping our planet.

Taking these factors into consideration and solving equation (2.90) is extremely difficult and no general, analytical solutions are known to date. The reason is that the underlying problem is, in general, mathematically ill-posed [Rieutord *et al.*, 2000]. It combines a hyperbolic differential equation (the Poincaré pressure equation (2.90)) with oblique-derivative boundary conditions at the

walls of the container (where normal velocity must vanish), rather than with initial conditions, and thus remains unsolvable.

Regular analytical solutions for internal waves in a fully bounded domain are available only for a selection of simplified cases (i.e. in the constant density, pure inertial case) in exceptionally symmetric geometries, such as for two-dimensions, the rectangle and the circle (see, for example, Barcilon [1968]), and the elliptic domain [Maas and Lam, 1995]; for the three-dimensional case: the axial cylinder [Lord Kelvin, 1880b; Høiland, 1962], the axial ellipsoid [Kudlick, 1966] and the full sphere [Bryan, 1889; Zhang *et al.*, 2001]. Quasi-analytical methods have been also used to compute regular inertial wave fields in the case of an untilted rectangular parallelepiped [Maas, 2003; Nurijanyan *et al.*, 2013]. Numerous attempts to handle the full inviscid problem of internal waves propagating in spherical shell were in vain. That is the reason why approximate methods, such as ray-tracing techniques (see the introductory sections in chapter 3 and 4) or pure numerical (viscous) approaches [Rieutord and Valdettaro, 1997; Dintrans *et al.*, 1999; Ogilvie and Lin, 2004; Favier *et al.*, 2014] are so widely adopted when more complex domain geometries are considered.

Summarising, no analytical solutions are available at the moment for a "realistic" finite, stratified and rotating ocean, in a low-latitude belt as well as anywhere else on Earth. However, under some assumptions, some solutions are found. This is the case in section 2.4.4. Perhaps one of the most fascinating difficulties encountered when dealing with internal waves is that internal wave behaviour is strongly domain-dependent. In non trivial containers, this gives rise to singular features such as the *internal wave attractors*, that, as we shall see in the next section, can influence the wave energy distribution within the domain of interest.

2.4.3 *Internal wave attractors*

A fascinating consequence of the monoclinicity of internal waves is the unique way they interact with the geometrical shape of their own container. The fact that the internal wave angle of propagation is conserved upon reflection on the boundary, while its wavelength can change (see figure 2.9), leads to the occurrence of asymptotically periodic (closed) trajectories of wave energy rays onto which all wave energy is focused and trapped. For this reason, these trajectories are called *attractor* [Maas *et al.*, 1997]. In this section, only a qualitative overview of this phenomenon will be presented, while a more rigorous description, occurrence, and possible relevance for equatorial dynamics, will be addressed in chapter 3.

Internal wave attractors occur in all *symmetry-breaking* domains. These are domains whose walls are somehow breaking the symmetry imposed by the
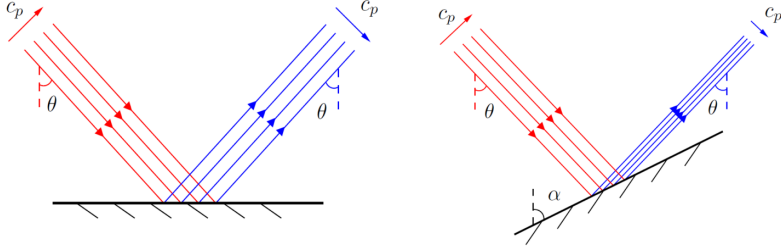
Figure 2.9: Ray tracing for reflection from horizontal boundary (left) and sloping boundary (right), sloping angle α. Since the angle of propagation θ is unchanged, reflection of internal waves from slopes leads to focusing when the wave propagates according to the arrows (or defocusing when propagating in the opposite direction). The direction of phase propagation c_p is indicated by cross beam arrows. Figure from Hazewinkel [2010].

restoring force(s) acting on the system (rotation and/or gravity). Examples are trapezoidal domains containing stratified water, or rotating, fluid spherical shell domains. We start from this latter case, since, as we have seen in the previous sections, it is the most relevant one for the study of oceanic internal waves.

Studying the role of internal waves in the equatorial regions of a thin spherical shell, Bretherton [1964] used a hybrid ray-tracing-analytical approach and was in fact the first to propose a trapping mechanism that could lead to inviscid solutions becoming singular at specific locations in the fluid domain. The first comprehensive mathematical treatment in this context was given by Stewartson and Rickard [1969]. They reported about so-called "pathological oscillations" of a homogeneous rotating fluid contained in a rotating spherical shell, which where found in the second order of an asymptotic expansion using the thickness of this shell as a small parameter. Interestingly, for a given frequency ω, the second order fields in this expansion develop a singularity originally located at

$$\phi = \pm \arcsin\left(\frac{\omega}{2\Omega}\right), \tag{2.100}$$

which exactly correspond to the associated critical latitudes as in equation (2.99), given that the fluid considered is homogeneous.

If in the mathematical description wave attractors appear as localised singularities (akin to the one presented in Stewartson and Rickard [1969] for the shell case), in the real world, friction regularises these divergences. In the laboratory, attractors can however easily be observed, for example, in the density anomaly field, as has been done for the first time by Maas *et al.* [1997], and as is still being studied in the fluid dynamics laboratory of the Physical Oceanog-
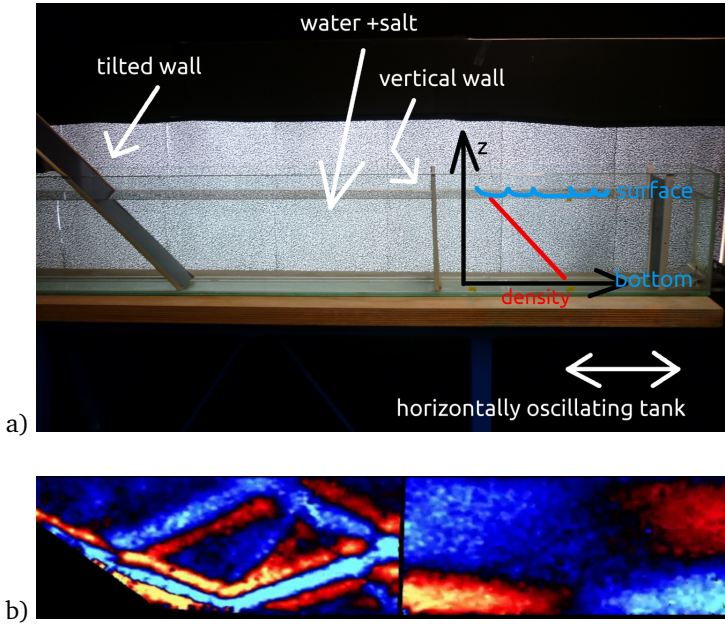
Figure 2.10: a) A scheme of the fluid dynamics laboratory settings at the Physical Oceanography Department of the Royal NIOZ. For reference, the visible part of the tank is about 1.5 m long. b) The tank is sloshed horizontally by an excursion of about 10 cm, and the vertical gradient of the density anomaly field (blue negative and red positive) is displayed. On the left, the response of the trapezoidal domain shows the presence of a diamond shape attractor, on the right, the response of the rectangular domain shows the presence of a regular mode. These two neighbouring basins are excited at the same time, and thus at the same frequency.

raphy Department at the Royal NIOZ (see figure 2.10). There a linear stratification in the tank is obtained by filling the domain with water whose salinity increases linearly with depth. Vertical or oblique walls can then be inserted to divide the tank in differently shaped basins. It is possible to slosh the tank horizontally at a controlled frequency, as it sits on a wheeled platform. The *synthetic schlieren* technique [Sutherland *et al.*, 1999; Dalziel *et al.*, 2000] is used to visualise the motion taking place in the interior of the fluid domain. This method is based on the fact that the refractive index of water varies with density. Images of the tank are processed with the DigiFlow software [Dalziel *et al.*, 2000], able to account for these variations in refractive index and providing the corresponding gradient of the density anomaly field, as the one depicted in figure 2.10b. In a trapezoidal basin, despite the presence of viscosity, the possible influence of non-linear effects and a free surface, attractors manifest themselves as stable scars in the density field (left hand side of figure 2.10b), in contrast with the regular, mode-like response observable in the rectangular basin (right hand side of figure 2.10b). Figure 2.10 is then an emblematic visual image of the domain-dependent response typical of internal waves. Given the symmetric role of N and 2Ω in the Poincaré equation, this example of attractor in stratified fluid is also representative of attractors occurring in homogeneous, rotating fluids. In case of a two-dimensional combination of rotation and stratification (in which gravity, rotation axis and wave vector all lie in one plane), internal wave rays would still undergo the same reflection laws and interactions with the containing walls, leading to analogous attracting features, the only difference being their more complicated trajectories, due to the presence of two restoring forces (and consequently two relevant spatial direction θ and α as in equation (2.92)), and possible internal scattering (see experiments with non uniform N in Hazewinkel *et al.* [2010]). It is in this context that it has been noted that the equatorial region of a rotating stratified shell, such as the ocean, provides a natural confinement for the internal wave rays and, at the same time, leads to trapping of inertia-gravity waves onto "equatorial wave attractors", see figure 2.11 [Dintrans *et al.*, 1999; Maas and Harlander, 2007; Harlander and Maas, 2007]. It is clear that the occurrence of equatorial attractors in our ocean would bear enormous consequences on the low-latitudinal dynamics and energy budget [Maas and Harlander, 2007]: investigating their existence has thus been one of the subjects of this thesis.

Are the mechanisms leading to two-dimensional attractors robust enough to be at the basis of more complex, three-dimensional attractors, as the ones that could occur in more realistic domains? We shall address this question in details in chapter 3 and 4. Can these attractors be observed in the real ocean and affect the local dynamics (localised enhanced mixing patches, anomalous vertical transport, or wave-wave interaction)? In principle, internal wave beams

a) $\omega = 0.777,\ \tau = -9.788 \times 10^{-3},\ N = 2.5$ b)
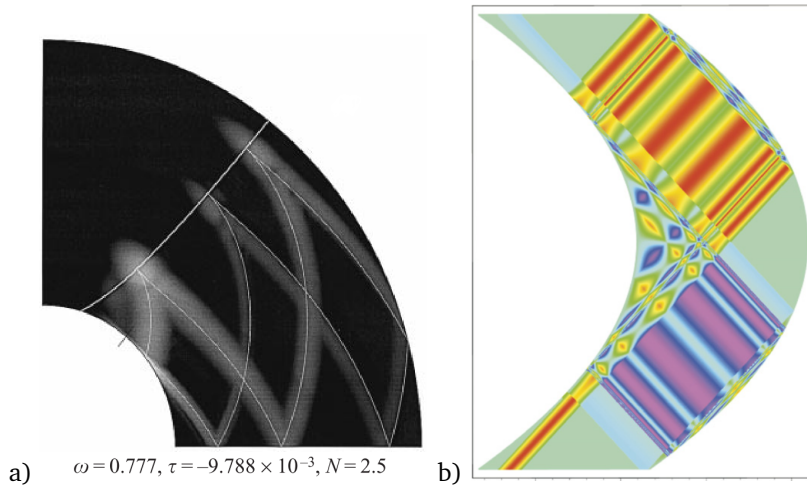
Figure 2.11: a) Numerical simulation of a rotating, radially stratified spherical shell containing a turning surface, from Dintrans *et al.* [1999]. b) Two-dimensional streamfunction of an equatorial attractor, from Harlander and Maas [2007]. Both images represent a portion of a meridional plane within the spherical shell domain.

are observed in the ocean [New and Pingree, 1992; Lam *et al.*, 2004; Gerkema *et al.*, 2004; da Silva *et al.*, 2012], however, to date no internal wave attractor has been reported using observations. However, due to the scarce and scattered nature of oceanographic observations, it might also well be that we have not looked for them carefully enough.

2.4.4   *The Stern equation without the assumption of axisymmetry*

As we now understand, the question whether internal waves play a pronounced role in the equatorial region is hard to address using analytical means only. Hence, further simplifications in the set of equations (2.1) are usually adopted, which can be achieved, for example, by means of scale analysis. Assuming time-harmonic motion $\propto e^{-i\omega t}$, and retaining non-traditional terms, classical derivations lead to Stern's equation, in case of an axisymmetric, linear, homogeneous, equatorial β-plane model [Stern, 1963], or to the extended Stern's equation, in case uniform stratification is included [Maas and Harlander, 2007]. In both cases, as we have anticipated in the previous section, the resulting boundary value problem is not separable, however, it is possible to compute exact solutions for the wave attractor regimes, and these solutions show that attractors correspond to singularities in the velocity field.

In this section, a generalisation of Stern's equation is performed: it will be shown how usage of anisotropic scales in (2.1), in fact, directly leads to the equation for axisymmetric motion ($\partial_x \equiv 0$) proposed by Stern [1963]. This strengthens the validity of the results in Maas and Harlander [2007] to a whole new class of waves that can account for zonal inhomogeneities, and go towards a more realistic representation of equatorial waves.

Commonly horizontally isotropic scales are used in (2.6) when rendering the governing equations dimensionless and proceeding then with the analysis for the relevant terms. In the following, two *different* scales are used for the meridional and the zonal directions. This is motivated by observations: equatorial motions and dynamics develop in a latitudinal equatorial belt, or "strip", rather than in an equatorial "square" [Stramma and Schott, 1999, see for example]. Besides, from theoretical arguments, the occurrence of the critical latitudes and corresponding turning surfaces (see section 2.4.1) in a stratified fluid also defines a meridional boundary for the dynamics confining it into a belt-shaped area. Therefore two different horizontal length scales are used, but only one horizontal velocity scale is considered, which is in good agreement with typical in situ observations at the Equator in literature [Send *et al.*, 2002; Gouriou *et al.*, 1999; Bunge *et al.*, 2007, see for example], as well as with the ones presented in this thesis in chapter 5. This also implies these terms weigh differently in the continuity equation preferring the term v_y over u_x. We thus employ the scaling

$$[x, y, z, \omega, u, v, w, p, b, N] = (L, B, H, 2\Omega H/B, U, U, UH/B, 2\Omega HU, 2\Omega U, 2\Omega).$$

Note that here the angular frequency 2Ω is used in the scaling of ω, rather than N (constant), as in section 2.1.2. Furthermore, two assumptions are made:

- the zonal length scale for our problem is $L = a$, the Earth radius,

- the meridional length scale B is chosen such that both the traditional and non-traditional Coriolis terms are of equal importance [Stern, 1963; Colin de Verdière and Schopp, 1994], thus $B = \sqrt{aH} \approx 160\ km$.

We can then define the small parameter $\varepsilon = B/L \sim H/B \sim 0.025$ and get the dimensionless equations:

$$-i\omega u - yv + w = -\varepsilon p_x \tag{2.101a}$$

$$-i\omega v + yu = -p_y \tag{2.101b}$$

$$-i\omega\left(\varepsilon^2 - \frac{N^2}{\omega^2}\right)w - u = -p_z \tag{2.101c}$$

$$\varepsilon u_x + v_y + w_z = 0. \tag{2.101d}$$

where the buoyancy equation has already been incorporated in equation (2.101c). An asymptotic expansion in power series of ε can thus be performed

$$\vec{u} = \vec{u}^0 + \varepsilon \vec{u}^1 + \cdots \qquad \text{and} \qquad p = p^0 + \varepsilon p^1 + \cdots . \qquad (2.102)$$

The lowest order balance is then given by

$$-i\omega u^0 - yv^0 + w^0 = 0 \qquad (2.103a)$$

$$-i\omega v^0 + yu^0 = -p_y^0 \qquad (2.103b)$$

$$i\frac{N^2}{\omega}w^0 - u^0 = -p_z^0 \qquad (2.103c)$$

$$v_y^0 + w_z^0 = 0. \qquad (2.103d)$$

We notice that the continuity equation (2.103d) allows for a stream function, such that $v^0 = -\psi_z$ and $w^0 = \psi_y$. The zonal velocity is then obtained from eq. (2.103a) as

$$u^0 = -\frac{i}{\omega}(y\psi_z + \psi_y), \qquad (2.104)$$

and from the remaining equations we get

$$(1 + N^2)\psi_{yy} + 2y\psi_{y,z} - (\omega^2 - y^2)\psi_{zz} + \psi_z = 0. \qquad (2.105)$$

This corresponds to the Stern equation, extended by the term $N^2\psi_{yy}$. It is thus a hybrid version between the classical Stern equation and the stratified Stern equation presented in Maas and Harlander [2007]. Its characteristics can therefore be considered representative of energy paths using the same arguments [Harlander and Maas, 2006].

It follows that using anisotropic scales broadens the validity of the established results obtained when a thin spherical shell is considered [Maas and Harlander, 2007], namely the occurrence of equatorial attractors confined between the ocean surface, bottom and turning surfaces. Remarkably, the scales used in this section match very well with the observed situation in an equatorial basin, where, for example, the zonal extent of equatorial deep jets has been estimated to reach at last 25°- 27°, meaning about 3000 km [Gouriou *et al.*, 2001; Schmid *et al.*, 2005]. The conventional isotropic scaling implies a derivation valid only on a smaller, isotropic area characterised by zonal and meridional length scales of $L \sim 160 \ km$. Finally, thanks to the anisotropic scaling, the assumption of zonal axisymmetry is not any more necessary to get to a treatable equation. It follows that the stream function ψ (and the pressure) can in principle still be a function of x, allowing for the insertion of zonal inhomogeneities (i.e. continents). In particular, a zonal boundary condition will enter the first order balance if and only if $\psi = \psi(x)$. In this way, the range of validity of results presented in Maas and Harlander [2007] is extended towards a more realistic setting for equatorial wave dynamics.

The current chapter constitutes an attempt of presenting an analytical description of equatorial wave dynamics. In particular, the possibility of including in the equation of motions the full Coriolis force has been explored. Surprisingly, this non-traditional approach to equatorial dynamics is rarely pursued in literature and in the most common oceanographic text books, and we believe we have here shown why. In this last section, we first summarise the main results achieved (section 2.5.1). Then, a brief discussion on possible implications of the findings will be presented in section 2.5.2. Approaches and methodologies used in the following chapters of this thesis also reflect the difficulties and the issues evidenced in this chapter, as they will try to address similar questions using different tools and perspectives.

2.5.1 *Summary*

In section 2.1 of this chapter, the relevant equations of motion for geophysical fluids have been presented, with special emphasis on the scale analysis, approximations and assumptions leading to the traditional and to the non-traditional equatorial β-plane.

SURFACE AND INTERFACE WAVES   The traditional equations have been solved in section 2.2 following the classical, shallow water approach described by Matsuno [1966] and broadly adopted in textbooks. This approach focuses ab initio on equatorially trapped waves, as an asymptotic boundary condition of vanishing velocity for large values of latitude is used. The first type of surface boundary condition adopted (section 2.2.1), in line with the shallow water approach, is the free surface, with the associated kinematic and dynamic boundary conditions.

The reduced gravity model (section 2.2.2) uses the modes found by Matsuno to describe waves travelling along an interface (thermocline), instead of at the sea surface. The resulting phase velocity better matches with observations, and surface elevation is determined by the thermocline elevation via equation (2.16). In the mathematical sense, Kelvin, Rossby, inertia-gravity, and mixed Rossby-gravity waves constitute a complete set of solutions in this traditional context. So far, textbook materials was presented, to put into context the next steps.

Non traditional terms have then been added to the system. The question whether equatorial Kelvin waves can still exist if the full Coriolis force is taken into account has been addressed in section 2.3.1. Solutions have been con-

structed by means of stream function-based methods, but they turned out to be incompatible with rigid boundaries like the sea bottom.

Solutions for non-traditional waves with non-zero meridional velocity component have been presented in section 2.3.2. Due to their vertical structure, they cannot be transformed into Matsuno's solutions by taking some suitable limit. In fact, in contrast to previous atmospheric works [Kasahara, 2003; Raymond, 2001; Fruman, 2009; Roundy and Janiga, 2012], the oceanic case is considered here, and the ansatz for solutions to be proportional to e^{ilz} is not taken a priori. Original, general free solutions are presented in terms of Hermite polynomials with imaginary argument. In the axisymmetric case, a similarity between their spatial patterns through all orders and the lowest order Rossby waves of Matsuno [1966] has been pointed out (see figure 2.4), which would challenge an observer in making a distinction between traditional and non-traditional waves, if these latter ones would actually occur in the real ocean. It has been pointed out in detail how, for all kind of waves, including the non-traditional Coriolis terms to the equations of motion, the vertical and meridional components of the equations of motion are no longer separable. Consequently, it is not possible to apply asymptotic boundary conditions in the meridional direction (equatorial trapping) while demanding a rigid bottom and/or a material surface on top.

INTERNAL WAVES   In section 2.4.1, general properties of internal inertia-gravity waves have been presented. A qualitative introduction to the challenging problem of internal waves in confined domains is given in section 2.4.2, with special attention to the spherical shell case. The spherical shell geometry is in fact a paradigmatic example of a geometry that is of relevance to all geophysical (and astrophysical) fluids. Besides, it also provides the proper geometrical setting to introduce the concept of *internal wave attractor* (section 2.4.3), that will be of use in the following chapters of this thesis. This is also done with an *in house* example from the NIOZ laboratory, which shows that attractors are easily observed in the laboratory in all "symmetry breaking" geometries, with dramatic consequences for the wave field in the whole domain. The possible occurrence of these features in the real (equatorial) ocean and their possible relevance for equatorial dynamics originally motivated this very thesis. As a new, analytical results for the internal wave case, in section 2.4.4 an equation describing internal wave motion in a confined domain has been derived using fully anisotropic length scales but two equal velocity scales. Remarkably, the resulting equation (2.105) can be related to Stern's equation [Stern, 1963] or to the stratified Stern's equation [Maas and Harlander, 2007], but with the new scaling adopted, no zonal axisymmetry is required. Though this may appear as a minor change, the validity of results in Maas and Harlander [2007] has been extended to more realistic settings, with length and velocity scales matching the observed situation at the equator and accounting for zonal inho-

mogeneities (meridional continents?). The relevance of this result will certainly be appreciated under the light of the picture emerging from chapter 3.

2.5.2 *Conclusions and implications*

It is remarkable that a well-established, classic textbook theory as the one presented in Matsuno [1966] on equatorial waves cannot be generalised to include the full Coriolis force, but rather very quickly starts showing its limitations and breaks down. The reason lies in the coupling between vertical and meridional coordinates caused by the non-traditional terms, whose inclusion, however, appears to be natural and well motivated when interested in purely equatorial wave dynamics. Moreover, the reduced gravity models also require the presence of an infinitely deep, motionless layer underneath the thermocline (few hundreds meters deep), that is just not observed (measured currents are up to 10 cm/s down to 2500 m, see for example Gouriou *et al.* [1999]; Dengler and Quadfasel [2002]; Send *et al.* [2002]). A different application of classical theory to the ocean is used, for example, by Hua *et al.* [2008]. They assume a constant stratification and separate the vertical dependence by means of a structure function. This allows for vertically variable motion in the entire water column, but the thermocline is lost in return. Finally, classical theories appear a weak tool to explain equatorial trapping of waves because the trapping itself (in the form of vanishing of the velocity for asymptotically high latitudes) constitutes one of their initial assumptions. In this thesis we are particularly interested in the possible wave-mean flow interaction phenomena that could in principle trigger, maintain, and/or dissipate the observed equatorial zonal jets. In order to do so, previous approaches, like the one presented in Hua *et al.* [2008] and in Muench and Kunze [1999, 2000], considered baroclinic instability of traditional equatorial Rossby and Kelvin waves, whose robustness, as we have seen in this chapter, appears to be very limited when put in a more realistic, non-traditional setting. Besides, deep dynamics seems to be of relevance to the equatorial jets: no clear relation with atmospheric forcing appears in fact in the observations, while, conversely, a possible oceanic forcing to atmospheric variability has been suggested [Brandt *et al.*, 2011].

With this new understanding, a special interest in *equatorial*, *non-traditional internal* wave dynamics has arisen, which motivates section 2.4. Most interestingly, phenomena such as the equatorial wave attractors may thus play a key part in focusing the oceanic wave action towards the low-latitudes (after Maas and Harlander [2007]), collecting energy from off-equatorial forcing events, such as storms and other atmospheric inputs, as well from internal forcing mechanisms, such as baroclinic tides, whereas the spatial patterns of the attractor would be controlled by the pressure distribution at the surface (which, how-

ever, does not constitute a forcing), and provide then the momentum needed at the low latitudes to trigger the observed, strong and coherent zonal flows.

We have seen, however, that also the analytical study of equatorial internal waves presents profound issues. The analytical difficulties listed in section 2.4.2 and 2.4.3 motivates the use of the ray tracing in the studies presented in chapters 3 and 4.

As we have seen in this chapter, when internal waves are considered in a spherical shell container, critical latitudes seem to play a prominent role in the determination of the wave field. This issue was originally brought to light in Stewartson and Rickard [1969], namely whether these singularities and discontinuities indicate an actual physical phenomenon or whether they are just a consequence of the choice of coordinates and/or the approximations:

> it is possible that the pathology we have just been describing is a creature of the particular limiting process adopted [Stewartson and Rickard, 1969].

However, singularities arise not only when Stern's solutions are inspected with a dedicated numerical model [Maas and Harlander, 2007; Schmidt, 2013], but also when ray tracing algorithms are applied to such geometries. All this suggests that critical latitudes do play a special role in the internal wave field, despite the choice of coordinates or of methodology.

Summarising, it seems that the three-dimensional character introduced in the system, either by considering non-traditional terms in the case of surface waves, or by considering internal waves in enclosed domains, is destroying the picture of equatorial wave dynamics as presented in all textbooks. The power of classical solutions, in fact, is *weakened* by the addition of simple realistic ingredient(s). This could have enormous consequences, for example, for our interpretation of global, low-latitude phenomena such as ENSO, and motivates the further quest for a robust framework of interpretation of equatorial wave dynamics.

3

MERIDIONAL TRAPPING AND ZONAL PROPAGATION OF
INERTIAL WAVES IN A ROTATING FLUID SHELL

Internal waves are ubiquitously present and of great importance in astrophysical and geophysical fluids as present in stars or planetary atmospheres and oceans, where they are considered responsible for a substantial part of the dynamics and mixing in the interior of the supporting medium [Wunsch and Ferrari, 2004; Ogilvie and Lin, 2004]. They propagate in all kinds of stratified fluids, and are generally referred to as *internal* (*gravity*) waves when the stratification in the fluid is built by means of vertical density changes, and as *inertial* waves when the supporting stratification is in angular momentum (homogeneous, rotating fluid). In this paper, we will use the generic term *internal* waves to refer to both situations, or to a combination of the two, stressing that we deal with a propagating perturbation whose maximum amplitude occurs in the interior of the fluid domains, instead of at the boundary, as for surface waves. Improving our theoretical understanding of internal wave behaviour in stratified fluids naturally confined to enclosed domains bears, as we may expect, important consequences for our general understanding of ocean or atmosphere dynamics.

Despite their broad interest and fundamental character, the nature of internal waves in confined domains is still largely unknown due to a variety of difficulties that undermine the study of these oscillations. For example, mathematical difficulties arise because of the combination of the hyperbolic character of internal waves (or of the mixed elliptic-hyperbolic nature in the case of a stratified and rotating fluid) and the confinement of motion to an enclosed domain. This problem, in particular in a spherical shell, has been already presented as a paradigmatic mathematically ill-posed Poincaré problem [Rieutord *et al.*, 2000], and it is limiting our capabilities of an analytical representation and comprehension of the mechanisms involved.

Analytical solutions for internal wave problems in enclosed domains are mostly known only for exceptionally symmetric geometries (such as the sphere, see Bryan [1889]), in which they lead to regular solutions. For this reason, ray theory [Whitham, 1974; Broutman *et al.*, 2004] has been developed to study propagation of internal waves in arbitrarily shaped enclosed geometries. Ray theory is based on the simple observation that in uniformly stratified, or uniformly rotating fluids, internal waves propagate along beams whose direction is set by the ratio of the perturbing frequency and a frequency representing the environmental conditions (rotation and/or density stratification) (see section 3.2 for derivation). Wave energy travels along these beams parallel to group velocity [Harlander and Maas, 2006, 2007], which can therefore provide a (partial) view on the energy distribution in the domain and on the regularity of the associated wave field in cases where no analytical solutions are available. It is worth noting that each different inclination of the rays represents

one frequency, and thus only linear phenomena, characterised by a single frequency, can be described by means of ray tracing studies. Because of its geophysical and astrophysical relevance, a two-dimensional meridional cut of the spherical shell geometry (an annulus) has been largely explored by means of this technique [Hughes, 1964; Bretherton, 1964; Dintrans *et al.*, 1999; Maas and Harlander, 2007], and the pathological character of its inviscid solutions has been established [Stewartson and Rickard, 1969; Stewartson, 1971, 1972]. Singular, discontinuous solutions have indeed to be expected in hyperbolic systems. These interesting features of internal waves in enclosed domains, the so called internal wave attractors [Maas and Lam, 1995], are easily captured by ray tracing analysis: ray trajectories in arbitrarily shaped containers are generally not closed but, by repeated reflections from the boundaries, converge to a limit cycle (the attractor), in which all the wave energy is concentrated [Maas, 2005]. Remarkably, in a two-dimensional framework, ray tracing leads to exact, yet geometrically constructed solutions of the inviscid, uniformly stratified fluid equations in arbitrarily shaped fluid domains. Only one exceptional case is known (that of a square-shaped attractor in a trapezoidal domain) where the singular solution is also expressed in terms of a Fourier series [Maas, 2009]. The energy scars left in the domain by attractors are observed in quasi two-dimensional laboratory demonstrations both in density stratified fluids as well as in homogeneous rotating fluids [Maas *et al.*, 1997; Maas, 2001; Manders and Maas, 2003; Hazewinkel *et al.*, 2008], and agree with two-dimensional numerical simulations [Hazewinkel *et al.*, 2011a].

High resolution, weakly viscous numerical experiments performed in astrophysical contexts [Dintrans *et al.*, 1999; Rieutord *et al.*, 2001; Ogilvie and Lin, 2004; Ogilvie, 2005; Calkins *et al.*, 2010] have brought some new insight on the occurrence of these attractors, in particular in the meridional cut of spherical shell geometries, showing a remarkable agreement with trajectories evaluated using a simple linear, geometrical ray tracing of the characteristics.

Interestingly, in literature, investigation of the spherical shell geometries by means of ray tracing has always been limited to rays constrained to meridional planes only (any plane containing the rotation axis, gravity and the geometrical centre of the domain). This is motivated by the symmetry of the problem in the azimuthal coordinate [Bryan, 1889; Friedlander and Siegmann, 1982; Friedlander, 1982; Dintrans *et al.*, 1999], present both in the domain's geometrical shape, as well as in the forcing mechanisms usually studied (tidal forcing, libration of the inner sphere). If in an astrophysical framework this approach seems natural and representative of the most common perturbations in the fluid, this appears less obvious when we regard ocean phenomena. The presence of meridional boundaries (continents) limits the assumption of axisymmetry of the domain; moreover, monochromatic (e. g. tidal), point-like sources (local storms, local conversion of barotropic into baroclinic tide on strong topographic fea-

tures) play a role in the dynamics. Thus, in principle, and especially if we are interested in the near field response to a forcing, there is no compelling reason why a single perturbation, locally and anisotropically forced, should propagate in a two-dimensional meridional plane only, and, in this way, lose the possibility to show the occurrence of any zonal inhomogeneities.

For this reason the aim of the present study is to extend the use of the ray tracing technique for internal wave characteristics to fully three-dimensional spherical shell domains, allowing also for zonal propagation. In this work we restrict ourselves to the study of pure *inertial* waves, while the role of density stratification, and the combination of the two mechanisms, will be briefly discussed at the end of the paper. Results for a homogeneous rotating shell are modified locally when radial stratification is present, where curved rays replace the straight characteristics considered here and where turning surfaces may limit the part of the fluid domain accessible to waves [Friedlander and Siegmann, 1982; Friedlander, 1982; Dintrans *et al.*, 1999]; on the other hand, the pure inertial problem summarises many of the difficulties and the features of the gravito-inertial problem, and findings in this partial case are supposed to have general validity.

The paper is built as follows: the three-dimensional geometrical ray tracing technique and its application to the case of the shell are described in section 3.2. In section 3.3 results of the application of the methodology are presented; the main outcomes consist in (1) the general occurrence of meridional attracting planes, where ray trajectories (energy paths) eventually converge, even when initially launched with a zonal component, (2) the existence of exceptional trajectories, representing waves that are not subject to meridional trapping that reflect endlessly around the domain. Clearly the dynamics of these waves is not captured by the classical, purely meridional approach and unveils a new class of solutions. Consequences of attracting planes and edge waves are then qualitatively discussed in section 3.4, with special attention to the possible oceanographic implications.

3.2 INERTIAL WAVE THREE-DIMENSIONAL RAY TRACING

3.2.1 *Governing equations*

In a Cartesian (x, y, z) reference frame (see figure 3.1a) the pressure field, p, of linear inertial waves in a homogeneous, inviscid, uniformly-rotating, Boussinesq fluid is conveniently described by the Poincaré equation [Cartan, 1922]

$$p_{xx} + p_{yy} - \frac{1 - \omega^2}{\omega^2} p_{zz} = 0. \tag{3.1}$$

where the fluid is rotating at rate Ω oriented parallel to the z-direction and subscripts denote partial derivatives. All fields are assumed to be proportional to $e^{i\omega t}$ and the Coriolis parameter $f = 2\Omega$ is taken as the characteristic time scale. Frequencies ω are thus regarded as normalised with respect to this parameter. Propagating inertial waves exist in the frequency range $0 < \omega < 1$, therefore the Poincaré equation is hyperbolic throughout the whole domain.

The momentum equations relate the velocity field to spatial gradients of the pressure:

$$
\begin{aligned}
u &= \frac{1}{\rho_0} \frac{1}{\omega^2 - 1} (i\omega p_x + p_y) \\
v &= \frac{1}{\rho_0} \frac{1}{\omega^2 - 1} (-p_x + i\omega p_y) \\
w &= \frac{1}{\rho_0} \frac{i}{\omega} p_z
\end{aligned}
\tag{3.2}
$$

where ρ_0 is the density of the fluid. For an inviscid fluid its boundaries are impermeable, requiring vanishing of the normal velocity component at the outer sphere ($x^2 + y^2 + z^2 = 1$) and at the inner sphere ($x^2 + y^2 + z^2 = \eta^2$). Here $\eta = r_{in}/r_{out}$, $0 < \eta < 1$, represent the ratio of the radii of the inner and outer shell, constituting the surface and the bottom of our idealised ocean respectively. Spatial variables are rescaled by using r_{out} as length scale. The pressure field therefore has to obey oblique derivative boundary conditions, which in general prohibits finding exact analytical solutions. Some indications of the behaviour of internal waves in such a domain can be obtained, as anticipated, by means of three-dimensional ray tracing in the fluid gap.

3.2.2 *Geometrical mapping*

In this section we will first motivate the use of three-dimensional ray tracing, together with the assumptions underlying the application of this methodology to the problem. The horizontal scattering of a single inertial wave ray is then presented at the end of the section as a map relating a reflected to an incident ray. The interested readers can refer to appendix A for the map construction and the computational details.

After horizontally reorienting the x-axis along the propagating direction of a single ray, the system can then be described in two-dimensions only, one vertical dimension and one horizontal dimension. Substituting a wave like solution $p = e^{i(kx+mz)}$ in the appropriately rotated version of equation (3.1), the dispersion relation follows:

$$
\omega^2 = \frac{m^2}{k^2 + m^2}
\tag{3.3}
$$

that can be rewritten as

$$\omega^2 = \sin^2 \theta. \tag{3.4}$$

where the wave vector is now expressed in polar coordinates as $\vec{k} = \kappa(\cos\theta, \sin\theta)$, with θ the angle between the wave vector and the horizontal. From equation (3.3) and (3.4) it follows that for internal waves, group velocity ($\vec{c}_g = \nabla_{\vec{k}}\omega$) is perpendicular to phase velocity ($\vec{c} = \frac{\omega}{\kappa^2}\vec{k}$), and forms an angle θ with the vertical. Moreover the factor preceding the second vertical derivative term in equation (3.1) is directly related to the ray's (group velocity's) inclination since:

$$\frac{1-\omega^2}{\omega^2} = \cot^2 \theta. \tag{3.5}$$

This explains why, differently from surface waves, internal wave group velocity in stably stratified fluids is directed along beams, the internal wave rays, whose inclination with respect to the restoring force is uniquely set by the frequency of the perturbation, and the environmental condition (density stratification and/or rotation) [Görtler, 1943; Greenspan, 1968], and this direction is conserved upon reflection at the domain's boundaries. Here, in analogy with the two-dimensional counterpart, we assume that in a three-dimensional domain, a uniquely connected set of characteristics (rays) exists. Therefore the perturbation will travel now along characteristic *cones* (given by the 2π rotation of the classical St. Andrew's cross), whose aperture 2θ, centred at the rotation axis, is uniquely set by the perturbation frequency and the stratification properties.

Tracing the geometrical trajectories of these rays in order to infer properties of the wave field provides, of course, just a limited perspective on the phenomenon. In parallel to the approach in geometrical optics for linear problems, in order to successfully apply ray tracing in the three-dimensional case, the propagating perturbation is idealised as a short, plane wave, reflecting on the curved boundary as if from the local tangent plane (see also Baines [1971]). It is clear that plane waves imply an infinite lateral extension, and its neglect of the (locally) curved character of the spherical domain's boundary constitutes a severe approximation. However, it is only under this strong (as well as popular, e.g. Whitham [1974]) assumption that the geometrical effects can be isolated and studied from the whole complicated excited wave field. It is remarkable though that the presence of an attractor strengthens the validity of the short wave hypothesis, consistently reducing the width of a wave beam (wave length) while it gets focused onto the limit cycle.

Now consider we want to trace the behaviour of a perturbation at definite frequency ω. In literature, the behaviour of a ray in the spherical shell domain has been traditionally inferred by employing a rotational symmetry of its two-dimensional trajectory, which is therefore traced on a meridional cut of the
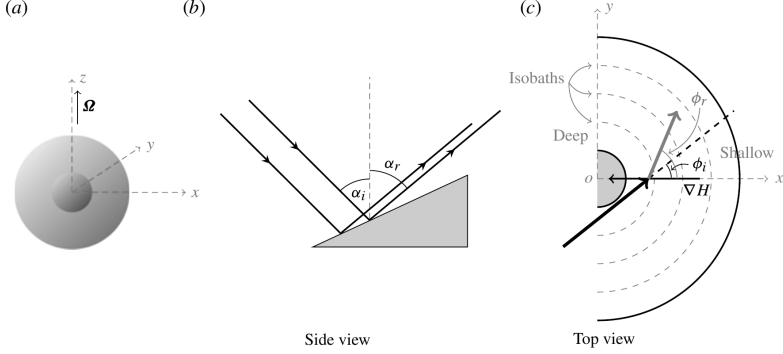
Figure 3.1: (a) Rotating fluid shell inserted in the Cartesian coordinate framework, (b) Side and (c) top view of a short internal wave packet that reflects subcritically from a sloping bottom. In (c) the rotation axis (coinciding with the z-axis) is pointing towards the reader. Modified after Maas [2005]. While incident and reflected rays lie on the same cone (whose angle θ with the vertical is fixed by the perturbing frequency), their angle α_i and α_r differ in a projection on the vertical plane perpendicular to the slope at the point of reflection. Reflecting waves refract instanteously changing the horizontal propagation direction from ϕ_i to ϕ_r.

shell domain solely. By contrast, in this work, a single ray will be followed in its fully three-dimensional trajectory, while it bounces around the domain. The perturbation is "launched" at one location on the boundary, at position $\vec{x}_0 = (x_0, 0, \sqrt{\eta^2 - x_0^2})$, on the inner sphere (bottom), or at $(x_0, 0, \sqrt{1 - x_0^2})$, on the outer sphere (surface). It is clear that we can choose $y_0 \equiv 0$ because of axial symmetry of basin and equations. We will then be able to trace one single ray at a time, and it will be uniquely defined by three parameters: ω, $\vec{x}_0$ and its initial horizontal direction ϕ_0, measured anticlockwise with respect to the x-axis, which distinguishes it from other rays belonging to the same excited internal wave cone.

Horizontal scattering of the ray from a reflecting boundary is assumed here to be as simple as possible, the adopted scheme being the same as in Phillips [1963] and in Hughes [1964], already successfully and repetitively used by Manders and Maas [2004]. Since the wave frequency does not change, also the beam's angle with respect to the vertical will not change upon reflections at the boundaries: this is equivalent to requiring that the incident and reflected waves obey the same dispersion relation, while the boundary condition of vanishing normal flow at the reflection point is also always satisfied. The mechanism of

horizontal scattering of the ray is sketched in figure 3.1, and explained in detail in appendix A.

While the wave vector component in the along-slope, tangential direction is unchanged, the wave vector component in the cross-slope direction changes due to a focusing or defocusing reflection. The new horizontal direction (ϕ_r) of the reflected ray is in fact completely determined by the local bottom slope $s = |\nabla H|$ and horizontal direction of the incoming wave, ϕ_i (which equals ϕ_0 plus the angle that the bottom gradient vector makes with the x-direction). Conservation and geometrical laws [Phillips, 1963; Eriksen, 1985; Gilbert and Garrett, 1989; Manders and Maas, 2004; Maas, 2005] yield the following relation between ϕ_i and ϕ_r, after the vertical has been correctly stretched to maintain $\tan \theta = 1$ (see appendix A for derivation):

$$\sin \phi_r = \frac{(s^2 - 1) \sin \phi_i}{2s \cos \phi_i + s^2 + 1}. \tag{3.6}$$

When the reflection takes place where the local bottom slope is smaller than the inclination of the ray ($s < 1$), the reflection is called subcritical, and it leads to a change in sign of the vertical component of the ray's group velocity. In the opposite scenario ($s > 1$), the reflection is called supercritical, and no change in sign is involved. Critical lines (latitudes) connect critical points at which the bottom slope equals the ray slope ($s = 1$), and they lead to an exceptional reflection, when non-linear effects are likely to come into play [Dauxois and Young, 1999; Thorpe, 1997].

The inertial wave ray path for a given frequency ω and initial launching position and direction ($\vec{x}_0, \phi_0$) can thus be followed as it bounces through the spherical gap applying the known reflection laws and computing subsequent reflection points, each characterised by $\omega, \vec{x}_n, \phi_n$. The behaviour of the ray path will provide us information about the features of the unknown solution of the corresponding Poincaré equation.

In two-dimensional frameworks, it appears that the existence or absence of eigenmodes in a system is related to the behaviour of these rays and their reflections from the boundaries of the domain: when each characteristic is closed, eigenmodes exist (although infinitely degenerate, [Münnich, 1996]). In more generic cases, when limit trajectories (attractors) arise, these are the signature of singular, discontinuous field solutions, as shown for the spherical shell [Harlander and Maas, 2007].

A universal, meaningful relation between rays, energy paths and characteristics in three dimensional domains is not completely established yet. The existence of a similar relation between wave rays and wave paths in three dimensional geometries is supported by recent numerical work [Drijfhout and Maas, 2007] and in laboratory experiments, performed in a non-centrally forced paraboloidal basin [Hazewinkel *et al.*, 2011b], but definitely deserves further investigation.
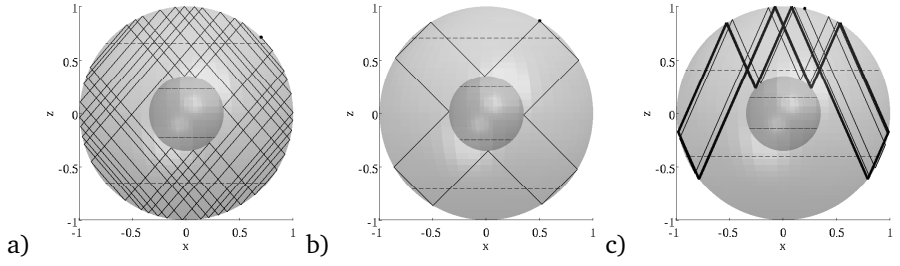
Figure 3.2: Examples of purely meridional trajectories: (a) ergodic-like orbit, obtained with parameter $\omega = \sqrt{\frac{3}{7}}$, $x_0 = 0.7$, (b) periodic orbit, $\omega = \sqrt{\frac{1}{2}}$, $x_0 = 0.5$ and (c) attractive orbit, $\omega = 0.4051$, $x_0 = 0.2$. For all cases $\eta = 0.35$. Horizontal lines correspond to critical latitudes. Black dot corresponds to the launching position x_0. In (c) the thick line indicates the wave attractor.

A need for three-dimensional ray tracing also emerges from the work by Rieutord and Valdettaro [2010], where the discrepancies between three-dimensional numerical simulations, analytical solutions, and the two-dimensional, meridional ray orbits, clearly show the limit of the latter approach.

3.3 RESULTS

3.3.1 *Summary of established results for meridional ray motion ($\phi_0 = 0, \pi$)*

It is known that in two-dimensional domains, such as a meridional section of a spherical shell (an annulus), ray trajectories show three possible kinds of behaviour [John, 1941; Maas and Lam, 1995; Dintrans *et al.*, 1999]: (1) a single (or denumerable set of) orbit(s) can be plane filling (ergodic, figure 3.2a), and represents an annihilating solution, (2) each orbit can be periodic (close onto itself after a number of reflections), representing regular solutions in the domain (figure 3.2b), or (3) each orbit can eventually be trapped on one (or a denumerable set of) limit cycle(s), attractor(s), representing singular solution(s) (figure 3.2c), which may include point attractors. In this annulus, periodic two-dimensional orbits are found when the critical latitude (λ_c), where boundary slope equals ray slope, is commensurable with π. For example, in the case depicted in figure 3.2b, $\omega = \sqrt{\frac{1}{2}}$ and $\lambda_c = \pi/4$ [Rieutord *et al.*, 2001].

Attractors are found in frequency windows in the inertial range $0 < \omega < 1$, as shown in Rieutord *et al.* [2001] and Maas and Harlander [2007]. In figure 3.3, a typical Poincaré plot for a meridional section of a spherical shell ($\eta = 0.35$)
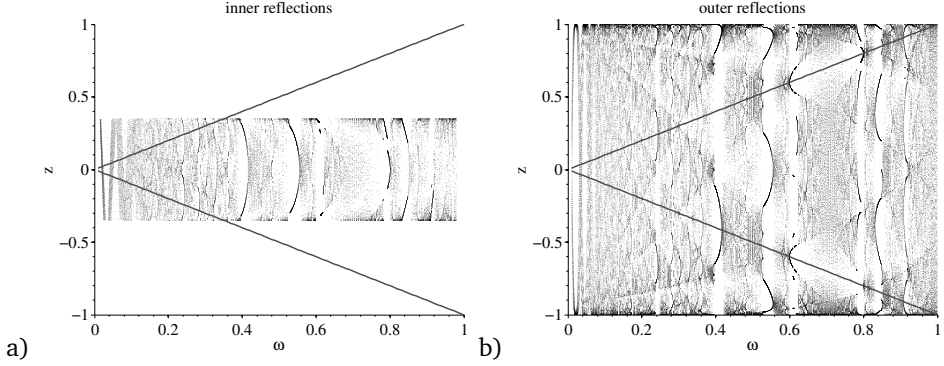
Figure 3.3: Poincaré plots for trajectories confined in a meridional section of a spherical shell ($\eta = 0.35$, $x_0 = 0.2$). On the horizontal axis, ω is running from 0.01 to 1 in steps of 0.0001. On the vertical axis, the z coordinate of reflection points on the inner sphere (a) and on the outer sphere (b) of the last 20 reflections (out of 200). Grey lines represent the locations of the critical latitudes.

is presented, where frequency is on the horizontal axis, and the vertical axis shows z coordinates of the last 20 (out of 200) reflections on the inner (a) and on the outer sphere (b). As noticed by Maas and Lam [1995], critical latitudes seem to act as repellors for ray trajectories, especially at the outer sphere (figure 3.3b). These Poincaré plots show a much more complicated pattern than similar plots evaluated for the paraboloidal basin (see for example figure 11 from Maas [2005]). The appearance of more elaborate combinations of super and sub critical reflections is due to the presence of both convex and concave regions of the boundary, respectively the outer and the inner sphere [Dintrans *et al.*, 1999].

3.3.2 *Three dimensional ray behaviour in shell geometries ($\phi_0 \neq 0, \pi$)*

In the following part of this section, differently from the approach that has been presented so far, ray motion will no longer be constrained to a meridional plane, and results will be presented for ray tracing of inertial waves in a fully three dimensional spherical shell geometry.

Doing so, we allow for azimuthal inhomogeneities to develop: waves, initially forced with a zonal propagation component, are subject to focusing and defocusing reflections from the boundaries and possibly refract towards a meridional plane, eventually becoming trapped in that plane. This mechanism, hy-
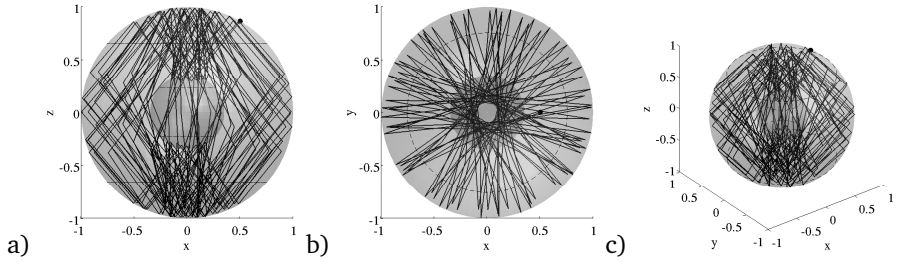
Figure 3.4: Example of an ergodic orbit in a three dimensional shell ($\eta = 0.35$). For $\omega = \sqrt{\frac{3}{7}}$ the ray is launched at the outer sphere at $x_0 = 0.15$, $\phi_0 = -7\pi/8$, and followed for 200 reflections. (a) meridional view (x, z plane), (b) top view (x, y-plane), (c) full 3D view (x, y, z perspective). Black circles correspond to critical latitudes. Black dot corresponds to the launching position x_0.
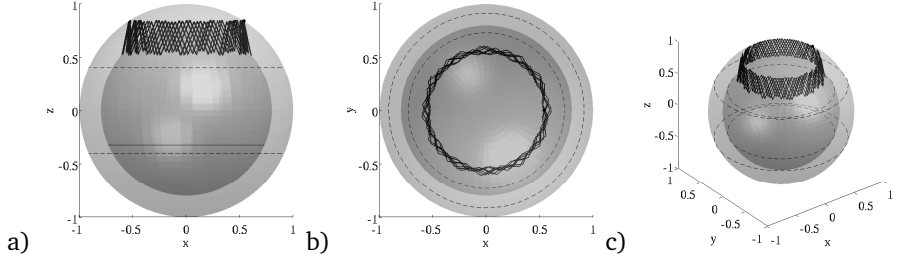
Figure 3.5: As figure 3.4 for a quasi-periodic, non converging trajectory. Here $\eta = 0.8$, $\omega = 0.4051$, $x_0 = 0.54$, $\phi_0 = 1.342$, 200 reflections. This trajectory corresponds to the star in figure 3.9a.
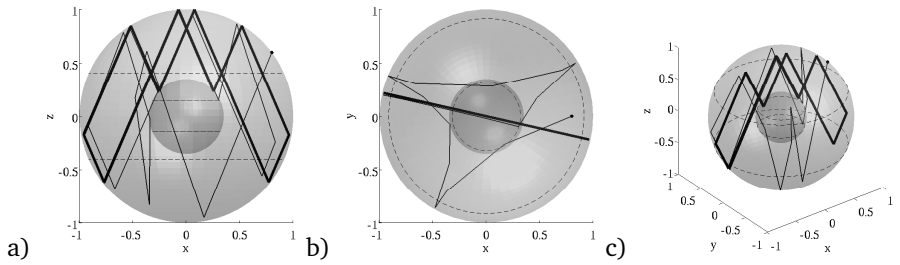
Figure 3.6: As figure 3.4, but for a meridional attractor in the three dimensional shell ($\eta = 0.35$). Here the ray at $\omega = 0.4051$ is launched at $x_0 = 0.8$, $\phi_0 = -7\pi/8$. Thick line marks the closed cycle of the final wave attractor. This trajectory also constitutes an example of a polar three-dimensional attractor (see text).

pothesised by Maas [2001] and Maas and Harlander [2007], is here observed for the first time. Three dimensional trajectories can be interpreted as follows. If a trajectory (fully determined by the domain geometry, launching position $\vec{x}_0$, launching direction ϕ_0 and frequency ω) is launched in a meridional plane (at $\vec{x}_0 = 0, \forall \phi_0$, or alternatively at $\phi_0 = 0, \pi, \forall \vec{x}_0$), it will never leave the plane, even if a full three-dimensional algorithm is used. This class of solutions corresponds to the known class of purely meridional trajectories. On the other hand, if a trajectory is launched outside a meridional plane (all other combinations of $\vec{x}_0$ and ϕ_0), either it will never cross the basin on a meridional plane (new class of zonally propagating solutions), or it will asymptotically approach one particular plane (occurrence of a meridional attractor), rendering the trajectory indistinguishable from a purely meridional trajectory after an appropriate number of reflections.

Results from three dimensional analysis are hard to be effectively presented on a two dimensional sheet of paper. In this work three perspectives for each example of trajectory will be presented: a meridional view (usually the x, z-plane), the top view (x, y-plane) and a full 3D perspective view (x, y, z). Note that the apparent change in vertical orientation of a wave ray is a visual effect due to the projection only; the ray always obeys equation (3.4), but in a three dimensional fashion. In analogy with the two dimensional studies, rays have different behaviour according to their launching position $\vec{x}_0$, launching direction ϕ_0, frequency ω and width of the spherical gap. Moreover, the combination of $\vec{x}_0$ and ϕ_0 influences the horizontal final orientation of the possibly occurring meridional attracting plane. In the following, we will refer to this final horizontal orientation of the meridional attractor as to ϕ_∞, an angle measured anticlockwise with respect to the x-axis, whose arbitrary orientation is defined by the location of the initial launching point $(x_0, 0, z_0)$.

Three kinds of behaviour are observed: the orbit can be domain filling (ergodic-like, figure 3.4); it can be quasi-periodic, its path filling a portion of the domain only (regular pattern, figure 3.5), or it can eventually be trapped, first onto a meridional plane (meridional attractor), and subsequently, within that plane, on a two-dimensional limit cycle (attractor, figure 3.6). It is worth noticing that here only trajectories reflecting from both inner and outer boundaries are listed. Of course, for certain combinations of $\eta, \omega, \vec{x}_0, \phi_0$, rays exist that do not touch the inner sphere at all. These trajectories can be thought of as living in a full sphere ($\eta = 0$), and we will discuss them separately in sections 3.3.5 and 3.3.6. Differently from the two-dimensional case, no three-dimensional periodic orbit has been observed so far. This is probably due to the appearance in the three-dimensional framework of an extra parameter in the problem: the initial launching direction. Whereas in the two-dimensional problem the only parameters are η, ω and $\vec{x}_0$, and periodicity is determined by ω only (ϕ_i, at every $\vec{x}_i$, being either 0 or π). Surprisingly or not, in the three-dimensional case

the combination of $\vec{x}_0$ and ϕ_0 (and therefore subsequent pairs $\vec{x}_n, \phi_n$) influences the occurrence of meridional trapping (and, in case, the final orientation ϕ_∞) and plays a crucial role in preventing/allowing a trajectory to close exactly onto itself. No universally valid relation between ω and $\phi_0, \vec{x}_0$ has been found so far to compute three-dimensional periodic orbits in a spherical shell, but we cannot exclude their presence. Obviously, because of the rotational symmetry of the problem and of the arbitrarily positioned x-axis, if one combination of ω, x_0, ϕ_0 exists for which the trajectory is closed, an infinite number of closed trajectories will exist in the same domain.

In analogy with the two-dimensional case, three-dimensional ray tracing thus allows us to explore singular solutions occurring in the shell, but does not say anything about the possible existence of regular modes in the domain. The occurrence of meridional attractors in the inviscid model strengthens the validity of all previous studies on inertial wave attractors in geophysical and astrophysical frameworks [Bretherton, 1964; Friedlander and Siegmann, 1982; Dintrans *et al.*, 1999; Rieutord *et al.*, 2001; Maas and Harlander, 2007]. The focusing power of an attractor is not limited to its two dimensional plane, but can act in some geometries, such as the shell, in a three dimensional fashion as well. The appearance of attractors in a spherical shell resembles what has been shown for a paraboloidal basin by Maas [2005] with an analogous ray tracing study. The latter study has found confirmation in laboratory experiments [Hazewinkel *et al.*, 2011b], and, for a parabolic channel geometry, in a (viscous) numerical experiment [Drijfhout and Maas, 2007]. All these works corroborate the existence and the power of three dimensional attractors, and suggest they could play an important role in non regular geometries (symmetry breaking geometries, as opposite to spherical or "flat" rectangular geometries), in focusing energy onto specific and predictable locations, triggering crucial mixing phenomena in all sorts of stratified, rotating fluids [Swart *et al.*, 2010].

As can already be noticed from figure 3.6, the number of reflections needed for the attractor to take place is relatively high, and the chances to see even one or two reflections in realistic media are quite low. Apart from observations in laboratories, there are no observations in Nature, so far, except for the ubiquitously observed peak at the local Coriolis frequency ($2\Omega \sin \phi$, where ϕ is now the latitude of the measurements) which bears evidence, in the stratified case, of a point attractor [Maas, 2001; Gerkema and Shrira, 2005]. Nevertheless, as will be shown in the following section, the trapped energy is collected over a broad range of possible latitudinal input locations and initial launching directions of the perturbation, and this makes unnecessary for the attractor to be fully developed in order to have a significant increase of energy in a restricted longitudinal range (see corresponding experimental evidences of complicated attractors in Hazewinkel *et al.* [2011b]).
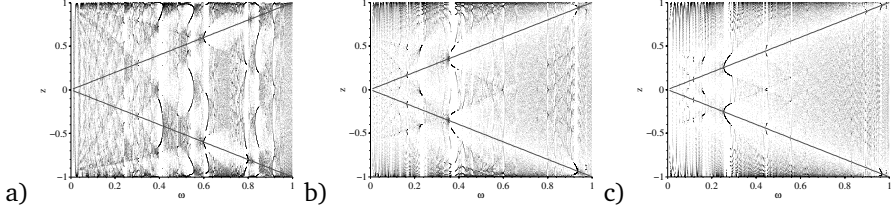
Figure 3.7: Poincaré plots for shell thickness $\eta = 0.35$ (a), 0.8 (b) and 0.9 (c). Here $x_0 = 0.2$ on the outer sphere, $\phi_0 = 5\pi/4$. On the $x-$axis, ω in the inertial range. On the $y-$axis, the z coordinate of reflection points on the outer sphere ("surface") of the last 20 reflections (out of 1000), both hemispheres. Grey lines represent the locations of the critical latitude for each ω.

3.3.3 *Meridional attractors*

In this section we will explore the parameter space for the shell case study, in order to show that meridional attracting planes (1) are not exceptional, (2) have η (geometry), ω (frequency), x_0 and ϕ_0 (initial conditions) dependencies, and (3) occur after a varying number of reflections (due to different focusing power of different combination of η, ω, x_0 and ϕ_0).

It is worth stressing that the occurrence of meridional attractors constitutes only the first step of the focusing process possibly experienced by inertial waves. Once the ray motion is restricted to a meridional plane, "classical" two-dimensional attractors arise, confining wave energy to their limit cycles within that plane, from which they can no longer escape. These "classical" two dimensional attractors have been broadly explored for the spherical shell case since Stewartson [1972], in both homogeneous and stratified rotating fluids [Rieutord *et al.*, 2001; Maas, 2001]. Therefore they will not be subject of the current analysis.

The appearance of meridional attractors is evident from the Poincaré plots (figure 3.7 for three different η values) resulting after a three-dimensional ray tracing in the shell. In these Poincaré plots, on the horizontal axis the inertial frequency range is scanned ($0 < \omega < 1$). On the vertical axes, the z coordinates of the reflection points on the outer sphere ("surface") of the last 20 reflections (out of $100, 1000, 1000$ reflections respectively) are depicted. Grey lines represent locations of the corresponding critical latitude for each value of ω. Different frequency windows representing "simple" attractors (characterised by a small number of boundary reflections) emerge for different values of shell thickness, visible as white vertical bands. We observe that even for the three dimensional meridional attractors the critical latitudes act as repellors for the
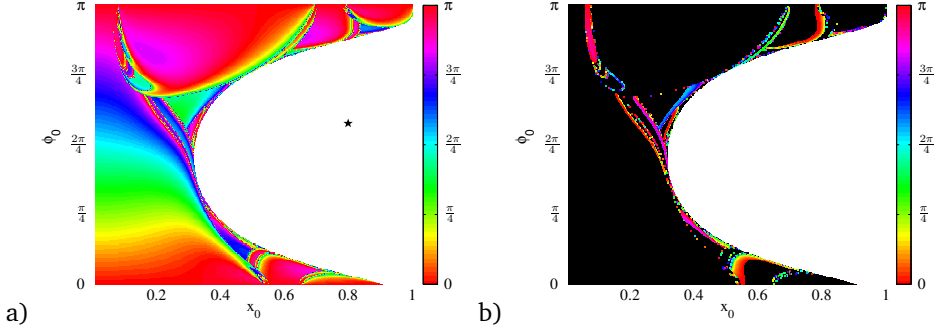
Figure 3.8: (a) plot of ϕ_∞ (colour, see legend in radians) as function of launching position and direction x_0, ϕ_0, for $\eta = 0.35$, after 1000 reflection. The perturbation frequency ω is taken to be equal to 0.4051 (see white vertical band in figure 3.7). On the x-axis, all possible x_0 are scanned, from zero to one. On the y-axis, ϕ_0 is scanned just between 0 and π, for symmetry reasons. Colours correspond to meridional trapping, white to zonally propagating rays. Black star in figure 3.8a corresponds to trajectory displayed in figure 3.11. (b) Same as figure (a) where black corresponds to coloured area in (a), hence to meridional trapping, whereas colours now represent *equatorial* type of attractors only (see section 3.3.4 for details), and their final horizontal orientation ϕ_∞. An example of *equatorial* attractor is visible in figure 3.10.
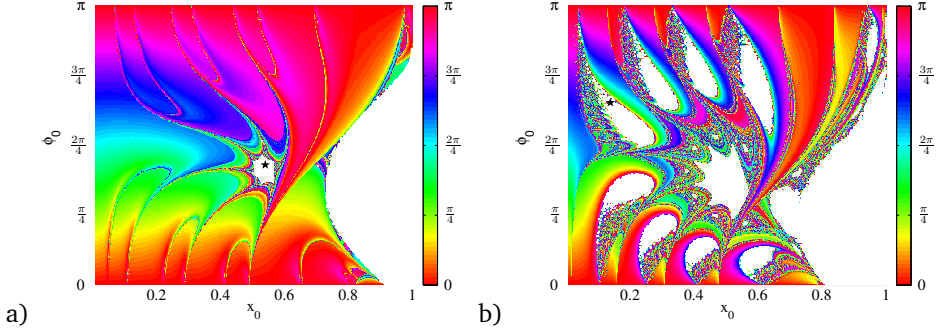
Figure 3.9: Same as in figure 3.8 for $\eta = 0.8$, $\omega = 0.4051$ (a) and $\eta = 0.9$, $\omega = 0.5842$ (b), after 5000 reflections. On the x-axis, all possible x_0 are scanned, from zero to one. On the y-axis, ϕ_0 is scanned just between 0 and π, for symmetry reasons. Colours represent meridional trapping, white areas non converging regions. Black star in figure 3.9a corresponds to trajectory displayed in figure 3.5. Black star in figure 3.9b corresponds to trajectory displayed in figure 3.12.

rays, and their repelling power seems to increase with η. Note that figures 3.7a and 3.3b are similar, but not identical, meaning that the frequency windows of the attractors are the same in the two- and in the three-dimensional cases, but the final attractor trajectories can show a different projection on the $\hat{z}$-axis, according to the final orientation of the attracting plane.

In figures 3.8a (for $\eta = 0.35$), 3.9a (for $\eta = 0.8$) and 3.9b (for $\eta = 0.9$) the fate of a whole characteristic cone is depicted after respectively 1000, 5000 and 5000 reflections, for frequencies for which meridional attractors occur according to figure 3.7. On the horizontal axis of these figures, all possible x_0 are considered, from zero to one. The perturbation is always launched on the surface of the outer sphere, in the northern hemisphere, $y_0 = 0$ and $z_0 = \sqrt{1-x_0^2}$, with an initial negative vertical velocity. On the vertical axes of figures 3.8a, 3.9a and 3.9b, for symmetry reasons, ϕ_0 is considered between 0 and π only. Colours indicate the presence of meridional trapping, and represent orientation of the final attracting plane (ϕ_∞), following the colours legend. White areas correspond to trajectories that are not subject to meridional focusing and they are interpreted as zonally propagating waves (see section 3.3.5 for comments). A single vertical column in figures 3.8a, 3.9a and 3.9b can be read as the final longitudinal location of the energy for the whole three dimensional cone excited at a single point on the surface: the three figures present all, for small x_0 ("polar" source), a horizontally striped structure, meaning that the meridional attractor of a single three-dimensional ray will preferentially approach a plane that has the same horizontal orientation as the original launching direction ($\phi_\infty \approx \phi_0$). This, in principle, would lead to a zonally homogeneous distribution of energy in the domain. Remarkably, the more equatorward we move the source, the more stripes are deformed and one final orientation of the attractors prevails (see for example the range $x_0 = [0.7-0.8]$ for figure 3.9b, for which $\phi_\infty \sim \pi$ for $\phi_0 \gtrsim \pi/2$ and no attractor occurs for $\phi_0 < \pi/2$). This tells us that, from the whole excited cone, containing rays with initial directions $\phi_0 \in [-\pi, \pi]$, most of the rays are meridionally trapped on planes that will have approximately the same orientation in the x, y-plane. Higher energy values are therefore expected in correspondence with those specific longitudinal ranges. This result is supported by observations performed in a three dimensional paraboloidal basin by Hazewinkel *et al.* [2011b]. In this experiment, a stable uniform stratification in density was disturbed by an off-centred oscillating sphere, and internal gravity waves were excited in a paraboloidal basin. A three-dimensional tomographic reconstruction of the amplitude (energy) distribution of these waves in the basin has shown the occurrence of a preferential vertical trapping plane. A centred wave source in the paraboloid would produce no preferential vertical plane, since energy would spread equally along the longitudinal coordinates. This is true for the shell as well, since a centred ("polar") launching position
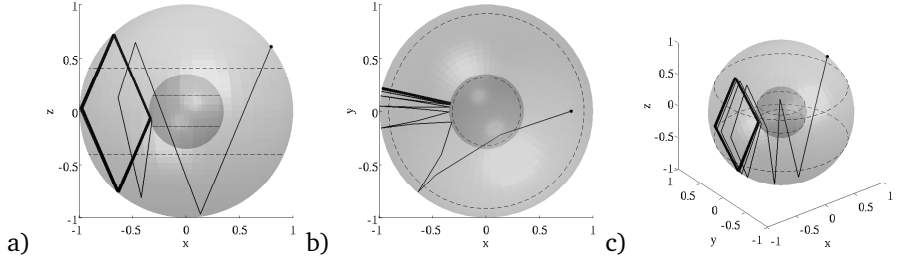
Figure 3.10: As figure 3.4, but for $\eta = 0.35$, $\omega = 0.4051$, $x_0 = 0.794$, $\phi_0 = -2.822$, showing an equatorial three-dimensional attractor. The wave attractor is drown with a thicker line.

of the ray will result in a purely meridional ray motion, that doesn't allow for longitudinal inhomogeneities.

We conclude that the present three-dimensional ray tracing study therefore not only confirms what was already shown by Bretherton [1964] and Stewartson [1971] and Stewartson [1972], that is that singular solutions (corresponding to attracting orbits) characterise the internal wave field in a shell domain. The present study extends the validity of this finding to cases in which a local source is considered, and three dimensional effects are taken into account.

Computing three-dimensional orbits clearly shows how, decreasing the thickness of the shell, a larger number of reflections is needed in order to completely develop attractors in the domain. This can be interpreted as follows: the attracting plane emerges after a combination of supercritical and subcritical reflections of the ray throughout the domain. If the thickness of the shell is small, the ray has to experience several reflections to reach a supercritical (subcritical) region of the domain, because the possible path between two subsequent reflections is small compared to the extent of these regions. Conversely, if the shell is thick, the path between two subsequent reflections is large, and less reflections are needed for the ray to experience both focusing and defocusing reflections. As already mentioned, this behaviour undermines the attracting power of attractors in thin shells (as the ocean on an aqua planet) and in more realistic (viscous, inhomogeneous) settings; nevertheless energy enhancement is possibly detectable even in absence of a fully developed attractor. Other computational experiments have shown that ϕ_0 also affects the number of reflections needed for the attractor to develop. This is because the amount of focusing depends on the incident angle.

3.3.4 *Equatorial and polar attractors*

Figure 3.7 shows that singular meridional attractors occur in specific and predictable frequency bands, when the width of the shell is given. As we have mentioned before, the asymptotic shape of trapped, initially three-dimensional trajectories, are two-dimensional objects, whose structure exactly corresponds to the ones found by a simpler two-dimensional (meridional) ray study. Therefore, in analogy with the discussion by Rieutord *et al.* [2001], we observe "simple" attractors (so called *equatorial* attractors, in figure 3.10), for example in the frequency band around $\omega = 0.4$ in figure 3.7a, characterised by only four reflections with the boundary), coexisting with more "complicated" attractors (so called *polar* attractors, in figure 3.6), characterised by a larger number of reflections.

Equatorial attractors occur in the low latitude range, and take place when reflections on the inner sphere occur below the inner critical latitude (supercritical reflections), whereas polar attractors, spanning from equatorial to polar regions, take place when reflections on the inner sphere occur poleward of the inner critical latitude (subcritical reflections). Equatorial attractors appear more robust and energetically relevant than polar ones, because of the fewer reflections needed to build their closed cycle, but how often do they occur? Their occurrence surely depends on shell thickness, being more likely to hit inner supercritical regions if the inner sphere is larger. Moreover, additional radial density stratification increases their frequency band width [Maas and Harlander, 2007]. An example of the occurrence of equatorial attractors is shown in figure 3.8b, for the case $\eta = 0.35$: black represents general meridional trapping (and corresponds exactly to the variously coloured areas in figure 3.8a); colours in figure 3.8b represent instead equatorial type of attractors only, and their horizontal orientation ϕ_∞, according to the colour map on the right hand side. As is clear by comparing figures 3.8a and b, equatorial attractors constitute the borders of the smooth areas in the parameter space.

Because of their simple shape, equatorial attractors are good candidates to have a strong influence on low-latitude dynamics. Moreover, oceanic equatorial regions are among the longitudinally widest ocean basins, therefore energy contribution to this kind of structures could be collected in principle from a wide range of possible longitudinal atmospheric or tidal inputs, and is potentially of relevance to the still largely unexplained equatorial dynamics.

Figure 3.11: As figure 3.4, example of a non converging trajectory, corresponding to star in figure 3.8a. Here $\eta = 0.35$, $\omega = 0.4051$, $x_0 = 0.8$, $\phi_0 = 1.8$ and 50 reflections are depicted.
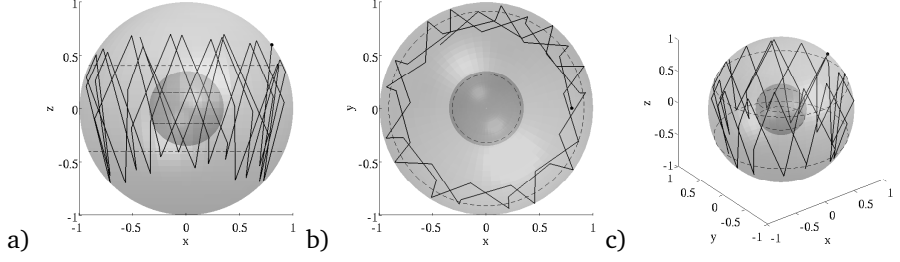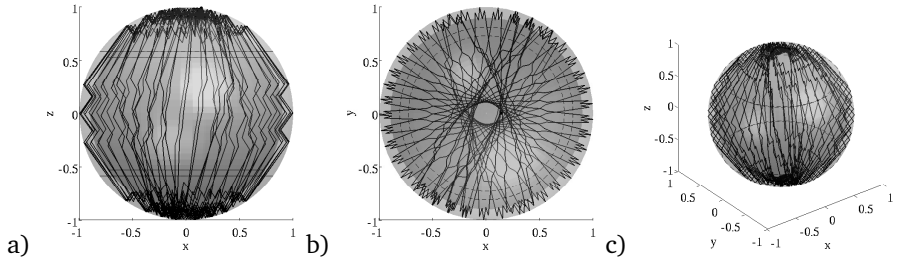

Figure 3.12: As figure 3.4, example of a non converging trajectory, corresponding to star in figure 3.9b. Here $\eta = 0.9$, $\omega = 0.5842$, $x_0 = 0.139$, $\phi_0 = -2.042$ and 1000 reflections are depicted.

3.3.5 *Zonally propagating waves*

As can be observed, for example, in figure 3.8a, even for a frequency value that gives rise to a meridional attractor, regions of the characteristic cone exist that are not subject to meridional trapping (white areas). In figure 3.11 the trajectory corresponding to the black star in figure 3.8a is displayed. This is representative of all the orbits in the white region on the right hand side of figure 3.8a, and it shows that these orbits do not interact with the inner sphere, that is, they behave as living in a full rotating sphere filled with fluid. As we expect from the known analytical solutions for this case, the full sphere does not support any singular orbits (attractors), and therefore the whole area of "spherical" orbits living in the shell coherently shows no trapping. We refer the reader to section 3.3.6 for comments on three dimensional ray tracing in the limit case of the full sphere. In this non-trapping area, the ray we are following within the three dimensional cone keeps on bouncing around the domain, experiencing subsequently focusing and defocusing reflections. It resembles the "edge waves" observed by Drijfhout and Maas [2007] in the paraboloidal channel, with the only difference that here the trajectory, instead of being trapped around a single critical line, is now trapped in the equatorial belt, hugging both critical circles of the outer sphere. As we can expect, the width of these non trapping areas reduces with increasing values of η (see analogous white lobes on the right hand side of both figures 3.9a and b): the bigger is the inner sphere, the more likely it is for the ray to touch it.

Interestingly, as we decrease the thickness of the shell, other white areas appear, according to a regular and fascinating pattern. In these white regions we can now distinguish two different kinds of behaviour. An example of non-converging orbits of the first type, corresponding to the black star in figure 3.9a, is shown in figure 3.5. We can describe this kind of trajectories as "polar" edge waves, in analogy with the previous "equatorial" ones, and, consistently, "polar" edge waves are not periodic nor present any attracting power. However, surprisingly, "polar" edge waves do not seem to interact with the outer nor with the inner critical latitudes. It can be at first hypothesised that the ray would sense not only the gradient of the topography, but also the gradient of the fluid depth, and it could behave like an edge wave around this secondary "critical" latitude. This does not seem to be the case for "polar" edge waves, whose nature remains unexplained. The second type of behaviour, displayed in figure 3.12 (black star in figure 3.9b), contrasting with the "equatorial" and "polar" edge waves, involves the whole fluid domain. The ray is never trapped onto a unique meridional plane, but it continuously and smoothly drifts in the zonal direction with no preferred direction of propagation.

Remarkably, all types of edge waves are not subject to meridional trapping, and therefore are invisible in a purely meridional (two-dimensional) ray trac-

ing in spherical shell domain. It may be argued that these trajectories do not represent a physical solution in the domain, being the three-dimensional counterpart of the two-dimensional, annihilating, domain filling trajectories. On the other hand, numerical results from Drijfhout and Maas [2007] show the same structures, and it has been speculated they could provide an explanation to areas near the bottom of the ocean where enhanced internal wave activity is detected [Horn and Meincke, 1976]. Moreover, the existence of zonally propagating modes could provide a rationale for the otherwise unexplained experimental results by Koch *et al.* [2013], where only 16% of the total energy measured in the wave field can be explained by purely meridional motion in a homogeneous, rotating spherical shell. In analogy with electromagnetic phenomena as electron orbits, we could expect to observe in a real fluid only those trajectories that interfere constructively and show a periodic character, and close onto themselves after one azimuthal revolution around the domain. These kind of periodic trajectories would act as three-dimensional traps for rays, forced to travel endlessly along the respective periodic orbit (as in a three-dimensional attractor). Promisingly, all kinds of edge waves show a regular pattern to a top view observer, but unfortunately no periodic edge wave has been observed so far, suggesting that this class of solution, if existing, does not posses any attracting properties.

It is fascinating, any way, how edge waves in the spherical shell reveal their strong dependency on the thickness of the domain. As can be observed, comparing figures 3.9a and 3.9b, the two structures are basically the same. Increasing the value of η, in figure 3.9b, we just witness an unfolding of the lobes already present in figure 3.9a, and a flourishing of a crown of smaller white areas around the central one, resembling a fractal type of behaviour.

3.3.6 *Limit cases: the full sphere and the infinitely thin shell*

Analytical solutions to equation (3.1) in a spherical geometry, completely filled with homogeneous or non homogeneous fluid, are well known since the work by Bryan [1889], Friedlander and Siegmann [1982], Friedlander [1982], and Greenspan [1968], and, more recently, explicit solutions for the corresponding velocity field have also been derived by Zhang *et al.* [2001]. Solutions are regular throughout the whole domain: three dimensional ray tracing analysis applied to the full sphere does not show indeed any longitudinal inhomogeneity, and consequently neither two- nor three-dimensional attractors occur. As anticipated in the previous section, because of its regularity, the full sphere could be a domain where (possibly) three-dimensional periodic trajectories appear, at frequencies corresponding to the known eigenvalues of the system. These periodic orbits would constitute the exact three-dimensional counterpart of

the two-dimensional periodic trajectories, being representative of the regular modes existing in the sphere.

Orbits like the one depicted in figure 3.11 seem appealing, but no three-dimensional periodic orbits have been found in the sphere, so far. They could either not exist, or they could be unstable, acting as repellors for the trajectories and in such a way prevent their observation. Dintrans *et al.* [1999], using a combination of two-dimensional ray tracing and a three dimensional numerical model, have already suggested that pure inertial modes in a sphere could constitute an example of the association of regular modes to quasi-periodic (ergodic) orbits, breaking the usual association valid in two-dimensional domains, between closed (periodic) orbits and regular solutions. However, we can not, in principle, exclude the existence of three-dimensional periodic orbits in the sphere, and consequently in the spherical shell as well, in which case the ray, because of its orientation, does not interact with the inner boundary (see, again, figure 3.11). These orbits, if existent, would represent a set of exceptional non-annihilating edge waves in the fluid, and constitute an entire new class of waves, neglected so far in the purely meridional studies, because of their intrinsic three-dimensional nature.

The opposite scenario, the case of an infinitely thin shell ($\eta \to 1$) also deserves some special attention. This case has been studied analytically in Stewartson and Rickard [1969]; Stewartson [1971, 1972], where for the first time a "pathological" (singular) behaviour has been described as characterizing solutions in a rotating fluid shell. Interestingly, frequency windows given by Stewartson [1972] are easily retrieved as attractor frequency windows in the limit of a numerically infinitely thin shell, as already verified in the two dimensional meridional plane by Maas and Harlander [2007]. The singular nature of inertial wave solutions in shell geometries appears thus to bear its evidences at all values of $\eta > 0$.

3.4 DISCUSSION AND CONCLUSIONS

Three-dimensional internal wave ray tracing has here been systematically applied to rotating spherical shell geometries of arbitrary ratio between inner and outer radii. In this work, the analysis is restricted to inertial waves only. Results for a homogeneous rotating shell are likely to be locally distorted in the presence of radial density stratification, but is assumed that the pure inertial problem summarises already many difficulties and features of the gravito-inertial problem (with the exception of the turning surfaces, occurring only in the density stratified case), and findings in this partial case are supposed to have general applications. We are conscious of the fact that a ray tracing study allows us to explore the behaviour of the inviscid linear solution only. However, even

this partial perspective can be of help in improving our poor understanding of internal wave field dynamics in arbitrarily shaped enclosed fluid domains where, generally, no analytical (inviscid) solution is known, the spherical shell constituting a paradigmatic example of this category. In spite of the azimuthal symmetry of the domain, in this work and differently from literature, ray motion is not restricted to the meridional plane only, but it is followed as it develops in a fully three-dimensional environment, allowing, in the first place, for a better representation of a local point source in the domain, and, secondly, for subsequent development of zonal inhomogeneities.

It is found that some frequency bands in the inertial wave range support meridional trapping of the rays. In these bands, internal wave ray trajectories, whose motion is initiated outside a meridional plane, are eventually trapped onto a meridional plane, from which they cannot escape any longer. We call this meridional plane a "meridional attractor", in analogy with the two-dimensional internal wave attractors described in Maas and Lam [1995]. Once on a meridional plane, rays are subject to the occurrence of two-dimensional attractors, as it has been shown already in Dintrans *et al.* [1999], Rieutord *et al.* [2001], and lately in Maas and Harlander [2007]. The fact that attractors in the shell act in a three-dimensional fashion comes with no surprise. In fact they are representative of the singular nature of internal wave field solutions in domains such as the spherical shell [Bretherton, 1964; Stewartson, 1971, 1972], and they comfortably emerge not only in the purely meridional, two dimensional representation of those solutions, but also when full, three-dimensional effects are taken into account.

If, on the one hand, the presence of meridional attractors justifies the use of ray tracing on meridional planes only, the present work on the other hand also points at the existence of zonally propagating waves in the inertial frequency range, whose trajectories could be traced here for the first time thanks to the adoption of a three-dimensional scheme. These ray trajectories constitute a new and interesting class of possible solutions, so far neglected in purely meridional studies. Even if the physical relevance of these type of orbits is not completely clear yet, they could help in the interpretation of some laboratory [Hazewinkel *et al.*, 2011b; Koch *et al.*, 2013] and numerical [Drijfhout and Maas, 2007] three-dimensional results. It is worth noticing that trajectories that do not interact with the inner boundary constitute a subset within the zonally propagating edge waves. They can be thought of as trajectories belonging to the limit case of the full sphere, as the inner sphere is not sensed by the rays. One of the main questions remaining about these edge waves, both living in the spherical shell and in the sphere, concern three-dimensional orbit periodicity. It is appealing to retrieve the usual association, valid in two-dimensional frameworks, that periodic orbits would represent regular solutions (the *modes*) of the studied sys-

tem, especially regarding the full sphere case, where eigenvalues are known. It is, however, beyond the scope of this paper to address such a question.

In the present work, conditions for the occurrence of meridional attractors have been explored, motivated by possible astrophysical and geophysical applications of the results. In fact, singular (attracting) type of solutions are supposed to play a role in diapycnal and angular momentum mixing, in regions where focusing reflections take place, and energy is localized to confined areas in the domain.

3.4.1 *Oceanographic implications*

Results presented in this study, obtained by means of ray tracing, are restricted to linear, inviscid fluid dynamics in three spatial dimensions and to a homogeneous rotating fluid, which clearly restricts their direct application to a real geophysical fluid. However, when it comes to geophysical applications, in the work of Broutman *et al.* [2004] the ray approach has been analysed in a selection of case studies, where it has been generally recognized to provide a unique contribution to the understanding of spatial structures and spectra of atmospheric and oceanic internal waves (in the usual WKB approximation). In the ocean, internal inertio-gravity waves are generated near ocean boundaries, at the surface by atmospheric perturbations, or over deep topographic features, by tidal forcing. These waves are observed to travel as confined energetic beams that can propagate through the ocean for thousands of kilometres [Zhao *et al.*, 2010] and they constitute, by means of breaking and other small scale processes, one of the contributors to the deep ocean vertical turbulent diffusivity, necessary for maintaining the stratification and, over all, the global overturning circulation [Wunsch and Ferrari, 2004]. In case features as internal wave attractors occur in Nature, they could supposedly be responsible for strong energy focusing in specific locations in the interior of the fluid domain, possibly far from boundaries, with consequent local enhancement of wave breaking, mixing, and small scale processes, because of the regularisation of the associated solution by means of enhanced viscous effects [Bretherton, 1964; Maas, 2001; Harlander and Maas, 2007; Maas and Harlander, 2007]. It is clear that various physical circumstances in planets, stars, oceans and atmospheres, may not always permit the numerous reflections that are needed by an attractor to develop. However, as already stated at the end of section 3.3.2, it is not necessary to have a fully developed attractor to observe an increase of energy in a limited portion of the domain. This hypothesis has been confirmed in the three-dimensional laboratory experiments performed by Hazewinkel *et al.* [2011b], and is at the base of any further speculations about the role of inertial waves (or,

more generally, gravito-inertial waves) in the ocean, as well as in other media, and their possible interaction with the mean flow.

In fact, density and angular momentum mixing due to internal wave breaking has already been observed to generate a mean flow [Maas, 2001; Tilgner, 2007; Swart *et al.*, 2010; Morize *et al.*, 2010; Sauret *et al.*, 2010; Grisouard and Bühler, 2012]. This kind of mean flow generation process has been proposed as feeding mechanism for highly coherent (prograde) zonal currents (jets) in media, [Maas, 2001; Maas and Harlander, 2007], especially in the low latitude regions, where trapped wave solutions [Stern, 1963] are generally focused onto periodic paths, leading to unstable regimes. Local effects such as internal wave attractors and consequent angular momentum mixing could thus be at the basis of general phenomena, as the Equatorial Deep Jets, observed in all equatorial oceans (Firing [1987] in the Pacific, Send *et al.* [2002] and Brandt *et al.* [2011] in the Atlantic, Dengler and Quadfasel [2002] in the Indian Ocean) as well as in the atmosphere [Galperin, 2004; Ogilvie and Lin, 2004], or the variability in the rotation rate of rapid stars [Balona *et al.*, 1996], phenomena whose forcing and maintenance have not yet been understood completely.

With the results presented in this work, attractor occurrence and related processes can now be understood afresh. Not only are they valid when a perfectly axisymmetric forcing (and, consequently, wave motion) is present, but, due to the meridional focusing power of geophysical domains as a shell-like ocean or atmosphere, they are likely to take place even when point source and meridional inhomogeneities come into play, certainly a more realistic condition for a medium as our ocean.

4

INERTIAL WAVE RAYS IN ROTATING SPHERICAL FLUID DOMAINS

Internal waves have long been subject of numerous studies, motivated by their fundamental character and the variety of possible applications. In fact, they are present in all stratified and/or rotating fluids, including astrophysical and geophysical fluids, where they are considered a key mechanism contributing to internal mixing and dynamics [Dintrans *et al.*, 1999; Ogilvie and Lin, 2004; Wunsch and Ferrari, 2004; van Haren and Gostiaux, 2012].

Interestingly, internal *gravity* waves and internal *inertial* (or gyroscopic) waves share many aspects in their dynamics and mathematical description, irrespective of the nature of the acting restoring force (gravity, or Coriolis acceleration respectively). In this work we will restrict ourselves to the study of pure inertial waves propagating in a homogeneous fluid, but it follows that results that are valid for one type of internal waves are generally of relevance for the whole class.

Despite the recent progress, especially regarding high-resolution numerical models [Nurijanyan *et al.*, 2013; Baruteau and Rieutord, 2013; Favier *et al.*, 2014], one key challenge is still limiting our ability to satisfyingly comprehend propagating internal waves: their hyperbolic character is hardly reconcilable with their confinement to a fully enclosed domain, resulting, for an arbitrarily shaped container, in a paradigmatic, mathematically ill-posed Poincaré problem (see Cartan [1922] and, for example, Stewartson and Rickard [1969] and Rieutord *et al.* [2000] for the case of a spherical shell container).

Because of this difficulty, regular, analytic solutions (smooth functions, finite in all points of the domain) for inertial wave problems in enclosed domains are known only for homogeneous fluids contained in exceptionally symmetric geometries, such as for two-dimensions, the rectangle and the circle (see for example Barcilon [1968]), and for the three-dimensional case, the axial cylinder [Lord Kelvin, 1880b; Høiland, 1962], the axial ellipsoid [Kudlick, 1966] and the full sphere [Bryan, 1889; Zhang *et al.*, 2001]. Quasi analytical methods have been also used to compute regular inertial wave fields in the case of an untilted rectangular parallelepiped [Maas, 2003; Nurijanyan *et al.*, 2013].

In order to study the propagation and the properties of internal waves in differently shaped, two-dimensional domains, where analytical solutions are unavailable, ray theory has been developed [Whitham, 1960, 1974]. When the amplitude of the propagating wave is assumed to be slowly varying in space and time compared to variations in the phase function and in the conditions of the supporting medium, it is possible to treat these slowly modulated waves as nearly planar waves, and solve the original equation in the short wavelength limit, often referred to as the Wentzel-Kramers-Brillouin-Jeffreys (WKBJ) approximation). This simplified approach is not only valid for describing internal waves, but has been also frequently used to describe the dynamics of inviscid,

short surface gravity waves. Since surface waves are exponentially trapped to the surface, they propagate strictly in the horizontal plane and their velocity potential is described by a Helmholtz equation [Maas, 2005]. It follows that for waves that are short compared to the scale over which water depth and radius of curvature of the wall change, WKBJ theory determines approximate solutions to the Helmholtz equation. Short surface waves propagating over flat bottoms, as well as two-dimensional inertial waves, trace then straight ray paths in real space, similar to the paths traced by balls bouncing elastically on a billiard.

In the case of internal waves, the tracing is performed by following the propagation of corresponding energy rays, whose inclination with respect to the restoring force direction (gravity or rotation axis) is determined by the ratio of the perturbing frequency and a frequency representing the local environmental conditions (density stratification and/or rotation). Rays are then supposed to provide a (partial) view on the energy distribution in the domain and on the regularity of the associated wave field (or the lack of it).

The correspondence between characteristic curves of the original partial differential equation and approximated, geometrical, internal wave energy rays is not trivial [Eckart, 1960]. However, the correspondence is exact for two-dimensional internal waves, propagating obliquely in the vertical plane, under a wide range of circumstances [Harlander and Maas, 2006]. Remarkably, despite the strong assumptions underlying ray tracing, this investigation tool has been proven useful even in applied, realistic cases, where the ray approach has been tested against laboratory observations [Maas *et al.*, 1997; Manders and Maas, 2004; Hazewinkel *et al.*, 2008, 2011a], numerical simulations [Dintrans *et al.*, 1999; Rieutord *et al.*, 2001], or analysed in a selection of geophysical applications [Broutman *et al.*, 2004]; in all these cases, ray tracing has been generally recognised to provide a unique contribution to the understanding of the spatial structure and spectra of internal wave fields.

As we have seen, in the short wave length limit, surface waves over flat-bottom basins also follow straight ray paths, which on non-trivially shaped domains are either periodic, invariant (never closing orbits, infinitely repeating the same spatial structure, while being slightly offset) or chaotic [Berry, 1981; Kudrolli *et al.*, 2001]. While the periodic paths, and the invariant modes, have measure zero amongst the chaotic paths, they dominate the response of higher modes, and are therefore referred to as scars [Heller, 1984]. By contrast, three different types of ray trajectories are observed when internal waves are obliquely propagating in two-dimensional vertical domains [John, 1941; Maas and Lam, 1995; Dintrans *et al.*, 1999]. A trajectory can be closed and periodic after a finite number of reflections on the boundary. A trajectory can be ergodic and plane filling, or, lastly, a trajectory can be attracting, meaning that there exist one or more limit cycles towards which neighbouring trajectories are attracted.

The first two kinds of trajectories are usually associated with the presence of regular modes in the system and with a dense spectrum, such as occurs in the untilted rectangular domain, or the circle [Barcilon, 1968]. In these domains, periodic ray trajectories occur at frequencies corresponding to eigenfrequencies of the system, while rays corresponding to other frequencies fill the fluid domain ergodically.

Besides being dense, the spectrum of two-dimensional regular systems is also infinitely degenerate [Münnich, 1996]: consequently, for each eigenfrequency, an infinite number of periodic orbits exist, that together cover the whole domain.

By contrast, the occurrence of attracting trajectories ('wave attractors') is the signature of the singular nature of solutions. Attractors can be observed in all "symmetry breaking" domains (e. g. trapezoidal, parabolic, tilted rectangular or annular domains), so called because the reflecting walls are not all parallel nor perpendicular to the restoring force. In this case, energy is collected from the whole basin and trapped onto the asymptotically closed trajectories (the attractors), focusing towards smaller and smaller scales till wave breaking, other nonlinearities and viscous effects come into play [Maas and Lam, 1995; Ogilvie, 2005; Harlander and Maas, 2007; Hazewinkel *et al.*, 2008; Scolan *et al.*, 2013]. Exceptionally, in the case of of a toroidal shell in the limit of long radius, analytical solutions are also known for modes focused along the emerging attractors [Rieutord *et al.*, 2002].

Once these two-dimensional ray tracing results were shown to be robust, an increasing interest in the three-dimensional representation of internal waves in three-dimensional containers has obviously arisen. In order to extend ray tracing to three dimensional, curved domains, however, a further consideration has to be made: considering the WKBJ limit, and its assumption that the wavelength needs to be short compared with the spatial scale of boundary variations, the propagating perturbation bouncing from a curved boundary is further idealised as if reflecting from a local tangent plane [see also Baines, 1971]. Given these approximations, a three-dimensional ray tracing algorithm can then be developed, and, in three-dimensional containers, rays can be geometrically traced and their behaviour studied [Manders and Maas, 2004; Maas, 2005; Hazewinkel *et al.*, 2011b] and chapter 3.

In analogy with the two-dimensional correspondence, in the presence of internal wave attractors, a relation between wave rays and energy paths in three dimensional geometries is supported by recent numerical work in a tidal channel [Drijfhout and Maas, 2007] and by laboratory experiments performed in a non-centrally forced paraboloidal basin filled with a uniformly stratified fluid [Hazewinkel *et al.*, 2011b].

However, all three-dimensional studies so far have been devoted to the investigation of symmetry breaking geometries, because of the possibly crucial role

played by wave attractors in the energy distribution in the basin, and consequently in relevant geophysical and astrophysical analogous contexts. But how robust is the analogy between two- and three-dimensional ray tracing, and how tight is the association between ray behaviour and properties of the underlying wave field?

In this study, the case of pure inertial waves in a homogeneous fluid contained in a three-dimensional, uniformly-rotating full sphere is considered. For this setting, in fact, three-dimensional analytic solutions are known [Bryan, 1889; Zhang *et al.*, 2001]. The ray tracing algorithm is the same as used in chapter 3 in a rotating spherical shell: it can be adopted here with little changes. Questions we wish to raise are: do three-dimensional periodic inertial wave ray trajectories ('scars') exist in a spherical domain? Is the classical, two-dimensional association between regular modes and periodic trajectories still valid in three-dimensions? How do the frequencies associated with periodic trajectories relate to the analytical spectrum of inertial waves in a sphere [Bryan, 1889]? And to experimental observations? How can real space trajectories in the sphere be classified in an appropriate phase space, in terms used in the description of quantum chaos [Berry, 1987]?

The plan of this paper is as follows. Methodologies are presented in section 4.2: analytical solutions for inertial waves in a sphere are briefly recalled in section 4.2.1, a WKBJ approach is sketched in section 4.2.2, whereas the geometrical formulation of the ray tracing algorithm is described in section 4.2.3. A short review on the relations between ray trajectories, eigenmodes and physical fields of a system is presented in section 4.2.4. Results from the application of the ray tracing algorithm are presented in section 4.3. Three-dimensional periodic trajectories are found in the full rotating sphere, and a first attempt at classifying these orbits is presented, based on the associated frequency and corresponding spatial structure. In section 4.3.9 the different class of real space trajectories are analysed in their corresponding phase space [Berry, 1981, 1987], where successive reflections are followed using the polar angle at subsequent reflection points and the angle of incidence of the ray relative to the normal at the same reflection point [Nöckel, 1997].

Even if a general picture is far from being complete, the significance of periodic (and of non periodic) orbits is discussed in section 4.4, both with respect to previous two-dimensional comparisons in literature as well as to wave field reconstruction. A summary of the findings is given in section 4.5, while comparisons with previous experimental studies and concluding remarks are presented in section 4.6.

4.2.1 *Analytical solutions*

In a homogeneous, inviscid, uniformly-rotating fluid, momentum and mass conservation lead to the linearised equations of motion for small amplitude perturbations of velocity $\vec{u}$ and pressure p:

$$\frac{\partial \vec{u}}{\partial t} + \vec{e}_z \times \vec{u} = -\vec{\nabla} p$$
$$\vec{\nabla} \cdot \vec{u} = 0$$

$$(4.1)$$

where the Coriolis parameter $(2\Omega)^{-1}$ is used as time scale, and the fluid is rotating at rate Ω oriented parallel to the vertical z-direction (see figure 4.1a). When all fields are assumed to have a $e^{-i\omega t}$ time dependency, the problem can then be conveniently cast in terms of pressure only and described by the Poincaré equation [Cartan, 1922]:

$$p_{xx} + p_{yy} - \lambda^2 p_{zz} = 0. \qquad (4.2)$$

with

$$\lambda^2 = \frac{1 - \omega^2}{\omega^2}. \qquad (4.3)$$

Propagating inertial waves exist in the frequency range $0 < \omega < 1$, when the Poincaré equation is hyperbolic. Note that, compared to two-dimensional internal wave problems, the additional second order horizontal derivative lends some aspects of an elliptic problem (like surface wave problems) to the Poincaré equation. When the fluid is fully confined, the boundary condition for internal waves requires vanishing of the normal velocity component at the container's walls. In case of a spherical container, this means vanishing of the radial velocity component $u_r = 0$ at $r = 1$, where the sphere's radius is used as spatial scale. This implies that the pressure field has to obey oblique derivative boundary conditions, that prohibits finding exact analytical solutions in arbitrarily shaped containers. However, when the container possesses some regularity and symmetry, the Poincaré problem is solvable. This happens, for instance, when the sidewalls of the container are parallel to the rotation axis and the vertical dependency can be split off, leaving a Helmholtz equation to be satisfied in the horizontal plane [Maas, 2003].

In the case of the spherical container, it was shown by Bryan [1889] that a transformation of equation (4.2) from a cylindrical coordinate system (ϕ, r, z), initially chosen because geostrophic contours on the sphere correspond to circles of constant cylindrical radii at fixed distances from the rotation axis, to a

pseudo-spheroidal coordinate system (ϕ, ξ, μ), where the radial and vertical coordinates are defined as follows:

$$\begin{cases} r^2 = \frac{(1-\xi^2)(1-\mu^2)}{1-\omega^2} \\ z = \frac{\mu\xi}{\omega}, \end{cases} \tag{4.4}$$

provides solutions for the Poincaré problem. These are expressed in terms of separable modal functions of the form

$$p = P_n^{|k|}(\xi) P_n^{|k|}(\mu) e^{ik\phi}, \tag{4.5}$$

where $P_n^{|k|}(\xi)$ and $P_n^{|k|}(\mu)$ are the associated Legendre functions of nth degree and k^{th} order and n and k are integers. Following Greenspan [1968]'s notation, the eigenfrequencies can then be explicitly evaluated, and are distinguished by a triple index $\omega_{n,m,k}$, where n and k vary over all integers and m (going from 1 to $n-|k|$ if $n-|k|$ is even, and from 1 to $n-|k|-1$ if $n-|k|$ is odd) corresponds to the mth solution of the transcendental eigenvalue equation:

$$kP_n^{|k|}(\omega) = (1-\omega^2) \frac{dP_n^{|k|}(\omega)}{d\omega}. \tag{4.6}$$

For this set of modes, the three components of the velocity field are also explicitly computable [Zhang *et al.*, 2001]. Experimental evidence of Bryan's modes had to wait 80 years, when Aldridge and Toomre [1969] directly measured inertial resonant eigenfrequencies of a rotating sphere, lately numerically confirmed by Rieutord [1991]. Although the experimental results are highly dependent on the measurement method [Zhang *et al.*, 2013], they showed excellent agreement with the ones theoretically predicted solving equation (4.6). Another experimental confirmation of the existence of inertial modes in precessing spheroidal cavities (and of their propagation along conical surfaces) is found in Noir *et al.* [2001].

4.2.2 *The WKBJ limit*

In the case of inertial waves in a spherical container, a new WKBJ formalism has been recently developed in astrophysical context in order to solve an approximated version of equation (4.6) and to investigate the inviscid spectrum and the spatial structure of the associated normal modes [Arras *et al.*, 2003; Wu, 2005a; Ivanov and Papaloizou, 2010]. This spectrum is well-defined despite the fact that inertial waves have a discrete but everywhere dense spectrum [Lockitch and Friedman, 1999].

One example of a spectrum obtained with this methodology is presented in Ivanov and Papaloizou [2010]. In order to meet the short wavelength limit,

required by WKBJ theory, the asymptotic form of the Legendre functions in the limit of large values of n is used. They then compute the approximate first-order expression for the eigenfrequencies from (4.6):

$$\omega^{WKBJ}_{n,m,k} = \cos(\pi \frac{m + 1/4 - |k|/2}{n + 1/2}).\tag{4.7}$$

Remarkably, this expression explicitly shows the degeneracy of the spectrum in terms of scale redundancy, obtained by replacing $(n, m, k) \to j(n, m, k)$. Eigenfrequencies obtained in the WKBJ limit have been tested against previous numerical results [Lockitch and Friedman, 1999; Dintrans and Ouyed, 2001] and have shown surprisingly good agreement even for the so called "global modes", whose perturbation involves the whole domain, and for which the WKBJ approach is not expected to constitute, in principle, a meaningful approximation.

In terms of direct comparison with eigenfrequencies computed solving equation (4.6) and equation (4.7), we can take, as an example, the least-damped axisymmetric inertial mode in the full sphere, $\omega_{4,1,0} = \sqrt{3/7}$ [Dintrans *et al.*, 1999; Rieutord *et al.*, 2001]. This corresponds, in this WKBJ formalism, to $\omega^{WKBJ}_{4,1,0} = \sin(2\pi/9)$. The difference between the two values is $\mathcal{O}(2\%)$.

Using this WKBJ limit, solutions for the associated wave field are computed [Wu, 2005a; Ivanov and Papaloizou, 2010], that can be compared with numerical and analytical results. A noteworthy feature is that the largest pressure perturbations, as well as the steepest spatial gradients for pressure and velocities, are to be found near the surface of the sphere, and in particular at the 'critical latitudes', where the inclination of the rays matches the inclination of the local tangent to the boundary. These locations have turned particularly important in, for example, the tidal dissipation problem Wu [2005b]. These hot spots are in general not visible for the low modes computed using Zhang *et al.* [2001]'s explicit formula, but will play a crucial role for ray trajectories, as we shall see in section 4.3.

4.2.3 *Three-dimensional ray tracing*

In addition to the analytical approach (section 4.2.1), and in parallel to the WKBJ approach introduced in section 4.2.2, geometrical ray tracing constitutes a third, useful technique for the study of inertial waves in enclosed domains. We briefly review in this section the three-dimensional ray tracing algorithm, while the interested reader is referred to section 3.2.2 and appendix A for the construction of the map that relates a reflected to an incident ray.

In fact, in an appropriately rotated version of equation (4.2), a plane wave perturbation can be described in two-dimensions only, containing the vertical axis (z), aligned with rotation, and one horizontal axis (x), aligned with

the propagation direction. Substituting a wave like solution for pressure $p \propto e^{i(kx+mz)}$, the dispersion relation follows:

$$\omega^2 = \sin^2 \theta, \tag{4.8}$$

where the wave vector is now expressed in polar coordinates as $\vec{k} = (k, m) = \kappa(\cos \theta, \sin \theta)$, with θ the angle between the wave vector and the horizontal. Since ω is independent of wave vector magnitude κ (equation (4.8)), it follows that for internal waves, group velocity ($\vec{c}_g = (c_{g,x}, c_{g,z}) = \nabla_{\vec{k}} \omega$) is perpendicular to phase velocity ($\vec{c} = \frac{\omega}{\kappa^2} \vec{k}$), and points along a direction having an angle θ with the vertical. In other words, this reveals the interesting fact that internal waves are *monoclinic* and not *monochromatic*.

It follows that internal wave group velocity in stably stratified fluids is directed along beams, the internal wave rays, whose inclination with respect to the restoring force is uniquely set by the frequency of the perturbation, and the environmental condition (density stratification and/or rotation) [Görtler, 1943; Greenspan, 1968], and this inclination is conserved upon reflection at the domain's boundaries.

Now we want to trace the behaviour of a perturbation at definite frequency ω. The perturbation is thus "launched" at one location, at position $\vec{x}_0 = (x_0, 0, z_0)$. Note that the x-axis is now defined by the position of the launching point, and not by the propagation direction as for equation (4.8). It is clear that we can choose $y_0 \equiv 0$ because of axial symmetry of basin and equations. We shall see in section 4.6 how this kind of experiment would be practically feasible.

One crucial difference with respect to the usual two-dimensional setting has to be pointed out. When a three-dimensional problem is studied, the launched perturbation is then allowed to travel along characteristic *cones*, given by the 2π revolution of the classical, two-dimensional St. Andrew's *cross*, whose aperture 2θ is uniquely set by the perturbation frequency and the stratification/rotation properties via the dispersion relation (4.8).

One single ray will then be uniquely defined by four parameters: ω, which sets the vertical propagation angle θ; $\vec{x}_0$, which fixes the launching position; the initial horizontal direction ϕ_0 in the xy-plane, measured anticlockwise with respect to the x-axis, which identifies one upward and one downward propagating rays from the others belonging to the same excited internal wave *double cone*, and $\gamma_0 = sign(c_{g,z})$, that finally and unequivocally distinguishes either the upward or the downward propagating ray.

In the subsequent ray path computations, we adopt a vertical coordinate stretching:

$$z' = \frac{z}{\lambda} = \frac{z}{\cot \theta} \tag{4.9}$$

in order to fix the ray's inclination to an angle $\theta' = 45°$ with respect to the vertical, for any perturbation frequency. This change of variable implies a strong

simplification in the calculations, the only price being the vertical compression or elongation of the spherical domain into an oblate ($\omega < 1/\sqrt{2}$) or prolate ($\omega > 1/\sqrt{2}$) spheroid. To facilitate the reader, all figures in this paper have been subsequently re-stretched back to the original spherical geometry, without compromising the validity of the results.

The new direction into which the ray (representing the energy propagation direction of an incident wave beam) scatters upon reflection from a sloping boundary is determined as follows [Phillips, 1963; Hughes, 1964]. Since the wave frequency does not change, also the beam's angle with respect to the vertical does not change at reflections from the boundaries: this is equivalent to requiring that the incident and reflected waves obey the same dispersion relation (4.8), while the boundary condition of vanishing normal flow at the reflection point needs to be also always satisfied. The mechanism of horizontal scattering of the ray is sketched in figure 4.1, and explained in detail in the appendix A. While the wave vector component in the along-slope, tangential direction is unchanged, the wave vector component in the cross-slope direction changes due to a focusing or defocusing reflection, depending on the local bottom slope $s = |\nabla H|$. The new horizontal direction (ϕ_r) of the reflected ray is in fact completely determined by the horizontal direction of the incoming wave, ϕ_i and the local bottom gradient itself (see figure 4.1c).

When the transformation in (4.9) is used, conservation laws and geometrical laws [Phillips, 1963; Eriksen, 1985; Gilbert and Garrett, 1989; Manders and Maas, 2004; Maas, 2005] yield the relation between ϕ_i and ϕ_r:

$$\sin \phi_r = \frac{|s^2 - 1| \sin \phi_i}{2s \cos \phi_i + s^2 + 1}. \tag{4.10}$$

When the reflection takes place where the local bottom slope is smaller than the inclination of the ray ($s < \tan(\theta') = 1$), the reflection is called subcritical and it leads to a change in sign of the vertical component of the ray's velocity $\gamma_r = -\gamma_i$. In the opposite scenario ($s > 1$), the reflection is called supercritical and no change in sign is involved. Critical latitudes (θ_c) connect critical points at which the bottom slope equals the ray slope ($s = 1$), and they lead, in the projection on the horizontal plane, to a specular reflection of the incident ray. A detailed description of the different reflection mechanisms in the different parts of the domain, with special attention to the critical latitudes, is given in the appendix A.

The inertial wave ray path for a given frequency ω and initial launching position and direction ($\vec{x}_0, \phi_0, \gamma_0$) can thus be followed as it bounces through the sphere applying the known reflection laws by computing subsequent reflection points.
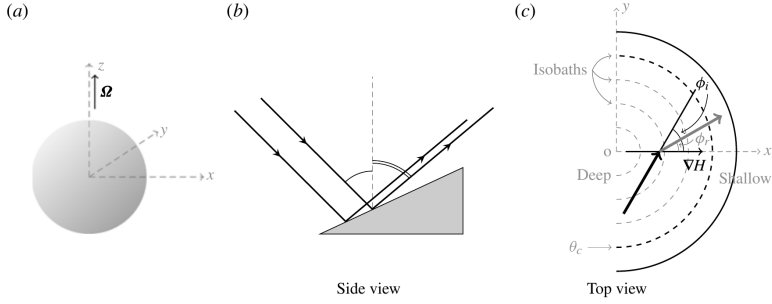
Figure 4.1: (a) Rotating fluid sphere in the Cartesian coordinate framework. (b) Side and (c) top view of a short internal wave packet that reflects subcritically (see text for explanation) from a sloping bottom. In (c) the rotation axis (coinciding with the z-axis) is pointing towards the reader. Modified after Maas [2005]. In (b), note that while incident and reflected rays lie on the same cone (whose angle θ with the vertical is fixed by the perturbing frequency), the angle with the vertical can differ in a projection on the vertical plane perpendicular to the slope at the point of reflection. In (c), reflecting waves refract, instantaneously changing the horizontal propagation direction from ϕ_i to ϕ_r. θ_c denotes the critical latitude, where the bottom slope equals the wave ray inclination.

4.2.4 *Ray tracing and wave field reconstruction*

An advantage of using ray theory in a two-dimensional context is that with simple geometrical arguments, given a perturbation frequency and a container shape, one is able to deduce properties of the corresponding internal wave field, such as its regularity, the nature of its spectrum and the spatial distribution of the energy in the domain.

In two-dimensional settings, the correspondence between closed trajectories and regular solutions on the one hand, and between attracting trajectories and singular solutions on the other hand, can be exploited also when reconstructing the physical field (velocity, pressure) underlying the system in consideration. In fact, rays carry an invariant quantity, called partial pressure, that can be set on specific intervals (so-called "fundamental intervals") along the boundary, and pressure can be consequently inferred at any location of a two dimensional domain by summing the two partial pressures carried by the two rays crossing that location and coming from/going to the fundamental intervals [Maas and Lam, 1995]. With this perspective, it follows that a two-dimensional ergodic orbit (that touches all points of the domain) corresponds to the trivial, motionless solution, since it carries in all points of the domain the same value of partial pressure, thus leading to a uniform pressure everywhere.

Similar arguments are also used in the case of two-dimensional surface gravity wave and electromagnetic wave systems, where the wave field is determined in any point of the fluid domain, combining waves following rays crossing that point from any direction. For periodic orbits this is a finite sum, for chaotic orbits a continuous sum over all possible directions [Heller, 1984]. In the related field of quantum chaos such a sum over chaotic orbits is determined by Gutzwiller's trace formula [Gutzwiller, 1990].

When two-dimensional, vertically propagating internal waves in a regular domain are considered, for any given eigenfrequency ω of the system, each trajectory is closed (periodic), regardless of launching position ($\vec{x}_0$) and direction ($\phi_0 = 0, \pi$, the only two possible directions in two dimensions). It follows that each eigenfrequency presents an infinite number of geometrically closed trajectories. Considering $\omega^2 = \sin^2(2\pi/3)$ in a circular domain, four periodic trajectories (out of the corresponding infinite set) are shown in figure 4.2. Their shapes depend on the position of the reflection points, so that any point of the domain boundary is touched by one of these closed orbits. Since the partial pressure on each trajectory can be set at will, this infinite ensemble of periodic orbits indicates, as in equation (4.7), the infinite degeneracy of the eigenspectrum, characteristic of symmetric internal wave problems [Münnich, 1996], and allows calculation of the wave field at each point of the domain. It follows that in sufficiently symmetric two dimensional domains the value of ω is the only parameter controlling the existence of closed ray trajectories and, consequently, of the regularity of the associated field. We will see in section 4.3.1 that this ceases to be valid for three-dimensional settings, and other parameters will come into play.

The complete three dimensional reconstruction of the underlying physical fields, using a three-dimensional analogue of the fundamental intervals (from segments to areas?) is far beyond the scope of this work. Thus, in the following, stress will be posed on the qualitative description of the newly observed three-dimensional orbits, while further effort is certainly needed towards a rigorous reconstruction of the corresponding pressure and velocity fields from these geometrically computed trajectories.

4.3 RESULTS

4.3.1 *Preliminary comments*

In this section, results from the application of the three-dimensional ray tracing algorithm in the fluid sphere are presented.

Before doing that, it is necessary to point out one fundamental difference between two-dimensional and three-dimensional ray tracing. As seen in sec-
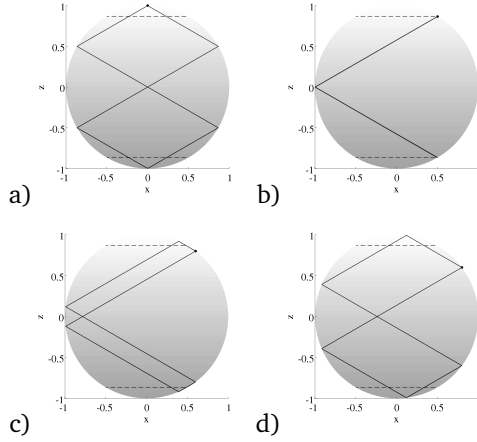
Figure 4.2: Four two-dimensional closed trajectories for $\omega^2 = \sin^2\left(\frac{2\pi}{3}\right)$ in the circle. The orbits differ in launching position x_0 (black dot): a) $x_0 = 0$, b) $x_0 = 0.5$, corresponding to the critical latitudes for this frequency, c) $x_0 = 0.6$ and d) $x_0 = 0.8$. Dashed lines mark the critical latitudes in the two hemispheres. One fundamental interval is $[x, \sqrt{1-x^2}]$, $x \in [0, x_{\theta_c}]$ [Maas and Lam, 1995], where x_{θ_c} corresponds to the radial distance from the rotation axis at the critical latitude.

tion 4.2.4, for the two-dimensional setting, when an eigenfrequency is excited, any point of the boundary can act as a source for a closed orbit. This leads to the results illustrated in figure 4.2, where ω is fixed, rays are launched in the meridional plane: $\phi_0 = 0$ or $\phi_0 = \pi$, corresponding to wave energy propagation along the ray path in one sense or the other, and $\vec{x}_0$ can vary.

By contrast, when the full three-dimensional sphere is considered, ϕ_0 can in principle assume any value in $[0, 2\pi[$, γ_0 can have both signs, and this generality is lost. In practice, of course, couples of ϕ_0 and γ_0 are considered valid only if they generate a ray lying inside the spherical domain, but this results, however, in multiple possible combinations.

In order to generate a geometrically periodic trajectory, frequency ω, position ($\vec{x}_n$), horizontal propagation direction (ϕ_n) and vertical propagating direction (γ_n) need to be known in at least one reflection point (n) along the ray path. For convenience, we will generally set such a point as the launching position ($n = 0$).

From this it is clear that the nature of three dimensional periodic trajectories is profoundly different from the known two dimensional periodic orbits. Without knowledge of the whole set of parameters ($\omega, \vec{x}_0, \phi_0, \gamma_0$), periodic trajectories are impossible to visualise geometrically. Because of this strong restriction
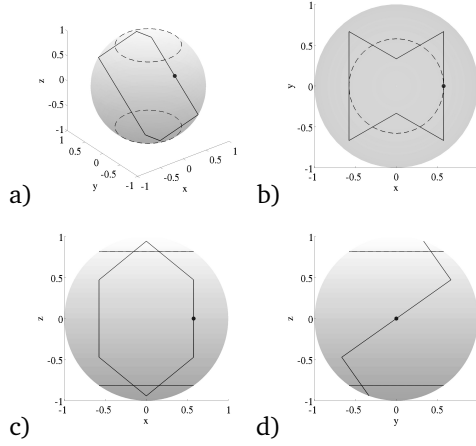
Figure 4.3: Bow-tie periodic trajectory at $\omega^2 = 2/3$: a) three-dimensional view (x, y, z), b) top view (x, y), c) side (x, z) and d) other side (y, z) view. Dashed lines correspond to critical latitudes; black dot corresponds to launching position.

it was initially believed that three dimensional periodicity was absent, even in fully symmetric three dimensional geometries, as hypothesised in Dintrans *et al.* [1999], where, however, only two-dimensional (meridional) ray tracing was contemplated.

4.3.2 *Finding one periodic orbit in the sphere*

Given the reflection laws as presented in section 4.2.3, it is possible, in principle, to estimate valid sets of parameters $(\omega, x_0, \phi_0, \gamma_0)$ representative of simple periodic trajectories in a sphere. In fact, in some simple cases, when the shape of a closed trajectory is known (or guessed), an *ad hoc* system of conditions on launching position $(\vec{x}_0)$, direction (ϕ_0, γ_0), and frequency of the perturbation (ω) can be solved analytically and all parameters can be determined at one single reflection point.

We started our search with one of the simplest possible trajectories, a "bow-tie" shaped trajectory (named after its top view appearance, figure 4.3b) and we solved the associated system (see appendix B for details), finding a three-dimensional periodic orbit in a sphere, associated to $\omega^2 = 2/3$ and displayed in figure 4.3.

Unfortunately, not all geometrically closed trajectories could be solved that easily, since the orbit shape is not known a priori, and these periodic orbits do not possess any attractive power, as we expect for a spherical geometry. How-

ever, the existence of this single periodic orbit motivated the challenging quest for more.

4.3.3 *Catalogue of periodic orbits in the sphere*

In figure 4.4 the frequencies corresponding to periodic orbits observed so far are presented. They are classified according to their geometrical properties and appearances. Whereas some of the frequencies associated to periodic orbits are known algebraically (i.e. the ones found thanks to the solution of simple algebraic systems as in appendix B or of equation (4.6)), the majority of the frequencies are known only up to numerical precision. Analogously, periodicity of the orbit has also been tested up to numerical precision, showing, however, its robustness and consistency, even when inspected in the corresponding phase space (see section 4.3.9).

Different markers in figure 4.4 correspond to different geometrical features of the orbits. A trajectory is called a "polygon trajectory" when, in the (x, y) top view it corresponds to a regular polygon (triangle, square, pentagon, hexagon, etc.), see examples in figures 4.5, 4.6 and 4.7. A trajectory is called a "star trajectory" when, in top view, it resembles a star, with its typical criss-cross pattern, see examples in figures 4.8, 4.9 and 4.22. Both polygon and star trajectories live in what could be called the "inner part" of the full sphere, that is inside the cylindrical inset determined by the northern and southern critical circles (indicated by dashed lines in the figures). By contrast, a trajectory is called "flower trajectory" when, seen from above, it presents rounded lobes (petals), as in figures 4.13, 4.14 and 4.23. These orbits live only in the "outer part" of the full sphere, defined as the part of the sphere outside the above mentioned cylinder. Periodic orbits in the higher frequency part of figure 4.4 ($\omega^2 > 1/2$) present less obvious and evocative geometrical properties, and examples are shown in figures 4.3, 4.10 and 4.11.

It is worth noting here that as the frequencies depicted in figure 4.4 are certainly not representative of all the periodic orbits existing in the sphere, it is also possible that entire other families of trajectory shapes live in the same domain, that have simply not been visualised yet, because, for example, of a counter intuitive three-dimensional behaviour.

In fact, even for simple shapes, as the triangle, the ray behaviour is complicated by the three-dimensionality of the system. Looking from above is indeed not enough to understand one orbit, and we have to move view point, from figure 4.5b to a three-dimensional view as in figure 4.5a to fully appreciate the trajectory. For many orbits, we observe that a ray needs to wind around the sphere multiple times before completing a period. Given a frequency ω, an initial launching position x_0 and an initial direction ϕ_0, γ_0, we define then the

winding number (w) of a trajectory as the total number of times that the trajectory travels around the centre before concluding a full period, defined after R reflections, when $\vec{x}_R = \vec{x}_0$, $\phi_R = \phi_0$ and $\gamma_R = \gamma_0$. Comparing figure 4.5a and 4.6a it is easy to acknowledge the difference between, respectively, an orbit characterised by $w = 1$ (the square) and one characterised by $w = 2$ (the triangle).

In figure 4.4a frequencies are plotted against the winding number; in figure 4.4b the same frequencies are plotted against the total number of reflections per period (R) over the winding number, while in figure 4.4c, they are plotted against the number of corners (for polygons, stars) or lobes (for flowers and others) over the winding number. Interestingly, looking at figure 4.4b and 4.4c, polygon and star trajectories seem to lie on certain lines, whose definition however remains obscure.

However, according to the geometrical behaviour of the trajectories it is possible to distinguish two fundamental frequency regimes: i) $\omega^2 < 1/2$, when, according to equation (4.9), the domain is compressed to an oblate spheroid; ii) $\omega^2 > 1/2$, when it is stretched to a prolate spheroid. In figure 4.4 the frequency $\omega^2 = 1/2$ is marked by a dashed line.

We shall revisit each regime in sections 4.3.4, 4.3.5. The special case when $\omega^2 = 1/2$, and the domain is thus maintained as a sphere, is presented in section 4.3.6. One geometrical behaviour is observed both for $\omega^2 < 1/2$ and for $\omega^2 > 1/2$ and is presented in section 4.3.7, whereas the great majority of the orbits, the non periodic ones, is discussed in section 4.3.8. We point out that all periodic orbits found so far in the sphere are "not isolated" [Berry, 1981], in the sense that, if one periodic orbit is given, a continuous family of new periodic orbits can be produced by revolution of the domain. Noticeably, this is true only if this revolution is performed around the stratifying direction (in this case, the z-axis). The whole family is then constituting an ensemble of infinite periodic orbits, filling however only a portion of the domain, and thus profoundly differing from the infinite set existing in two-dimensions and presented in section 4.2.4. Properties of the observed orbits in their corresponding phase space are discussed in section 4.3.9. We remind that we do not consider here frequencies of the kind $\omega = \sin(\frac{p\pi}{q})$, since they have already been extensively studied in two-dimensional (meridional) settings [Barcilon, 1968; Dintrans et al., 1999; Rieutord et al., 2001].

4.3.4   *Periodic orbits for $\omega^2 < 1/2$*

Two classes of trajectories are found in the frequency regime $\omega^2 < 1/2$: polygon and star trajectories.
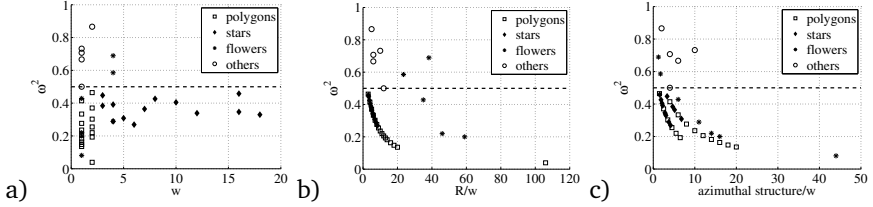
Figure 4.4: Symbols denote squared frequency - azimuthal feature corresponding to observed periodic orbits in the sphere. Different symbols indicate different shapes of the orbits, according to the legend. Names of the categories are explained in the text. In the three sub figures, the same frequencies are classified according to different aspects of their geometrical behaviour. On the x-axis, in a): the winding number, in b): total number of reflections per period (R) over the winding number, and in c): number of corners (for polygons, stars) or lobes (for flowers and others) over the winding number. The frequencies here presented do not represent the complete spectrum.

Regarding the polygon trajectories, we observe that polygons with an even number of vertices, are characterized by winding number $w = 1$ (see figure 4.6 and 4.7), while polygons with an odd number of vertices have $w = 2$ (see figure 4.5). Two examples of star trajectories are shown in figures 4.8, 4.9.

Qualitatively, all trajectories in this frequency range present extremely regular spatial patterns, from a triangle up to a 20-sided polygon, and similarly for the star shapes. Moreover, in this regime, it is clear that the critical latitudes play a crucial role in confining all trajectories to the equatorial belt of the cylinder inscribed in the spherical domain, a role that is lost in the orbits in the higher frequency range (see section 4.3.5). Exploiting the regularity of the trajectories and the prominent role played by the critical latitudes in this regime, we have been able to deduce some general rules that can be used to evaluate the parameters $(\omega, \vec{x}_0, \phi_0, \gamma_0)$ needed to find a closed orbit. These rules are listed in appendix B.1, and constitute the reason why periodic orbits of polygon or star shapes are the most numerous in figure 4.4. Following these rules it is easy to evaluate, for example, the parameters for the square trajectory (figure 4.6). If we set as launching point $P_0 = \{x_0, 0, 0\}$ (not on the boundary), as in figure 4.6b, and $\phi_0 = \pi/2$, then the following conditions for the upper right corner P_1 (in the xy-plane) follow: 1) $x_1 = x_0$; 2) $x_1^2 + y_1^2 = r_{\theta_c}^2 = 1 - \omega^2$, the point belongs to the circle corresponding to the critical latitude (see appendix B.1 for details); and 3) $z_1^2 = x_1^2$, the ray moves at $\pi/4$ with respect to the vertical. The system is then easily solved and gives $\omega^2 = \sqrt{2} - 1$.
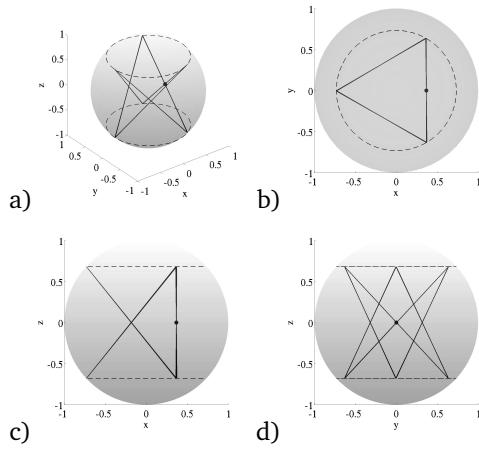
Figure 4.5: Periodic polygon trajectory (triangle) at $\omega^2 = 2\sqrt{3} - 3$, as in figure 4.3. Winding number is equal to 2.
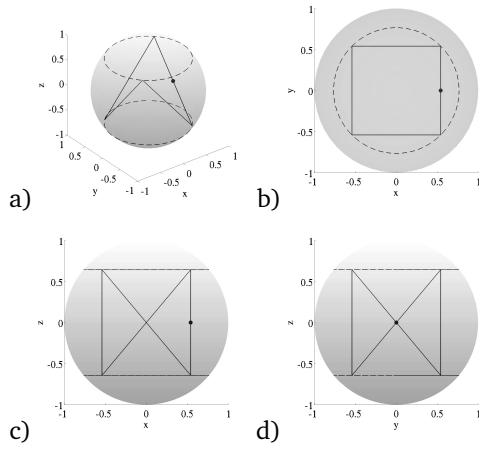

Figure 4.6: Periodic polygon trajectory (square) at $\omega^2 = \sqrt{2} - 1$, as in figure 4.3. Winding number is equal to 1.
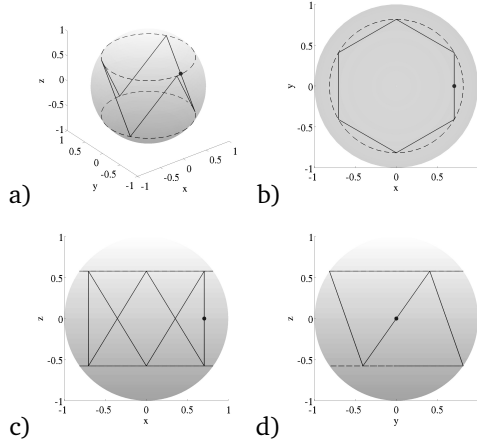
Figure 4.7: Periodic polygon trajectory (hexagon) at $\omega^2 = 1/3$, as in figure 4.3. Winding number is equal to 1.

The other frequency regimes do not present such a regularity in the trajectory patterns, thus no rules have been deduced and consequently less closed trajectories have been visualised.

From a top view, these two orbit categories closely resemble the two types of orbits present in a classical, two-dimensional ellipsoidal billiard (see section 6 of Berry [1981]), where the critical latitudes of the sphere act as the boundary of the two-dimensional elliptical domain. The apparently inconsistent fact that we observe the same pattern emerging from a perfectly circular two-dimensional projection (on the x, y-plane) of the sphere is due firstly, to the different reflection laws, and secondly to the complexity introduced here by the third dimension. More on this kind of comparisons will be discussed in section 4.3.9.

4.3.5 *Periodic orbits for $\omega^2 > 1/2$*

In the prolate case, $\omega^2 > 1/2$, the closed trajectories here presented have been evaluated analytically one by one, solving ad hoc systems of equations, in order to construct geometrically simple closed trajectories (see an example of these systems in appendix B). Examples of periodic trajectories for this regime are shown in figures 4.3, 4.10 and 4.11.

Due to their irregular patterns, no general rules have been deduced for closed trajectories in this frequency regime, and this is also why orbits in this regime are scarce and scattered (see figure 4.4). Moreover, in this case, the critical
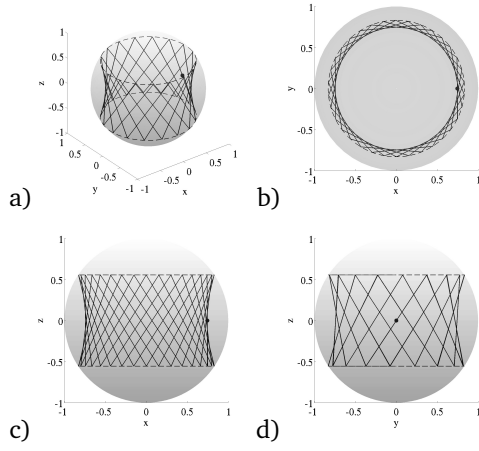
Figure 4.8: Periodic star trajectory at $\omega^2 = 0.3083$, as in figure 4.3. Winding number is equal to 5.
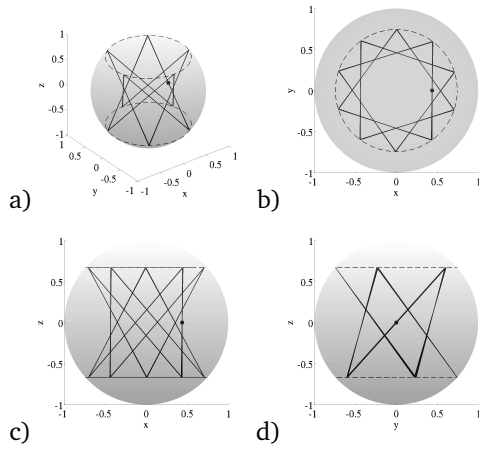

Figure 4.9: Periodic star trajectory at $\omega^2 = 0.4473$, as in figure 4.3. Winding number is equal to 3.
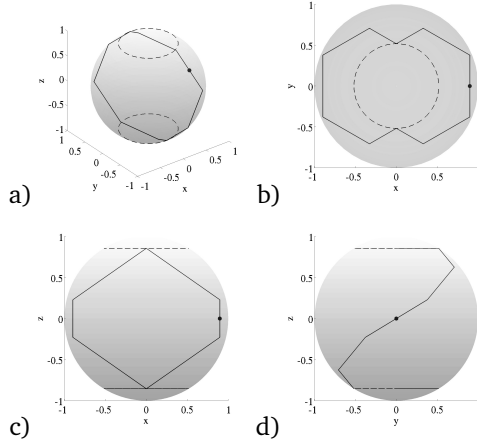
Figure 4.10: Periodic trajectory at $\omega^2 = \sqrt{3} - 1$, as in figure 4.3. Winding number is equal to 1.

circles do not seem to play such a prominent role in the trajectories, meaning that rays are not confined to the outside or to the inside of the cylindrical inset defined by the critical latitudes (see for example figure 4.3).

In contrast to the general regularity and azimuthal symmetry characterising trajectories in the oblate regime, closed trajectories in the prolate spheroid show a more asymmetrical behaviour, especially with regards to the reflection locations in the Northern and in the Southern hemisphere (see figures 4.3d, 4.10d or 4.11c). We shall come back to this aspect at the end of section 4.6.

4.3.6 *Periodic orbit for $\omega^2 = 1/2$*

A regular, three-dimensional periodic orbit is found at $\omega^2 = 1/2$, corresponding to the case when rays have a genuine inclination of 45° with respect to the vertical, and the domain is therefore unstretched by equation (4.9). The trajectory is shown in figure 4.12. Remarkably, the critical latitudes are not part of this orbit, nor constitute a spatial barrier for the ray, rendering this orbit similar in features to the ones presented for $\omega^2 > 1/2$ in section 4.3.5.

Interestingly, the existence of a frequency value that separates two frequency regimes (and consequently, two different orbit dynamics) resembles the role of the parameter δ in Berry [1981]. The latter was used for the parametric defini-

Figure 4.11: Periodic trajectory at $\omega^2 = 0.8660$, as in figure 4.3. Winding number is equal to 2.

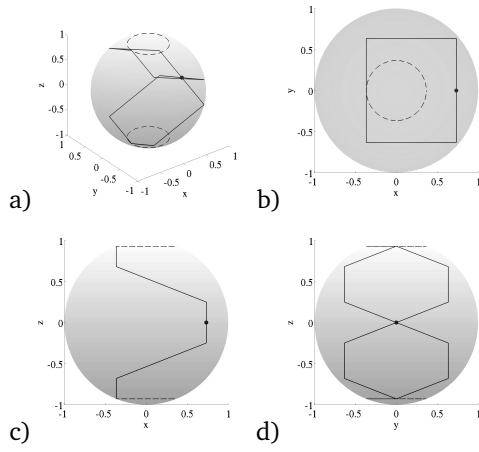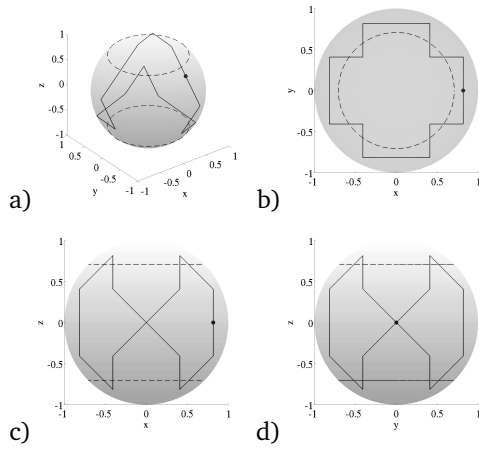Figure 4.12: Closed trajectory at $\omega^2 = 1/2$, as in figure 4.3. Winding number is equal to 1.

tion of the external boundary of the Snellian oval billiard, and also determines two different regimes for periodic orbits in that setting.

4.3.7 *Periodic orbits for $\omega^2 \lessgtr 1/2$*

Only one family of trajectories is found both when $\omega^2 < 1/2$ and $\omega^2 > 1/2$: the "flower" trajectory (examples in figures 4.13 and 4.14). Even for this type of trajectory, no general laws have been deduced, although in this case, in parallel to the case of $\omega^2 < 1/2$, the critical latitudes are observed to constitute a spatial barrier for the orbit, confining in this case the rays to the "outer" part of the sphere, and to the equatorial belt.

Remarkably, all frequencies corresponding to flower trajectories, both with winding number $w = 1$ (in the frequency regime $\omega^2 < 1/2$) or $w > 1$ (in the frequency regime $\omega^2 > 1/2$), are also obtained as solutions of an eigenvalue problem of the kind (4.6) with $k = 0$ (axisymmetric modes) and $n \in \mathbb{N}$ (Bryan modes). In figure 4.13, for example, we are looking at the Bryan mode $\{4, 1, 0\}$, where $\omega^2 = 3/7$, a frequency that is of particular interest because, as seen in section 4.2.2, it has been identified as the least-damped axisymmetric inertial mode in the full sphere [Dintrans *et al.*, 1999; Rieutord *et al.*, 2001]. This trajectory has winding number equal to 1.

In figure 4.14, the Bryan mode $\{6, 1, 0\}$, $\omega^2 = \frac{1}{33}(15 + 2\sqrt{15}) \approx 0.6892$ is presented, selected from the possible eigenfrequencies:

$$\omega_{6,1-4,0} = \pm\sqrt{\frac{1}{33}(15 \pm 2\sqrt{15})}. \tag{4.11}$$

This trajectory has winding number equal to 4, differently from what it appears looking at figure 4.14b, that misleads the reader superposing points that belong to different hemispheres (see figure 4.14a).

4.3.8 *Non periodic orbits*

So far we have presented only periodic orbits of inertial wave ray trajectories in the full sphere. However, the great majority of combinations of $\omega, \vec{x}_0, \phi_0, \gamma_0$ leads to non periodic orbits. In fact, initial conditions for each ray can be taken from two cubes, spanning $\omega \in [0, 1]$, $\vec{x}_0 \in [0, 1]$ and $\phi_0 \in [0, 2\pi]$ with either $\gamma_0 = 1$ or $\gamma_0 = -1$, and periodic orbits are observed to have a measure zero inside these two cubes. As already mentioned in section 4.3.4, periodic trajectories so far have been found only because somehow showing regular behaviour, an example of which is explained in appendix B.1 for the lower part of the fre-
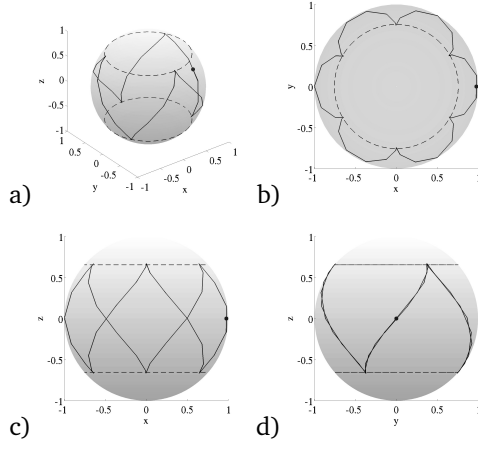
Figure 4.13: Periodic flower trajectory at $\omega^2 = 3/7 \approx 0.4286$, as in figure 4.3. Winding number is equal to 1.
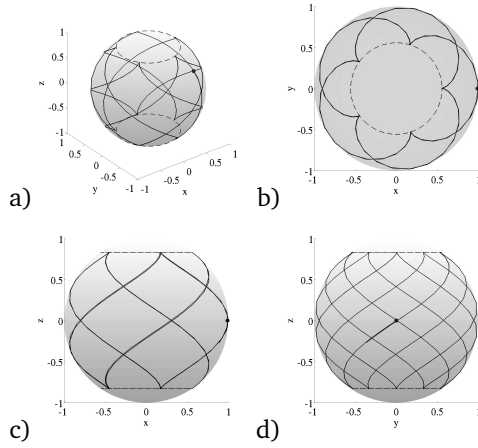

Figure 4.14: Periodic flower trajectory at $\omega^2 = \frac{1}{33}(15 + 2\sqrt{15}) \approx 0.6892$, as in figure 4.3. Winding number is equal to 4.

quency spectrum, while a random search would not lead to the visualization of any closed trajectory.

Moreover, the periodic orbits found so far seem to act as repellors (and thus provide a big contrast to the two-dimensional attractors found in Maas and Lam [1995] and to the three-dimensional attractors found in the spherical shell in chapter 3, which is why the search has been so challenging. It seems that the sphere exhibits some of the properties characteristic of quantum chaos encountered in elliptic systems, in which repelling periodic orbits dominate the response. We shall come back to this aspect in sections 4.3.9 and 4.4.

Interestingly, chaotic and fully ergodic orbits are not found in the sphere. Even if chaos and ergodicity can not be proved numerically, and a behaviour of this type is suggested by orbits as the one presented in figure 4.15, when the orbit is inspected in the corresponding parameter space [Berry, 1981; Nöckel, 1997] it becomes clear that a certain regularity persists, preventing the occurrence of chaotic areas (see section 4.3.9). With ergodic orbits we mean orbits that fill the sphere homogeneously, and, after an infinite number of reflections, touch each point of the domain an infinite amount of times (approaching it from all possible directions on the cone through that point). It follows that ergodic trajectories, as the ones present in the case of two-dimensional internal wave rays in the circle, are domain filling, and this is not true for orbits like the one in figure 4.15 nor for others.

The non periodic orbits observed in the sphere are, on the other hand, of the so-called 'invariant' type (see section 4.3.9). Invariant orbits are trajectories that, even if not periodic, are confined to a portion of the domain only, which is usually the equatorial belt (defined between the two critical latitudes), and are continuously repeating themselves and circulating around the domain. An example of these trajectories is given in figure 4.16. In this case the rays, given an infinite amount of reflections, will densely touch only a subset of points of the full domain. Given a periodic orbit, invariant orbits are easily found by slightly perturbing the frequency, launching point or initial direction. It follows that, for frequencies corresponding to a periodic orbit (as in figure 4.13), an associated invariant orbit (figure 4.16) can be obtained by small alteration of x_0 and it fills the same surface that rays would fill in case of axisymmetric forcing at that frequency. This surface corresponds in fact to the subset of boundary points touched by simultaneous excitation (azimuthally symmetric) of the whole ensemble of non isolated periodic orbits for that specific frequency (see section 4.6 for application to experimental results).

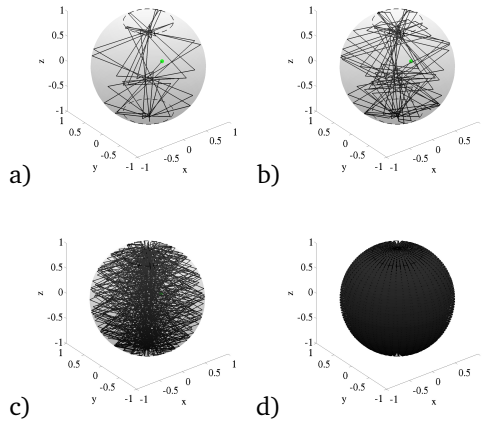Figure 4.15: Three-dimensional view of invariant trajectory at $\omega^2 = 0.8100$ after a) 50, b) 100, c) 500 and d) 5000 reflections.
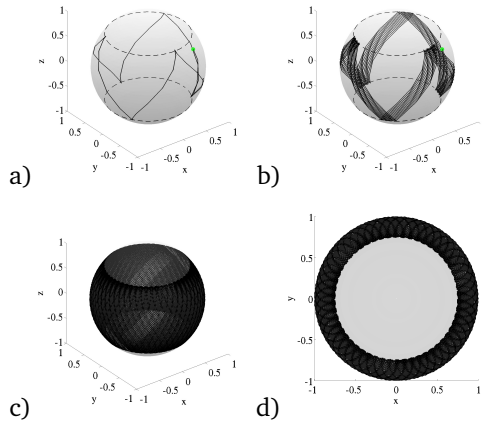

Figure 4.16: Three-dimensional view of invariant trajectory at $\omega^2 = 3/7$ after a) 50, b) 500, c) 5000 reflections and d) top view after 5000 reflections. This figure is obtained using the same parameters of figure 4.13, but slightly changing the launching position x_0.

4.3.9 *Phase space mapping of the orbits*

So far we have been looking at ray trajectories in real space, however, an alternative representation in the corresponding phase space is also possible, instructive and already used for studying two-dimensional ray dynamics of different nature in closed cavities [Berry, 1981, 1987; Nöckel, 1997].

In fact, successive reflections can be captured not only by direct ray tracing, as in the previous sections, but also by monitoring the polar angle (χ) at subsequent reflection points as measured from the domain's centre. Combining this polar angle χ at the reflection point with the angle of incidence of the ray relative to the local x-axis (ϕ_i, see figure 4.1c) presents a phase space, in which ray dynamics can be conveniently studied [Nöckel *et al.*, 1996].

In this work, even if tracing three-dimensional trajectories, only a two-dimensional projection of the orbit - on the x, y-plane - has been considered, the so-called Poincaré surface of section [SOS, Nöckel, 1997]. This is motivated by the fact that the third parameter defining each reflection, the inclination with respect to the vertical, is here fixed by the inertial wave dispersion relationship (equation (4.8)). The neglect of the three-dimensional representation of the reflection position certainly constitutes a limit to the understanding of these orbits' behaviour, however, we shall present in the following the application of classic SOS to the three-dimensional inertial wave ray trajectories presented in the previous sections, while a definition of a new, three-dimensional phase space, perhaps more appropriate, is left for future work.

In classical mechanics, in phase space (SOS), a periodic orbit appears as a set of isolated points. This is true for two-dimensional as well as for three-dimensional periodic trajectories of internal wave rays. Examples of this phase space in the sphere are shown in figure 4.17a for the oblate case (corresponding to the real space trajectory in figure 4.7) and in figure 4.17b for the prolate case (corresponding to the real space trajectory in figure 4.12); remarkably, all three-dimensional periodic orbits found in the sphere are unstable, and thus referred to as repellors (as opposed to attractors). This means that a small perturbation to the initial conditions is sufficient to infinitely deviate the orbit from the periodic path. As seen at the end of section 4.3.8, this behaviour is characterizing the majority of the inertial wave orbits in the sphere. Examples of this behaviour are shown in figures 4.18 and 4.19, but similar plots (not shown) would be also representative of orbits like the ones displayed in figures 4.15 and 4.16. This kind of trajectories is characterized, in the corresponding phase space, by the existence of a structure (although highly non-trivial) to which the orbit is confined, and which is therefore called "invariant". If looking at SOS of two-dimensional surface gravity wave rays in the circle, these structures are simple straight line (see figure 3d in Berry [1981]): in the sphere the regularity of the two-dimensional circular case is probably destroyed by the presence of
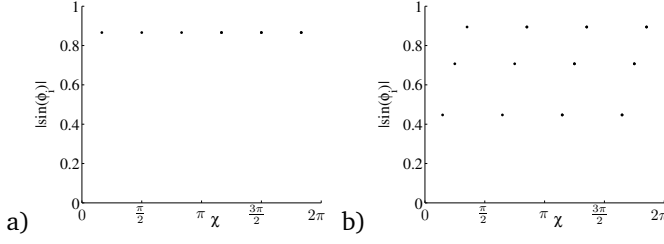
Figure 4.17: a) Poincaré surface of section (SOS) for the polygonal periodic orbits in figure 4.7. b) SOS for the high frequency periodic orbits in figure 4.12. χ corresponds to the polar angle pointing at subsequent reflection positions as measured from the domain's centre. ϕ_i corresponds to the local angle of incidence of the ray as measured from the local x-axis (see figure 4.1c).

three dimensional subsequent (and compensating) focusing and defocusing reflections in a three-dimensional domain, leading to the high level of complexity in figures 4.18b and 4.19b.

It is possible, however, to obtain simpler structures. The trajectory in figure 4.20a is obtained from the real space orbit in figure 4.12, when the launching position is moved to the critical latitude. It shows a relatively simple representation in the phase space (figure 4.20b), although its real space azimuthal symmetry properties (figure 4.20a) appear to be exceptional when compared to the most common structures, similar to the ones in figure 4.18a and 4.19a.

Remarkably, this kind of pattern in phase space resembles the one characterizing two-dimensional ergodic internal wave orbits, propagating obliquely in the vertical plane in a circle, as shown in figure 4.21b. However, even if phase space structures are similar in the two cases, in the real space three-dimensional invariant orbits (figure 4.20a) profoundly differ from two-dimensional ergodic orbits (figure 4.21a). In particular, the latter are by definition domain filling, while invariant trajectories are clearly limited to a portion of the three-dimensional domain only. This hybrid aspect of the trajectories would probably become clear once studied in an ad-hoc defined phase space, taking into consideration the full three dimensional problem.

The third possible type of orbit, the chaotic orbit, would occupy an area in the phase space. Chaotic trajectories are present in two-dimensional elliptical systems in non regular domains, like the stadium [Berry, 1981], and are likely to be found in three-dimensional hyperbolic systems in symmetry breaking domains as well. On the other hand, as expected from the overall regularity of
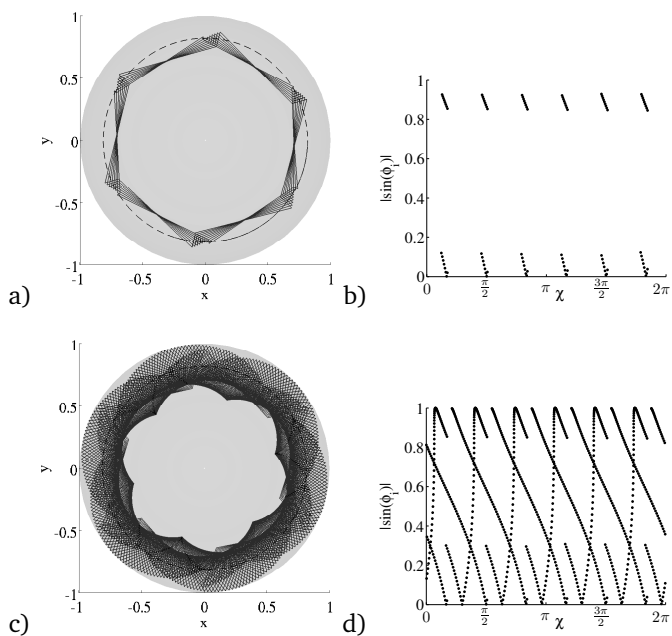
Figure 4.18: a) Top view of invariant trajectory (100 reflections) obtained from the trajectory in figure 4.7 after perturbing the horizontal launching direction by 0.5%. b) SOS for the trajectory in a). c) same as a), after 1000 reflections. d) SOS for the trajectory in c).
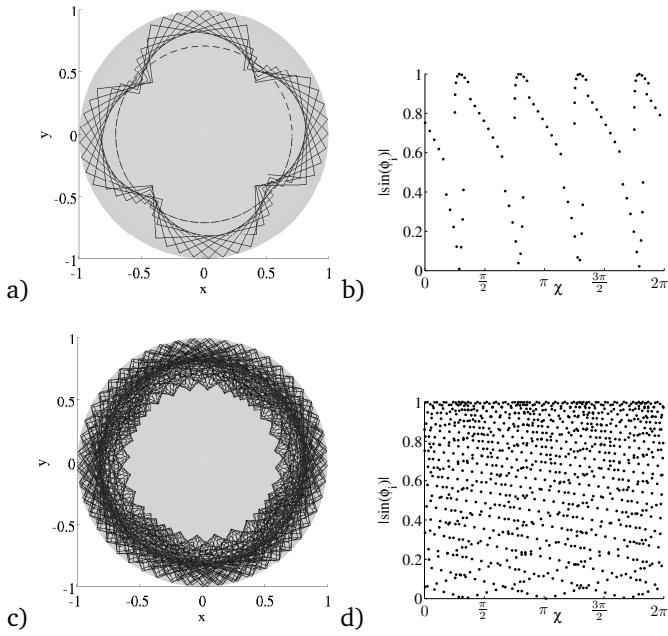
Figure 4.19: a) Top view of invariant trajectory (100 reflections) obtained from the trajectory in figure 4.12 after perturbing the launching position by 0.5%. b) SOS for the trajectory in a). c) same as a), after 1000 reflections. d) SOS for the trajectory in c)
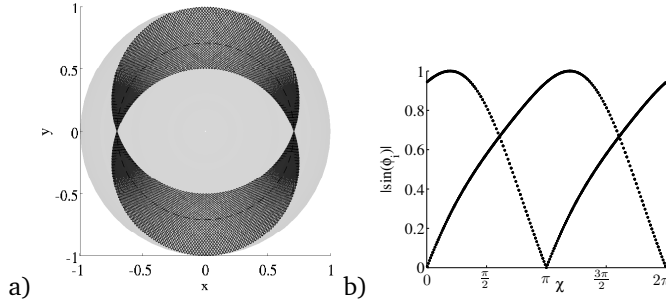
Figure 4.20: a) Top view of invariant trajectory (100 reflections) obtained from the trajectory in figure 4.12 after setting the launching position at the critical latitude. b) SOS for the trajectory in a).

the system in analysis, no genuinely chaotic orbit is observed in the case of three-dimensional inertial waves in the full sphere.

4.4 DISCUSSION

In this work, we have established the existence of three-dimensional periodic orbits for internal wave rays in the full sphere. However, several questions remain on the nature of these orbits, of the associated frequencies and of the underlying wave field.

In the last decades, two-dimensional (meridional) ray tracing has been used to investigate the inviscid limit case of inertial waves in the sphere and its known analytical solutions [Dintrans *et al.*, 1999; Rieutord *et al.*, 2001]. In this setting the association between periodic orbits and eigenfrequencies has not been retrieved, for reasons that we now understand. After all, looking at ray tracing only on a meridional plane constitutes a strong limitation if one is interested in the behaviour of inertial modes of the full three-dimensional sphere. In fact, in a spherical domain, if a perturbation is excited within a meridional plane, even when three dimensional effects are included, it will never escape its original plane. Conversely, if a perturbation is initiated outside a meridional plane, its spatial structure will never collapse onto a meridional plane. But note that this behaviour is strictly representative of that in a regular domain as the sphere, and it is not valid, for example, in a spherical shell, where the interaction of the ray trajectory with the outer and inner sphere gives rise to meridional attracting planes (see chapter 3).
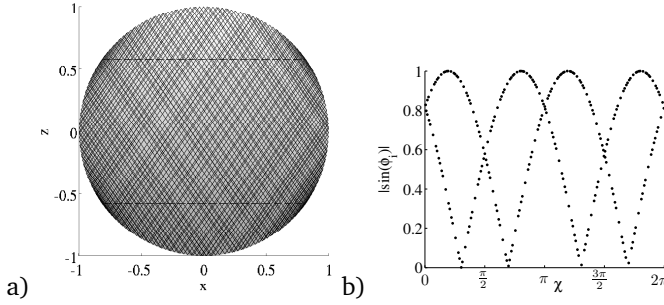
Figure 4.21: a) Ergodic trajectory (250 reflections) in the circle corresponding to the frequency $\omega = \sqrt{1/3}$ (not an eigenvalue). b) SOS for the trajectory in a), here the angle χ refers to the polar angle in the x,z-plane, and ϕ_i to the local angle of incidence relative to the outward radial direction at the point of reflection.

Among all possible zonally propagating waves, existing also in the three-dimensional fluid shell (see chapter 3) and in the parabolic channel [Drijfhout and Maas, 2007], the presence of periodic trajectories in the full sphere is suggestive of the resonant character of inertial modes in a regular domain, where the term 'resonance' has here not been used in terms of amplitude of the response (see Zhang *et al.* [2013] for a detailed, multi-approach analysis on this subject), but in terms of trajectory coherency.

However, a direct correspondence between closed orbits and classical Bryan's modes is hardly retrieved (so far, only for the flower trajectories, described in section 4.3.7). Moreover, the spatial structure of the orbits has been also suggestive of the existence of a relation between the azimuthal wave number (when known) and one of the orbit features (winding number, number of reflections, lobes, or corners). Even this correspondence has not yet been retrieved.

One other - perhaps unexpected - aspect of these three-dimensional periodic orbits is encountered if one is interested in the reconstruction of the underlying physical wave field using the ray's structure. In fact, the observed winding numbers of many trajectories present values larger than one, which is on the one hand puzzling, but on the other hand suggestive of the possibility of adopting non integer (azimuthal) wave numbers. We speculate that a pressure function of the separable form (4.5) with *rational* wave numbers n and k would also constitute a set of valid solutions for inertial waves in a full sphere, provided that boundary conditions are satisfied (no energy flux through the boundaries, and finiteness in the whole domain, rotation axis and equatorial plane included).

Three-dimensional ray orbits could thus be not only possibly representative of non separable, zonally propagating solutions, but also of eigenmodes differ-

ent from the ones classically obtained from equation (4.6) using integer degree and order, whose completeness is so far unknown. This would explain the difficulty in relating the periodic orbit with the classic eigenfrequencies of the system.

Furthermore, it is worth noting that in the two-dimensional fluid dynamics case, spatially coherent internal wave beams and trajectories become evident only as a result of the superposition of several modes associated to a single frequency. Because of the lack of correspondence between rays and eigenfrequencies, and of the complexity of the inversion of equation (4.6), a rigorous test in this direction could not been performed.

Matching of rays and modes, as also previously pointed out in section 4.2.2, is also usually expected only in the case of short wavelength limit, and not in the case of large scale modes. For the higher modes, in fact, the scales of the underlying waves is much smaller than the basin size. Since inertial waves of given frequency have no definite scale, short waves have here to be intended not as, for example, in the quantum chaos case, modes within a certain frequency range, but as modes characterised by large n and k indexes (including those of the Legendre functions having non-integer indices n and k), for which it is possible to make good use of asymptotic expansions of the associated Legendre functions. Again, the lack of understanding of the relation between n and k and spatial trajectories has prevented to focus on valid comparison - for high indices Legendre modes - only.

Interestingly, repelling and unstable periodic orbits such as the ones observed in this study, profoundly differ both from the plane-filling ensemble of periodic orbits characterising regular, hyperbolic systems, as described in section 4.2.4 (see figure 4.2), and from the classical annulus-filling non-isolated periodic orbits in the circular billiard (elliptic system).

In fact, even if the closed orbits in the sphere are non isolated under rotation around the z-axis, they remain isolated in a three-dimensional sense, because of the strong interdependency between the parameters $(\omega, \vec{x}_0, \phi_0, \gamma_0)$.

In this sense, they resemble more the isolated, unstable ray trajectories found in elliptic, classically chaotic systems, as those describing surface waves in a stadium [Berry, 1981, 1987; Kudrolli *et al.*, 2001]. If we may continue the analogy, it follows that, even if in three-dimensions we have no one-to-one correspondence between classic orbits and 'quantum' levels of the system (eigenfrequencies), we can still use the behaviour of the rays as an ingredient for deriving general information on the spectrum and on the regularity properties of a system. This would also help in explaining why only few periodic orbits found their counterpart in terms of Bryan [1889]'s modes. Moreover, when inspected in the corresponding phase space, three-dimensional invariant orbits show a similar behaviour to the ones of two-dimensional ergodic orbits, although without the crucial characteristics of being domain filling. This combination of different

behaviours could be the result of tracing trajectories in a highly anisotropic three-dimensional space, whose anisotropy is set by the presence of the rotation axis (aligned in this case with the vertical). Focusing and defocusing in the vertical direction coexist then with spreading and scarring in the horizontal plane (perpendicular to the stratification/rotation), also because focusing reflections in the vertical plane lead to a change in cross-slope momentum, while not affecting the momentum in the along-slope, tangential direction.

In addition, we have seen from equation (4.2) that for general (non-symmetric) three-dimensional domain shapes, the system acquires a hybrid character, in between hyperbolic and elliptic problems. Consequently, it may well show asymptotically both periodic attracting orbits, as in the spherical shell (chapter 3), as well as periodic repelling orbits, as the ones here observed in the sphere, characteristic respectively of singular and regular wave fields. It is also worth noting that such repelling periodic orbits are living in the spherical shell too, provided that rays do not interact with the inner boundary, and that thus attractors, periodic and invariant modes could in principle coexist in the same three-dimensional domain: in fact Maas [2005]; Drijfhout and Maas [2007] as well as chapter 3 have already shown that attractors and invariant modes (there also called 'edge' or 'whispering gallery' modes), can indeed occur simultaneously in a stratified paraboloid, channel and spherical shell (all symmetry breaking geometries). In terms of energy content, however, attracting orbits will always prevail over periodic orbits in symmetry breaking geometries, because of the formers' focusing power.

Despite the possible presence of all these different orbits, we are still far from formalising a field reconstruction on the basis of ray trajectories only. In fact, it is clear that even if an annulus-filling ensemble of periodic orbits exists at a specified ω, this does not constitute the three-dimensional counterpart of the domain-filling infinite ensemble of periodic trajectories that occurs in two-dimensions in regular domains for each eigenfrequency (see section 4.2.4 and figure 4.2). The infinite three-dimensional periodic orbits are all identical, and summed up they do not cover the whole basin. This implies that evaluating the associated field in the whole domain from rays only remains a non trivial (if not impossible) challenge.

However, we did find an example of one frequency (although numerical) presenting two differently shaped closed trajectories (figures 4.22 and 4.23). It is therefore possible, in principle, that an infinite set of differently shaped periodic orbits exists for each eigenfrequency, mirroring a degeneracy of the associated spectrum. Only if this is true it would be possible to reconstruct the underlying wave field using a two-dimensional generalization of the one-dimensional
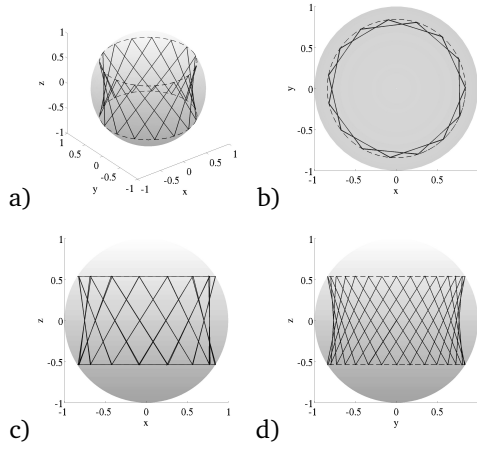
Figure 4.22: Periodic star trajectory at $\omega^2 = 0.2890$, as in figure 4.3. Winding number is equal to 4.
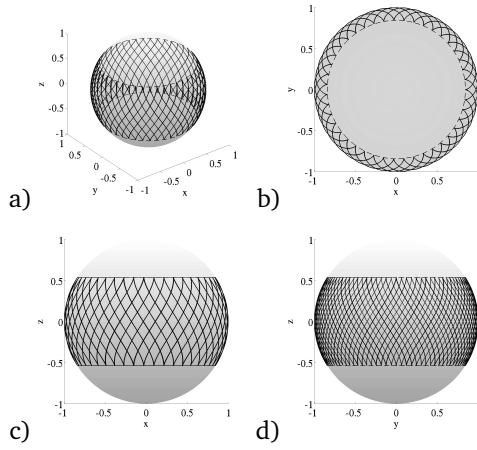

Figure 4.23: Periodic flower trajectory at $\omega^2 = 0.2890$, as in figure 4.3. Winding number is equal to 4.

fundamental intervals arising in the two-dimensional problems [Maas and Lam, 1995].

It has to be clear, in fact, that our limited understanding on how to determine valid parameters ω, $\vec{x}_0$, ϕ_0 and γ_0, necessary to visualise the ray pattern, restricts our ability to geometrically check and visualise periodicity, but it does not reduce the number of physically valid eigenvalues of the system and, with this, the number and degeneracy of the modes in the system.

4.5 SUMMARY

Understanding the behaviour of internal waves in fully enclosed domains constitutes one of the big challenges in fluid dynamics, especially because of the numerous possible applications both in astrophysical and geophysical fluid dynamics. Since analytical solutions for internal waves in arbitrarily shaped domains are not available, numerical approaches or geometrical ray tracing techniques have been widely used in order to infer properties of the underlying wave field and energy distribution in the container. Ray tracing, commonly used in two-dimensional settings, has recently been extended as a three-dimensional tool, in the direction of a more realistic representation of the corresponding wave field and of the source of perturbation. However, the significance of three-dimensional internal wave rays has not been completely understood.

In this work, a three dimensional algorithm of ray tracing has been applied for the first time to the full homogeneous rotating sphere, in order to investigate the nature of three-dimensional inertial wave ray orbits. The sphere in fact is one of the few domains where analytical solutions are known for the linear, inviscid case, and where WKBJ theory has also been commonly applied.

Three-dimensional periodic orbits have been then observed in the sphere. Moreover, two main frequency regimes can be distinguished, according to the different behaviour of the orbits: $\omega^2 < 1/2$ and $\omega^2 > 1/2$.

In the low frequency regime, three "families" of periodic orbits are found: polygon, star and flower trajectories, classified because of their appearance in top view. In this regime, the critical circles define an inscribed cylinder that acts as a physical barrier for the orbits, confining the rays to the equatorial belt. This crucial role played in the ray dynamics by the critical latitudes finds its counterpart in the model proposed by Wu [2005a], where the critical circles are named "singularity belts" and right so.

In the high frequency regime, no regular pattern but of flower type is observed. However, periodic orbits are still present, even if critical circles do not play such a prominent role.

Difficulties in relating the observed periodic trajectories to the simplest eigenfrequencies computed using equation (4.6) (the Bryan modes) could be due to

several reasons, discussed in section 4.4. Perhaps the most intriguing one is the fact that when a three-dimensional ray tracing algorithm is used, the absence of any assumption on separability of the solutions could unveil the structure of intrinsically three-dimensional modes in the sphere, which remained hidden so far because of the particular form of solutions (equation (4.5)), and because of the requirement for the n and k indices to be integer. This perspective certainly requires further investigation.

We are led to think, that the periodic orbits observed so far have been limited by our poor understanding of the geometrical properties of these trajectories, and by the human tendency to prefer regular and repetitive patterns such as, indeed, polygons, stars, and flower shapes. We also know that the inertial wave spectrum in the sphere is dense [Bryan, 1889], therefore a complete catalogue of existing periodic orbits would be of no practical use. In this work only the first proof of the existence of such trajectories is given: further investigations would contribute to a more general perspective on the geometrical features of these trajectories, and to a complete understanding of plots like the ones in figure 4.4 and of the emerging patterns.

Nevertheless, enough and differently shaped closed patterns have been found to deduce some general properties on the periodicity of the orbits and the observation of other trajectories would not change the overall picture of the system. The existence, in fact, of inertial wave, periodic orbits in a regular three-dimensional container such as the sphere allows to extend the usual two-dimensional correspondence between modes and periodic ray trajectories, previously discarded [Dintrans *et al.*, 1999], to a three-dimensional setting.

Moreover, the presence of repelling periodic orbits, such as the ones here observed, and of invariant orbits presenting ergodic aspects, points out the interesting fact that the three-dimensional hyperbolic problem of inertial waves in the homogeneous full sphere presents, in terms of quantum chaology [Berry, 1987], some properties typical of elliptic systems. The three-dimensional orbits found so far in the sphere seem to be only of the periodic and of the invariant kind. However, the existence of two different orbit regimes (as in the oval billiard [Berry, 1981]), and of isolated orbits (isolated with respect to rotation around an axis different from the z-axis), are suggestive of a more heterogeneous dynamics. A three-dimensional phase space study will possibly provide further insight in the hybrid nature of these trajectories.

4.6 FINAL REMARKS

We are conscious that geometrical patterns constitute a widely general and fascinating feature of several fluid dynamical systems, including geophysical [Lewis and Hawkins, 1982] and astrophysical [Godfrey, 1988] contexts. It is

therefore worth pointing at the immediate association that arises between the closed hexagonal trajectory in figure 4.7 (corresponding to an exact frequency $\omega^2 = 1/3$), and the famous hexagonal vortex observed over Saturn's North Pole [Godfrey, 1988]. Experimental results in a differentially rotating spherical gap [Hollerbach *et al.*, 2004], as well as in cylindrical systems [Barbosa Aguiar *et al.*, 2010], have shown that polygonal patterns may arise from destabilization of a zonal jet, in the case of meandering of the Stewartson layers that form tangent to the inner boundary, a situation that substantially differs from the configuration object of the present study. To the authors' knowledge, no polygonal pattern has been experimentally observed in a full sphere so far. However, this evidence does not tell much about the possible existence of resonant periodic orbits in the full sphere for axisymmetric forcing mechanisms like, for example, libration. In this context, in fact, a single periodic orbit as the ones presented in this study can not be visualised, since it implies not only a point source of the disturbance, namely, a single launching position $\vec{x}_0$, but also the selection of a single ray (identified by ϕ_0 and γ_0) within the excited double cone. In practice, this would need an oscillating source, setting the frequency of the radiating perturbation. The selection of a single ray (in two dimensions), or at least of a portion of one of the two cones (in three dimensions), could be then achieved putting the forcing oscillator in one basin (basin 1) that is different from the container in analysis (basin 2), and orienting an aperture between the two basins such that only one single beam, or a portion of one of the cones, is able to propagate from basin 1 to basin 2. In the case of axisymmetric forcing (given by an azimuthal revolution of the launching position), rays will on the other hand occupy a surface, given by the azimuthal revolution of the corresponding periodic trajectory, resembling the corresponding invariant orbits, see figure 4.16. In this regard, the prominent role played by the critical latitudes in the ray trajectories is in agreement not only with the three-dimensional numerical simulations as the ones in Wu [2005a], but also with some laboratory experiments in rotating sphere and shell, such as those by Noir *et al.* [2001]; Le Bars *et al.* [2007] and Koch *et al.* [2013].

Another possible association between previous findings and the newly observed periodic trajectories arises when we look at their symmetry properties. As we have already noticed at the end of sections 4.3.4 and 4.3.5, the geometrical patterns of periodic trajectories of the rays show a strong difference in the two frequency regimes. The low frequency case ($\omega^2 < 1/2$) shows a strong regularity in the azimuthal and in the vertical direction, while this is not true for the high frequency case ($\omega^2 > 1/2$). We remind that when we use the variable transformation (4.9), and we do not re-stretch back our domain, this results in a deformation of the spherical domain into an oblate or a prolate spheroid respectively, according to the frequency explored, while the ray inclination is fixed to 45°with respect to the vertical. This observation recalls some old, and

so far not completely explained, experimental results from the end of the XIX century [Lord Kelvin, 1877, 1880a], when Lord Kelvin and assistants performed a series of experiments to investigate gyroscopic properties of respectively a rotating oblate and prolate spheroidal domain filled with liquid. While the oblate container behaved not noticeably different from the ordinary solid gyrostat, the prolate spheroid presented a "truly wonderful contrast" as its failure as a gyrostat resulted in the prolate container stopping turning only after a few seconds after its release.

A possible interpretation of the different response between the two geometrical settings comes from the different symmetry properties and ray distributions observed in the three-dimensional periodic orbits found in this study. It is not obvious whether, in general, analysing a frequency in differently shaped containers (Kelvin's approach) or, instead, fixing the inclination of the rays and consequently deforming the container (ray tracing approach) would lead to the same physical system or not, but, if we consider as key parameters only the relative inclinations between 1) the restoring force, in this case rotation, and 2) the ray trajectory, and 3) the local tangent to the boundary at the reflection point, the two approaches appear at a first view to be completely equivalent. If this is the case, a non axisymmetric forcing at the surface of the prolate (oblate) ellipsoid would result in a non axisymmetric (axisymmetric) response of the domain, with (without) consequent triggering of instabilities and possibly of a net torque on the container. Further experimental investigations would certainly provide new light on these historic findings.

Discussing robustness of three-dimensional inertial wave ray tracing in the case of a homogeneous, rotating fluid-filled sphere may seem far from any possible application of practical use, however, inertial waves in the sphere constitute a paradigmatic case for the more general case of internal waves in arbitrarily shaped, fully enclosed domains. Extending our general understanding on wave ray dynamics can thus be crucial towards more realistic, three-dimensional, internal wave field reconstructions and regularity (or, more commonly, singularity) analysis, as called for by many geophysical and astrophysical challenges.

5

OBSERVATIONAL STUDY OF THE "EQUATORIAL BOUNDARY LAYER" IN THE WESTERN ATLANTIC OCEAN

The complexity of the equatorial circulation was brought to light by deep velocity profiles made in the three oceans [Cromwell, 1953; Cromwell *et al.*, 1954; Firing, 1987; Ponte and Luyten, 1989; Weisberg and Horigan, 1981; Reppin *et al.*, 1999; Gouriou *et al.*, 2001; Send *et al.*, 2002; Dengler and Quadfasel, 2002]. This revealed current patterns common among the three basins, that contrast with mid-latitude patterns. Despite seasonal changes, mainly due to the moving intertropical convergence zone in the atmosphere [Stramma and Schott, 1999; Dijkstra and Burgers, 2002], current measurements at the equator show a permanent, strong anisotropy between the horizontal current components. Variability in the zonal current component is dominated by semiannual, annual, and interannual signals, while the meridional velocity component varies much faster, and over much shorter vertical scales in all three Oceans [O'Neill, 1984; Reppin *et al.*, 1999; Dengler and Quadfasel, 2002; Bunge *et al.*, 2007; Dengler and Quadfasel, 2002].

Interannual to annual zonal variability is generally associated with the so called equatorial deep jets (EDJs) [Bunge *et al.*, 2008]. EDJs are strong zonal currents (typical velocities are about 0.2 m/s) with alternating direction, confined to a narrow equatorial band (approximately between latitudes ±1.5°) and to depths between the thermocline (about 100 m) and 2500 m [Firing, 1987; Gouriou *et al.*, 1999; Dengler and Quadfasel, 2002; Bourlès *et al.*, 2003], or bottom [Brandt *et al.*, 2011]. These currents are conventionally referred to as jets, although a time variability is usually associated to their magnitude and direction.

To date, the mechanisms for their formation and maintenance are still not completely understood, but they seem to be representative of low-latitude dynamics, given their presence in the three Oceans, and also, given the presence of similarly stacked jets in the equatorial regions of the Earth atmosphere as well as in the atmosphere of rotating planets or stars [Galperin, 2004].

It has been speculated [Send *et al.*, 2002] that, while the strong and coherent zonal currents are the most evident (and measurable) property of the equatorial dynamics, their interaction with meridionally propagating waves and meridional currents would actually be the most dynamically important factor, not only in terms of generation, propagation, maintenance and dissipation mechanisms of the zonal jets themselves, but also in terms of cross-equatorial transport.

So far, differences in behaviour between the two horizontal components of the current have been usually interpreted as due to the presence of trapped equatorial planetary waves (Kelvin, Rossby and Yanai waves) which are the only wave solutions presenting small or vanishing meridional currents on the equator [Matsuno, 1966]. However, all theories involving equatorial planetary

waves alone, or their combination [Eriksen, 1981, 1982a; Hua *et al.*, 1997; Muench and Kunze, 1994, 1999, 2000; Hua *et al.*, 2008; Fruman *et al.*, 2009; Ascani *et al.*, 2010], have failed to capture the observed strength, time and spatial scales of the equatorial current system.

Focusing onto the intermediate to deep dynamics, the equatorial internal wave field with its intrinsically three-dimensional spatial structure, could, in principle, play a crucial role in the intertwining of the three components of the velocity field in the low-latitude dynamics [Muench and Kunze, 1999, 2000]. The equatorial belt is, in fact, the place in our oceans where the internal wave band is widest, as its lower bound, the local inertial frequency, proportional to the sine of the latitude, vanishes there. Moreover, it is also the place where classical geostrophy breaks down, and where internal wave properties (i.e. internal wave polarization or its connection to vertical mixing characteristics) are less univocally defined and understood [Colin de Verdière and Schopp, 1994; Gregg *et al.*, 2003; van Haren, 2005; Gerkema *et al.*, 2008].

The puzzle posed by these elements, all contrasting with mid-latitude behaviour, suggests an interpretation of the low-latitude regions in terms of an "equatorial boundary layer". A first interpretation of this definition views the equatorial belt as a wave-guide for planetary waves such as equatorial Kelvin and Rossby waves, or Yanai waves [Stern, 1963; Edwards and Pedlosky, 1998; D'Orgeville *et al.*, 2007]. Secondly, "equatorial *internal* boundary layers" [Harlander and Maas, 2006, 2007], emerging for solutions of hyperbolic boundary value problems in fully confined domains, are also theoretically predicted to occur at the equator, as a result of the interaction of internal wave characteristic paths with the local geometry [Bretherton, 1964; Stewartson and Rickard, 1969; Stewartson, 1971, 1972; Dintrans *et al.*, 1999]. A third interpretation of "equatorial boundary layer" emerges as a region encapsulated by the ocean surface and the cylindrical surface tangent to the ocean floor and parallel to the Earth's rotation axis. The latter surface, given an average ocean depth of 4 km, would surface at ±2.0°of latitude (at ±2.3°for a 5 km deep ocean). From this simple argument, it follows that the area confined within ±2°is characterised by a different dynamics, when compared to that at higher latitudes. Outside the equatorial band, the height of the water column parallel to the rotation axis increases with distance from the axis, while the opposite is in fact true in the near-equatorial region, where the height of the water column parallel to the rotation axis decreases with distance from this axis, vanishing at the equatorial surface. This, for example, bears repercussions for the direction of propagation of topographic Rossby waves in the equatorial region. We can thus expect the equatorial dynamics to somehow follow, or to be related to, the isolines of planetary angular momentum, which are deformed into parabolic profiles in the tangent meridional-vertical plane [Colin de Verdière and Schopp, 1994]. It follows that, finally, the transition zone from the equator to the mid-latitudes,

at $\pm 2°$, might also itself be considered a boundary layer, as a matching surface between two, differently behaving, domains. In general, the existence of a boundary layer implies the local breakdown of the classical dynamical balances (i.e. geostrophy, Sverdrup relation) and that terms in the equations of motion, which are negligible in other parts of the domain (at mid-latitudes) become important near this boundary [Pedlosky, 1982]. Internal boundary layers, for example are defined as boundary-detached singularities in the velocity field, that might have a prominent role in the equatorial dynamics, comparable to the one played by critical layers for Rossby waves: in both types of layers, wave energy density blows up and waves can break. Consequences can then be enormous in terms of wave momentum flux, that can drive zonal mean flows as observed in laboratory experiments, and diapycnal mixing [Maas, 2001].

In this study, we elaborate on some of the differences in behaviour between equatorial and off-equatorial regions making use of an *ad hoc* set of observations collected in the deep equatorial West Atlantic Ocean. The set consists of a Conductivity-Temperature-Depth (CTD) and Lowered Acoustic Doppler Current Profiler (LADCP) transect from the equator to 2°N, and five 1.5 year long moorings between the equator and 2.5°N. This allows us to have a quasi-synoptic, meridional-vertical overview of the hydrographic and hydrodynamic characteristics of the transect. Moreover, thanks to the moored instrumentation, we also have access to the temporal scales of the near-equatorial current and wave field, together with the meridional and vertical spatial scales given by the spatial distribution of the moorings and by the instrument locations along the moorings lines respectively.

The instrumentation, data set and methods will be described in section 5.2. Results will be then presented in section 5.3. The quasi-synoptic hydrographic and hydrodynamic transect will be shown in section 5.3.1. Here measurements will be also used to point out at the spatial distribution of steppiness and for a *non-traditional* geostrophic analysis. Time series from the moorings will be presented and described in section 5.3.2, while spectral and polarization analysis of the time series are in sections 5.3.3 and 5.3.4. A summary of the observed features and a discussion follow in section 5.4 both for the transect data and for the time series. In section 5.4.3 focus will be posed on how the observed features can be related to the spatial distribution of angular momentum (planetary and total) in the equatorial region. section 5.5 continues with some conclusive thoughts and perspectives.
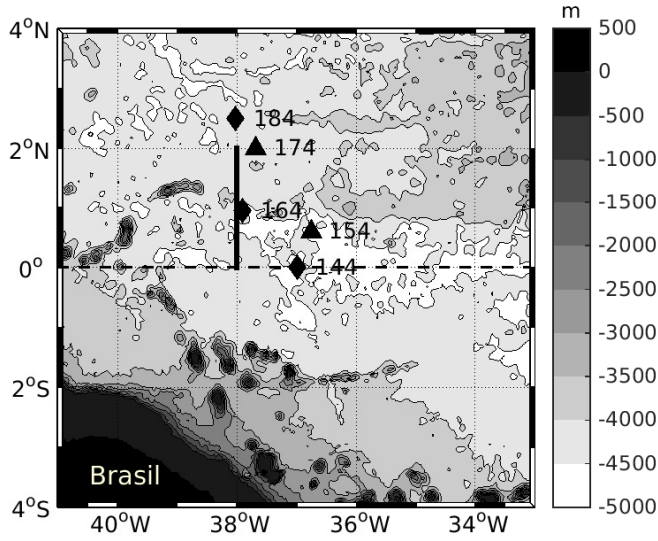
Figure 5.1: Bathymetric map of the study area in the Ceará basin. The dashed line indicates the equator. Triangles indicate the positions of 1.5 year long moorings equipped with current meters only, diamonds indicate 1.5 year long moorings equipped with ADCP and current meters. Details of the five moorings are given in table 5.1; the solid meridional line indicates the CTD/LADCP transect (16 stations along 38°W, evenly distributed between 0 and 2°N).

5.2.1   *Study area*

The study area is located in the Ceará basin, a nearly zonal, abyssal "channel" about 250 km wide, 1000 km long and 4000 km wide, in the Western equatorial Atlantic Ocean (figure 5.1). The Ceará basin corresponds to a major east-west offset of the Mid-Atlantic Ridge and the continental margin of Brazil [McCartney and Curry, 1993], and is a conduit for antarctic bottom waters flowing northward.

The area has been chosen to be relatively far from prominent topographic features, in order to avoid strong internal tides generated by the interaction between sea mounts and barotropic tidal currents. In this way, the dataset is supposed to capture relevant equatorial dynamics, marginally affected by local topography.

5.2.2   *Instrumentation*

Five $3000-3500\ m$ long subsurface moorings have been deployed between 0 and 2.5°N, and between 37 and 38°W, equipped with different current meters (figure 5.1). Details for the five moorings are given in table 5.1. In the five moorings, single point current meter measurements are made at about 1200, 1800, 2500, 3200 and 3900 m. Three types of current meters were used: mechanical Valeport BFM-308 (shallow positions), acoustic Nortek AquaDopp (intermediate positions) and acoustic Aanderaa RCM-11 (deep positions). Current meters sampled at a rate of 900 or 1200 s, depending on the instrument.

In the top positions of moorings 144, 164 and 184 (marked with diamonds in figure 5.1) Teledyne RDI 75 kHz Long Ranger Acoustic Doppler Current Profilers (ADCPs) were mounted at about 1000 m, looking upward, downward and upward respectively. ADCP data have been collected in 50 bins of 10 m vertical resolution, with an ensemble averaging period of 900 s, and average error in current speed of 0.04 ms^{-1} per ensemble.

For the purpose of this study, all time series have been resampled at 900 s resolution, over the common 1.5 years deployment, from mid December 2007 to mid June 2009. With these time series, motions that vary periodically from the buoyancy period to seasonal period can be identified; variations on longer time scales fall beyond the scope of this set of measurements. Spectra are obtained using the multitaper method, with three discrete prolate spheroidal sequences as data tapers for the multitaper estimation [Thomson, 1982; Percival, 1993].

During the mooring deployment cruise, a Sea Bird 911-plus CTD transect was performed, consisting of 16 stations equally spaced between the equator and 2°N, along 38°W (solid line in figure 5.1). After post-processing, pressure, temperature and salinity data have a vertical resolution of 1 m, with a range between about 5 m below the surface to 5 m above the bottom. The whole transect took about 84 h of combined measurements and sailing time. The CTD Rosette was also equipped with an LADCP (lowered-ADCP). The system consists of two Teledyne RDI 75 kHz Workhorse ADCPs in a master/slave configuration, downward and upward looking respectively. This setting gives a velocity profile over a maximum of two times 120 m in fifteen 8m-bins in waters with ample scatterers and about two times 60 m in clearer waters. Unfortunately, one of the Workhorses broke down at the beginning of the cruise and all the transect casts were done with only the downward-looking ADCP.

The LADCP measurements were integrated with simultaneous vessel-mounted ADCP (VM-ADCP) measurements in the upper 600 m near the surface, that partially compensated the absence of the upward-looking ADCP. The LADCP data are processed using the velocity inversion method developed at Lamont-Doherty Earth Observatory (LDEO) by M. Visbeck and now maintained by A. M. Thurnherr, resulting in 16 profiles with 8 m vertical resolution. All stations present a qualitatively similar error profile. Error values are almost constant between 80 m to 1800 m, increase to a maximum between 3000 and 3500 m and eventually decrease again toward the bottom, probably due to the vertical distribution of scatterers. Among the stations, the error values are however quantitatively different. The depth-averaged error for measurements below 80 m is about 0.05 m/s for stations 1 (at the equator) to 6, 8, and 12. For stations 7, 9, and 13 the averaged error is about 0.1 m/s, while for stations 10, 11 and 14 to 16 it is 0.15 to 0.2 m/s. From the diagnosis, the differences in error between stations do not seem to be related to different distributions of scatterers, or to topographic effects. The precise reason is unknown.

5.3 RESULTS

5.3.1 *Quasi-synoptic transect*

Buoyancy frequency (N) values obtained from the CTD transect are shown in figure 5.2 as $N/2\Omega$ ratio, where Ω is the Earth rotation rate ($7.292 \times 10^{-5} s^{-1}$). Throughout the whole water column the ratio $N/2\Omega > 4$, with few exceptions (corresponding to a buoyancy period of about 3 hour or shorter). Relatively strong stratification is present above 2000 m, with little latitudinal structure. A secondary enhancement in N is present just below 4000 m, where the highest topography is impinging the isopycnals. In this area it is usually explained as

mooring	latitude N	longitude W	water depth [m]	ADCP depth [m]	current meter depth [m]
LOCO 14/4	00 °00.013'	36 °59.466'	4492	1063	1828, 2535, 3200, 3900
LOCO 15/4	00 °36.050'	36 °45.651'	4504		1228,1866, 2555, 3200, 3900
LOCO 16/4	00 °57.052'	37 °54.258'	4475	1040	1958, 2690, 3250, 3950
LOCO 17/4	02 °00.106'	37 °40.822'	4420		1200, 2048, 2797, 3197, 3900
LOCO 18/4	02 °30.171'	38 °01.640'	4450	1002	1200, 1817, 2500, 3200, 3900

Table 5.1: Details for the five moorings; for map see figure 5.1.
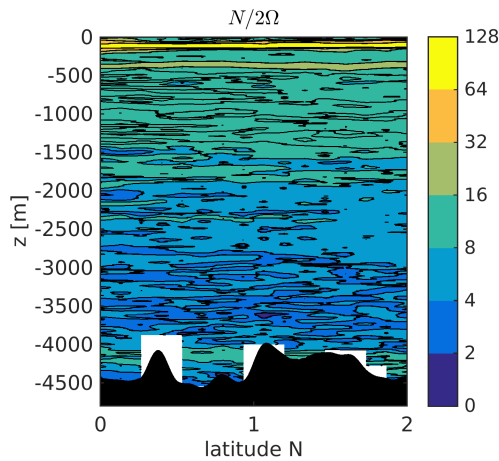

Figure 5.2: Buoyancy frequency N scaled with 2Ω, vertically smoothed over 40 m. Note the logarithmic colour scale.
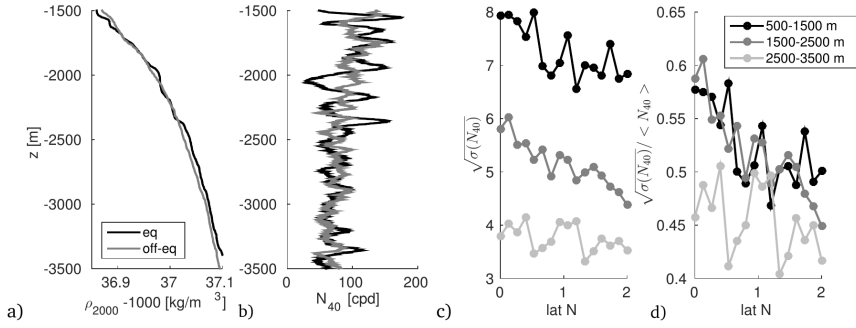
Figure 5.3: a) Potential density referred to 2000 dbar at the equator (red line) and off the equator (2°N, black line) between 1500 m and 3500 m. The depth range has been chosen to appreciate the changes taking place around 2500 m. Potential density steps of vertical extension of about 100 m are visible in the equatorial profile down to 2500 m. Below 2500 m till the bottom the two profiles show a similar behaviour; b) N_{40} profiles in cycle per day for the equatorial (red line) and off-equatorial (black line) stations between 1500 m and 3500 m. Down to 2500 m, the off-equatorial profile shows the similar large-scale mean values as the equatorial one, but the variability is visibly reduced. Below 2500 m the two profiles present a similar behaviour; c) latitudinal comparison for three depth ranges of a measure of steppiness (evaluated as $\sqrt{std(N_{40})}$ [van Haren, 2005], see text for definition); d) same as in c), but here the measure of steppiness is normalised the vertical average of local N_{40} in the correspondent depth layer.

the transition zone between the lower branch of the NADW (North Atlantic Deep Water) and the AABW (Antarctic Bottom Water) [St. Laurent *et al.*, 2001; Schmid *et al.*, 2005] and approximately corresponds to the 2°C isotherm.

To enlighten the latitudinal structure of the density and stratification properties of the transect, in figure 5.3a, two single profiles of potential density anomalies (referred to 2000 m) are plotted between 1500 m and 3500 m: the equatorial station (in red) and the northernmost station (in black). Layering characterised by a vertical scale of about 100 m is present in the equatorial profile down to 2500 m. On the other hand, no layering is present in the northernmost station, which instead shows a uniform behaviour over the depth range displayed. This is also clear looking at the corresponding N_{40} profiles (figure 5.3b), where N_{40} is the buoyancy frequency N smoothed over 40 m intervals. In the same depth interval between 1500 m and 3500 m, the equatorial and the off-equatorial show similar large-scale mean values, but variability is in the off-equatorial profile is largely reduced. Below 2500 m, instead, the two profiles present a similar behaviour. We then quantify the presence of layers ("steppi-
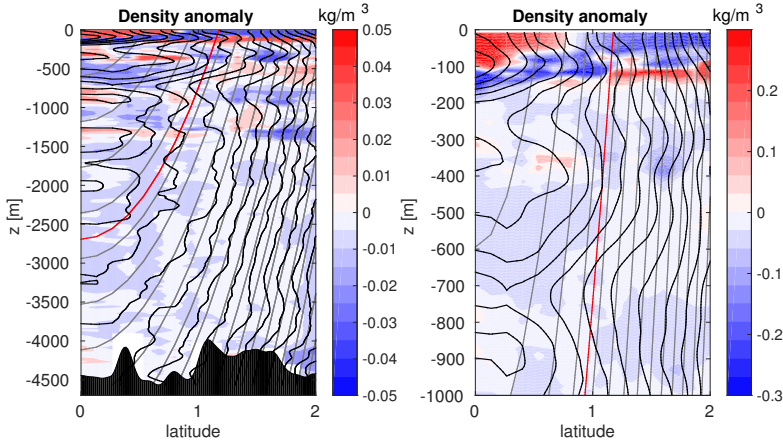
Figure 5.4: (left) Density anomaly with respect to the meridional mean from the CTD transect; (right) zoom on the first 1000 m below the surface (note different colour scale). Contours: grey lines are isolines of angular momentum due to the Earth rotation only (in red the one approximately embracing the EDJ area), black lines are isolines of total angular momentum, see section 5.4.3 for details.

ness") following van Haren [2005] as the $\sqrt{std(N_{40})}$. Results are plotted for the whole transect in the central panel of figure 5.3. High level of steppiness is usually associated to enhanced, small scales internal wave activity as well as to a lack of large-scale smoothing mechanisms [Turner, 1979]. Steppiness is thus regarded as a reciprocal measure for mixing. Near the equator, a latitudinal dependence of "steppiness" has been already reported in van Haren [2005], however, with these new synoptic measurements, we can confirm this behaviour at much smaller meridional scales. Moreover, we can now look at the entire water column: in the two layers 500 to 1500 m and 1500 m to 2500 m, the behaviour is similar, we can almost superpose the two profiles when normalised to the local values of N_{40} (right panel in figure 5.3, blue and red lines). However, below 2500 m (purple line in the central and right panel in figure 5.3), the situation is latitudinally homogeneous, and comparable with the level of steppiness in the northernmost stations in the two upper layers.

Figure 5.4 shows, for each profile of the transect, the density anomaly with respect to the meridional mean at each depth. Along the vertical, alternating structures in the density field are present along the whole transect, with a spatial scale of almost half a degree ($\sim 50\ km$), down to 1500 m. Anomalies of comparable strength are present down to 1500 m, with the strongest signals at about 100 m, at the thermocline (see right panel in figure 5.4). In figure 5.4,

as in figure 5.5, isolines of planetary angular momentum (in grey) and of total angular momentum (in black) are superposed, and will be discussed in section 5.4.3.

The corresponding, instantaneous velocity field from LADCP measurements is displayed in figure 5.5. In the left panels of figure 5.5 (zoom of the first 1000 m in the bottom-left panel) the expected westward surface current [Stramma and Schott, 1999] is not detected, while the deeper eastward current, conventionally named Equatorial Under Current (EUC), seems to surface within half a degree from the equator. The EUC is centred at around 100 m and is visible up to 1°N, showing thus only half of the width reported by Schott *et al.* [2003] for measurements at 35°W. At 1°N, a transition occurs between the eastward EUC and the strong westward flow present in the northern part of the transect. This corresponds to the nSEC (the northern branch of the Southern Equatorial Current), usually centred at around 2.5°N [Stramma and Schott, 1999; Schott *et al.*, 2003]. In our dataset, the EUC is presenting a peak at depths between 50 and 100 m, with velocity peaks of 0.75 m/s, and mean velocity values of 0.43 m/s when averaged over the current area. Below the EUC, a lower, weaker (0.12 m/s) eastward peak is also present at 310 m. In the right panel of figure 5.4 it is evident that the strongest density anomalies correspond to the core of the EUC.

Below the EUC, two branches of the westward Equatorial Intermediate Current (EIC) are present, at 250 m and at 750 m. In these measurements, a third velocity peak appears, around 1100 m, before the zonal direction of the velocity is reversed to eastward at around 1300 m. The westward EIC signal is measured as far north as 2°N (see left panel in figure 5.5), and its average velocity is westward ($-0.073\ m/s$). For its time variability (see section 5.3.2), the EIC might be considered as the first of the Equatorial Deep Jets. In this dataset, the equatorial profile displays about 6 alternating zonal jets between 150 m and 2500 m (figure 5.5, upper left panel). While, as observed before, EUC and EIC show a meridional extent of one degree or more in the northern hemisphere, deeper EDJs are narrower, with a meridional extent of less then 0.5°. The observed vertical scales for the alternating zonal currents are very diverse, ranging from 100 to 800 m.

When the two components are compared (figure 5.5, left and right panels), the meridional one, besides being weaker in the upper part of the water column, shows, in general, smaller vertical scales, and a more uniform behaviour throughout the water column. No evident correlation between meridional currents and the zonal EDJ currents is detectable. Near the surface, the highest values for the meridional component of the velocity are encountered at 1°N, and correspond to a southward flow.
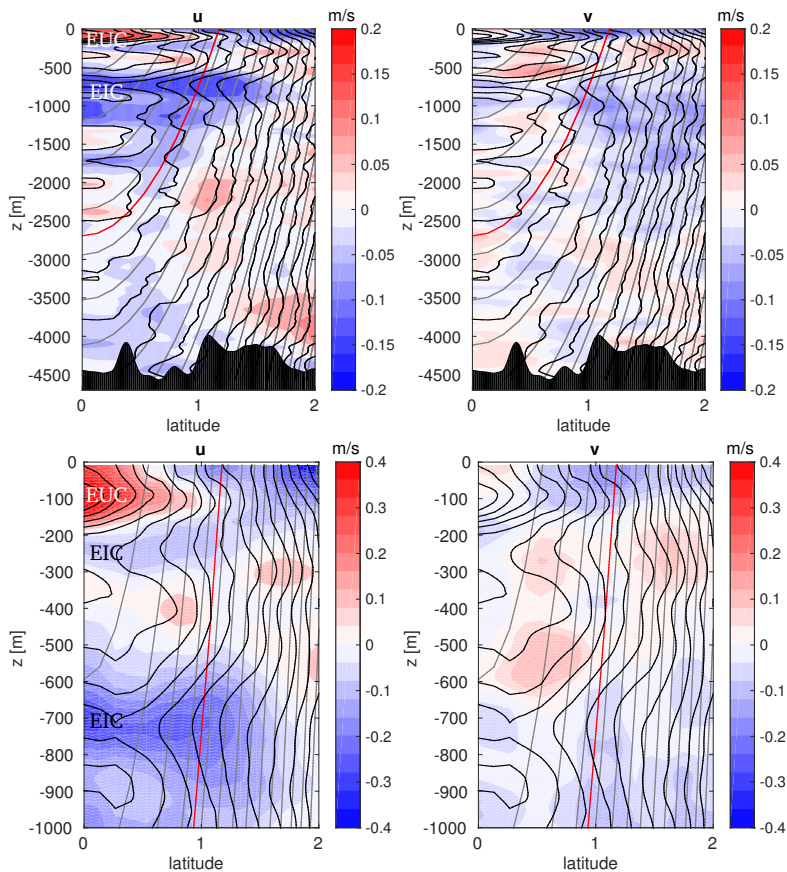
Figure 5.5: Zonal (left) and meridional (right) component of the current from the LADCP measurements. Positive values represent Eastward and Northward motion, respectively. Top panels: whole water column; bottom panels: zoom on the first 1000 m below the surface. Grey/black contours are the same as in figure 5.4.
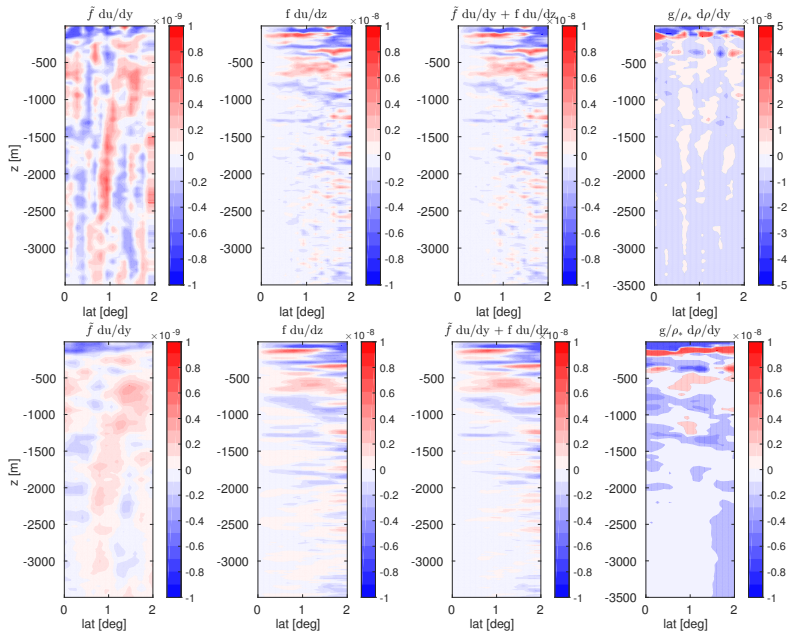
Figure 5.6: Evaluation of the single terms of equatorial geostrophic balance as in equation (5.1): see title of each panel. Top panels: no meridional smoothing. Bottom panels: meridional smoothing on a 30 km spatial scale. Note the different colour scales.

Below the EDJs (at about 2500 m), zonal currents decrease, but a bottom enhancement of a westward current is observed below 3500 m, visible in the profiles equatorward of 1°N) and peaking at about 400 m above the sea bottom (upper-left panel in figure 5.5). Analogously, a bottom enhancement of the eastward flow is observed below 3500 m in the northernmost profile (upper-left panel in figure 5.5). This corresponds to the location of the local maximum in stratification observed in figure 5.2, and previously identified as the transition area between the NADW and the AABW.

We have shown that alternate structures are present both in the density field (figure 5.4) and in the velocity field (figure 5.5). This correspondence suggests the presence of a equatorial geostrophic balance (Eriksen [1982a]; Hayes [1982]; Lukas and Firing [1984]; Muench and Kunze [1994] for the Pacific Ocean, Gouriou *et al.* [1999] for the Atlantic Ocean). A rigorous balance between density contributions and velocity contributions in the geostrophic equation cannot be present in our dataset, as we are resolving variations at spatial scales smaller than 15 km and at times shorter then 4 days (figure 5.6, upper

panels), conditions under which the equatorial geostrophic balance does not hold [Picaut *et al.*, 1989; Moum *et al.*, 1987]. However, the balance qualitatively holds in the transect, especially if results are smoothed over a horizontal scale > 30 km (figure 5.6, lower panels). Most interestingly, using the available velocity data, we can explicitly evaluate the so-called *non-traditional* geostrophic balance

$$2\Omega\cos(\phi)u_y + 2\Omega\sin(\phi)u_z = \frac{g}{\rho_*}\rho_y \qquad (5.1)$$

where ϕ is the latitude and subscripts denote partial derivatives. The *non-traditional* term (first term on the left hand side of equation (5.1)), which is usually neglected, is related to the horizontal component of the Coriolis force and hypothesised to play an important role in the equatorial belt [Joyce *et al.*, 1988; Colin de Verdière and Schopp, 1994; Gerkema *et al.*, 2008]. In our data, however, the *non-traditional* term always appears at least one order of magnitude smaller then the traditional term (second term on the left hand side of equation (5.1)), except at the equator, where it is the only term contributing to the balance, as $\sin(0°) = 0$. Even at this station, however, it brings no significant contribution to the balance, as the density structure (figure 5.4) shows a much stronger signature due to the term ρ_y. Perhaps other terms like $\partial u / \partial t$ or advective terms need to be included to close the momentum balance. However, these terms cannot be directly evaluated from this dataset.

5.3.2   *Current time series*

For the sake of clarity, in this section we will first consider only the measurements made in the depth range 500 m to 1000 m, and obtained using ADCPs (5.3.2.1): we will then compare currents measured at the equator and 2.5°N, the most off-equatorial mooring in the dataset. In subsection 5.3.2.2, we will then consider the deeper measurements (1000 m to bottom), obtained with both ADCP (at 1°N) and single-point current meters at all locations.

5.3.2.1   *Intermediate depths (500 to 1000 m) from ADCP measurements*

EQUATORIAL MOORING   The westward Equatorial Intermediate Current (EIC) signature is visible in the ADCP measurements at the Equator between 500 m to 1000 m (figure 5.7a). The current is westward for most of the time series: the annual mean is displayed in figure 5.9a, showing a peak of 0.15 m/s. In our dataset, however, the EIC also presents a strong temporal and spatial variability. The westward current, when present, appears to be centred at 730 m, whereas
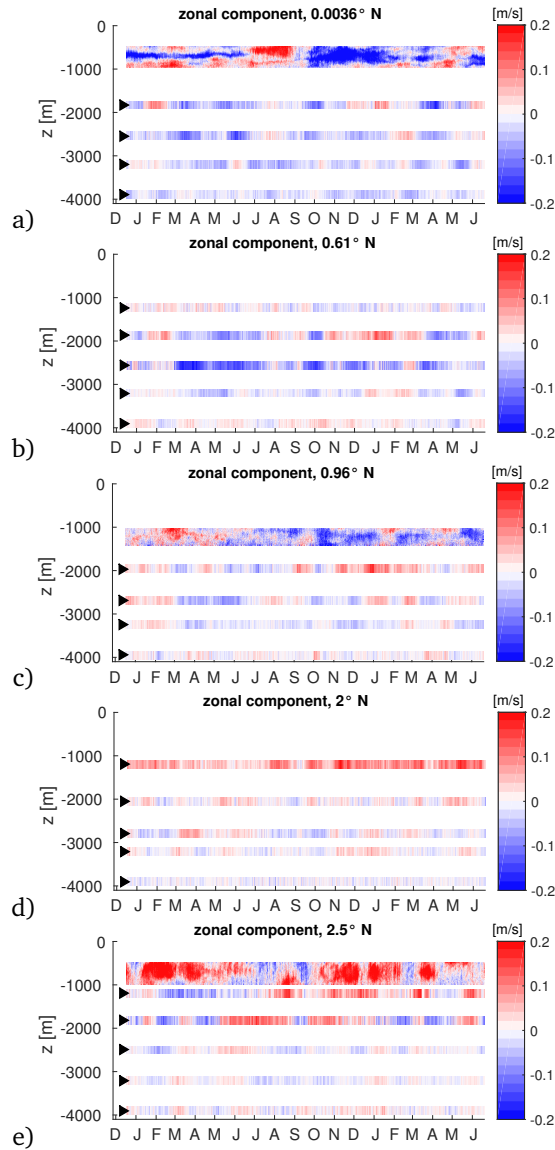
Figure 5.7: Depth-time series of zonal (positive eastward) current component along 38°W, (a) at the equator, (b) at 0.61°N, (c) at 0.96°N, (d) at 2°N, (e) at 2.5°N. Time goes from December 2007 to July 2009. Black triangles mark instrument locations, except for ADCPs.
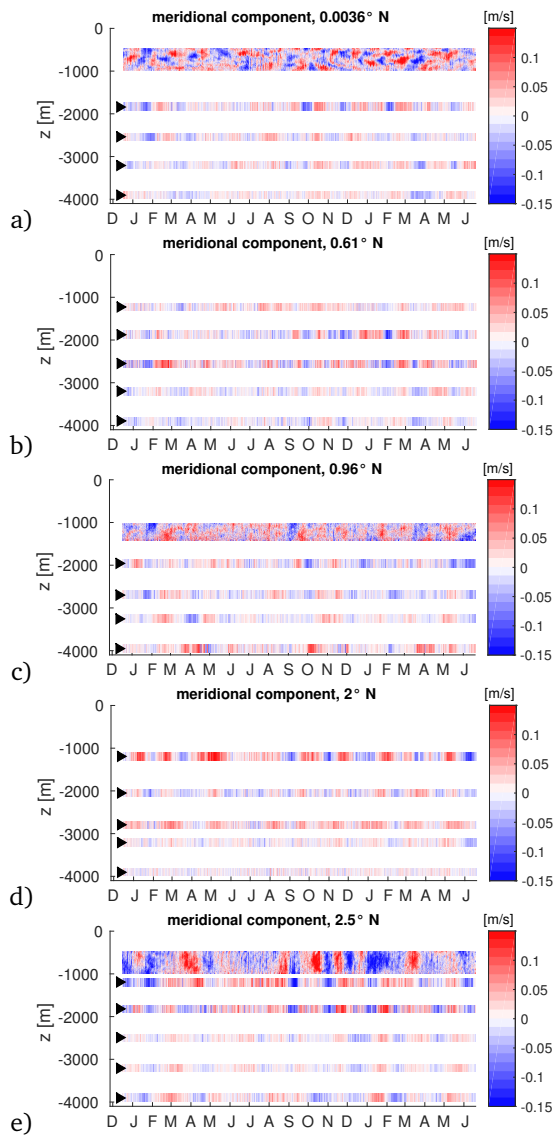
Figure 5.8: As figure 5.7 but for meridional current component.
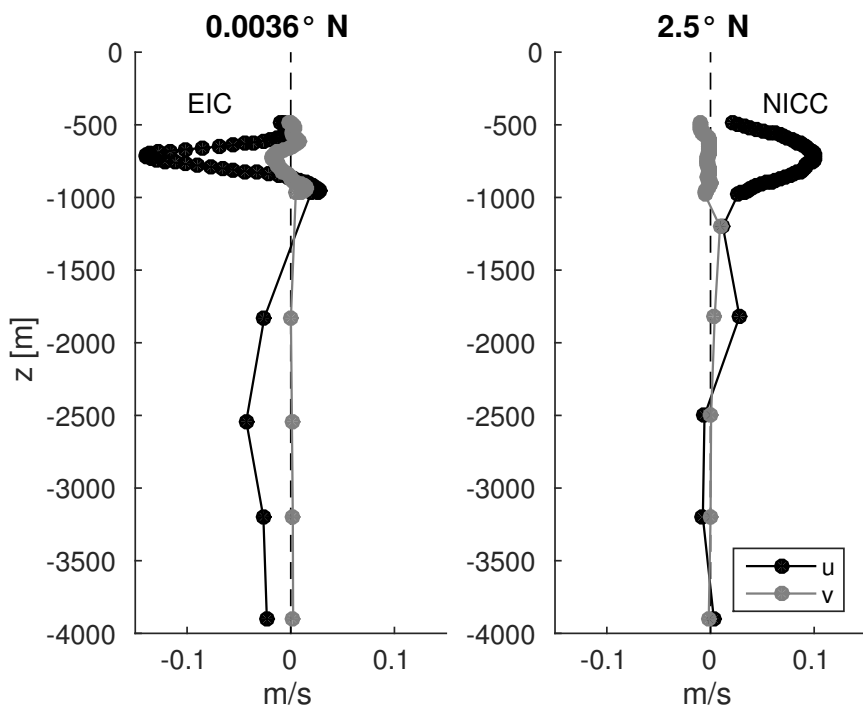
Figure 5.9: Yearly mean of zonal (black, positive eastward) and meridional (grey, positive northward) velocity (left) at the equator, (right) at 2.5°N. Circles mark measurement depths.

its vertical extension varies from tens of meters in July, August and September 2008 to the whole 500 m in October, November and December 2008 (figure 5.7a). In terms of current magnitude, it presents its maximum during Autumn, with an average of 0.28 m/s, but with instantaneous values up to 0.58 m/s at the beginning of November (03/11/2008). In the zonal current, small vertical scales of the order of 100 m (as for example in February and March 2008) occur at the equatorial mooring only. At the same depth level, measurements at 2.5°N show more vertical coherence, spanning about the whole 500 m measured by the ADCP for most of the time (compare figures 5.7a and 5.7e).

From this time series the EIC appears to show an intermittent character, with a maximum westward flow between October 2008 and February 2009, a narrowing of the vertical extension in March and April, and an almost complete shut off in August and September. This seasonal cycle is captured using the annual and semiannual components of the signal alone. Moreover, in this record, the behaviour of the EIC does not suggest any vertical propagation of the jet. In the months of June, July and August 2008, we register an isolated eastward pulse at 575 m (up to 0.26 m/s on the 21/07/2008).

Equatorial meridional currents in the vertical range of 500 m to 1000 m (figure 5.8a) present smaller vertical scales (of about 150 m) compared to off-equatorial measurements (at least 500 m, figure 5.8e). This difference in vertical scales is even more pronounced than the one shown by the zonal current components.

We notice that, as in the LADCP transect, correlation between zonal and meridional currents is not present in the time series. For example, in September/October 2008, when a sudden reversal of the zonal component is detectable (figure 5.7a), no particular change is detectable in the meridional component, which seems to show instead a uniform spatial and temporal behaviour throughout the whole record (figure 5.8a). The seasonal modulation of the meridional component appears very small when compared to the zonal modulation, and the meridional current is dominated by variations at shorter time scales. The annual mean (figure 5.9a) presents a southward peak in correspondence with the EIC, embraced by two northward currents. Total transport is therefore mainly northward in this water portion. This can be seen as part of the North Brazilian Current, that flows north along South America at this longitude [Richardson and Fratantoni, 1999].

OFF THE EQUATOR   At the northernmost mooring, at 2.5°N (figure 5.7e), the vertical structure of the zonal currents is different from the equatorial one. At 2.5°N the current signal appears coherent almost throughout the whole 500 m, and the eastward signature of the NICC (Northern Intermediate Countercurrent), clearly emerges in the annual mean (see figure 5.9b). The current, centred at 700 m, is eastward nearly the whole year, with an average of 0.19

m/s, up to a maximum of 0.40 m/s in late January (24/01/2008). During Summer time, the jet reverses to a weak westward jet, with an average of 0.05 m/s, up to a maximum of 0.42 m/s on 17/07/2008.

The annual mean of the meridional component is almost zero (figure 5.9b, red line). Although the zonal seasonal signal appears still stronger than the meridional, the difference between the two is reduced in comparison with what is observed in the equatorial measurements.

5.3.2.2 *Deep dynamics (1000 m to bottom)*

The reversal of the flow just below the EIC seems a permanent feature as it also emerges in the annual mean (figure 5.9a). Its vertical extension, however, probably varies in time as the EIC does. As a general comment, currents below 1000 *m* present a more isotropic field, if we compare the two components of the velocity (figures 5.7 and 5.8), both in time scale and in intensity.

Because of the partial information available, it is not always easy to identify the vertical scales of the current pattern. However, vertical coherence exceeding 1000 m is often suggested in the zonal current, not only in the equatorial mooring (February/March 2008, October 2008, February/March 2009 between 1800 m and 3200 m), but even more in the off-equatorial moorings. When we look at measurements from 2.5°N (figures 5.7e and 5.8e) pulses emerge with a striking vertical coherency throughout most of the water column. The most evident examples are the eastward pulses in Spring/Summer and Winter 2008 at 2.5°N, where the signal seems to propagate upward (figure 5.7e). In this case, such pulses seem to be also accompanied by similar structures in the meridional component (northward) (figure 5.8e). Other coherent meridional pulses appear as well, for example the northward pulses in November/December 2008 and January/February and May/June 2009).

Horizontal, latitudinal coherence of 1°can be retrieved by comparing the deepest measurements from the ADCP at the equator and the shallowest measurements of the ADCP at 0.96°N, where the strong eastward events in February/March 2008, February 2009 and May 2009 are visible in both datasets.

In the annual mean (figure 5.9a), below 1000 m, flow in the equatorial mooring appears to be coherently westward throughout the whole sampled part of the water column. This is associated with a weak northward annual mean for the meridional component.

Relatively strong currents have been measured by the current meter at 2500 m from 0.61°N and are suggestive of a possible hot spot for current enhancement.
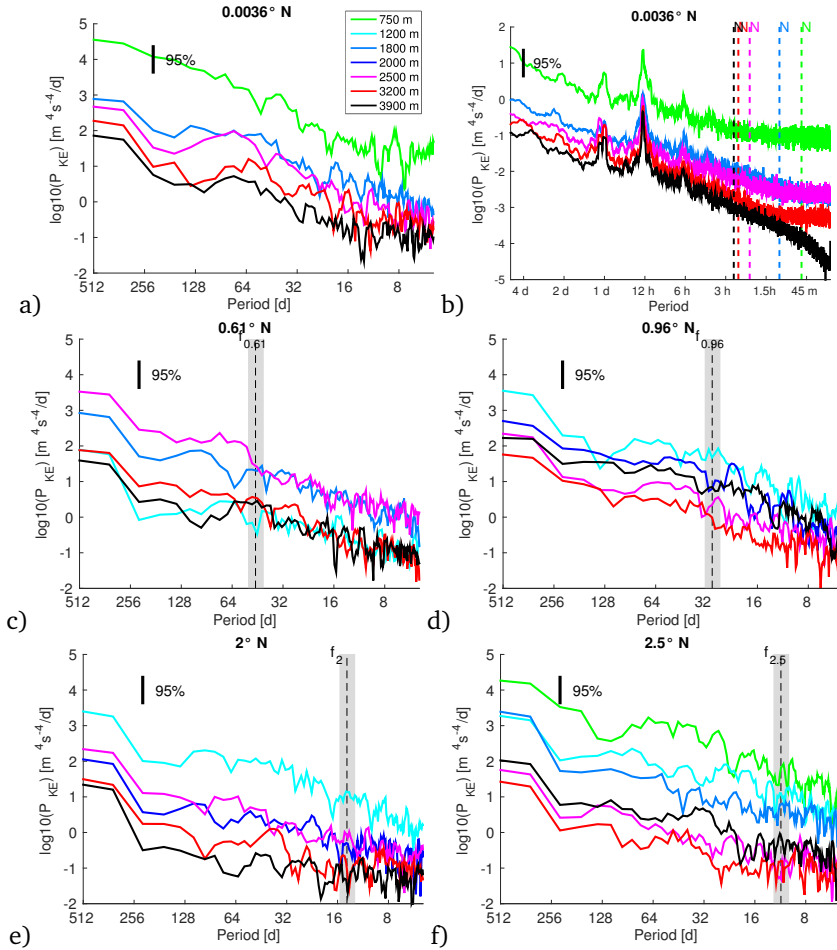
Figure 5.10: Power spectral density of kinetic energy from the velocity time series. (a) at the equator, periods longer than 5 d; (b), at the equator, periods shorter than 5 days (note the different axis); average buoyancy period for each depth portion is estimated by the CTD measurements and marked following the depth colour code in the legend. For the short periods only this plot is shown, all other moorings presenting similar characteristics. (c) Power spectral density for periods longer than 5 d at 0.61°N, (d) at 0.96°N, (e) at 2°N and (f) 2.5°N. The common colour legend serves for all panels, with depths indicative ±200 m. Inertial periods ±10% for the off equatorial moorings have been shadowed. Of the ADCP measurements, in (a) and (f) only the spectrum at 750 m is displayed, while in (d) only the spectrum at 1250 m is displayed.

5.3.3 *Spectral content*

Power spectral density plots of kinetic energy for each mooring are presented in figure 5.10. Periods longer than 5 days are presented for all moorings (figure 5.10a, c, d, e and f), while periods between 30 minutes and 5 days are shown only for the equatorial mooring (figure 5.10b), since all other moorings show similar characteristics. In the long-period plots, the local inertial periods for the off-equatorial mooring locations are shadowed (±10%), to account for the near-inertial band [van Haren and Millot, 2004]. In the short-period plot (figure 5.10b) the average buoyancy frequency is marked for each depth level. N is obtained from the CTD transect (as in figure 5.2). We notice that the whole internal wave range is covered by our measurements, at all depths. While in figure 5.10 the total kinetic energy content is inspected, the different behaviour of the horizontal components of the velocity will be investigated in section 5.3.4.

From figure 5.10b, it is clear that the noise level of ADCP measurements is considerably higher than for other instruments (see green line). Note that the current meter at the equator at 3900 m (black line in (a) and (b)), and the current meter at 2.5°N at 2500 m (magenta line in (i) and (j)) were sampling at 1200 s, while all others were sampling at 900 s or 300 s. This explains the drop in kinetic energy at periods of about 40 minutes in figure 5.10b (black line).

5.3.3.1 *Periods longer than 5 days*

In the shallower measurements, at 750 m, kinetic energy content for periods > 200 d is similar at the equator and 2.5°N. At 2.5°N, however, a drop in kinetic energy is present between 100 and 200 d. This is probably due to the stronger seasonal signal present at the equator, when compared to the seasonal signal present at 2.5°N.

With the available data set we are able to focus on the local inertial period at each mooring (shadowed in figure 5.10). The inertial peaks, in general, do not emerge as prominent features of the energy spectra, as we would expect from all the off-equatorial moorings, and as is the case for general mid-latitude spectra (see for example Emery and Thomson [2001]). This is true despite the different vertical and meridional locations of the considered signals. The same is also true if we consider the zonal and meridional component of the velocity alone (not shown).

The inertial "peak" at 0.61°N is barely visible at 1800, 3200 and 3900 m (figure 5.10c). All peaks are spread beyond the ±10% of the local inertial period. Measurements at 2500 m and 1200 m do not present any feature at the inertial period. At 0.96°N, a weak inertial peak is visible only at 1200 m (figure 5.10d). At 2°N, at 1200 m, a very wide plateau is present, that includes the local inertial

period (figure 5.10e). At 2.5°N, an inertial peak is present only at 750 m and at 3900 m (figure 5.10f).

In the moorings at 2°N (at 1200 m, 2000 m, 3900 m) and 2.5°N (at 750 m and 3900 m) a sudden drop in energy content occurs coherently around 20 days (a period in between the inertial periods of 1°N and 2°N). This suggests that a transition of regimes might take place somewhere in between 1°N and 2°N.

We notice that the power content is not always monotonically decreasing with depth, although the ADCP measurements between 500 m and 1000 m always present the most energetic signals, both at 0°and at 2.5°N. At 0.61°N, for example, we observe a mid-depth (2500 m) enhancement in kinetic energy over the whole spectrum. A similar enhancement at 2500 m is also present at 2°N.

5.3.3.2 *Periods shorter than 5 days*

Spectra of kinetic energy show similar behaviour at all locations (see figure 5.10b for the equatorial mooring), with dominant peaks at the tidal diurnal, semi-diurnal and 6 h periods.

5.3.4 *Wave polarization*

A polarization analysis of the time series of current allows to investigate properties of the wave field and its changes with latitude and depth. Moreover, it complements the spectral analysis of the kinetic energy in terms of information on the orientation of the wave motion. We perform a polarization analysis of the whole water column, following the approach by Gonella [1972], using data from ADCPs as well as from the deeper current meters.

In figure 5.11, the depth average of the absolute value of the rotary coefficient is plotted for each of the five moorings. In short, rotary analysis consists in the separation of the measured current vector for each frequency ω into anticyclonic (clockwise in the northern hemisphere) and cyclonic (anticlockwise in the northern hemisphere) rotating circular components, to whom it is possible to assign amplitudes ($A^\pm(\omega)$) and phases ($\theta^\pm(\omega)$) [Gonella, 1972]. From the rotary spectra, the rotary coefficient is defined

$$c_r = \frac{A^+(\omega)^2 - A^-(\omega)^2}{A^+(\omega)^2 + A^-(\omega)^2}. \tag{5.2}$$
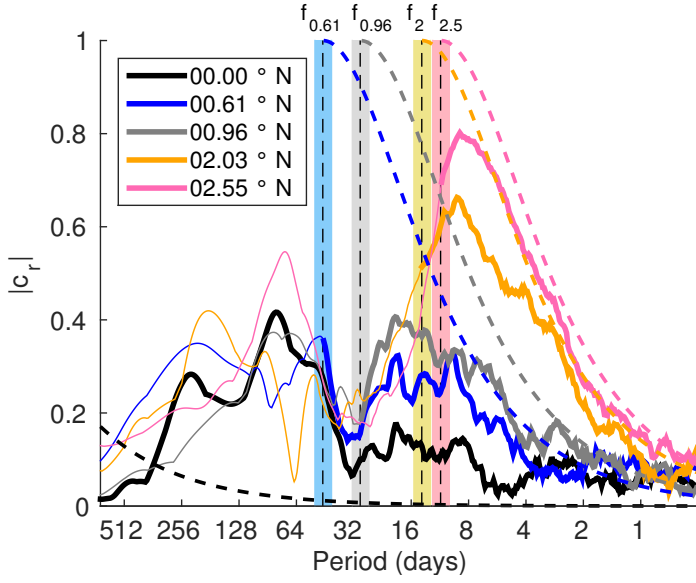
Figure 5.11: Depth-averaged, absolute values of rotary coefficients for the five moorings. Dashed lines correspond to the theoretical predictions for superinertial propagating internal waves [Gonella, 1972]. Superinertial periods are plotted with bold lines, while subinertial periods, for which the theoretical linear polarization analysis is not valid, are plotted with thin lines. Inertial periods ±10% have been shadowed for the off-equatorial moorings.

The theoretical curve for the rotary coefficient for linear, freely propagating internal waves, is

$$r_\omega = \frac{2f\,\omega}{f_{loc}^2 + \omega^2} \tag{5.3}$$

and is valid only for the superinertial part of the spectrum [Gonella, 1972]. In figure 5.11 it is drawn with a dashed line, while the five local inertial periods ±10% are shadowed with different colours.

Inertial oscillations present a peak in the rotary coefficient at 0.61°N only at 1800 and 3900 m, while no relevant features are present at other depths (not shown). At 1°N, no inertial peak is present. Instead, measurements at 2°and 2.5°N seem to follow more closely the theoretical curves. However, at all moorings, we observe a non-monotonic depth variability of the polarization, particularly evident in the long period (larger than 30 days) part of the spectra (not shown). In theory, this signal cannot be representative of freely propagating internal waves, being everywhere subinertial (except at the equator).

From figure 5.11, we conclude that superinertial frequencies appear to follow the theoretical curves only at the two northernmost locations, resembling typical off equatorial spectra [van Haren, 2005]. In contrast, averaged rotary coefficient values relative to locations equatorward of 2°N do not exceed the value of 0.5, we do not observe any circularly polarized peaks at the local inertial periods. We only observe a local maximum ($|C_r| \approx 0.3$) at the inertial period for the mooring at 0.61°N, still far from being representative of circularly polarized waves.

The presence of these values, neither representative of circularly nor rectilinearly polarized motion, are indicative of a more complex equatorial dynamics, not explained by linear internal wave theory, and perhaps representative of non linear dynamics. As a last comment, we note that at about 30 days, rotary spectra at all location approximately coincide, and show a nearly rectilinear behaviour.

We present in figure 5.12 the hodographs for the five mooring locations, at comparable depths. For each mooring, the two current components have been filtered and only oscillations in the local near-inertial frequency band (±10%) are presented. For the equatorial mooring, periods longer than 100 days are displayed. This information complements the polarization analysis. In fact, comparing hodographs at different latitudes, it is clear that the behaviour of near inertial frequencies in the equatorial moorings is different from the off-equatorial ones. At the equator, at the shallowest depth, an almost purely zonal motion is present, most likely due to the presence of the jets, and in particular of the EIC in the shallowest measurements. An analogous hodograph at 2.5°N shows instead an almost circular pattern. A jet is also present at this latitude, but the
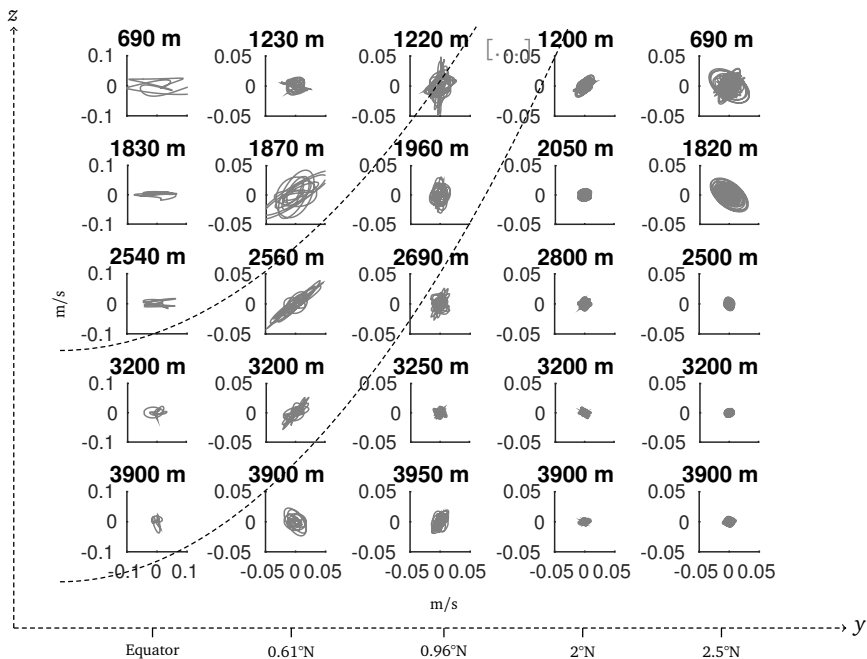
Figure 5.12: Hodographs of band-pass filtered horizontal current signals (u,v) at the local inertial frequency (±10%) displayed in the y,z-plane. At the equator, where the inertial period is not existing, all periods longer than 100 d are considered. Parabolic iso-angular momentum lines as in figures 5.4 and 5.5 are drawn on top of the subplots. Distances between the two plotted parabola are not preserved through the subplots due to the inhomogeneous vertical and meridional distribution of the measurements.

near-inertial period (about 11 days) is much shorter than typical time scales of the jet. When we look at deeper measurements, the circular nature of near-inertial motion in off-equatorial moorings becomes even more evident (figure 5.12, lower panels). At the equator, instead, at 1830 m and 2540 m, a specific orientation of the motion emerges and seems coherent throughout these 700 m. This coherence seems lost in the deeper two measurements.

5.4 DISCUSSION

5.4.1 *Transect*

The high meridional and vertical resolution of the CTD/LADCP transect allows for a detailed analysis of quasi-synoptic phenomena taking place near the equator. The strongest density anomalies correspond to the cores of the EUC and of the eastward deeper jets down to 2500 m (figure 5.4). However, this correspondence holds only within ±0.5 to 1 degree from the equator. Alternating structures are present both in the density and in the current fields (figures 5.4 and 5.5) in the whole transect, suggesting the presence of a geostrophic balance. The alternating structures are qualitatively in geostrophic balance if smoothed on a 30-50 km meridional scale (see figure 5.6, bottom panels). We learn from the mooring data that although the strongest jet variability has a seasonal time scale (figures 5.7 and 5.10), variability at short, tidal time scales is also present in the equatorial belt, and hence a time independent geostrophic balance can be achieved only after some smoothing processes (as in Moum *et al.* [1987]; Picaut *et al.* [1989]).

With the available data set, it has been appealing to check the role of the *non-traditional* term in the geostrophic balance on the equatorial β-plane (equation (5.1), Colin de Verdière and Schopp [1994]; Gerkema *et al.* [2008]). However, the stratification appears everywhere relatively strong compared to the Earth rotation (figure 5.2, general values $N/2\Omega > 4$). This suggests a weak role of the *non-traditional* term in the area, at least in the measured transect. In fact, when traditional and *non-traditional* geostrophic balances are checked against the observations, it emerges that *non-traditional* effects, and thus pure inertial dynamics, bring a contribution to the balance of about one order of magnitude weaker than the traditional term. Analogously, in the Pacific [Joyce *et al.*, 1988], the effects of the *non-traditional* term, there referred to as *non-hydrostatic* term, were found to account for only about 10% of the equatorial transport. Moreover, both in our Atlantic data set and in Joyce *et al.* [1988]'s data set, the non-hydrostatic correction does not constitute a uniform improvement in the agreement between measured and geostrophic currents. It is interesting to note, though, that below 1500 *m*, despite the difference in strength of the signals, the

spatial structure of the *non-traditional* term (upper left panel in figure 5.6) is much more similar to the spatial structure of the density term (upper right panel in figure 5.6), than that of the traditional term.

Although stratification appears to be relatively strong almost uniformly along the transect, the analysis of the presence of layering presents evidence of complex vertical and meridional structures. First, step-like layers are not uniformly distributed at all depths between the permanent pycnocline and the bottom, as was the case in D'Orgeville *et al.* [2004]. Density layering at 50-100 m vertical scale is here observed only down to about 2500 m, with a limited meridional extent (up to about 1°N in our observations). Similar density layering has also been observed in the equatorial Pacific surface layers (Richards and Banks [2002], as temperature/salt intrusions), and in the equatorial Indian Ocean [Dengler and Quadfasel, 2002]. figure 5.3 suggests that the presence of strong steps in stratification quickly decreases with latitude, and is confined to the EDJs part of the water column (500-2500 m, as shown in figure 5.5. With this dataset, it is not possible to determine whether the layering is part of the generation and/or maintenance of the EDJs, or is part of their dissipation process.

It is interesting to notice, however, that in this data set, EDJs are observed down to 2500-2700 m and not deeper. This vertical range for the jet region corresponds to the one found by Gouriou *et al.* [1999] and Schmid *et al.* [2005] in the Atlantic, while in Brandt *et al.* [2011] a range down to 3500 m is proposed. Similar restricted vertical ranges for the EDJs are indicated for the Pacific [Eriksen, 1981; Firing, 1987; Ponte and Luyten, 1989] and the Indian Ocean [Dengler and Quadfasel, 2002]. The observed vertical scales for the alternating zonal currents are very diverse, spanning from 100 to 800 m. It has been remarked in previous papers [Gouriou *et al.*, 1999] that typical Atlantic Equatorial Deep zonal Jets show a larger vertical scale (of about $400 - 600$ m) in comparison with the Pacific ones (of about $250 - 400$ m), and that the vertical scale of the zonal jets is supposed to increase with depth. This last feature seems not to be true in our data set (nor in other Atlantic data sets, see for example Brandt *et al.* [2011]), where a vertically extended westward EIC (centred at about 750 m) lies above a series of smaller alternating jets, whose zonal direction at depth seems to alternate with decreasing vertical scales. EDJs in this data set are in fact narrower with depth. It is clear, however, that an elevated temporal variability of not only the jet's intensities, but also of their vertical scale is present, if we compare the LADCP profile with the initial, final and mean values of the current time series at one location (see section 5.3.2), suggesting that it is difficult to give a unique value as representative for the vertical scale of the jets. Compared to zonal velocities, meridional velocities exhibit shorter vertical spatial scales and their vertical scales appear more uniform in depth. In general, amplitudes of zonal currents are larger than those of meridional currents, as already observed for the Equatorial Indian Ocean in Dengler

and Quadfasel [2002]. However, this is the case for the shallower depths, while zonal and meridional amplitudes are comparable below 1000 m. No significant correlation between meridional and zonal current structure emerges neither in the transect, nor in the time series observations.

5.4.2 *Mooring data*

With the shallowest measurements at the equator and at 2.5°N, we best unveil the different vertical scales and time scales characterising these two relatively close locations.

In the off-equatorial location, time series of zonal and meridional currents show that the two components can have a similar vertical structure, while this never happens at the equatorial mooring. Moreover, we learn that coherence between equatorial zonal currents and the corresponding meridional currents is also not present in the time series.

From the measurements it is also clear that the shallow and the deep peaks of the EIC in the Atlantic are not consisting of constant westward currents (figure 5.7a), as already observed in the equatorial Pacific [Firing, 1987]. However, the annual mean transport of AAIW is indeed westward (figure 5.9a).

Perhaps the most fascinating feature that emerges from the present measurements is the latitudinal change in vertical structure of the flow between equatorial and off-equatorial moorings, especially in the meridional current component measured by the ADCPs at 0° and 2.5°N (compare shallower measurements in figure 5.8a and 5.8e). Anisotropy between the two current components is a well-known characteristic of the equatorial currents, however, time series of the two components have rarely been compared with such a high time and vertical resolution. This, in fact, also allows to point out a difference between the anisotropy present at the equator and the one present at 2.5°N. At the equator, anisotropy between the two current components seems to affect both time and vertical spatial structure. At the off-equatorial mooring only the time scales seem to differ between the two components, while the vertical structure is comparable, and spans the whole 500 m sampled by the ADCP. The measurements also suggest that this change in vertical structure of the flow has to take place somewhere between 1°N and 2.5°N. The small-scale structure of the portion of the water column measured by the ADCP at 0.96°N, in fact, resembles more the complex, equatorial one than the northern location. This recalls the work of van Haren [2005], where the latitude $|\lambda| = 1.5 \pm 0.5°$ has been identified as the location where a sharp near-equatorial transition could occur in the near-inertial wave field with possible consequences for the mean flow.

In the ADCP measurements, large vertical structures seem to occur especially at the off-equatorial locations, and current meter measurements also suggest

the occurrence of vertical coherence exceeding 1000 m. This, however, might be an artefact of the vertical spatial distribution of our instrumentation. Such large structures are not present in data sets as the one in Brandt *et al.* [2011]. Moreover, Brandt *et al.* [2011] also show an extremely coherent picture of the jets at 23°W, profoundly different from what is observed in our data set. Possibly, the difference in longitude between the two study areas plays a role. However, it is suggesting that a zonal coherence of the jets of 15 to 27°[Gouriou *et al.*, 1999; Schmid *et al.*, 2005] might be overestimated.

We notice that, despite the strong anisotropy in the current distribution in the shallower measurements, that the deeper current meters present a more isotropic distribution.

A spectral analysis of the energy content sheds some more light on the temporal behaviour of equatorial and off equatorial currents and waves (figures 5.10). Low frequency features prevail at all depths and at all locations, and, below 1000 m, the energy content is not monotonically decreasing with depth.

For the low frequency range (periods longer than 5 d), the most striking feature is perhaps that inertial peaks, well in the resolved frequency range for all off-equatorial moorings, are simply not present. This is found at all depths and for all locations covered by this data set. Moreover, inertial peaks are absent in total kinetic energy spectra (figure 5.10), but the same is valid even if we consider the two components of the current individually. This might be due to the fact that the low frequency spectrum is everywhere enhanced, thus masking the local inertial peaks.

Moreover, in the spectra, a sudden drop in energy content occurs coherently between the inertial periods of 1°N and 2°N, at around 20 days, in the moorings at 2°N (at 1200 m, 2000 m, 3900 m) and 2.5°N (at 750m, at 3900 m). This might suggest, again, that a transition of regimes might take place around 1.5°, coherently with what we observed with the angular momentum analysis, and with the vertical structure of the current distribution.

In the high frequency range (periods shorter than 5 days), the signals appear more familiar, with the tidal peaks shaping all spectra.

The polarization analysis helped to retrieve the inertial peaks, at least for the moorings at 2°and at 2.5°N (figure 5.11). In fact, although invisible in the kinetic energy spectra, they emerge as (almost) circularly polarized waves when the rotary coefficient is considered. Polarization analysis of equatorial waves in van Haren [2005] showed that when the equator is approached, near-inertial internal wave motions suddenly change polarization from near-circular, typical for mid-latitude values down to 5°, to near-rectilinear. The collapse was hypothesised to take place, again, across latitudes 1.5°±0.5 [van Haren, 2005]. With the meridional resolution of this dataset, we can confirm that at latitudes smaller then 2°N, a clear signature of circularly polarized near-inertial waves is lost (see summarising sketch in figure 5.13).

We wonder if the rectilinear nature at the long periods, evident in all moorings, is perhaps representative only of the strong anisotropy of the current field. Here, in fact, the zonal component of the current prevails at low frequencies, and thus overlaps in frequency the local near-inertial band, perhaps masking the circularly polarized near-inertial signal. This emerges clearly from the hodographs in figure 5.12, where near-inertial motions are displayed for the five moorings, at different depths. At the equator, rectilinear motion prevails down to about 2500 m, while it is mainly circular at the northernmost mooring, throughout the whole water column. We have to remember, however, that at each location of figure 5.12, the frequency range we are looking at is different. We speculate that at the equator, time scales of near inertial motion and jet variability superpose, influencing each other, while this is not the case at 2.5°N, where the time scale of near-inertial motion (around 11 d) differs from the longer time scale typical of jet dynamics (at least seasonal). However, if we performed the polarization analysis using only the pseudo-baroclinic part of the two current components (obtained by subtracting at each time the measured pseudo-barotropic current, defined as the vertical average using only ADCP data), the general picture does not drastically change, suggesting that the collapse of the near-inertial circular polarization might not be entirely explained by the presence of the zonal jets, or that the jet vertical scales should be also taken into consideration for a more accurate analysis. Unfortunately, from our observational data set, we cannot separate more precisely low frequency jet dynamics and other dynamical mechanisms present in the system at the same time scales.

From figure 5.12 we also observe a change from mainly zonal currents at the equator to strongly meridional near-inertial currents at 1°N. This tendency towards a meridional motion is reminiscent of low-frequency internal wave equatorial focusing [Stern, 1963; Bretherton, 1964; Stewartson, 1971, 1972], and, in particular, of meridional trapping of internal waves (see chapter 3). This trapping mechanism is based on the nature of internal wave propagation in stratified and rotating fluids, and has been subject of numerous theoretical and laboratory analysis [Maas, 2001; Harlander and Maas, 2006; Maas and Harlander, 2007]. It is here of particular interest since equatorial trapping of internal waves could trigger zonal flow (such as the EDJs) in stratified and rotating fluids, and that indeed depends upon angular momentum distribution in the domain [Harlander and Maas, 2006; Maas and Harlander, 2007; Calkins *et al.*, 2010; Noir and Cébron, 2013; Scolan *et al.*, 2013; Vantieghem *et al.*, 2015]. The observed confinement of small vertical spatial scales at the near-equatorial latitudes, especially evident in the meridional component of the current (compare figures 5.7a and 5.7e, and figures 5.8a and 5.8e), can be interpreted as a direct observational evidence of the occurrence of internal wave focusing in the area, due to trapping of the low-frequency waves within the corresponding

critical latitudes [Maas and Harlander, 2007] and chapter 3. In this perspective, small vertical scales would correspond to vertical (oblique) propagation of a certain frequency throughout the water column, while larger vertical scale would correspond to a standing wave pattern. Using the present dataset, preliminary analysis of the amplitude and phase of the time series in the portion of the water column measured by the ADCP confirms this low-frequency trapping.

Polarization characteristics do not only vary with latitude, but they also present a very strong, and non-monotonic, variability with depth. Despite this variability, spectral peaks at around 60 and 120 d are present in all moorings, at different depths. These peaks present polarization values of about 0.5/0.6, and, most importantly, they are subinertial everywhere but at the equator. The presence of strong, subinertial internal waves could be evocative of the occurrence of low-stratification episodes, that would support low frequency waves to propagate more polarward of what is expected for a classical rotating, stratified ocean case (see for example figure 11 in Gerkema *et al.* [2008]). However, this situation is not supported by the measurements in the quasi-synoptic CTD transect. Otherwise, subinertial waves must be interpreted in terms of planetary equatorial waves: Rossby, Kelvin and Yanai waves [Matsuno, 1966], or the evanescent tail of the inertial-gravity wave range [Maas, 2001]. The fact that the equatorial polarization spectrum is expected to be rectilinear, in principle, not only for equatorial Kelvin waves, but also for equatorial Rossby waves [Weisberg *et al.*, 1979], supports this interpretation. Moreover, at a period of about 30 d, all locations present an evident rectilinear behaviour (figure 5.11) that could be also read as a strong presence of equatorial planetary waves, typically characterised by this time scale. Both an improved theoretical understanding of equatorial wave dynamics, especially regarding the deep dynamics, and additional data on zonal and vertical wave numbers are needed to be able to further explore this hypothesis.

5.4.3 *A note on isolines of angular momentum and EDJ spatial structure*

We have noticed a correspondence between regions of high-steppiness and equatorial deep jets. In our transect, both of them span a meridional range between 0° and 1° N, and a vertical range down to about 2500 m. In D'Orgeville *et al.* [2004] equatorial stratification layers, mainly present within westward jets, have been interpreted as the by-product of angular momentum mixing due to the occurrence of inertial instabilities. Equatorial inertial instabilities occur whenever the angular momentum decreases with increasing distance from the rotation axis, but obviously instabilities of mean flow require explaining why the flow can turn unstable in the first place. D'Orgeville *et al.* [2004] found that the presence of alternating jets with realistic spatial scales can change the spa-

tial distribution of angular momentum, and cause these instabilities. However, this seems not to be the case in our data set, where the highest zonal current amplitude values are centred at the equator. Instead, temporal instabilities may be produced by large amplitude waves at different time scales (as we have seen in the geostrophic calculations) and be the mechanism leading to the unstable flow.

Colin de Verdière and Schopp [1994] predicted density homogenisation within closed lines of angular momentum, for the case of a longitudinally independent, eastward equatorial jet. The homogenisation of density (or other tracers) inside closed vortex lines implies a quasi-conservative flows with zero Ertel potential vorticity, constituting another factor to fulfil inertial instability condition [Hua *et al.*, 1997; Send *et al.*, 2002].

Using the CTD/LADCP transect data, we can superpose lines of constant total angular momentum Γ to the density and current fields (figures 5.4 and 5.5 respectively), with Γ defined as

$$\Gamma = \Omega r^2 \cos^2(\phi) + ur\cos(\phi) \tag{5.4}$$

where ϕ is latitude, Ω is the Earth rotation rate, u is the measured zonal current and r is the radial coordinate [Colin de Verdière and Schopp, 1994]. Constant planetary angular momentum lines are drawn as grey contours (first term in equation (5.4)), while constant total Γ-lines are superimposed as black contours. The radial coordinate choice is particularly appropriate for the equatorial case: the curvature of the Earth is evident from the parabolic lines representing planetary angular momentum only (grey lines in figures 5.4 and 5.5).

In figures 5.4 and 5.5, no closed lines of angular momentum are visible, as predicted by Colin de Verdière and Schopp [1994]. This is because the transect does not cross the equator line. However, closing of the lines is observed in correspondence with eastward jets (see figure 5.5a) if a mirrored image is hypothesized for the southern hemisphere. Density anomalies in the EUC (figure 5.4) area appear to closely follow constant Γ lines in the first half to one degree from the equator. Others relatively strong anomalies also occur in correspondence with semi-closed angular momentum lines (eastward jets). The signature of density homogenisation within the EUC has been supported also from previous data sets, where this has been observed in terms of oxygen content [Stramma and Schott, 1999].

We wonder if the spatial structure of lines of constant planetary angular momentum could also tell something on the vertical and meridional distribution of equatorial jets. In fact, highest steppiness values are enclosed in the iso-angular momentum line that also encloses the EDJs (red line in figures 5.4 and 5.5). This would further support a spatial relation between EDJs and steppiness, although different from the correspondence between stratification steps and westward jets found in D'Orgeville *et al.* [2004]. Even when the inertial hodographs are

compared at different latitudes and depths, the parabolic iso-angular momentum lines seem to divide the latitudinal transect in areas where inertial motion is more or less circular, highlighting the profound difference between moorings north and south of 1.5°N, but also suggesting an explanation for the depth variability of the wave orientation.

From figures 5.4 and 5.5 it seems that the relative angular momentum (determined by the second term on the right hand side of equation (5.4)) acts only as a secondary disturbance to the isolines of planetary angular momentum. From figure 5.9 it is clear that on the time scale of a year, only the signature of the jets will remain and change the robust structure due to Earth rotation.

From figure 5.5 we thus conclude that the isoline embracing the EDJs is the one emerging at the surface around 1°N, and crossing the equator at about 2500 m. But why should this isoline be somehow different from the others? We can exclude here mechanisms related to the presence of Stewartson layers, such as the ones playing a role in the formation of zonal mean flow in laboratory experiments as in Hollerbach [2003] or Koch *et al.* [2013]. If this would be the case, the "special" isoline would be the one tangent to the ocean floor, and emerging at about 1.5°N. Although appealing, the relatively strong stratification observed (figure 5.2) makes this mechanism unlikely to play any significant role in this context. However, it is interesting to note that also in other laboratory experiments [Noir *et al.*, 2009; Sauret *et al.*, 2010], zonal jets have been triggered in the equatorial regions of rotating shells only in areas confined close to the outer boundary, not reaching the inner core of the shells (the ocean "bottom"). The mechanisms determining the depth penetration of the jets are not fully understood yet, but ocean EDJs seem to resemble a similar spatial distribution.

5.5 CONCLUSIONS

A summary of all the observed features is sketched in figure 5.13. We have tried to systematically point at all those features and phenomena characterising the "equatorial boundary layer" and distinguishing it from the off-equatorial regions. We suggest that this "equatorial boundary layer" might be identified dynamically as the region where EDJs, and small vertical scales are observed in the current field (alternating grey/black structures in figure 5.13). This region seems to follow the spatial distribution of planetary angular momentum down to a certain depth (around 2500 m, black thin parabola in figure 5.13). In the same region, density layering ("steppiness") is also enhanced, reinforcing the link between the presence of small vertical structure in the current field, and anomalous mixing properties. Whether the layering phenomenon is part of the generation and/or maintenance of the jets, or is part of their dissipation
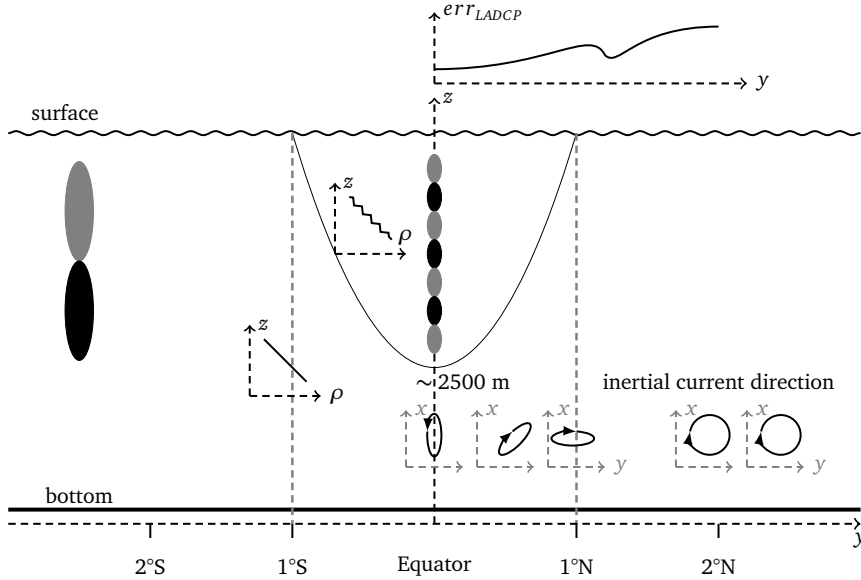
Figure 5.13: Summary of the observed features in the near-equatorial region. Note that some of the results found in the northern hemisphere are represented as occurring in the southern. Density profiles are depicted inside and outside the black parabolic iso-angular momentum line tangent to 2500 m. Large vertical variability of zonal and meridional velocities (alternating in direction grey/black, indicating positive and negative values) in the off-equatorial regions are contrasted to smaller vertical variability in the equatorial region. Differences in the polarization properties and in the main direction of near-inertial waves are depicted near the bottom in the northern hemisphere. They are observed to have a meridional dependency, but not a vertical one, within the dashed, grey line around ±1° (where the black parabola surfaces). LADCP errors (upper-right corner) also present a meridional variability with a discontinuity at 1°N, while the vertical variability is associated, as usual, with the scatterers distribution in the water column. Note the unusual orientation of the zonal-meridional axis, to better represent the equatorial geometry, displaying a change in the near-inertial motion orientation.

process, remains unclear. Also the polarization properties of the near-inertial waves present a strong latitudinal dependency.

In figure 5.13, note the unusual orientation of the zonal-meridional axis, to better represent the equatorial geometry, displaying a change from mainly zonal currents at the equator to strongly meridional near-inertial currents at 1°N. The tendency towards a meridional motion can be interpreted as an observational evidence of meridional trapping of low-frequency internal waves in the equatorial regions [Stern, 1963; Bretherton, 1964] and chapter 3. This mechanism is here of relevance, since, in principle, it could trigger and support equatorial, zonal flow, collecting energy from off-equatorial regions and focusing it in the equatorial regions [Maas and Harlander, 2007]. Moreover, relatively high energy levels measured at intermediate depths (such as the one at 2500 m from 0.61°N), are also suggestive of energetic hot spots as the one that would occur along internal wave trapped paths. Hodographs like the ones in figure 5.12, but at single, selected frequencies (and in a WKB-stretched geometry) could help investigating in this direction. However, a more complete vertical coverage of the measurements is certainly necessary to make conclusive statements on this issue.

Around $1-1.5°N$, all these equatorial features disappear, and the dynamics resembles the one typical of mid-latitudes. This is the end of the "equatorial boundary layer", and it is interesting to note that it corresponds to an unexplained enhancement in the velocity errors (top right panel in figure 5.13), and to a local maximum of steepness at all depths (figure 5.3d).

We are obviously still far from a comprehensive understanding of the interaction of between meridional currents and EDJs, and of the role of the internal waves in the near-equatorial region. This is due to a combination of factors, as the scarcity of long-term time series of the equatorial current field and their poor meridional and vertical resolution. In this work, we have brought together observational evidence from different perspectives, from a quasi-synoptic hydrographic and hydrodynamic transect to a set of deep, long term moorings. All features suggest the presence of a near-equatorial "boundary layer", spatially well identified, and characterised by dynamical properties that clearly differ from the ones at mid-latitudes. As we have seen in the introduction, the idea of an "equatorial boundary layer" is not new from a theoretical point of view, but it has been here for the first time explored using *in situ* observations. The results suggest that this framework of interpretation can indeed be used to guide and support future theoretical and observational efforts in understanding this key region in the Earth ocean system, e.g. in formulating and verifying hypotheses for the generation and maintenance mechanism of the strong zonal currents.

<div style="text-align: right; font-size: 3em;">6</div>

CONCLUSIONS AND FUTURE PERSPECTIVES

In this thesis we have investigated the notion of an equatorial boundary layer from different angles. A simple reason to be interested in the ocean dynamics of the low latitude belt is that, to date, we know very little about it, despite the critical role this portion of the ocean plays in the local and global climate. We have seen that difficulties in interpreting equatorial ocean dynamics come both from theoretical and from observational shortcomings. Trying to connect all the unknowns has been one of the aims of this thesis. This enabled us to propose some answers to the research questions we started out with (see chapter 1). It also helped us to formulate questions more precisely, and to point out where our knowledge is suffering from a deep lack of information, or comprehension. Thus, in section 6.5, a few ideas for future work and research are listed that we did not have the occasion to pursue here. Let us now look back at the research questions posed in chapter 1 one by one.

6.1 EQUATORIAL WAVE DYNAMICS

Is the classical set of equatorial waves, commonly used in literature [Matsuno, 1966], a valid tool for describing equatorial dynamics? If not, what are its limitations and how can it be improved?

One of the major difficulties in understanding equatorial dynamics certainly lies in its geographical position. On our planet, the equator is indeed the place where many of the approximations usually adopted in oceanography to simplify the equations of motion break down, with truly unknown consequences on our mathematical and physical representation of equatorial currents and waves. In chapter 2 we tackle this first question, taking into consideration surface, interfacial and internal waves. It came as a true surprise how easily a well-established, widely used and classic textbook theory as the one presented in Matsuno [1966] can show its limitations. The addition to the system of a simple realistic ingredient, such as the full Coriolis force is enough. Its inclusion, however, appears

to be natural and well motivated when interested in low-latitude wave dynamics. The main reason of the theory's shortcomings lies in the coupling between vertical and meridional coordinates caused by the non-traditional terms, leading to the non-separability of the resulting equations of motion. Restoring the neglected Coriolis terms gave us the possibility of finding new analytical solutions in the case of surface and interfacial waves both of Kelvin type and with non-vanishing meridional velocity. If, on the one hand, we have pointed out where the theory fails, on the other hand the picture is not so pessimistic in the light of the observational results from chapter 5. There, non-traditional terms have been shown to be just too weak to either be measured in a quasi-synoptic transect, or to actively play a role in the dynamics, at least in the geostrophic context. This does not mean that the classical, equatorial geostrophy is sufficient. Because of the strong baroclinic pressure gradient, no balance is in fact observed in the quasi-synoptic transect without at least a 30 km spatial smoothing, suggesting the importance of the inertial (time dependent) terms. However, the non-traditional term is still one order of magnitude smaller than the traditional one. This indicates that practically it can be neglected, or at least its contribution can be neglected when one is interested in the steady dynamics of the upper part of the water column. This would mean that our traditional understanding and representation of equatorial waves [Matsuno, 1966] should suffice to capture and realistically describe and reproduce some equatorial features, at least the ones affecting the surface and thermocline dynamics, such as, most importantly, ENSO.

This is still puzzling, though, as the traditional dynamics could not be described as a particular limiting case of a more general and robust non-traditional theory, but instead supports waves that simply cannot exist when the full Coriolis force is considered. Moreover, another limitation of the classical equatorial wave theory is that it only concerns surface and interfacial waves, leaving out the whole class of internal waves. Requiring the presence of an infinitely deep, motionless layer underneath the active one (either the surface, or thermocline, only a few hundreds meters deeper), as commonly assumed in traditional approaches, might come as a surprise in a location where currents measure up to 10 cm/s down to 2500 m, see for example, besides chapter 5, Gouriou *et al.* [1999]; Dengler and Quadfasel [2002]; Send *et al.* [2002]. The complex dynamics of the strong, alternating equatorial deep jets is in fact still demanding an explanation, most likely in terms of wave-mean flow interaction phenomena that could in principle trigger, maintain, and dissipate the jets.

Considering internal waves in the equatorial ocean, however, brought into the discussion a whole lot of new, fascinating issues, related to the very nature of this particular type of waves. Their oblique propagation, their domain-dependent solution, and the occurrence at the equator of internal wave attracting trajectories made immediately clear that a classical, analytical approach is

simply not feasible in the internal wave case. In short, the three-dimensional internal wave problem in an enclosed domain is an ill-posed hyperbolic boundary value problem [Rieutord *et al.*, 2000], and smooth solutions exist only for very few symmetric geometries (for instance, for a fluid contained in a full sphere or in a cylinder). This brings us to the next question, that takes advantage of an alternative approach to the problem of internal waves in arbitrarily shaped enclosed geometries (such as the spherical shell, our idealised ocean): the ray-tracing technique [Whitham, 1974; Broutman *et al.*, 2004].

6.2 INTERNAL WAVES IN SPHERICAL SHELL DOMAINS

> *In literature, theoretical studies on internal wave rays have been restricted to two-dimensional domains. In the context of geophysical studies, this corresponded to meridional (zonally symmetric) settings. Only recently, numerical and laboratory experiments have started investigating a three-dimensional approach to ray tracing [Manders and Maas, 2004; Maas, 2005; Hazewinkel, 2010; Hazewinkel et al., 2011b]. Is the idea of equatorial internal wave attractors still valid when we allow waves to propagate zonally too, a step towards a more realistic representation of the real phenomenon?*

Previous studies [Dintrans *et al.*, 1999; Rieutord *et al.*, 2001; Maas and Harlander, 2007] had in fact hypothesised that the behaviour of internal waves confined in a thin shell such as our ocean could be responsible of large energetic input in the equatorial belt, with unknown consequences on the local currents, wave field and mixing properties. This was based on axisymmetric, two-dimensional numerical and ray tracing studies of internal inertial waves in the spherical shell domain (or better, in one of its infinite meridional planes), as a paradigmatic case study for the broader class of inertia-gravity waves in domains of geophysical and astrophysical relevance. Maas and Harlander [2007] proved the occurrence of strong (short) internal wave attractors in the equatorial belt of the domain, but what if the rays, here classically interpreted as representative of energy paths, were launched with a non-zero initial zonal component? This would not only allow a more realistic, localised forcing, but also a three-dimensional propagation of the waves, as well as the development of azimuthal inhomogeneities, ruled out in the two-dimensional case. In chapter 3 we developed an appropriate three-dimensional algorithm to follow the rays in the three-dimensional spherical shell geometry. Thanks to this numerical algorithm, it is found that some frequency bands in the inertial wave range support meridional trapping of the rays. In these bands, internal wave ray trajectories, whose motion is initiated outside a meridional plane, are eventually

trapped onto a meridional plane, from which they cannot escape any longer. We call this meridional plane a "meridional attractor". Once on a meridional plane, rays are further subject to the occurrence of the expected two-dimensional attractors [Maas and Harlander, 2007]. In addition, the existence of trajectories that are not meridionally trapped is also observed, whose dynamics was not captured by previous, purely meridional studies. These ray trajectories constitute a new and interesting class of possible solutions for inertial waves in the spherical shell. Even if the physical relevance of these type of orbits is not clear yet, they could help in the interpretation of some recent laboratory [Hazewinkel *et al.*, 2011a; Koch *et al.*, 2013] and numerical [Drijfhout and Maas, 2007] three-dimensional results. Certainly one of the questions these propagating waves raise concerns three-dimensional orbit periodicity. In fact, it is appealing to adopt, in the three-dimensional context, the usual association, valid in two-dimensional frameworks [Harlander and Maas, 2007], that attractive orbits are representative of the singular nature of internal wave field solutions in domains such as the spherical shell [Bretherton, 1964; Stewartson, 1971, 1972], while periodic orbits represent regular solutions (usually referred to as the *modes*) of the studied system. But are we allowed to do so? This brought us to tackle the third research question.

6.3 INTERNAL WAVES IN SPHERICAL DOMAINS

> *Which are actually the power and the limitations of the three-dimensional ray tracing approach in studying internal waves dynamics in enclosed domains?*

If one is interested in assessing the value of three-dimensional ray trajectories and their significance for the underlying wave field and energy distribution in the domain, one has to compare ray tracing paths with something else, namely numerical or analytic solutions for the domain in analysis. However, as we have seen, analytical solutions for internal waves in a spherical shell geometry do not exist [Rieutord *et al.*, 2000]. This brought us to chapter 4, and to apply the same three-dimensional ray tracing algorithm to the full homogeneous rotating sphere. Although an even more simplified shape of the domain may seem a step backwards, far away from our equatorial ocean, the sphere is one of the very few domains where analytical solutions are known for the linear, inviscid case [Bryan, 1889], and where (two-dimensional) ray tracing theory has also been already applied [Dintrans *et al.*, 1999; Rieutord *et al.*, 2001]. In this setting the association between periodic orbits and the modes of the sphere (corresponding to the eigenfrequencies) has not been retrieved, for reasons that we now understand.

Restricting the rays to a meridional plane only, in fact, constitutes a dramatic limitation if one is interested in the behaviour of inertial modes of the full three-dimensional sphere, as we have learned in chapter 3. On the other hand, once a three-dimensional ray tracing algorithm is applied to the three-dimensional sphere, three-dimensional periodic orbits are retrieved.

Two main frequency regimes can be distinguished, according to the different behaviour of the orbits: $\omega^2/4\Omega^2 < 1/2$ and $\omega^2/4\Omega^2 > 1/2$, where Ω is the angular velocity of the sphere. In the low frequency regime, three "families" of periodic orbits are found: polygon, star and flower-shaped trajectories, classified according to their appearance in the top view. Interestingly, in this regime, the critical circles, where rays and the domain boundaries have the same inclination, define an inscribed cylinder that acts as a physical barrier for the orbits, confining the rays to the equatorial belt. In the high frequency regime, no regular pattern but of flower type is observed. However, periodic orbits are still present, while critical circles stop playing such a prominent role. A correspondence between closed, periodic ray orbits and classical Bryan wave modes is hardly retrieved (so far, only for the flower trajectories). Moreover, and unexpectedly, observed winding numbers of many trajectories (the required number of loops around the sphere before the ray repeats itself) present values larger than one. This is on the one hand puzzling, especially if one is interested in the reconstruction of the underlying physical wave field using the ray's structure, but on the other hand is suggestive of a new possibility. We speculate that a pressure function (of the separable form, $p = P_n^{|k|}(\xi)P_n^{|k|}(\mu)e^{ik\phi}$, in terms of Legendre polynomials, as in equation (4.5)) with *rational* wave numbers n and k, could also constitute a set of valid solutions for inertial waves in a full sphere, provided that boundary conditions are satisfied (no energy flux through the boundaries, and finiteness in the whole domain, rotation axis and equatorial plane included). Three-dimensional ray orbits could possibly thus not only be representative of non-separable, zonally propagating solutions, but also of eigenmodes different from the integer degree and order ones classically obtained from equation (4.6), whose mathematical completeness is, in fact, so far unknown. This would explain the difficulty in relating the periodic orbit with the classic eigenfrequencies of the system. Nevertheless, enough and differently shaped closed patterns have been found to deduce some general properties on the periodicity of the orbits and the observation of other trajectories would not change the overall picture of the system. The existence, in fact, of inertial wave, periodic orbits in a regular three-dimensional container such as the sphere allows to extend the usual two-dimensional correspondence between regular solutions and periodic ray trajectories, previously discarded [Dintrans *et al.*, 1999], to a three-dimensional setting.

In chapter 4, we also analysed three-dimensional ray trajectories in terms of quantum chaology [Berry, 1987]. Interestingly, repelling and unstable pe-

riodic orbits such as the ones observed in the sphere profoundly differ both from the plane-filling ensemble of periodic orbits characterising regular, hyperbolic, two-dimensional systems (as for example, the circular domain), as well as from the classical annulus-filling non-isolated periodic orbits typical of elliptic systems (as for example, the case of surface waves in the circular billiard). In fact, even if the closed orbits in the sphere are non-isolated under rotation around the z-axis, they remain isolated in a three-dimensional sense. Thus, they resemble more the isolated, unstable ray trajectories found in elliptic, classically chaotic systems [Berry, 1981, 1987; Kudrolli *et al.*, 2001]. This different type of orbits could be the result of a highly anisotropic three-dimensional space, whose anisotropy is set by the presence of the rotation axis (along the vertical). Focusing and defocusing in the vertical direction coexist then with spreading and scarring in the horizontal plane (perpendicular to the rotation axis), also because focusing reflections in the vertical plane lead to a change in cross-slope momentum, while not affecting the momentum in the along-slope, tangential direction. In addition, we have seen from equation (4.2) that for general (non-symmetric) three-dimensional domain shapes, the system acquires a hybrid character, in between hyperbolic and elliptic problems. Consequently, it may well show asymptotically both periodic attracting orbits, as in the spherical shell (chapter 3), as well as periodic repelling orbits, as the ones observed in the sphere (chapter 4), characteristic respectively of singular and regular wave fields. It is also worth noting that such repelling periodic orbits are living in the spherical shell too, provided that rays do not interact with the inner boundary, and thus that attractors, periodic and invariant modes could in principle coexist in the same three-dimensional domain: in fact Maas [2005]; Drijfhout and Maas [2007] and chapter 3 have already shown that attractors and invariant modes (there also called "edge" or "whispering gallery" modes), can indeed occur simultaneously in a stratified paraboloid, channel and spherical shell (all symmetry breaking geometries). In terms of energy content, however, attracting orbits will always prevail over periodic orbits in symmetry breaking geometries, because of the former's focusing power.

The existence of such a rich behaviour confirms that, even if in three-dimensions we have not observed a one-to-one correspondence between classic orbits and *modes* of the system (eigenfrequencies), we can still use the behaviour of the three-dimensional rays as an ingredient for deriving general information on the spectrum and on the regularity of a system, when no other information is available.

We are conscious that all results obtained by means of ray tracing are restricted to linear, inviscid fluid dynamics, and bear clear limits to their direct application to realistic, geophysical fluids. However, when it comes to geophysical applications, successful and meaningful applications of a two-dimensional ray approach to a realistic context is not exceptional [Broutman *et al.*, 2004]

and has been recognised to provide a unique contribution to the understanding of both spatial structures and spectra of atmospheric and oceanic internal waves.

In the ocean, internal inertia-gravity waves are generated near ocean boundaries, at the surface by atmospheric perturbations, or over deep topographic features, by tidal forcing. These waves are observed to travel as confined energetic beams that can propagate through the ocean for thousands of kilometres [Zhao *et al.*, 2010] and they constitute, by means of breaking and other small scale processes, one of the contributors to the deep ocean vertical turbulent diffusivity, necessary for maintaining the stratification and, over all, the global overturning circulation [Wunsch and Ferrari, 2004]. Interestingly, density and angular momentum mixing due to internal wave breaking has already been observed to generate a mean flow [Maas, 2001; Tilgner, 2007; Noir *et al.*, 2009; Swart *et al.*, 2010; Calkins *et al.*, 2010; Morize *et al.*, 2010; Sauret *et al.*, 2010; Grisouard and Bühler, 2012; Le Bars *et al.*, 2015], generally linked to the formation of highly coherent (prograde) zonal currents (jets), [Maas, 2001; Maas and Harlander, 2007; Seelig, 2014; Seelig and Harlander, 2014]. The possible link between features due to internal wave focusing and breaking, and the complex, low-latitude dynamics observed in our ocean (EDJs, unexpected internal wave properties), atmosphere [Galperin, 2004; Ogilvie and Lin, 2004], and stars [Balona *et al.*, 1996], is appealing.

It is then time to move to observations, and try to relate the theoretical findings obtained so far to the *in situ* measurements recently collected in the equatorial Atlantic Ocean. Would this be even possible?

6.4 IN SITU OBSERVATIONS FROM THE EQUATORIAL ATLANTIC OCEAN

> *Turning to observations, in which sense can the equatorial region be considered a boundary layer? And how do the observed equatorial features, distinguishing it from the mid-latitudes, relate with the previous theoretical findings and with literature?*

Unfortunately, the answers to these questions are not as straightforward as one would like them to be. Mainly, this is due to the ocean vastness and complexity, combined to our limited capability of observing ocean processes. To try to bridge theory and observations, a relatively rich data set has been considered for this study as has been presented in chapter 5. The data set consists of a CTD/LADCP transect at 38°W, between 0° and 2°N, and of current time series from December 2007 to July 2009. We have been able to isolate various equatorial features, brought to light by different and independent measurements (hydrography and currents). We schematically summarised them in figure 5.13. All processes indeed suggest the existence of an "equatorial boundary

layer", spatially well-defined and dynamically distinct from the off-equatorial regions. Interestingly, this "equatorial boundary layer" seems to be related to the distribution of planetary angular momentum in the region, and the spatial superposition of small vertical structure in the velocity field, anomalous mixing properties and latitudinally varying near-inertial wave polarization properties seem to reinforce the link between these equatorial features, that at first sight appear unrelated.

If on the one hand we have been able to explicitly point at an observable and measurable "equatorial boundary layer", on the other hand the bridge between the measured features and the theoretical interpretations of an "equatorial boundary layer" that we explored in previous chapters is not completely built yet.

So far, only few indications that we are applying the correct concepts to interpret equatorial dynamics emerged. First, for example, troubles are encountered when one is interested in quantifying the role of non-traditional terms in the dynamics. The relevance of these terms seems obvious from a theoretical point of view (see chapter 2), but their presence is elusive in the actual measurements. Non-traditional terms are just too weak to be measured and/or actively play a role in the dynamics, and thus they can indeed be practically neglected. As we have already seen, however, because of the strong baroclinic pressure gradient, no balance is in fact observed in the transect without at least a 30 km spatial smoothing, meaning that the classical, equatorial geostrophy is also not able to capture the relevant dynamics. It seems that unsteady, temporal (slow and fast) dynamics plays here a major role, but unfortunately, due to the quasi-synoptic nature of the dataset (it took about 84 h of combined measurements and sailing to complete the data acquisition) it is not possible to assess the relevance of the non-traditional terms at these time scales. However, when we look at the orientation of the near-inertial currents, we do observe a general tendency towards a meridional motion, reminiscent of the meridional trapping of equatorial internal waves occurring in our three-dimensional ray tracing studies (chapter 3). Interestingly, we like to remark that this focusing phenomenon can only occur when the non-traditional effects are taken into account.

The observed confinement of small vertical spatial scales at the very low-latitudes, especially evident in the meridional component of the current, also constitutes an indication for internal wave focusing in the area, due to trapping of the low-frequency waves within the corresponding critical latitudes (Maas and Harlander [2007] and chapter 3). From this perspective, small vertical scales in the meridional velocity would correspond to the (oblique) propagation of waves of certain frequency in the vertical-meridional plane, while larger vertical scales in the meridional velocity would correspond to a standing wave pattern in the vertical-meridional plane. Analysis of the amplitude and phase of the time series in the portion of the water column measured by the ADCP

seems to confirm this low-frequency trapping. Unfortunately, the available vertical resolution of the measurements is still not enough (only covering 500 m out of 4500 m) for making conclusive statements on this issue. Relatively high energy levels measured at intermediate depths are also suggestive of energetic hot spots as the one that would occur along internal wave trapped paths. At the end of chapter 5, we can conclude that the intrinsic three-dimensional nature of non-traditional dynamics, combined with internal wave motions, is indeed hard to capture with standard datasets. These waves seem to remain hidden in the gaps between our observations, in the whole lot of ocean we are actually not measuring.

6.5 FUTURE PERSPECTIVES

We would like to close this work with a few suggestions for possible, future investigations. First, as we have seen from chapters 2, 3 and 4, a renewed interest in the role of critical latitudes has emerged. These locations appear to shape the wave field in all, differently shaped, domains. Certainly further investigation is needed to understand and check with numerical, experimental and observational studies what the theoretical findings suggest. We are aware of a few experimental studies going into this direction, such as Seelig [2014]. However an experimental test of three-dimensional ray tracing poses some interesting, technical challenges (e.g. the isolation of a single ray from the whole set covering the internal wave cone, or the non-axisymmetric forcing mechanism, see section 4.6 for details), that constitutes a possible research path *per se*.

From chapter 4, several questions remained open. These are mostly related to the fact that when a three-dimensional ray tracing algorithm is used, the absence of any assumption on separability of the solutions could unveil the structure of intrinsically three-dimensional modes in the sphere, which remained hidden so far because of the particular form of solutions. The existence of periodic trajectories characterised by winding numbers larger than one is in fact suggestive of the possibility of adopting non integer (azimuthal) wave numbers. This perspective certainly requires further investigation.

Furthermore, several questions arise when one is interested in the wave field reconstruction on the basis of ray trajectories only. The three-dimensional periodic orbits observed so far in the sphere in chapter 4 are in fact very different from the domain-filling infinite ensemble of periodic trajectories that occurs in two-dimensional regular domains for each mode: most importantly, they are not domain-filling. This implies that evaluating the associated field in the whole domain from rays only remains a non trivial (if not impossible) challenge, although the existence of two differently shaped periodic orbits for a single fre-

quency (figures 4.22 and 4.23) might indicate a solution to this issue. We indeed leave the association between ray's structures, eigenfrequencies and modes, as well as a formulation of a three-dimensional equivalent of a trace formula for the wave field reconstruction [Gutzwiller, 1990] for future work. The answers to all these questions will help in compiling a more complete version of figure 4.4, and in interpreting the emerging patterns. Also, from chapter 4, a need for a three-dimensional phase space study of the orbits in terms of quantum chaology emerges [Berry, 1987], to shed some light on the hybrid nature of these new three-dimensional trajectories. Finally, in the light of the findings in chapter 4, we suggest to re-perform more rigorously the experiments by Lord Kelvin and assistants on rotational properties of oblate and prolate spheroids [Lord Kelvin, 1877, 1880a]. These experiments would certainly require a non trivial laboratory apparatus, both in terms of basin shapes and of rotation and visualisation facilities, but with the technology now available they would possibly provide answers to long lasting questions on the stability of inertial modes in spheroids, besides their undisputed historical interest.

From chapter 5, we also get some indications for future research. It is trivial to suggest that a better meridional-vertical resolution of measurements will certainly help in assessing both the equatorial trapping of low-frequency waves, as well as the oblique propagation of internal waves, and their role in the water column. However, we are conscious that *in situ* data are extremely demanding in terms of money and infrastructure. Hodographs like the ones in figure 5.12, but at single, selected frequencies could also help in determining wave propagation direction, together with an *ad hoc* ray tracing study in realistic (stratified) ocean conditions. Comparison of findings in chapter 5 with other analogous data sets acquired in different equatorial regions would also be interesting: this would require an additional observational effort, or, better, a fruitful collaboration with groups focused on other geographical areas, different from the Atlantic Ocean, or on other planets or stars.

THREE-DIMENSIONAL ALGORITHMIC RECONSTRUCTION OF RAY PATH IN A SPHERICAL SHELL

We discuss here the algorithmic reconstruction of the three dimensional path of an inertial wave beam in a spherical gap, subsequently reflecting on the curved boundaries of the convex (outer) sphere and of the concave (inner) sphere. The reflection of internal/inertial waves from a linearly sloping bottom was considered previously for plane waves in Phillips [1963], Phillips [1966], Greenspan [1968], Wunsch [1968], Wunsch [1969], Eriksen [1982b], Thorpe [1997], Thorpe [2001] and, from a curved bottom, by Gilbert and Garrett [1989]. Here we follow the derivation in Phillips [1963], as proposed in Manders and Maas [2004]. However, we will not use as framework of reference the plane defined by the incident and reflected rays, useful to study a single reflection alone [Phillips, 1963]. When considering multiple, subsequent reflections, it is much more convenient to choose a reference framework having a fixed direction with respect to the restoring force acting in the system. Here we thus align the vertical with the rotation axis, and the horizontal frame will be re-oriented at each reflection, the x-axis pointing in the direction of decreasing depth (outward).

Now consider we want to trace the behaviour of a perturbation at definite frequency ω. This will travel along a double cone (one propagating upward and one propagating downward) of internal wave rays. We will trace one single ray at a time, and it will be uniquely defined by the sign of its initial vertical velocity and three parameters: ω, $\vec{x}_0$ and its initial horizontal direction ϕ_0, measured anticlockwise with respect to the x-axis, which distinguishes it from other rays belonging to the same excited internal wave cone. Let the nth segment of the ray we are following be defined by a line l_n, and denote the time-derivative of the position along this ray, $\frac{d\vec{x}}{dt} = (u, v, w)$, which are the three components of the group-velocity vector. The group velocity will by definition be parallel to l_n. It is assumed further that the vertical has been stretched according to the

perturbation frequency so as to maintain the angle of the ray with the vertical fixed at 45°:

$$z' = z \frac{\omega}{\sqrt{1-\omega^2}}. \tag{A.1}$$

This approach has general validity, and bears a strong simplification in the calculations, the only price being the compression or elongation of the spherical shell domain into an oblate ($\omega < 1/\sqrt{2}$) or a prolate spheroidal ($\omega > 1/\sqrt{2}$) shell. To facilitate the reader, all figures in this paper have been subsequently re-stretched back to the original geometry. Moreover, in this study we are not interested in the group velocity magnitude [Shen and Keller, 1975], but in its direction only, therefore we can write without loss of generality

$$\vec{c}_g = (\mathsf{w}\cos\phi_i, \mathsf{w}\sin\phi_i, \mathsf{w}) \tag{A.2}$$

where

$$\mathsf{w} = \pm 1 \tag{A.3}$$

according to the initial launching direction. Here ϕ_i represents the "incoming" horizontal direction of the ray approaching a boundary, after the x-axis has been reoriented, pointing outward at the location where l_i intersects the boundary figure 3.1. As shown in §3.2.2, since the wave frequency does not change under reflection, the internal wave beam's angle with respect to the rotation axis (vertical) will also not change under reflection with the boundary: this is equivalent to requiring that the incident and reflected waves obey the same dispersion relation, equation (3.3). However, the group velocity vector changes magnitude upon reflection from the bottom, because, in the cross-slope direction, rays change distance, as is clear from figure 3.1a. This unusual property, typical of internal waves, and due to their anisotropic character, causes the wave number to change under reflection and energy to be transferred from one wave number to another. In an inviscid fluid, at reflection, the boundary condition of vanishing normal flow of the group velocity (energy flow) has to be also satisfied. This requires that in the incident and in the reflected ray the group velocity component in the along-slope direction (along the y-axis in the rotated framework), v, is unchanged, and is aligned with the isobaths. No net group velocity at reflection means

$$(\mathsf{w}_r \cos\alpha + \mathsf{u}_r \sin\alpha) = -(\mathsf{w}_i \cos\alpha + \mathsf{u}_i \sin\alpha) \tag{A.4}$$

where we define α as the angle which the bottom makes with the up-slope directed x-axis, where subscriptions r and i denote the reflected and incident ray respectively. With $s = |\nabla H| = \tan\alpha$, this can be simplified to

$$\mathsf{w}_i + \mathsf{w}_r = -s(\mathsf{u}_i + \mathsf{u}_r). \tag{A.5}$$

180

Since in this framework v is constant we can also write

$$v_i^2 = w_i^2 - u_i^2 = w_r^2 - u_r^2 = v_r^2 \qquad (A.6)$$

that can be rewritten as

$$(w_i - w_r)(w_i + w_r) = (u_i - u_r)(u_i + u_r) \qquad (A.7)$$

and therefore, with equation (A.5), $w_i + w_r$ can be eliminated:

$$u_r + sw_r = u_i + sw_i, \qquad (A.8)$$

where we assume no vertical wall ($u_i + u_r \neq 0$). The vertical wall case is treated later in this appendix. From equations (A.5(and (A.8) w_r and u_r immediately follow

$$
\begin{aligned}
w_r &= \frac{-2su_i - (1+s^2)w_i}{1-s^2} \\
u_r &= \frac{(1+s^2)u_i + 2sw_i}{1-s^2}.
\end{aligned}
\qquad (A.9)
$$

Together with the conditions $u_{i,r} = w_{i,r} \cos\phi_{i,r}$ and $v_{i,r} = w_{i,r} \sin\phi_{i,r}$, this implies an explicit relation between the incident and reflected angle:

$$\sin\phi_r = \frac{(s^2 - 1)\sin\phi_i}{2s\cos\phi_i + s^2 + 1} \qquad (A.10)$$

(equation (3.6) in section 3.2.2) which conforms with the expression in Eriksen [1982b]. The angle of reflection thus depends only on the angle of incidence of the ray, ϕ_i, and on the bottom slope s. Regarding the sign of the vertical component of the group velocity w, this is maintained when the bottom slope is locally supercritical (bottom slope larger than ray inclination), and reverses otherwise. These transformations also apply at the flat surface ($s = 0$), where they imply $(u_r, v_r, w_r) = (u_i, v_i, -w_i)$, meaning that the ray proceeds in the same horizontal direction while just reversing its vertical motion, and at a vertical wall ($s = \pm\infty$), where $(u_r, v_r, w_r) = (-u_i, v_i, w_i)$. It is possible to investigate the focusing or defocusing nature of a single reflection looking at the changes in the group velocity magnitude upon reflection. Because of energy conservation, after a focusing reflection, and the consequent decrease in wave length (see figure 3.1b for example: rays propagate according to the arrows), group velocity magnitude must decrease. Conversely, after a defocusing reflection (see again figure 3.1b for example, but with rays propagating in a direction opposite to the arrows), group velocity magnitude must increase. In the first case (focusing reflection) initial parameters are $w_i = -1$, $u_i = 1$ (case of normal incidence, $v_i = 0$) and $s < 1$. Applying equation (A.9) we obtain $|w_r| < |w_i|$ and $|u_r| < |u_i|$. Knowing $|v_r| = |v_i|$, $|\mathbf{c}_{g,r}| < |\mathbf{c}_{g,i}|$ follows, as expected. In the second case (defocusing reflection) initial parameters are $w_i = -1$, $u_i = -1$ and

$s < 1$. Applying equation (A.9) we obtain the reverse result, with $|\mathbf{c}_{g,r}| > |\mathbf{c}_{g,i}|$ as expected. Interestingly, if we approach a critical reflection ($s = 1$) in the first case, $|\mathbf{c}_{g,r}| \to 0$, this means that all rays are reflected along one single line approximately coinciding with the sloping wall itself. But if we approach a critical reflection in the second case, $|\mathbf{c}_{g,r}| \to \infty$, this means the incident ray is already travelling approximately along the slope, and two neighbouring rays could, in this limit, reflect infinitely far from each other. The geometrical mechanism of repeated reflections of internal waves can thus be studied provided at each reflection point we realign the x-axis with decreasing depth prior to application of the reflection laws.

Given the dimensionless topography, which defines the domain, determined by the outer sphere, $z = h_{out}(x,y) = \pm\sqrt{1 - x^2 - y^2}$, and the inner sphere, $z = h_{in}(x,y) = \pm\sqrt{\eta^2 - x^2 - y^2}$, we choose an initial location (x_0, y_0, z_0), on the outer or on the inner sphere, an initial horizontal direction, ϕ_0 (one ray on cone), and the initial sign of the vertical group velocity component $w_0 = +1$ or -1, in accordance with the location of the initial point. The magnitude $|w_0|$, not relevant to our problem, has arbitrarily been set equal to 1 here, and $|w_i|$ is reset to 1 prior to each reflection. Consistently, we thus do not reconstruct algorithmically the changes in wave amplitude along the ray path. This problem has been investigated in detail in the work by Shen and Keller [1975], in the specific case of oceanic or atmospheric propagating waves. We remark that the topography is described in stretched coordinates, so that, as already mentioned, the vertical inclination of the ray is always $\theta = 45°$. It is then possible to determine iteratively the subsequent intersections with bottom and surface, (x_n, y_n, z_n), as well as the horizontal angle ϕ_n and group velocity u_n, v_n, w_n (of which only the direction is relevant) applying the following algorithm.

1. According to the launching point and the direction of propagation, determine the proper time t of intersection between the ray and the inner or the outer sphere:

$$(x, y, z) = (x_n, y_n, z_n) + w_n t (\cos\phi_n, \sin\phi_n, 1). \qquad (A.11)$$

Care is needed in order to reject all trajectories passing through the core of the shell. Denote that point by $(x_{n+1}, y_{n+1}, z_{n+1})$. At the time of intersection $t_{n+1}, z_{n+1} = h_{in,out}(x_{n+1}, y_{n+1})$, while $w_n t_{n+1} = h(x_{n+1}, y_{n+1}) - z_n$, where h is intended from now on to be the intersection with the appropriate boundary (inner or outer shell) and the appropriate sign (northern or southern hemisphere). Then the horizontal coordinates (x_{n+1}, y_{n+1}) follow from simultaneous solution of the equations

$$x_{n+1} = x_n - (h(x_{n+1}, y_{n+1}) + z_n) \cos\phi_n \qquad (A.12)$$

$$y_{n+1} = y_n - (h(x_{n+1}, y_{n+1}) + z_n)\sin\phi_n \tag{A.13}$$

2. Determine the local gradient of the bottom:

$$\nabla h = (h_x(x_{n+1}, y_{n+1}), h_y(x_{n+1}, y_{n+1})), \tag{A.14}$$

which leads to slope $s = |\nabla h|$ and direction $\sigma = \tan^{-1}(h_y/h_x)$.

3. Determine the along-slope velocity component

$$v_{n+1} = v_n = w_n \sin(\phi_n - \sigma) \tag{A.15}$$

and the cross-slope velocity component

$$u_n = w_n \cos(\phi_n - \sigma), \tag{A.16}$$

from which follows

$$u_{n+1} = \frac{(1+s^2)u_n + 2sw_n}{1-s^2} \tag{A.17}$$

and the vertical velocity component

$$w_{n+1} = \frac{-2su_n - (1+s^2)w_n}{1-s^2}. \tag{A.18}$$

4. The angle $\phi_n - \sigma$ is the angle of incidence ϕ_i with respect to the local up-slope direction. From the horizontal velocity components in the cross- and along-slope direction follows the new direction with respect to the original frame of reference

$$\phi_{n+1} = \tan^{-1}(v_{n+1}/u_{n+1}) + \sigma \tag{A.19}$$

and the algorithm can be iterated.

B

GEOMETRIC DERIVATION OF A CLOSED TRAJECTORY: THE
BOW-TIE CASE

According to the reflection laws described in section 4.2.3, one of the simplest periodic trajectories we can think of is depicted in figure 4.3. In order to derive its parameters, it is worth remembering that the horizontal refraction law, equation (4.10), is valid only if angles are defined in the local reference framework of reflection, as shown in figure 4.1c for a general case, and in figure B.1 for this specific trajectory. The latter is easily prescribed, the local positive x-axis corresponding to the line of local maximum bottom slope, pointing outwards. In figure B.1 the different local reference frameworks are referred to as (x, y), relative to the point P_0, (x', y'), relative to the point P_1 and (x'', y''), relative to the point P_2 and they are depicted as grey dashed lines. Moreover, we recall that in the used algorithm, in order to have rays that always move with an inclination of 45°with respect to the vertical, the surface of the sphere is deformed according to (4.9), depending on the perturbation frequency ω, and described therefore by

$$x^2 + y^2 + \lambda^2 z^2 = 1. \tag{B.1}$$

where λ is defined in (4.3). It is now possible to cast the problem in a system of equations, in order to evaluate analytically which combination of ω, x_0, ϕ_0 and γ_0 reproduces this trajectory. The orbit in figure B.1 has been constructed as follows: we prescribe a launching point, $P_0 = \{x_0, 0, 0\}$, that lies on the equatorial plane, an initial launching direction $\phi_0 = \pi/2$ and a negative sign of the initial vertical component of the group velocity ($\gamma_0 = -1$). In $P_1 = \{x_1, y_1, z_1\}$ a supercritical reflection takes place: the vertical component of the group velocity does not change its direction, $\gamma_1 = \gamma_0 = -1$, and the ray is refracted inwards, towards the central region of the sphere. By contrast, in $P_2 = \{x_2, y_2, z_2\}$, a subcritical reflection takes place, vertical velocity reverses its sign, $\gamma_2 = -\gamma_1 = 1$, and a defocusing reflection sends the trajectory back up, towards the outer part of the prolate spheroid.
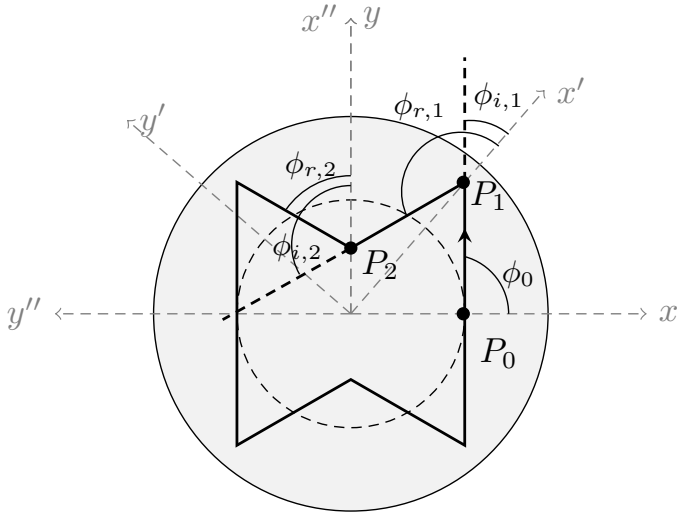
Figure B.1: Top view projection of bow tie orbit (solid) for $\omega^2 = 2/3$, obtained by three-dimensional ray tracing (as figure 4.3b). Inside (outside) the dashed circle rays reflect subcritically (supercritically) from the bounding sphere. Launching point is at P_0 (on the equatorial plane), initial ray vertical direction is downward, while horizontal direction is ϕ_0. The ray is thus travelling in the direction indicated by the black arrow. The two reflection points in the first quadrant are P_1 (in the supercritical area, southern hemisphere) and P_2 (in the subcritical area, southern hemisphere). The three points are depicted together with their local reference framework (denoted with a corresponding number of primes) where angles of incidence (ϕ_i) and reflection (ϕ_r) are also defined, in the appropriate reference framework.

For symmetry reasons, we can restrict the study to the first quadrant of the x, y-plane, setting the condition that a reflection occurs in P_2 that is perfectly symmetric with respect to the x''-axis (coinciding with the y-axis): the ray's path would therefore reproduce in the second quadrant (and in the Northern hemisphere) the mirrored pattern of the first one, and so on.

From P_0 the ray is moving parallel to the y-axis, with an inclination of 45° with respect to the z-axis (common for all reference frameworks), hence $x_1 = x_0$ and $z_1 = -y_1$.

Moreover, P_1 has to belong to the southern hemisphere of the spheroid, yielding

$$y_1^2 = \frac{1 - x_0^2}{1 + \lambda^2} \tag{B.2}$$

with $y_1 > 0$. Then, we prescribe P_2 to lie on the y-axis, $x_2 = 0$, and to be part of the southern hemisphere of the spheroid as well:

$$y_2^2 + \lambda^2 z_2^2 = 1 \tag{B.3}$$

with $z_2 < 0$. The ray connecting P_1 and P_2 forms an angle of 45° with the vertical, therefore it follows that the projection on the horizontal plane of the segment connecting the two points is equivalent in length to the projection on the vertical plane of the same segment. Since the length of this segment is invariant under rotation of the reference framework and equal to $\sqrt{x_0^2 + (y_1 - y_2)^2}$, we can write

$$z_2 = z_1 - \sqrt{x_0^2 + (y_1 - y_2)^2} = -y_1 - \sqrt{x_0^2 + (y_1 - y_2)^2}. \tag{B.4}$$

According to the horizontal refraction law (4.10), a horizontally symmetric subcritical reflection (as the one needed in P_2) occurs when the incident direction in the local reference framework, ϕ_i, satisfies

$$\phi_i = \cos^{-1}(-s) \tag{B.5}$$

where $s = |\nabla H|$ represents the local bottom slope. In that case $\sin \phi_r = \sin \phi_i$, implying $\phi_r = \pi - \phi_i$. Since, as can be seen in figure B.1,

$$\phi_{i,2} = \phi_{r,1} - \phi_{i,1}, \tag{B.6}$$

where the second subscript corresponds to the framework of the definition of the angle, a symmetric subcritical reflection will occur in P_2 only if

$$\phi_{r,1} = \cos^{-1}(-s_2) + \phi_{i,1} \tag{B.7}$$

with

$$\phi_{i,1} = \pi/2 - \tan^{-1}(y_1/x_0). \tag{B.8}$$

This implies

$$\sin(\phi_{i,1}) = 1/\sqrt{1 + (\tfrac{y_1}{x_0})^2}$$
$$\cos(\phi_{i,1}) = 1/\sqrt{1 + (\tfrac{x_0}{y_1})^2}$$

(B.9)

Knowing that the reflection in P_1 must be supercritical, equation (4.10) reads:

$$\frac{\sin(\phi_{r,1})}{\sin(\phi_{i,1})} = \frac{s_1^2 - 1}{1 + 2s_1\cos(\phi_{i,1}) + s_1^2}.$$

(B.10)

Using (B.2),(B.7) and (B.8) and the local bottom slopes:

$$s_1 = \frac{\sqrt{1 - \lambda^2 y_1^2}}{\lambda^2 |y_1|}$$
$$s_2 = \frac{y_2}{\lambda^2 |z_2|},$$

(B.11)

equation (B.10) can then be rewritten in terms of point coordinates only, and yields:

$$\frac{y_2}{\lambda^2 |z_2|} - \frac{y_1}{x_0}\sqrt{1 - (\frac{y_2}{\lambda^2 |z_2|})^2} = \frac{-1 + \lambda^2(1 - x_0^2)}{1 + \lambda^2(1 - x_0^2)}.$$

(B.12)

The last condition relates the position of P_1 to the angle of incidence required at P_2. Indeed $x_0\ (= x_1)$ has to satisfy the condition

$$x_0 = \sqrt{x_0^2 + (y_1 - y_2)^2}\,\sin(\cos^{-1}(-s_2)).$$

(B.13)

Using that

$$\sin(\cos^{-1}(-s_2)) = \sqrt{1 - s_2^2},$$

(B.14)

it follows that

$$\frac{x_0^2}{(y_2 - y_1)^2} = \frac{\lambda^2}{y_2^2} - (1 + \lambda^2).$$

(B.15)

Equations (B.2), (B.3), (B.4), (B.12) and (B.15) now form a system in $(x_0, \lambda, y_1, y_2, z_2)$ that can be solved analytically:

$$\begin{cases} x_0 = 1/\sqrt{3} \\ \lambda = 1/\sqrt{2} \\ y_1 = 2/3 \\ y_2 = 1/3 \\ z_2 = -4/3. \end{cases}$$

(B.16)

The corresponding eigenfrequency for this closed orbit, following from the value of λ, is $\omega = \sqrt{2/3}$.

When $\omega^2 < 1/2$ the sphere is transformed into an oblate spheroid, according to (4.9). We have noticed that in this case, if a polygon or star-shaped periodic trajectory exists at a certain frequency $\hat{\omega}$, it crosses the equatorial plane at $P = \{x_{eq}, 0, 0\}$ with x_{eq} given by:

$$x_{eq} = \sqrt{\frac{1 - 2\hat{\omega}^2}{1 - \hat{\omega}^2}} \tag{B.17}$$

and with a direction $\phi_{eq} = \pi/2$. Remarkably, the value of the Cartesian coordinate x_{eq} corresponds to the eccentricity ϵ of the stretched spheroid obtained using (4.9). It follows that $\pm\epsilon$ corresponds also to the distance in the (x, z) or (y, z)-plane of the foci of the ellipse from the centre. The full set of parameters needed for the periodic trajectory then immediately follows:

$$\begin{cases} \hat{\omega} \\ \vec{x}_0 = \{x_{eq}, 0, 0\} \\ \phi_0 = \pi/2 \\ \gamma_0 = \pm 1 \end{cases} \tag{B.18}$$

where the sign of the vertical group velocity will only determine the direction of propagation of the ray.

Moreover, for polygon-shaped orbits, it is also possible to predict a valid set of parameters ω, x_0, ϕ_0 and γ_0 with x_0 part of the boundary and in particular of the critical latitude θ_c. Giving the eigenfrequency $\hat{\omega}$, the distance from the rotation axis r_{θ_c} of the critical latitude θ_c is

$$r_{\theta_c} = \sqrt{1 - \hat{\omega}^2}. \tag{B.19}$$

The launching direction ϕ_0 at the critical latitudes, then, immediately follows according to the number of sides (L) constituting the polygonal top view shape of the orbit. The full set of parameters needed for the periodic trajectory then reads:

$$\begin{cases} \hat{\omega} \\ \vec{x}_0 = \{r_{\theta_c}, 0, \sqrt{1 - r_{\theta_c}^2}\} \\ \phi_0 = \pi - \pi/L \\ \gamma_0 = -1. \end{cases} \tag{B.20}$$

Here $z_0 > 0$ and $\gamma_0 < 0$, since we are assuming the launching point is on the Northern hemisphere.

Looking at figure 4.4, it is clear that these simple rules have helped the authors to visualize a larger set of periodic orbits in the low frequency regime ($\omega^2 < 1/2$) than in the high frequency regime. However, these rules can only be applied once the geometrical pattern of an orbit (number of vertices, winding number) is known or can be predicted, which enabled the visualisation of periodic trajectories only for the polygon and star families, because of their regularity and their monotonic behaviour with frequency (i.e. the number of vertices of the polygon decreases with frequency). The key role played by the critical circles has also been of help.

BIBLIOGRAPHY

Aldridge, K. D. and Toomre, A. (1969). Axisymmetric inertial oscillations of a fluid in a rotating spherical container. *Journal of Fluid Mechanics*, **37**, 307–323.

Alford, M. H. (2003). Improved global maps and 54-year history of wind-work on ocean inertial motions. *Geophysical Research Letters*, **30**(8), 1424.

Alford, M. H. and Zhao, Z. (2007a). Global Patterns of Low-Mode Internal-Wave Propagation. Part I: Energy and Energy Flux. *Journal of Physical Oceanography*, **37**(7), 1829–1848.

Alford, M. H. and Zhao, Z. (2007b). Global Patterns of Low-Mode Internal-Wave Propagation. Part II: Group Velocity. *Journal of Physical Oceanography*, **37**(7), 1849–1858.

Alford, M. H., Gregg, M. C., Zervakis, V., and Kontoyiannis, H. (2012). Internal wave measurements on the Cycladic Plateau of the Aegean Sea. *Journal of Geophysical Research*, **117**, C01015, doi:10.1029/2011JC007488.

Alford, M. H., Peacock, T., MacKinnon, J. a., Nash, J. D., Buijsman, M. C., Centuroni, L. R., Chao, S.-Y., Chang, M.-H., Farmer, D. M., Fringer, O. B., Fu, K.-H., Gallacher, P. C., Graber, H. C., Helfrich, K. R., Jachec, S. M., Jackson, C. R., Klymak, J. M., Ko, D. S., Jan, S., Johnston, T. M. S., Legg, S., Lee, I.-H., Lien, R.-C., Mercier, M. J., Moum, J. N., Musgrave, R., Park, J.-H., Pickering, A. I., Pinkel, R., Rainville, L., Ramp, S. R., Rudnick, D. L., Sarkar, S., Scotti, A., Simmons, H. L., St Laurent, L. C., Venayagamoorthy, S. K., Wang, Y.-H., Wang, J., Yang, Y. J., Paluszkiewicz, T., and (David) Tang, T.-Y. (2015). The formation and fate of internal waves in the South China Sea. *Nature*, **521**(7550), 65–69.

Arras, P., Flanagan, E. E., Morsink, S. M., Schenk, A. K., Teukolsky, S. A., and Wasserman, I. (2003). Saturation of the r-mode instability. *The Astrophysical Journal*, **591**, 1129–1151.

Ascani, F., Firing, E., Dutrieux, P., McCreary, J., and Ishida, A. (2010). Deep Equatorial Ocean Circulation Induced by a Forced-Dissipated Yanai Beam. *Journal of Physical Oceanography*, **40**(5), 1118–1142.

Baines, P. G. (1971). The reflexion of internal/inertial waves from bumpy surfaces. *Journal of Fluid Mechanics*, **46**, 273–292.

Balona, L. A., Bohm, T., Foing, B. H., Ghosh, K. K., Janot-Pacheco, E., Krisciunas, K., Lagrange, A.-M., Lawson, W. A., James, S. D., Baudrand, J., Catala, C., Dreux, M., Felenbok, P., and Hearnshaw, J. B. (1996). Line profile variations in γ Doradus. *MNRAS*, **281**(4), 1315–1325.

Barbosa Aguiar, A. C., Read, P. L., Wordsworth, R. D., Salter, T., and Hiro Yamazaki, Y. (2010). A laboratory model of Saturn's North Polar Hexagon. *Icarus*, **206**(2), 755–763.

Barcilon, V. (1968). Axi-symmetric inertial oscillations of a rotating ring of fluid. *Mathematika*, **93**, 93–102.

Baruteau, C. and Rieutord, M. (2013). Inertial waves in a differentially rotating spherical shell. *Journal of Fluid Mechanics*, **719**, 47–81.

Berry, M. V. (1981). Regularity and chaos in classical mechanics, illustrated by the three deformations of a circular "billiad". *European Journal of Physics*, **2**, 91–102.

Berry, M. V. (1987). Quantum chaology. *Proceedings of the Royal Society of London A*, **413**, 42–45.

Boulanger, J.-P. and Fu, L.-L. (1996). Evidence of boundary reflection of Kelvin and first-mode Rossby waves from TOPEX/POSEIDON sea level data. *Journal of Geophysical Research*, **101**(C7), 16361–16371.

Bourlès, B., Andrie, C., Gouriou, Y., Eldin, G., du Penhoat, Y., Freudenthal, S., Dewitte, B., Gallois, F., Chuchla, R., Baurand, F., Aman, A., and Kouadio, G. (2003). The deep currents in the Eastern Equatorial Atlantic Ocean. *Geophysical Research Letters*, **30**(5), 8002, doi:10.1029/2002GL015095.

Brandt, P., Rubino, A., and Fischer, J. (2002). Large-Amplitude Internal Solitary Waves in the North Equatorial Countercurrent. *Journal of Physical Oceanography*, **32**(5), 1567–1573.

Brandt, P., Funk, A., Hormann, V., Dengler, M., Greatbatch, R. J., and Toole, J. M. (2011). Interannual atmospheric variability forced by the deep equatorial Atlantic Ocean. *Nature*, **473**(7348), 497–500.

Bretherton, F. P. (1964). Low frequency oscillations trapped near the equator. *Tellus*, **16**(2), 181–185.

Broutman, D., Rottman, J. W., and Eckermann, S. D. (2004). Ray Methods for Internal Waves in the Atmosphere and Ocean. *Annual Review of Fluid Mechanics*, **36**(1), 233–253.

Bryan, G. H. (1889). The Waves on a Rotating Liquid Spheroid of Finite Ellipticity. *Proceedings of the Royal Society of London*, **45**, 42–45.

Buijsman, M. C., Klymak, J. M., Legg, S., Alford, M. H., Farmer, D., MacKinnon, J. a., Nash, J. D., Park, J.-H., Pickering, A., and Simmons, H. (2014). Three-Dimensional Double-Ridge Internal Tide Resonance in Luzon Strait. *Journal of Physical Oceanography*, **44**(3), 850–869.

Bunge, L., Provost, C., and Kartavtseff, A. (2007). Variability in horizontal current velocities in the central and eastern equatorial Atlantic in 2002. *Journal of Geophysical Research*, **112**, C02014, doi:10.1029/2006JC003704.

Bunge, L., Provost, C., Hua, B. L., and Kartavtseff, A. (2008). Variability at Intermediate Depths at the Equator in the Atlantic Ocean in 2000-06: Annual Cycle, Equatorial Deep Jets, and Intraseasonal Meridional Velocity Fluctuations. *Journal of Physical Oceanography*, **38**(8), 1794–1806.

Calkins, M. A., Noir, J., Eldredge, J. D., and Aurnou, J. M. (2010). Axisymmetric simulations of libration-driven fluid dynamics in a spherical shell geometry. *Physics of Fluids*, **22**(8), 086602.

Canziani, P. O., Holton, J. R., Fishbein, E., Froidevaux, L., and Waters, J. W. (1994). Equatorial Kelvin Waves: a UARS MLS view. *Journal of Atmospheric Sciences*, **51**(20), 3053–3076.

Canziani, P. O., Holton, J. R., Fishbein, E., and Froidevaux, L. (1995). Equatorial Kelvin wave variability during 1992-1993. *Journal of Geophysical Research*, **100**(D3), 5193–5202.

Cartan, M. E. (1922). Sur les petites oscillations d'une masse de fluide. *Bulletin des Sciences Mathématiques*, **46**, 317–369.

Carter, G. S., Gregg, M. C., and Lien, R.-C. (2005). Internal waves, solitary-like waves, and mixing on the Monterey Bay shelf. *Continental Shelf Research*, **25**(12-13), 1499–1520.

Chan, I. H. and Shepherd, T. G. (2013). Balance model for equatorial long waves. *Journal of Fluid Mechanics*, **725**, 55–90.

Chelton, D. B. and Schlax, M. G. (1996). Global observations of Oceanic Rossby Waves. *Science*, **272**(5259), 243–238.

Colin de Verdière, A. and Schopp, R. (1994). Flows in a rotating spherical shell: the equatorial case. *Journal of Fluid Mechanics*, **276**, 233–260.

Constantin, A. (2012a). An exact solution for equatorially trapped waves. *Journal of Geophysical Research*, **117**(C5), C05029, doi:10.1029/2012JC007879.

Constantin, A. (2012b). On the modelling of equatorial waves. *Geophysical Research Letters*, **39**, L05602, doi:10.1029/2012GL051169.

Constantin, A. and Germain, P. (2013). Instability of some equatorially trapped waves. *Journal of Geophysical Research: Oceans*, **118**(6), 2802–2810.

Courant, R. and Hilbert, D. (1953). *Methods of mathematical physics*, volume 1. Interscience, New York.

Cromwell, T. (1953). Circulation in a meridional plane in the central equatorial pacific. *Journal of Marine Research*, **12**, 196 – 213.

Cromwell, T., Montgomery, R. B., and Stroup, E. D. (1954). Equatorial under-current in pacific ocean revealed by new methods. *Science*, **119**, 648 – 649.

Cushman-Roisin, B. and Beckers, J. (2011). Equatorial Dynamics. In *Introduction to geophysical fluid dynamics: physical and numerical aspects*, volume 101, chapter 21, pages 643–663. Academic Press.

da Silva, J., Magalhaes, J., Gerkema, T., and Maas, L. R. M. (2012). Internal Solitary Waves in the Red Sea: An Unfolding Mystery. *Oceanography*, **25**(2), 96–107.

Dalziel, S. B., Hughes, G. O., and Sutherland, B. R. (2000). Whole-field density measurements by 'synthetic schlieren'. *Experiments in Fluids*, **28**(4), 322–335.

Dauxois, T. and Young, W. R. (1999). Near-critical reflection of internal waves. *Journal of Fluid Mechanics*, **390**(September 2000), 271–295.

Dengler, M. and Quadfasel, D. (2002). Equatorial Deep Jets and Abyssal Mixing in the Indian Ocean. *Journal of Physical Oceanography*, **32**(4), 1165–1180.

Dijkstra, H. A. (2008). *Dynamical oceanography*. Springer, Berlin.

Dijkstra, H. A. and Burgers, G. (2002). Fluid dynamics of El Niño Variability. *Annual Review of Fluid Mechanics*, **34**, 531–558.

Dintrans, B. and Ouyed, R. (2001). On Jupiter's inertial mode oscillations. *Astronomy & Astrophysics*, **375**, L47–L50.

Dintrans, B., Rieutord, M., and Valdettaro, L. (1999). Gravito-inertial waves in a rotating stratified sphere or spherical shell. *Journal of Fluid Mechanics*, **398**, 271–297.

Dong, C., McWilliams, J. C., Liu, Y., and Chen, D. (2014). Global heat and salt transports by eddy movement. *Nature Communications*, **5**, Article number: 3294, doi:10.1038/ncomms4294.

D'Orgeville, M., Hua, B. L., Schopp, R., and Bunge, L. (2004). Extended deep equatorial layering as a possible imprint of inertial instability. *Geophysical Research Letters*, **31**, L22303, doi: 10.1029/2004GL020845.

D'Orgeville, M., Hua, B. L., and Sasaki, H. (2007). Equatorial deep jets triggered by a large vertical scale variability within the western boundary layer. *Journal of Marine Research*, **65**, 1–25.

Drijfhout, S. and Maas, L. R. M. (2007). Impact of Channel Geometry and Rotation on the Trapping of Internal Tides. *Journal of Physical Oceanography*, **37**, 2740–2763.

Eckart, C. (1960). *Hydrodynamics of oceans and atmospheres*. Cambridge Monographs on Mechanics and Applied Mathematics. Pergamon Press, Oxford, London, New York and Paris.

Edwards, C. A. and Pedlosky, J. (1998). Dynamics of Nonlinear Cross-Equatorial Flow. Part I : Potential Vorticity Transformation. *Journal of Physical Oceanography*, **28**, 2382–2406.

Emery, W. J. and Thomson, R. E. (2001). *Data Analysis Methods in Physical Oceanography*. Elsevier Science, Amsterdam.

Eriksen, C. C. (1981). Deep Currents and their interpretation as Equatorial Waves in the Western Pacific Ocean. *Journal of Physical Oceanography*, **11**, 48–70.

Eriksen, C. C. (1982a). Geostrophic equatorial deep jets. *Journal of Marine Research*, **40**, 143–157.

Eriksen, C. C. (1982b). Observations of internal wave reflection off sloping bottoms. *Journal of Geophysical Research*, **87**, 525–538.

Eriksen, C. C. (1985). Implications of ocean bottom reflection for internal wave spectra and mixing. *Journal of Physical Oceanography*, **15**, 1145–1156.

Eriksen, C. C. (1998). Internal wave reflection and mixing at Fieberling Guyot. *Journal of Geophysical Research*, **103**(C2), 2977–2994.

Favier, B., Barker, A. J., Baruteau, C., and Ogilvie, G. I. (2014). Nonlinear evolution of tidally forced inertial waves in rotating fluid bodies. *MNRAS*, **439**(1), 845–860.

Fedorov, A. V. and Brown, J. N. (2009). Equatorial waves. In *Encyclopedia of Ocean Science*, pages 3679–3695. Academic Press, j. steele edition.

Firing, E. (1987). Deep zonal currents in the central equatorial Pacific. *Journal of Marine Research*, **45**(4), 791–812.

Friedlander, S. (1982). Internal waves in a rotating stratified fluid in arbitrary gravitational field. *Geophysical and Astrophysical Fluid Dynamics*, **19**, 267–291.

Friedlander, S. and Siegmann, W. L. (1982). Internal waves in a contained rotating stratified fluid. *Journal of Fluid Mechanics*, **114**, 123–156.

Fruman, M. D. (2009). Equatorially Bounded Zonally Propagating Linear Waves on a Generalized β Plane. *Journal of the Atmospheric Sciences*, **66**(9), 2937–2945.

Fruman, M. D., Hua, B. L., and Schopp, R. (2009). Equatorial Zonal Jet Formation through the Barotropic Instability of Low-Frequency Mixed Rossby-Gravity Waves, Equilibration by Inertial Instability, and Transition to Superrotation. *Journal of the Atmospheric Sciences*, **66**(9), 2600–2619.

Gallagher, I. and Saint-Raymond, L. (2007). *On the influence of the Earth's rotation on geophysical flows*, volume 4 of *Handbook of Mathematical Fluid Mechanics*. Academic Press, Amsterdam.

Galperin, B. (2004). The ubiquitous zonal jets in the atmospheres of giant planets and Earth's oceans. *Geophysical Research Letters*, **31**(13), L13303, doi:10.1029/2004GL019691.

Gerkema, T. and Exarchou, E. (2008). Internal-wave properties in weakly stratified layers. *Journal of Marine Research*, **66**(5), 617–644.

Gerkema, T. and Shrira, V. I. (2005). Near-inertial waves in the ocean: beyond the "traditional approximation". *Journal of Fluid Mechanics*, **529**, 195–219.

Gerkema, T. and Zimmerman, J. T. F. (2008). *An introduction to internal waves*. Lecture notes, Royal NIOZ, Texel.

Gerkema, T., Maas, L. R. M., and Lam, F.-P. A. (2004). Internal tides in the Bay of Biscay: conversion rates and seasonal effects. *Deep Sea Research II*, **51**(25-26), 2995–3008.

Gerkema, T., Zimmermann, J. T. F., Maas, L. R. M., and van Haren, H. (2008). Geophysical and astrophysical fluid dynamics beyond the traditional approximation. *Reviews of Geophysics*, **46**, RG2004, doi:10.1029/2006RG000220.

Giese, B. S. and Harrison, D. E. (1990). Aspects of the kelvin wave response to episodic wind forcing. *Journal of Geophysical Research: Oceans*, **95**(C5), 7289–7312.

Gilbert, D. and Garrett, C. (1989). Implications for ocean mixing of internal wave scattering off irregular topography. *Journal of Physical Oceanography*, **19**, 1716–1729.

Gill, A. E. (1971). The equatorial current in a homogeneous ocean. *Deep-Sea Research*, **18**, 421–431.

Gill, A. E. (1982). *Atmosphere–Ocean Dynamics*. Academic Press, San Diego, USA and London, UK.

Godfrey, D. A. (1988). A hexagonal feature around Saturn's north pole. *Icarus*, **76**(2), 335–356.

Gonella, J. (1972). A rotary-component method for analysing meteorological and oceanographic vector time series. *Deep-Sea Research*, **19**, 883–846.

Görtler, H. (1943). Uber eine schwingungserscheinung in flussigkeiten mit stabiler dichteschichtung. *Zeitschrift für angewandte Mathematik und Mechanik*, **23**, 165.

Gouriou, Y., Bourlès, B., Mercier, H., and Chuchla, R. (1999). Deep jets in the equatorial Atlantic Ocean. *Journal of Geophysical Research*, **104**(c9), 21217–21226.

Gouriou, Y., Andrie, C., Bourlès, B., Freudenthal, S., Arnault, S., Aman, A., and Eldin, G. (2001). Deep Circulation in the Equatorial Atlantic Océan. *Geophysical Research Letters*, **28**(5), 819–822.

Greenspan, H. P. (1968). *The theory of rotating fluids*. Cambridge Monographs on Mechanics and Applied Mathematics. Cambridge University Press, Cambridge.

Gregg, M. C., Sanford, T. B., and Winkel, D. P. (2003). Reduced mixing from the breaking of internal waves in equatorial waters. *Nature*, **422**(6931), 513–515.

Grisouard, N. and Bühler, O. (2012). Forcing of oceanic mean flows by dissipating internal tides. *Journal of Fluid Mechanics*, **708**, 250–278.

Gutzwiller, M. C. (1990). *Chaos in Classical and Quantum Mechanics*. Springer, New York.

Harlander, U. and Maas, L. R. M. (2006). Characteristics and energy rays of equatorially trapped, zonally symmetric internal waves. *Meteorologische Zeitschrift*, **15**(4), 439–450.

Harlander, U. and Maas, L. R. M. (2007). Internal boundary layers in a well-mixed equatorial atmosphere/ocean. *Dynamics of Atmospheres and Oceans*, **44**(1), 1–28.

Hayes, P. (1982). A comparison of geostrophic and measured velocities in the Equatorial Undercurrent. *Journal of Marine Research*, **40**, 219–229.

Hazewinkel, J. (2010). *Attractors in stratified fluids*. Phd thesis, Utrecht University.

Hazewinkel, J., Van Breevoort, P., Dalziel, S. B., and Maas, L. R. M. (2008). Observations on the wavenumber spectrum and evolution of an internal wave attractor. *Journal of Fluid Mechanics*, **598**, 373–382.

Hazewinkel, J., Tsimitri, C., Maas, L. R. M., and Dalziel, S. B. (2010). Observations on the robustness of internal wave attractors to perturbations. *Physics of Fluids*, **22**(10), 107102, doi: 10.1063/1.3489008.

Hazewinkel, J., Grisouard, N., and Dalziel, S. B. (2011a). Comparison of laboratory and numerically observed scalar fields of an internal wave attractor. *European Journal of Mechanics - B/Fluids*, **30**(1), 51–56.

Hazewinkel, J., Maas, L. R. M., and Dalziel, S. B. (2011b). Tomographic reconstruction of internal wave patterns in a paraboloid. *Experiments in Fluids*, **50**, 247–258.

Helland-Hansen, B. and Nansen, F. (1909). The Norwegian Sea - its Physical Oceanography based upon the Norwegian researches 1900-1904. *Report on Norwegian Fishery and Marine Investigations*, **2**.

Heller, E. J. (1984). Bound-state eigenfunctions of classically chaotic hamiltonian systems: Scars of periodic orbits. *Physical Review Letters*, **53**, 1515–1518.

Høiland, E. (1962). Discussion of a hyperbolic equation relating to inertia and gravitational fluid oscillations. *Geophysical Publications*, **26**, 211–227.

Hollerbach, R. (2003). Instabilities of the Stewartson layer Part 1. The dependence on the sign of Ro. *Journal of Fluid Mechanics*, **492**, 289–302.

Hollerbach, R., Futterer, B., More, T., and Egbers, C. (2004). Instabilities of the Stewartson layer Part 2 . Supercritical mode transitions. *Theoretical and Computational Fluid Dynamics*, **18**, 197–204.

Horn, W. and Meincke, J. (1976). Note on the tidal current field in the continental slope area of Northwest Africa. *Mémoires de la Société Royale des Sciences Liège*, **6**(9), 31–42.

Hua, B. L., Moore, D. W., and LeGentil, S. (1997). Inertial nonlinear equilibration of equatorial flows. *Journal of Fluid Mechanics*, **331**, 345–371.

Hua, B. L., D'Orgeville, M., Fruman, M. D., Menesguen, C., Schopp, R., Klein, P., and Sasaki, H. (2008). Destabilization of mixed Rossby gravity waves and the formation of equatorial zonal jets. *Journal of Fluid Mechanics*, **610**, 311–341.

Hughes, B. (1964). Effect of rotation on internal gravity waves. *Nature*, **201**(4921), 798–801.

IPCC (2014). *Climate Change 2014: Synthesis Report. Contribution of Working Groups I, II and III to the Fifth Assessment Report of the Intergovernmental Panel on Climate Change [Core Writing Team, R.K. Pachauri and L.A. Meyer (eds.)].* IPCC, Geneva, Switzerland.

Israeli, M. (1972). On trapped modes of rotating fluids in spherical shells. *Studies in Applied Mathematics*, **51**, 219–232.

Ivanov, P. B. and Papaloizou, J. C. B. (2010). Inertial waves in rotating bodies: a WKBJ formalism for inertial modes and a comparison with numerical results. *Monthly Notices of the Royal Astronomical Society*, **407**(3), 1609–1630.

Izumo, T. (2005). The equatorial undercurrent, meridional overturning circulation, and their roles in mass and heat exchanges during El Niño events in the tropical Pacific ocean. *Ocean Dynamics*, **55**(2), 110–123.

Jochum, M., Briegleb, B. P., Danabasoglu, G., Large, W. G., Norton, N. J., Jayne, S. R., Alford, M. H., and Bryan, F. O. (2013). The impact of oceanic near inertial waves on climate. *Journal of Climate*, **26**, 2833–2844.

John, F. (1941). The Dirichlet problem for hyperbolic equation. *American Journal of Mathematics*, **63**, 141–154.

Johnson, E. S. and McPhaden, M. J. (1993). Structure of intraseasonal Kelvin Waves in the Equatorial Pacific Ocean. *Journal of Physical Oceanography*, **23**, 608–625.

Joyce, T. M., Lukas, R., and Firing, E. (1988). On the hydrostatic balance and equatorial geostrophy. *Deep Sea Research*, **35**(8), 1255–1257.

Juliano, M. F. and Alves, M. L. G. R. (2007). The Atlantic Subtropical Front/Current Systems of Azores and St. Helena. *Journal of Physical Oceanography*, **37**(11), 2573–2598.

Kasahara, A. (2003). The Roles of the Horizontal Component of the Earth's Angular Velocity in Nonhydrostatic Linear Models. *Journal of the Atmospheric Sciences*, **60**(8), 1085–1095.

Koch, S., Harlander, U., Egbers, C., and Hollerbach, R. (2013). Inertial waves in a spherical shell induced by librations of the inner sphere: experimental and numerical results. *Fluid Dynamics Research*, **45**(3), 35504.

Kudlick, M. D. (1966). *On transient motions in a contained rotating fluid*. Phd thesis, MIT.

Kudrolli, A., Abraham, M. C., and Gollub, J. P. (2001). Scarred patterns in surface waves. *Physical Review E*, **63**(2), 1–8.

Kunze, E., Rosenfeld, L., Carter, G. S., and Gregg, M. C. (2002). Internal Waves in Monterey Submarine Canyon. *Journal of Physical Oceanography*, **32**(6), 1890–1913.

Lam, F.-P. A., Maas, L. R. M., and Gerkema, T. (2004). Spatial structure of tidal and residual currents as observed over the shelf break in the Bay of Biscay. *Deep-Sea Research I*, **51**, 1075–1096.

Laplace, P. S. (1878). *Oeuvres completes de Laplace*, volume 1. Gauthier-Villars, Paris.

Le Bars, M., Le Dizès, S., and Le Gal, P. (2007). Coriolis effects on the elliptical instability in cylindrical and spherical rotating containers. *Journal of Fluid Mechanics*, **585**, 323.

Le Bars, M., Cébron, D., and Le Gal, P. (2015). Flows Driven by Libration, Precession, and Tides. *Annual Review of Fluid Mechanics*, **47**, 163–193.

LeBlond, P. H. and Mysak, L. A. (1978). *Waves in the ocean*, volume 20 of *Elsevier Oceanography Series*. Elsevier Science Publishers, Amsterdam.

Lewis, B. M. and Hawkins, H. F. (1982). Polygonal eye walls and rainbands in hurricans. *Bulletin of the American Meteorological Society*, **63**(11), 1294–1300.

Lien, R.-C., D'Asaro, E. A., and McPhaden, M. J. (2002). Internal Waves and Turbulence in the Upper Central Equatorial Pacific : Lagrangian and Eulerian Observations. *Journal of Physical Oceanography*, **32**, 2619–2639.

Lighthill, M. J. (1969). Dynamic Response of the Indian Ocean to the onset of the Southwest Mosoon. *Philosophical Transactions of the Royal Society of London, Series A, Mathematical and Physical Sciences*, **265**(1159), 45–92.

Lockitch, K. H. and Friedman, J. L. (1999). Where are the r-modes of isentropic stars? *The Astrophysical Journal*, **521**(764-788).

Lord Kelvin (1877). On the Precessional Motion of a Liquid. *Nature*, **15**, 297–298.

Lord Kelvin (1880a). On an experimental illustration of minimum energy. *Nature*, **23**, 69–70.

Lord Kelvin (1880b). Vibrations of a columnar vortex. *Philosophical Magazine*, **10**(5), 155–168.

Ludescher, J., Gozolchiani, A., Bogachev, M. I., Bunde, A., Havlin, S., and Schellnhuber, H. J. (2013). Improved El Niño forecasting by cooperativity detection. *Proceedings of the National Academy of Sciences of the United States of America*, **110**(29), 11742–11745.

Lukas, R. and Firing, E. (1984). The geostrophlc balance of the Pacific Equatorial Undercurrent. *Deep Sea Research*, **31**(1), 1–6.

Lvov, Y. and Tabak, E. G. (2001). Hamiltonian formalism and the Garrett-Munk spectrum of internal waves in the ocean. *Physical Review Letters*, **87**, 168501, doi: 10.1103/PhysRevLett.87.168501.

Lvov, Y., Polzin, K. L., and Tabak, E. (2004). Energy Spectra of the Ocean's Internal Wave Field: Theory and Observations. *Physical Review Letters*, **92**(12), doi:10.1103/PhysRevLett.92.128501.

Maas, L. R. M. (2001). Wave focusing and ensuing mean flow due to symmetry breaking in rotating fluids. *Journal of Fluid Mechanics*, **437**, 13–28.

Maas, L. R. M. (2003). On the amphidromic structure of inertial waves in a rectangular parallelepiped. *Fluid Dynamics Research*, **373**, 373–401.

Maas, L. R. M. (2005). Wave attractors: linear yet nonlinear. *International Journal of Bifurcation and Chaos*, **15**(9), 2757–2782.

Maas, L. R. M. (2009). Exact analytic self-similar solution of a wave attractor field. *Physica D: Nonlinear Phenomena*, **238**(5), 502–505.

Maas, L. R. M. and Harlander, U. (2007). Equatorial wave attractors and inertial oscillations. *Journal of Fluid Mechanics*, **570**, 47–67.

Maas, L. R. M. and Lam, F.-P. A. (1995). Geometric focusing of internal waves. *Journal of Fluid Mechanics*, **300**, 1–41.

Maas, L. R. M., Benielli, D., Sommeria, J., and Lam, F.-P. A. (1997). Observation of an internal wave attractor in a confined, stably stratified fluid. *Nature*, **388**, 557–561.

Manders, A. M. M. and Maas, L. R. M. (2003). Observations of inertial waves in a rectangular basin with one sloping boundary. *Journal of Fluid Mechanics*, **493**, 59–88.

Manders, A. M. M. and Maas, L. R. M. (2004). On the three-dimensional structure of the inertial wave field in a rectangular basin with one sloping boundary. *Fluid Dynamics Research*, **35**, 1–21.

Matsuno, T. (1966). Quasi-Geostrophic Motions in the Equatorial Area. *Journal of the Meteorological Society of Japan*, **44**(1), 25–43.

McCartney, M. S. and Curry, R. A. (1993). Transequatorial flow of Antartic Bottom water in the western Atlantic Ocean: abyssal geostrophy a the Equator. *Journal of Physical Oceanography*, **23**, 1264–1276.

Mercier, M. J., Gostiaux, L., Helfrich, K., Sommeria, J., Viboud, S., Didelle, H., Ghaemsaidi, S. J., Dauxois, T., and Peacock, T. (2013). Large-scale, realistic laboratory modeling of M2 internal tide generation at the Luzon Strait. *Geophysical Research Letters*, **21**, 5704–5709.

Morize, C., Le Bars, M., Le Gal, P, and Tilgner, a. (2010). Experimental Determination of Zonal Winds Driven by Tides. *Physical Review Letters*, **104**(21), 28–31.

Moum, J. N., Chereskin, T. K., Park, M. M., and Regier, L. A. (1987). Monitoring geostrophic currents at the equator. *Deep Sea Research*, **34**(7), 1149–1161.

Muench, J. E. and Kunze, E. (1994). The potential vorticity of the Equatorial Deep Jets. *Journal of Physical Oceanography*, **24**, 418–428.

Muench, J. E. and Kunze, E. (1999). Internal Wave Interactions with Equatorial Deep Jets. Part I: Momentum-Flux Divergences. *Journal of Physical Oceanography*, **29**(7), 1453–1467.

Muench, J. E. and Kunze, E. (2000). Internal Wave Interactions with Equatorial Deep Jets. Part II: Acceleration of the Jets. *Journal of Physical Oceanography*, **30**(8), 2099–2110.

Münnich, M. (1996). The influence of bottom topography on internal seiches in stratified media. *Dynamics of Atmospheres and Oceans*, **23**, 257–266.

New, A. L. and Pingree, R. D. (1992). Local generation of internal soliton packets in the central Bay of Biscay. *Deep Sea Research*, **39**(9), 1521–1534.

Nikurashin, M. and Ferrari, R. (2013). Overturning circulation driven by breaking internal waves in the deep ocean. *Geophysical Research Letters*, **40**(12), 3133–3137.

Nöckel, J. U. (1997). *Resonances in Nonintegrable Open Systems*. Ph.D. thesis, Yale University.

Nöckel, J. U., Stone, A. D., Chen, G., Grossman, H. L., and Chang, R. K. (1996). Directional emission from asymmetric resonant cavities. *Optical Letters*, **21**, 1609–1611.

Noir, J. and Cébron, D. (2013). Precession-driven flows in non-axisymmetric ellipsoids. *Journal of Fluid Mechanics*, **737**, 412–439.

Noir, J., Brito, D., Aldridge, K., and Cardin, P. (2001). Experimental evidence of inertial waves in a precessing spheroidal cavity. *Geophysical Research Letters*, **28**(19), 3785–3788.

Noir, J., Hemmerlin, F., Wicht, J., Baca, S., and Aurnou, J. (2009). An experimental and numerical study of librationally driven flow in planetary cores and subsurface oceans. *Physics of the Earth and Planetary Interiors*, **173**, 141–152.

Nurijanyan, S., Bokhove, O., and Maas, L. R. M. (2013). A new semi-analytical solution for inertial waves in a rectangular parallelepiped. *Physics of Fluids*, **25**(12), 126601, doi: 10.1063/1.4837576.

Ogilvie, G. I. (2005). Wave attractors and the asymptotic dissipation rate of tidal disturbances. *Journal of Fluid Mechanics*, **543**, 19–44.

Ogilvie, G. I. and Lin, D. N. C. (2004). Tidal dissipation in rotating giant planets. *The Astrophysical Journal*, **610**, 477–509.

Olbers, D. and Eden, C. (2013). A Global Model for the Diapycnal Diffusivity Induced by Internal Gravity Waves. *Journal of Physical Oceanography*, **43**(8), 1759–1779.

Ollitrault, M. and Colin de Verdière, A. (2014). The Ocean General Circulation near 1000-m Depth. *Journal of Physical Oceanography*, **44**(1), 384–409.

O'Neill, K. (1984). Equatorial Velocity Profiles. Part I: Meridional Component. *Journal of Physical Oceanography*, **14**, 1829–1841.

O'Neill, K. and Luyten, J. (1984). Equatorial Velocity profiles. Part II: Zonal Component. *Journal of Physical Oceanography*, **14**, 1842–1852.

Pedlosky, J. (1982). *Geophysical fluid dynamics*. Springer-Verlag, New York and Berlin.

Percival, D. B. (1993). *Spectral analysis for physical applications*. Cambridge University Press, Cambridge and New York, USA.

Philander, S. G. (1990). *El Niño, La Niña and the Southern Oscillations*, volume 46 of *International Geophysics Series*. Academic Press, California, elsevier edition.

Philander, S. G. H. (1973). Equatorial undercurrent: measurements and theories. *Reviews of Geophysics and Space Physics*, **2**, 513–570.

Philander, S. G. H. (1980). The equatorial undercurrent revisited. *Annual Review of Earth and Planetary Sciences*, **8**, 191–204.

Phillips, O. M. (1963). Energy transfer in rotating fluids by reflection of inertial waves. *Physics of Fluids*, **6**, 513–520.

Phillips, O. M. (1966). *The Dynamics of the Upper Ocean*. Mechanics and Applied Mathematics. Cambridge University Press, Cambridge.

Picaut, J., Hayes, P., and McPhaden, M. J. (1989). Use of the Geostrophic Approximation to Estimate Time-Varying Zonal Currents at the Equator. *Journal of Geophysical Research*, **94**, 3228–3236.

Ponte, R. M. and Luyten, J. (1989). Analysis and Interpretation of Deep Equatorial Currents in the Central Pacific. *Journal of Physical Oceanography*, **19**, 1025–1038.

Rao, R. R., Girish Kumar, M. S., Ravichandran, M., Rao, A. R., Gopalakrishna, V. V., and Thadathil, P. (2010). Interannual variability of Kelvin wave propagation in the wave guides of the equatorial Indian Ocean, the coastal Bay of Bengal and the southeastern Arabian Sea during 1993-2006. *Deep Sea Research I*, **57**(1), 1–13.

Raymond, W. H. (2001). Kelvin waves: rotationally induced circulations. *Dynamics of Atmospheres and Oceans*, **34**(1), 23–43.

Reppin, J., Schott, F. A., Fischer, J., and Quadfasel, D. (1999). Equatorial currents and transports in the upper central Indian Ocean: Annual cycle and interannual variability. *Journal of Geophysical Research*, **104**(C7), 15495–15514.

Richards, K. J. and Banks, H. (2002). Characteristics of interleaving in the western equatorial Pacific. *Journal of Geophysical Research*, **107**(C12), 3231, doi:10.1029/2001JC000971.

Richardson, P. L. and Fratantoni, D. M. (1999). Float trajectories in the deep western boundary current and deep equatorial jets of the tropical Atlantic. *Deep Sea Research II*, **46**, 305–333.

Rieutord, M. (1991). Linear theory of rotating fluids using spherical harmonics part II, time-periodic flows. *Geophysical and Astrophysical Fluid Dynamics*, **59**, 185–208.

Rieutord, M. and Valdettaro, L. (1997). Inertial waves in a rotating spherical shell. *Journal of Fluid Mechanics*, **341**, 77–99.

Rieutord, M. and Valdettaro, L. (2010). Viscous dissipation by tidally forced inertial modes in a rotating spherical shell. *Journal of Fluid Mechanics*, **643**, 363.

Rieutord, M., Georgeot, B., and Valdettaro, L. (2000). Wave Attractors in Rotating Fluids: A Paradigm for Ill-Posed Cauchy Problems. *Physical Review Letters*, **85**(20), 4277–4280.

Rieutord, M., Georgeot, B., and Valdettaro, L. (2001). Inertial waves in a rotating spherical shell: attractors and asymptotic spectrum. *Journal of Fluid Mechanics*, **435**, 103–144.

Rieutord, M., Valdettaro, L., and Georgeot, B. (2002). Analysis of singular inertial modes in a spherical shell: the slender toroidal shell model. *Journal of Fluid Mechanics*, **463**, 345–360.

Roundy, P. E. and Janiga, M. a. (2012). Analysis of vertically propagating convectively coupled equatorial waves using observations and a non-hydrostatic Boussinesq model on the equatorial beta-plane. *Quarterly Journal of the Royal Meteorological Society*, **138**(665), 1004–1017.

Sauret, A., Cebron, D., Morize, C., and Le Bars, M. (2010). Experimental and numerical study of mean zonal flows generated by librations of a rotating spherical cavity. *Journal of Fluid Mechanics*, **662**, 260–268.

Schmid, C., Bourlès, B., and Gouriou, Y. (2005). Impact of the equatorial deep jets on estimates of zonal transports in the Atlantic. *Deep Sea Research II*, **52**(3-4), 409–428.

Schmidt, E. (2013). *Equatorial Wave Dynamics*. Master's thesis, Technische Universität München.

Schott, F. A., Dengler, M., Brandt, P., Affler, K., Fischer, J., Bourlès, B., Gouriou, Y., Molinari, R. L., and Rhein, M. (2003). The zonal currents and transports at 35°W in the tropical Atlantic. *Geophysical Research Letters*, **30**(7), 1349.

Scolan, H., Ermanyuk, E., and Dauxois, T. (2013). Non-linear fate of internal wave attractors. *Physical Review Letters*, **110**(23), 1–5.

Seelig, T. (2014). *Inertial wave propagation, focusing and mean flow excitation: theory and experiments.* Phd thesis, Brandenburg University of Technology Cottbus.

Seelig, T. and Harlander, U. (2014). Can meridionally propagating inertial waves drive a zonal mean flow? *Submitted to Tellus A*.

Send, U., Eden, C., and Schott, F. A. (2002). Atlantic equatorial deep jets: Space-time structure and cross-equatorial fluxes. *Journal of Physical Oceanography*, **32**, 891–902.

Shen, M. and Keller, J. (1975). Uniform Ray Theory of Surface, Internal and Acoustic Wave Propagation in a Rotating Ocean or Atmosphere. *SIAM Journal on Applied Mathematics*, **28**(4), 857–875.

Soares, J., Wainer, I., and Wells, N. C. (1999). Reflection of equatorial Kelvin waves at eastern ocean boundaries Part II: Pacific and Atlantic Oceans. *Annales Geophysicae*, **17**, 827.

St. Laurent, L. C. (2002). Estimating tidally driven mixing in the deep ocean. *Geophysical Research Letters*, **29**(23), 19–22.

St. Laurent, L. C., Toole, J. M., and Schmitt, R. W. (2001). Buoyancy Forcing by Turbulence above Rough Topography in the Abyssal Brazil Basin. *Journal of Physical Oceanography*, **31**, 3476–3495.

Stern, M. E. (1963). Trapping of low frequency oscillations in an equatorial "boundary layer". *Tellus*, **15**, 246–250.

Stewart, A. L. (2011). *The role of the complete Coriolis force in cross-equatorial transport of abyssal ocean currents*. Ph.D. thesis, University of Oxford.

Stewartson, K. (1971). On trapped oscillations of a rotating fluid in a thin spherical shell I. *Tellus*, **23**, 506–510.

Stewartson, K. (1972). On trapped oscillations of a rotating fluid in a thin spherical shell II. *Tellus*, **24**, 283–287.

Stewartson, K. and Rickard, J. A. (1969). Pathological oscillations of a rotating fluid. *Journal of Fluid Mechanics*, **35**, 759–773.

Stramma, L. and Schott, F. A. (1999). The mean flow field of the Tropical Atlantic Ocean. *Deep Sea Research II*, **46**, 279–303.

Sutherland, B. R., Dalziel, S. B., Hughes, G. O., and Linden, P. F. (1999). Visualization and measurement of internal waves by 'synthetic schlieren'. Part 1. Vertically oscillating cylinder. *Journal of Fluid Mechanics*, **390**, 93–126.

Swart, A., Manders, A. M. M., Harlander, U., and Maas, L. R. M. (2010). Experimental observation of strong mixing due to internal wave focusing over sloping terrain. *Dynamics of Atmospheres and Oceans*, **50**(1), 16–34.

Thomson, D. (1982). Spectrum estimation and harmonic analysis. *Proceedings of the IEEE*, **70**, 1055–1096.

Thomson, W. (1879). On gravitational oscillations of rotating water. *Proceedings of the Royal Society of Edinburgh*, **10**, 92–100.

Thorpe, S. A. (1997). On the Interactions of Internal Waves Reflecting from Slopes. *Journal of Physical Oceanography*, **27**, 2072–2078.

Thorpe, S. A. (1999). On the Breaking of Internal Waves in the Ocean. *Journal of Physical Oceanography*, **29**(9), 2433–2441.

Thorpe, S. A. (2001). On the Reflection of Internal Wave Groups from Sloping Topography. *Journal of Physical Oceanography*, **31**(1999), 3121–3126.

Tilgner, A. (2007). Zonal Wind Driven by Inertial Modes. *Physical Review Letters*, **99**(19), 1–4.

Turner, J. S. (1979). *Buoyancy Effects in Fluids*. Cambridge University Press, New York.

van Haren, H. (2005). Sharp near-equatorial transitions in inertial motions and deep-ocean step-formation. *Geophysical Research Letters*, **32**(1), L01605, doi:10.1029/2004GL021630.

van Haren, H. and Gostiaux, L. (2010). A deep-ocean Kelvin-Helmholtz billow train. *Geophysical Research Letters*, **37**(3), L03605, doi:10.1029/2009GL041890.

van Haren, H. and Gostiaux, L. (2012). Energy release through internal wave breaking. *Oceanography*, **25**(2), 124–131.

van Haren, H. and Millot, C. (2004). Rectilinear and circular inertial motions in the Western Mediterranean Sea. *Deep Sea Research I*, **51**(11), 1441–1455.

van Haren, H. and Millot, C. (2005). Gyroscopic waves in the Mediterranean Sea. *Geophysical Research Letters*, **32**(24), L24614, doi:10.1029/2005GL023915.

van Haren, H., Maas, L. R. M., and van Aken, H. M. (2002). On the nature of internal wave spectra near a continental slope. *Geophysical Research Letters*, **29**(12), 57–59.

van Haren, H., Gostiaux, L., Laan, M., Van Haren, M., and Van Haren, E. (2012). Internal Wave Turbulence Near a Texel Beach. *PloS ONE*, **7**(3), e32535. doi:10.1371/journal.pone.0032535.

Vantieghem, S., Cébron, D., and Noir, J. (2015). Latitudinal libration driven flows in triaxial ellipsoids. *Journal of Fluid Mechanics*, **771**, 193–228.

Wakata, Y. (2007). Frequency-Wavenumber Spectra of Equatorial Waves Detected from Satellite Altimeter Data. *Journal of Oceanography*, **63**, 483–490.

Wallace, J. and Kousky, V. E. (1968). Observational evidence of Kelvin Waves in the tropical Stratosphere. *Journal of Atmospheric Sciences*, **25**, 900–907.

Wang, B. and Rui, H. (1990). Dynamics of the coupled Moist Kelvin-Rossby Wave on an Equatorial beta-Plane. *Journal of the Atmospheric Sciences*, **47**, 397–413.

Weisberg, R. H. and Horigan, A. M. (1981). Low-frequency variability in the Equatorial Atlantic. *Journal of Physical Oceanography*, **11**, 913–920.

Weisberg, R. H., Horigan, A., and Colin, C. (1979). Equatorially trapped Rossby-gravity wave propagation in the Gulf of Guinea. *Journal of Marine Research*, **37**(1), 67–86.

Whitham, G. B. (1960). A note on group velocity. *Journal of Fluid Mechanics*, **9**, 347–352.

Whitham, G. B. (1974). *Linear and non linear waves*. John Wiley & Sons, New York.

Winters, K. B., Bouruet-Aubertot, P., and Gerkema, T. (2011). Critical reflection and abyssal trapping of near-inertial waves on a β-plane. *Journal of Fluid Mechanics*, **684**, 111–136.

Wu, Y. (2005a). Origin of Tidal Dissipation in Jupiter. I. Properties of Inertial Modes. *The Astrophysical Journal*, **635**, 674–687.

Wu, Y. (2005b). Origin of tidal dissipation in Jupiter. II. The value of Q. *The Astrophysical Journal*, **13**, 688–710.

Wunsch, C. (1968). On the propagation of internal waves up a slope. *Deep-Sea Research*, **15**, 251–258.

Wunsch, C. (1969). Progressive internal waves on slopes. *Journal of Fluid Mechanics*, **35**, 131–141.

Wunsch, C. and Ferrari, R. (2004). Vertical Mixing, Energy, and the General Circulation of the Oceans. *Annual Review of Fluid Mechanics*, **36**(1), 281–314.

Yang, C. and Giese, B. S. (2013). El Niño Southern Oscillation in an ensemble ocean reanalysis and coupled climate models. *Journal of Geophysical Research: Oceans*, **118**(9), 4052–4071.

Youngs, M. K. and Johnson, G. C. (2015). Basin-Wavelength Equatorial Deep Jet Signals Across Three Oceans. *Journal of Physical Oceanography*, **45**, 2134–2148.

Zhang, K., Earnsahw, P, Liao, X., and Busse, F. H. (2001). On inertial waves in a rotating fluid sphere. *Journal of Fluid Mechanics*, **437**, 103–119.

Zhang, K., Chan, K. H., Liao, X., and Aurnou, J. M. (2013). The non-resonant response of fluid in a rapidly rotating sphere undergoing longitudinal libration. *Journal of Fluid Mechanics*, **720**, 212–235.

Zhao, Z., Alford, M. H., MacKinnon, J. A., and Pinkel, R. (2010). Long-Range Propagation of the Semidiurnal Internal Tide from the Hawaiian Ridge. *Journal of Physical Oceanography*, **40**(4), 713–736.

Zheng, Q. (1995). Observation of equatorially trapped waves in the Pacific using Geosat altimeter data. *Deep Sea Research I*, **42**(5), 797–817.

LIST OF PUBLICATIONS

1. A. Rabitti, H. van Haren, T. Gerkema, and L. R. M. Maas (2015). Observational study of the "equatorial boundary layer" in the western Atlantic Ocean. submitted to *Journal of Marine Research*.

2. M. Lipizer, E. Partescano, A. Rabitti, A. Giorgetti, and A. Crise (2014). Qualified temperature, salinity and dissolved oxygen climatologies in a changing Adriatic Sea. *Ocean Science*, **10**(5), 771–797.

3. A. Rabitti and L. R. M. Maas (2014). Inertial wave rays in rotating spherical fluid domains. *Journal of Fluid Mechanics*, **758**, 621–654.

4. A. Rabitti and L. R. M. Maas (2013). Meridional trapping and zonal propagation of inertial waves in a rotating fluid shell. *Journal of Fluid Mechanics*, **729**, 445–470.

ACKNOWLEDGMENTS

Surely this whole doctoral experience would have been completely different, and poorer, with a promotor other than prof. Leo Maas. My deepest thanks go to him, who has welcomed me in the warmest way, and led me during these years with the enthusiasm of a person who is truly in love with what he does. His daily example of passion, dedication, imagination, curiosity, scientific rigour and out of the box-thinking has been a great motivation and inspiration to me. An extra thanks to Leo for promptly translating the abstract of this thesis. I would like to thank also Theo Gerkema and Hans van Haren, who always found the time for replying to my questions, discussing my work, and have always given sharp and constructive remarks on my work.

In the lonely life of a wannabe scientist, luckily, scientific discussions do not only occur with supervisors. For this, I would like to thank all the people, at NIOZ, at IMAU, at various conferences, summer schools, workshops, and elsewhere, who contributed to this work, answering my questions, asking me questions, suggesting new points of view and keeping me enthusiastic about what I was doing, about Oceanography and, in general, about the world of scientific research. Concerning enthusiasm, the captain(s), crew and technicians of the R/V Pelagia surely deserve a loud thanks, to be heard wherever they are at this moment. A special thanks to Prof. dr. Eric Gubel and Dominique Hoornaert from the Royal Museums of Art and History of Brussels for kindly providing me the picture on the cover.

I cannot help mentioning here a few other people that, besides their scientific (or other field's) expertise, have helped me daily with the challenging adventure of surviving in a foreigner country as the Netherlands, and in particular on Texel. Thanks for simply inviting me out for a spritz, wine or a beer, according to each one's local tradition, in no particular order: Matias, Sjoerd, Femke, Jenny, Jordy, Borja, Simona, Sara, Carlo, Alessandro, Alexandra, Dewi, Martina, Martina, Martina, Marta, Luca, Claudia, Roberta, Michela, Alvise, Sara, Marco, Roald, Meinard, Jurre, Carola, Laura, Janine, Leandro, Paolo, Michela, Daniele, Sofia, Costanza, Elisa, Moka. This has been my community during the last years, and I can only thank them all for having been the sunny part of my working days and weekends.

Last, thanks to Cima and to my family, who, in these years, have been supporting, understanding, and constantly close to me despite their highly variable spatial positions.

CURRICULUM VITAE

Anna Rabitti was born in Venice, Italy, on the 1st of January 1985. She attended the Liceo Classico Statale Marco Foscarini, where, with the help of the ancient Latin and Greek, she learned how to truly appreciate the Mediterranean Sea, its cultures, heroes, myths and cuisine. During the Summers, she sailed with her family in the northern Adriatic Sea and travelled the world. It came with no surprise then that, after the teachings of the ancient φιλόσοφοι, she committed herself with studying Physics, first at Padua University, then at Trieste University, slowly shifting her interests from the φύσις in general to the θάλασσα in particular, that constitutes still a vast field of research, but it is at least bounded (as we have seen in this thesis). After a Bachelor's Thesis on Plasma Physics at the RFX Consortium (Padua, Italy), she graduated with a Master's thesis in Physical Oceanography on her beloved Adriatic Sea at the OGS Istituto di Oceanografia e Geofisica Sperimentale (Trieste, Italy). Shortly afterwards, she moved to the Island of Texel (NL), at the NIOZ Royal Institute for Sea Research, surrounded by the cold, fresh and unknown North Sea, to unveil the secrets of the equatorial ocean. A spiced mix of islands, seas, currents and waves that has led her to complete this doctoral thesis.